In-Situ Investigation of Cavity Nucleation and Growth in Hydrogen-Exposed EPDM during Decompression

Mahak Fazal

THESE

Pour l'obtention du Grade de
DOCTEUR DE L'ECOLE NATIONALE SUPERIEURE DE MECANIQUE ET D'AEROTECHNIQUE
(Diplôme National – Arrêté du 25 mai 2016)

Ecole Doctorale :
Sciences et Ingénierie en Matériaux, Mécanique, Energétique

Secteur de Recherche :
Mécanique des Solides, des Matériaux, des Structures et des Surfaces

Présentée par :

Mahak FAZAL

****

IN-SITU INVESTIGATION OF CAVITY NUCLEATION AND GROWTH IN HYDROGEN-EXPOSED EPDM DURING DECOMPRESSION

****

Directrice de thèse : **Sylvie CASTAGNET**
Co-encadrant : **Shin NISHIMURA**

****
Soutenue le 04 Décembre 2019
devant la Commission d'Examen
****

JURY

Gerald PINTER,	Full Professor, Leoben University
Lucien LAIARINANDRASANA	Directeur de Recherche, Centre des Matériaux, Mines ParisTech
Olivier LAME	Professeur, laboratoire MATEIS, INSA de Lyon
Shin NISHIMURA	Professor, Hydrogenius Laboratory, Kyushu University
Sylvie GIRAULT	Ingénieur R&D, Arkema – ENSAM Paris
Azdine NAIT-ALI	Maître de Conférences ISAE-ENSMA, Institut Pprime
Sylvie CASTAGNET	Directrice de Recherche CNRS, Institut Pprime

Acknowledgements

This work, much like any other research project, is a result of hard work, guidance and support of many people and I would be remiss to not express my gratitude here.

I am grateful for the help and guidance from my director, Sylvie Castagnet and for her insistence that I pace myself while working and put down phone during writing. I am also thankful to Azdine for being an irreverent guide who has in fact taught me the most important lesson, that to have fun, to Mikael for his help with numerical simulations, to David and Guillaume for the experimental work. I am also grateful to the Hydrogenius team at Kyushu University for being such outstanding hosts during my stay at their lab.

To my friends in the lab (especially the B001 crew): thank you for the discussions both scientific and otherwise; they have helped me be sane in the lonely quest that PhD is. A big thank to Ravi for being my soundboard during the PhD and especially during thesis-writing, to Sylvie Girault for her time during the discussions about the SAXS technique.

I would have not been here without the unconditional support from my family. Faza and Saud, you are the source of my motivation for everything I undertake in life. Abu, Mom, thank you for being my most ardent cheerleaders.

Table of Contents

General introduction

The depletion of fossil fuels and environmental issues arising from using them has long since been a focus of studies leading to exploration of alternate sources of energy viable enough for commercial and daily use. In particular, the conventional vehicles using fossil fuels contribute much to the environmental pollution and therefore require an intensification in the developments of transportation with zero-emissions.

Consequently, fuel cell vehicles (FCVs) using energy derived from hydrogen have attracted a lot of attention recently as being an alternative means of transport and addressing the environmental issues at the same time. However, to ensure the adequate cruising range of FCVs, it is necessary to improve the volume energy density of hydrogen by storing the gas at a high pressure of 70 MPa. With this pressure in the fuel cell vehicle tank systems, a range of 600 km can be attained.

These relatively high pressures combined with the safety measures required for the usage of hydrogen itself pose serious challenges with respect to the seals in terms of material and design. These seals are used in various places in the equipment used for storage and transport of hydrogen as well as in the fuel recharging stations. The safety risk associated with hydrogen leakage makes specific demands on the rubber materials used as seals in terms of durability when exposed to repeated cycles of exposure to high-pressure hydrogen gas.

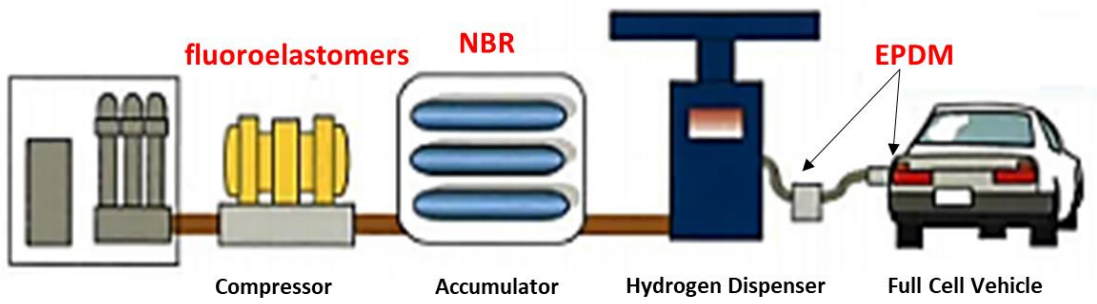

Figure i Illustration of various types of elastomers used as seals at various points of the hydrogen-FCV system (Nishimura 2014)

Figure i illustrates the use of different elastomers as sealing materials at different parts of the hydrogen production facility and the fueling station for the FCVs. Every sealing material has been chosen for a specific set of pressure and temperature conditions that it will be subjected to during usage.

EPDM, which is the material of focus in the present study, is used mainly in the form of O-rings at connectors and receptacles for charging the tanks of the FCVs and as such undergoes cyclic exposure to high pressure hydrogen leading to diffusion of the gas into the rubber followed by a rapid decompression to atmospheric pressure. These conditions lead to the formation of cavities and cracks in the rubber material, a damage that has previously been termed an explosive decompression failure in the literature. However, this term can be misleading since cavitation and blister fracture (see Figure ii) in elastomers is not limited to high pressures and fast pressure release.

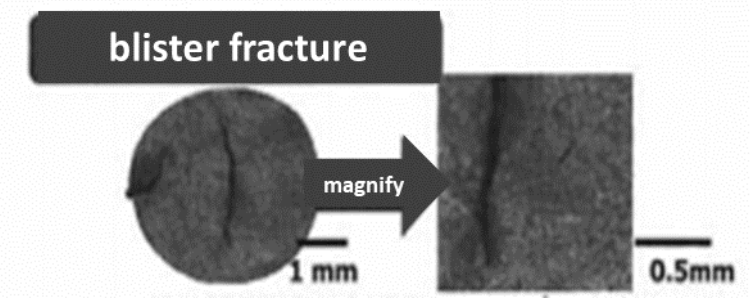

Figure ii. Blister fracture EPDM (Hs70) O-ring by exposure to hydrogen gas at 35 MPa and 100 °C for 15 hours (Nishimura 2014)

This thesis addresses this phenomenon of cavitation due to hydrogen exposure and subsequent decompression in EDPM. The rapid decompression results in multiple processes occurring inside the rubber materials which leads to loss of material coherence in the form of appearance of cavities. These cavities can appear as isolated ones in the bulk or within clusters depending on the exposure pressure and pressure release rate. In the latter case, they have been suspected to interact in the earlier studies, especially because cluster morphology evolves during cycling. The present study aims to utilize the new state of the art experiments that can shed light on this phenomenon of interaction of a cavity with another cavity and with a free surface, in a more efficient way. The interaction between cavities is an important factor of study since it could very well define the evolution of damage from cavitation to cracking. This is a first step towards building a robust model for prediction of failure as well as development of new materials with

optimized properties leading to better sealing materials for hydrogen fuel storage and delivery system.

This document is divided into 5 chapters. The first chapter introduces the concepts associated with the phenomenon of cavitation in elastomers and the corresponding studies in literature.

The second chapter describes the material of focus of the present study (Ethylene Propylene Diene Monomer) and details the mechanical parameters of the said material as well as the diffusion parameters of hydrogen in EPDM.

The third chapter is focused on the study of the heterogeneity of the EPDM-hydrogen system at sub-micron scale using Small Angle X-ray scattering. A correlation between the network heterogeneity of EPDM and nucleation of cavities is analysed with the help of novel in-situ tests. In addition, the changes of the network structure after hydrogen exposure are examined during and after complete desorption of hydrogen.

The fourth chapter describes the tracking of the cavitation so described at higher scales using the new technique of time resolved 3D X-Ray computer tomography. The focus is mainly on the effect of a free surface and on the interaction of cavities at the local scale; the parameters describing this interaction in terms of spatial and temporal evolution are detailed.

Finally the fifth chapter depicts the attempts to simulate the growth of cavities (isolated or close to another one) as a coupled problem of diffusion and mechanical pressure using the internal numerical tool Foxtrot developed at Institut Pprime. Since the tool is still in its early development stages, the simulation done here do not strictly adhere to the realistic experimental conditions in which the tests for the EPDM samples were conducted.

The present work was funded by the French Government program “Investissements d’Avenir” LABEX INTERACTIFS (reference ANR-11-LABX-0017-01). Additionally the tomography bench used in this study was funded by EQUIPEX GAP (reference ANR-11-EQPX-0018).

Chapter 1 Bibliography

This chapter focuses on the studies available in literature carried out on cavitation in elastomers to provide a background towards understanding the results obtained in the present thesis. In the first part, a brief introduction about the structure and mechanical properties of elastomers is given. Next, a global view on the studies of cavitation in literature is introduced and the later part is focused on the specific study of cavitation due to gas exposure in elastomers and the techniques to track this damage. Finally, the new ideas and experiments that will be addressed in this work are summarized with focus on the spaces in existing studies.

1.1 Molecular structure:

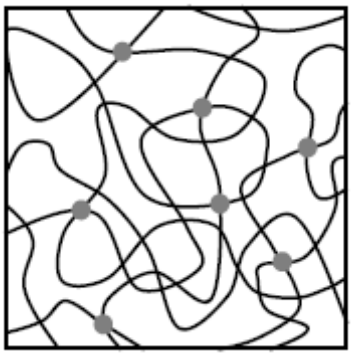

Figure1.1 Schematic representation of a network of cross-linked carbon chains (represented with gray circles).

Structurally, rubber is a macromolecule consisting of long molecular chains which are entangled and intertwined to form a network of non-uniform density. These entanglements act as physical cross-links thereby imparting certain rigidity to the network which otherwise retains freedom of movement between the long molecular chains, Figure 1.1. This relative mobility of chains is responsible for the large deformation of rubber which may be up to several 100 percent of the original dimensions. As a result, chemical crosslinking called vulcanization is introduced in order to enhance mechanical properties of rubber. This is done by creating chemical bonds or crosslinks between the long chains that restrict their relative motion and change the overall mechanical response of rubber. The magnitude of the modulus of elasticity is directly proportional to the density of the crosslinks. Stress–strain curves for vulcanized and un-vulcanized natural rubber are presented in Figure 1.2, and it can be seen that in the vulcanized rubbers the larger strain is accompanied by a sudden increase in the stress.

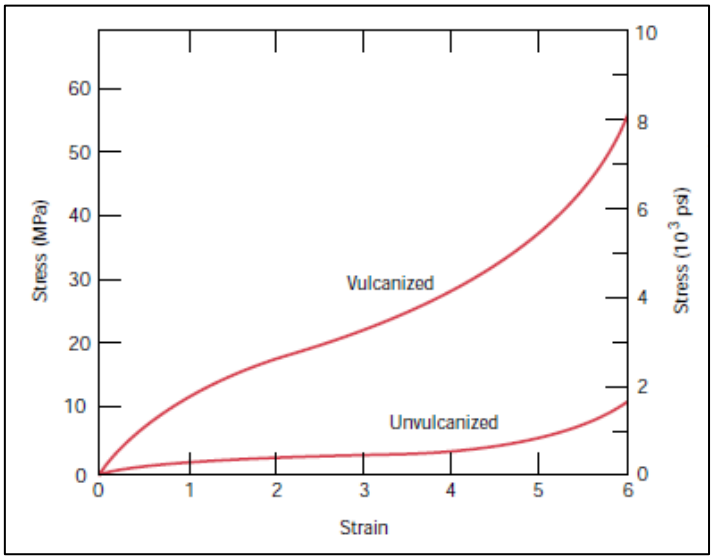

Figure1.2 Stress–strain curves for unvulcanized and vulcanized natural rubber upto 600% elongation (Callister and Rethwisch 2007)

The degree of crosslinking is expressed as “crosslink density". Conventionally, the crosslink density of rubber is measured by methods like gel fraction measurements, swelling tests, or shear modulus tests. As for the latter, the storage shear modulus (G') is related to the cross-link density v_c by the following equation

$$G' = v_c RT \qquad eqn\ 1.1$$

where R is the universal gas constant and T is the temperature. Plotting the storage modulus against temperature, the value of cross-link density can be measured by measuring the measuring the slope of the resulting curve (Jiang et al. 1999)

Crosslinking is also measured by swelling tests in which case the cross-linked samples are placed into a solvent at a specific temperature. Subsequently, the either the change in mass or the change in volume of the sample is measured. Thereafter, based on several parameters: the Flory Interaction Parameter, and the density of the polymer and the solvent, the theoretical degree of crosslinking can be calculated (Flory 1953).

As a consequence of cross-links, the movement of the long chains is restricted but molecular segments between the cross-links remain flexible. As such, the crosslink density affects the maximum extensibility of rubber. Only the rubber with relatively few and widely separated crosslinks is capable of large extensions without rupture of the primary chain bonds.

Since, the rubber molecules consist of folded and convoluted chains in the relaxed state, the molecular weight between the cross-links is an important parameter to characterise the cross-link density via the equation

$$\upsilon_c = \frac{\rho}{M_c} \qquad eqn\ 1.2$$

Where υ_c is the cross-link density, M_c is the average molecular weight between cross-links and ρ is the bulk density of the dry rubber.

Moreover, since these crosslinking points are created in non-uniform fashion throughout the network, there is an increase in the inhomogeneity of the structure microscopically, which is well known in literature to influence permeability and diffusion and consequently the elastic and swelling properties in polymer gels. Consequently, several studies consisting of X-ray scattering experiments can be found in literature to analyse the concentration heterogeneities in gels at submicron scales and their effects on their properties. The same techniques (SAXS, SANS) could be extended to characterize cross-linked rubber network at submicron scales which has been tackled in the later part of this chapter. Macroscopically, maximum deformation of the rubber varies with change in cross-link density which is a quantification of chemical cross-links in the rubber matrix. This is due to lower chain flexibility in rubbers with low cross-link density. Network heterogeneity has also been linked to improved physical properties in Poly-isoprene (Grobler and McGill 1994). Ono et al in their recent studies on unfilled NBR exposed to high pressure hydrogen showed that the bulk expansion of NBR samples due to hydrogen exposure varied linearly with the increase in the molecular weight between crosslinks of the NBR chains, M_c; the higher value of M_c corresponds to larger distances between cross-links and therefore low cross-link density. This linear relationship was true for both sulphur and peroxide cross-linked NBR (Ono, Fujiwara, and Nishimura 2018b).

1.2 Mechanical properties:

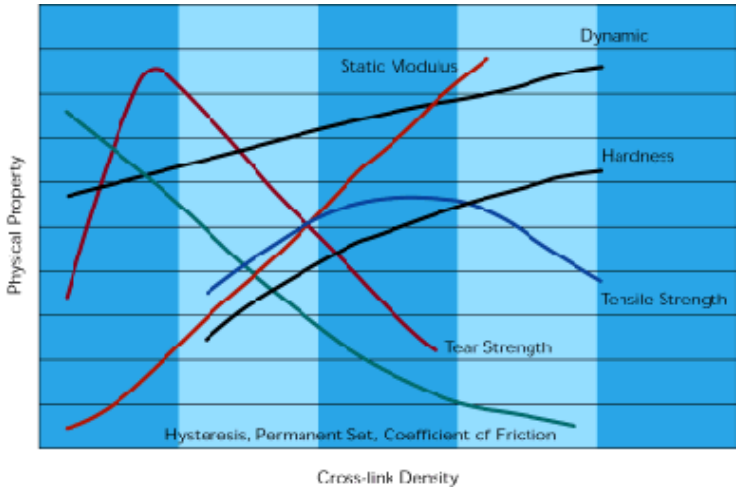

Figure 1.3 Effect of crosslink density on physical properties of vulcanized polymers (Thoguluva and Vijayaram 2019)

The mechanical properties of elastomers are not single valued functions of the chemical nature of their corresponding macromolecules. They vary in accordance with other factors such as degree of cross-linking, molecular weight, nature and amount of additives as well as temperature. For our study, most of the variables were kept constant; only the degree of cross-linking was varied, which in turn could affect the mechanical properties like hardness, modulus, and fatigue of the samples under study, see Figure 1.3.

Generally, elastomers are highly deformable and nearly incompressible with the Poisson's ratio ν close to 0.5. However, their properties depend more strongly on temperature and time of testing in comparison with metallic materials. This is due to the fact that as the temperature is sufficiently lowered, the elastomers become glassy and brittle and consequently lose the property of rapid recovery. This temperature at which the elastomers transition from rubbery to glassy state is called glass transition temperature. T_g is practically important as it sets a temperature range for the abrupt behavior changes due to local conformational changes leading to relaxation in elastomers and hence set a practical lower temperature limit for rubbery behavior of an elastomer. The transition of physical state of amorphous polymers with change in temperature varies with molecular weight as shown in Figure 1.4.

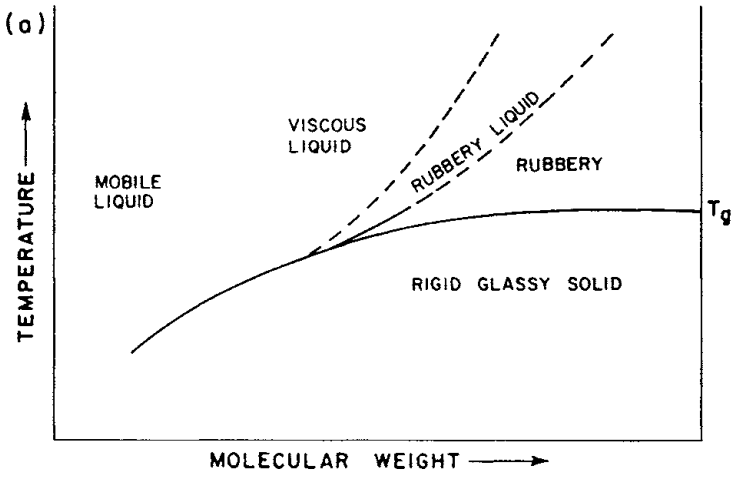

Figure 1.4 Relationship between temperature, molecular weight, and physical state for an amorphous polymer.(Rudin and Choi 2013)

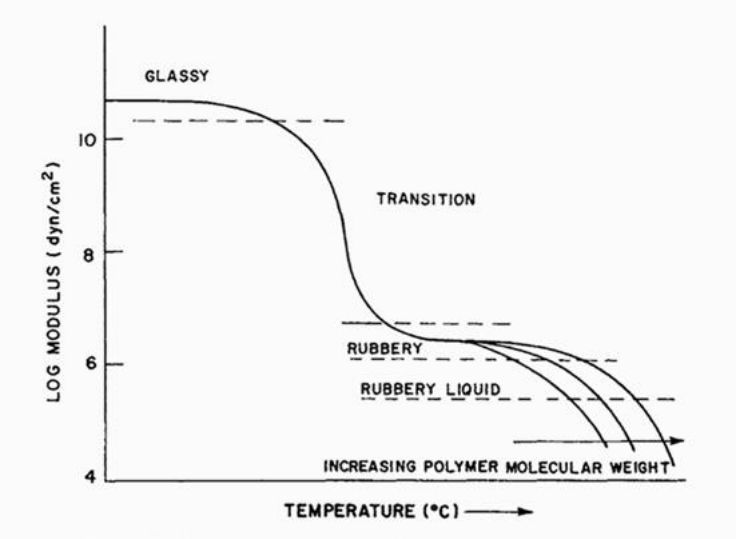

Figure 1.5 Relationship between temperature and modulus for an amorphous polymer

The modulus of elastomers varies as a function of temperature typically as is seen in Figure 1.5 and is a good indicator of their mechanical response. The degree of cross-linking affects the mechanical modulus of the uncross-linked elastomer as seen in Figure 1.6 in the rubbery plateau which is directly linked to the higher molecular weight elastomers that will have higher degree of entanglements. In case of cross-linked elastomers, the rubbery plateau region persists until the temperature is high enough to cause chemical degradation of the macromolecules as

seen in Figure 1.6. At very high cross-link densities, the mobility of chain segments is eliminated so that the material in the glassy state at all practical usage temperatures for example in some cases of phenolics (Rudin and Choi 2013).

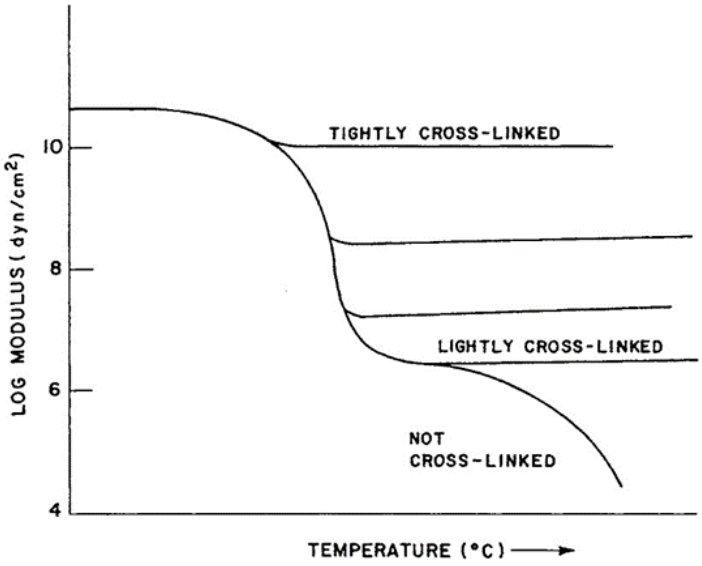

Figure 1.6 Variation of modulus of an amorphous polymer with temperature with varying cross-link density

1.2.1 Viscoelasticity:

Elastomers show the mechanical properties intermediate between Hookean solids and Newtonion liquids. The characteristic property of reversibility of elastomers on relaxation in elastic region is time dependent and is reflective of the testing conditions. This is termed as viscoelastic behavior. In fact, during cyclic tests this becomes evident in form of hysteresis loops that appear during the unloading part of the cycle.

1.2.2 Mullins effect:

Another characteristic of rubbers, which is more commonly observed in filled rubbers, is the Mullins effect which refers to the decrease in the stress, during cyclic loading, required to attain deformation of the same value the first cycle during subsequent cycles,. Microscopically, it is explained by the molecular structure of rubber with certain macromolecular chains having different extensibility which broken in the first cycle causing a softening effect (Diani, Fayolle, and Gilormini 2009).

1.2.3 Payne effect:

Similar to the Mullins effect at large deformation, Payne effect is observed for small deformations, especially in carbon black filled rubbers. Payne effect is observed under cyclic loading and refers to the decrease in storage modulus with increase in the strain amplitude. This effect is dependent on the filler content and is not observed in unfilled elastomers. (Payne 1962; Lion, Kardelky, and Haupt 2003; Chazeau et al. 2000).

1.3 Cavitation in elastomers: a global view

Cavitation in elastomers refers to the appearance of damage corresponding to the growth of defects present intrinsically in the rubber matrix. These intrinsic defects may either refer to the pre-existing sub-micron voids present in the rubber matrix as a result of network inhomogeneity or impurities that can cause local stress concentrations leading to nucleation of cavities under external stresses in an otherwise void less matrix. Roughly, under the application of sufficiently large external stresses, these defects grow elastically upto the maximum extensibility of surrounding macromolecular chains.

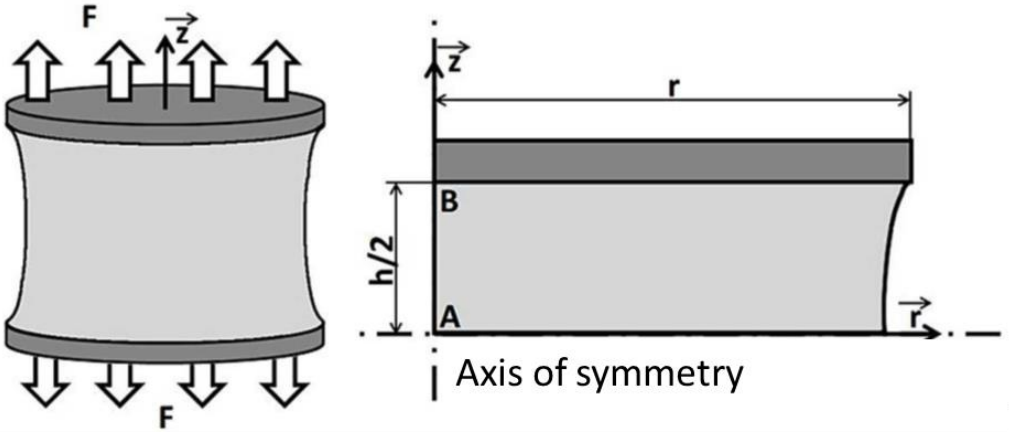

Figure 1.7 Schematic representation of the "Poker Chip Test" test (Gent, 1959)

This kind of damage in rubbers was first observed by Busse, Yerzley in the 1930s in samples under tension (Busse 1938; Yerzley 1939). In 1959, Gent conducted the poker chip test on carbon black filled rubber. The test consisted of subjecting a rubber sample glued between two

metal cylinders to uniaxial tension to generate hydrostatic stress at the centre of the sample, see Figure 1.7.

Analyzing the stress fields, the negative hydrostatic pressure was found to be maximum at the centre of the sample (at A in Figure 1.7) and was connected to the tensile stress exerted by the following relation:

$$\frac{F}{A} = \frac{1}{2} Tr(\bar{\bar{\sigma}}) \left(1 + 2\frac{h^2}{r^2}\right) \qquad eqn\ 1.3$$

Where F is the force exerted on the surfaces A of the metal cylinders, r and h are the radius and the height of the rubber sample respectively and $Tr(\bar{\bar{\sigma}})$ is the trace of the stress tensor at the centre of the sample. The appearance of cavitation was accompanied by the change of the slope in the tensile curve which varied with the thickness of the sample as shown in Figure 1.8.

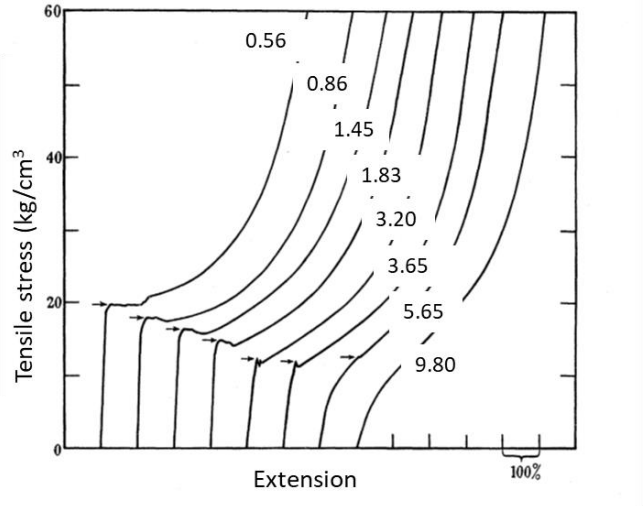

Figure 1.8 Relationship between load and elongation of the cylindrical sample of 10mm radius as a function of thickness (Gent and Lindley 1959)

This was due to the influence of geometry, more particularly due to the ratio between the radius and the height of the cylinder, on stress distribution in the sample. The central zone of the samples was dilated homogenously under negative hydrostatic pressure in samples of less thickness. With the increase in thickness of the sample, there was a greater decrease in the negative hydrostatic pressure in the centre of the sample for the same tensile stress, thereby decreasing the force required to induce cavitation. Figure 1.8 shows the evolution of the tensile stress as a function of the elongation of the samples with varying thicknesses showing the effect of the geometry of the samples on the curves.

They established a linear relationship between the elastic modulus and the hydrostatic pressure required to induce cavitation from the simple elasticity theory as

$$P_c = \frac{5}{6}E \qquad eqn\ 1.4$$

where P_c is the critical stress for appearance of cavitation and E is the elastic modulus, see Figure 1.9.

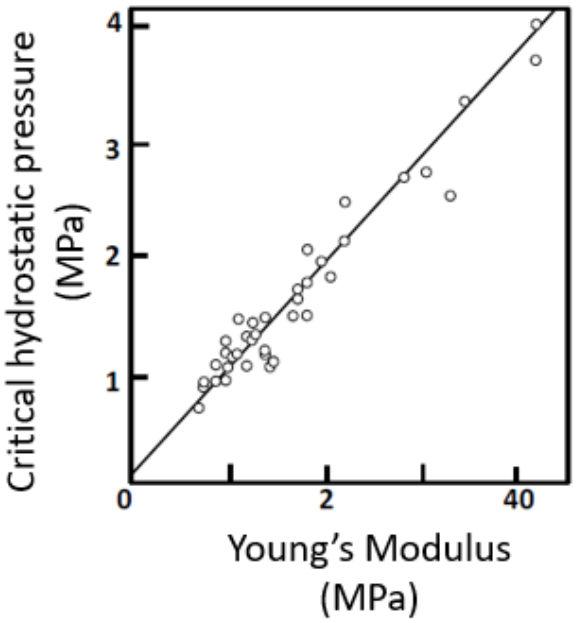

Figure1.9 Hydrostatic pressure required to have cavitation of the elastomer in function of the Young's modulus of the material (Gent and Lindley 1959)

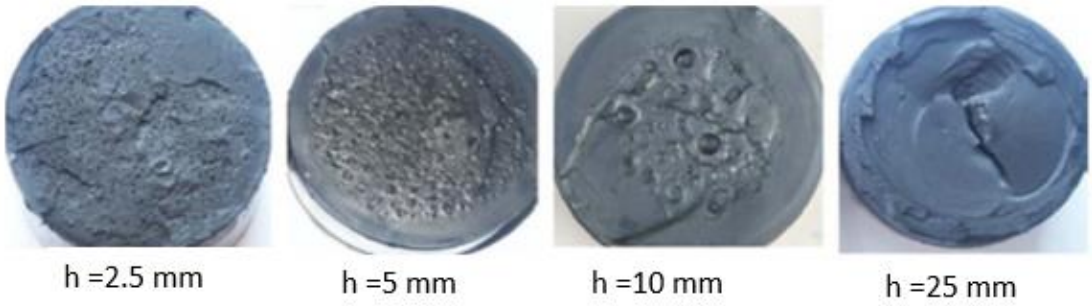

Figure 1.10 Fractured surfaces of styrene-butadiene rubber specimens of 100 mm diameter with varying thicknesses, h, subjected to uniaxial tension. (Hocine et al. 2011)

The morphology of damage is also influenced by the geometry of the sample as seen by Hocine et al in his study on carbon black-filled styrene-butadiene rubber (SBR) vulcanizate subjected to uniaxial tension as shown in Figure 1.10.

1.4 Modelling approaches

In their study, Gent and Lindley considered the initiation cavitation as an elastic instability, examining the problem as an elastic growth of an initial cavity of infinitesimal size embedded at the centre of a Neo-Hookean rubber ball under uniform hydrostatic pressure.

At the critical value of applied pressure, the cavity became finite. As the theoretical results agreed well with the experimental observations ones in their study, most of the work that followed was based on the same approach. (Oberth and Bruenner 1965; Gent and Park 1984; Lopez-pamies 2009; Nakamura and Lopez-Pamies 2012; Kabaria, Lew, and Cockburn 2015).

Williams and Schapery extended the radially symmetric calculation of Gent and Lindley (1959a,b), to include the Griffith approach (Griffith 1921) taking into consideration that the cavity surface stretches far more than the elastic values for rubber. They allowed for the cavity embedded at the centre of a Neo-Hookean ball of finite size to deform not only plastically but also by creation of new surfaces, treating cavitation as a fracture phenomenon. They also accounted for the surface energy associated with the surface area increase from cavity expansion (Williams and Schapery 1965). The relationship between the critical hydrostatic pressure P_{cr} and surface energy was expressed as follows:

$$P_{cr} = \mu\left[5/2 - \lambda_a^{-4}/2 - 2\lambda_a^{-1}\right] \qquad eqn\ 1.5$$

Where λ_a is the solution of the equation $C(\lambda_a) = \mu[2\lambda_a^{-1} - \lambda_a^2 - 1] + 2\gamma/a_0 = 0$; μ denotes the initial shear modulus of the Neo-Hookean medium and γ is the material constant denoting the surface energy per unit undeformed area that is created. The analysis takes into consideration the dependence of P_{cr} on the initial cavity size a_0 through the parameter $\kappa = 2\gamma/\mu a_0$. Assuming the range of values for parameters μ between 0.1 and 1 MPa, γ between 1 and 10 J/m^2, a_0 between 10^{-8} to 10^{-7} m and κ between 20 and 20,000 leading to P_{cr} between 2.045μ and 2.486μ. These values were quite same as that of Gent and Lindley. Most of the studies thereafter have followed the approach of Gent of treating cavitation as an elastic growth

of pre-existing defects. Lefevre et al carried out full field simulations of the Gent and Lindley, and Gent and Park experiments under the assumption of nonlinear elasticity of rubber specimens and the random and isotropic distribution of initial vacuous defects (Ravi-chandar and Lopez-pamies 2014). Their findings have agreed with the theories of Williams and Schapery (1965) the local stretches around the defects at which cavitation initiates far exceed the elastic limit of the rubber making it obvious that cavitation in rubber is primarily a fracture process. Moreover, their studies have indicated a need for more in depth experimental analysis to understand the phenomenon of cavitation in rubber.

From a modelling point of view, two different approaches are possible with respect to the origin of cavities: In the first approach cavitation is considered to be an expansion of pre-existing voids in the rubber matrix whereas in the second approach the cavities are presumed to be nucleated from an otherwise void-less material.

The second step in the classification is with respect to the scale of the modelling: i) at a local scale for a single cavity or ii) at macroscopic scale for the global field of cavities, taking into account both approaches of origin of cavities. In the first approach, a single cavity is assumed to be representative of the whole phenomenon for which a cavitation criteria is defined. This subsumes the cavities in the material to be far apart so as to not interact. The second approach necessitates an introduction of statistical damage variable for the distribution of cavities and implies a knowledge of the morphology of damage. In any case, it is necessary to predefine a representative element volume (REV) of damage for the modelling.

1.4.1 Single cavity models

Looking at the theoretical description of cavitation, Ball was among the first people to develop a robust mathematical representation of the cavitation phenomenon, taking into consideration the nonlinear elastic solids in addition to Neo-Hookean ones (Ball 1982). He considered the problem of a unit sphere with a spherical cavity embedded in it subjected to hydrostatic loading on its outer surface, Figure 1.11.

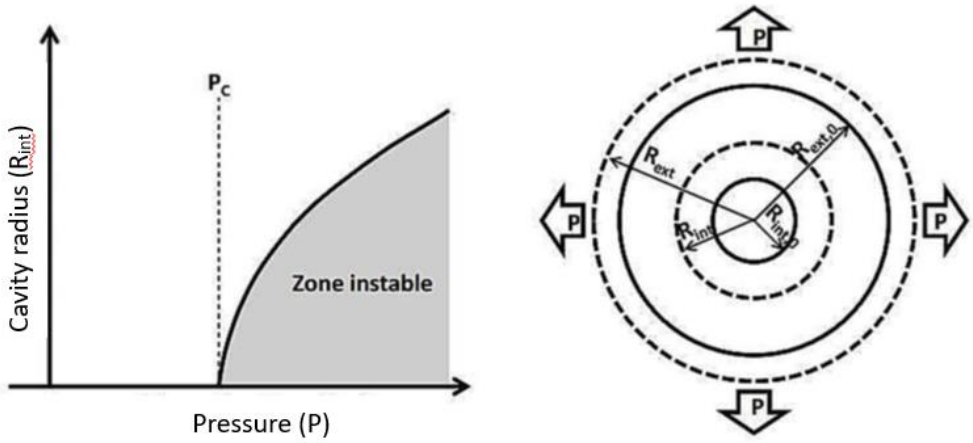

Figure1.11 Evolution of the inner radius of a spherical cavity (on the left and representation schematic of the evolution of the dimensions of the hollow sphere subjected to a negative hydrostatic pressure, P).

Through his calculations, he concluded that under a sufficiently large pressure, the nucleation of a spherical cavity at the centre of the sphere was favourable with respect to energy considerations. The evolution of potential energy E_{pot} of a hollow sphere with an initial radius R_{int0} under hydrostatic pressure can be determined as a function of the tangential elongation λ of the inner radius where $\lambda = R_{int}/R_{int0}$ and can be used to determine single or multiple allowable dimensions of the cavity (Dollhofer et al. 2004). The potential energy is calculated from the work due to tensile stress on the outer surface of the hollow sphere taking into consideration the contribution of the surface tension, which tends to prevent the opening of the cavity, and the energy density defined in equation:

$$E_{pot} = W + E_{\gamma} - W_{Pext} = \iiint_{R_{int}}^{R_{ext}} wdR + 4\pi\gamma R_{int}^2 + P_{ext}A_{ext}(R_{int} - R_{int0}) \qquad eqn\ 1.6$$

Where W is the strain energy calculated as the integral on the hollow sphere of the strain energy density w, E_{γ} is the surface energy, A_{ext} is the surface area of the hollow sphere REV and W_{Pext} is the work due to external stress. For lower mechanical pressures, this calculated energy has only an overall minimum, which corresponds a single possible cavity size. For larger values of mechanical pressures, there is a local maximum in addition to this global minimum, which implies several possible sizes of cavity. Dollhofer et al showed from their study that the surface tension plays a predominant role. The calculation performed with a cavity of 50 µm initial radius, and therefore with a contribution of the lower surface tension compared to a cavity 100 times smaller, showed that only one cavity size could be possible to attain a stable system, for

any imposed hydrostatic pressure (Dollhofer et al. 2004). The role of surface tension was confirmed by Muralidharan in his study on the evolution of the radius of cavities observed in-situ in an adhesive film (Muralidharan et al. 2006). He observed different growth kinetics for cavities of different initial size as seen in Figure 1.12. For the larger cavity, the growth is weak and constant in the initial stage whereas the smaller cavity barely shows any growth initially and later inflates rather fast until it reaches a size of 70 microns.

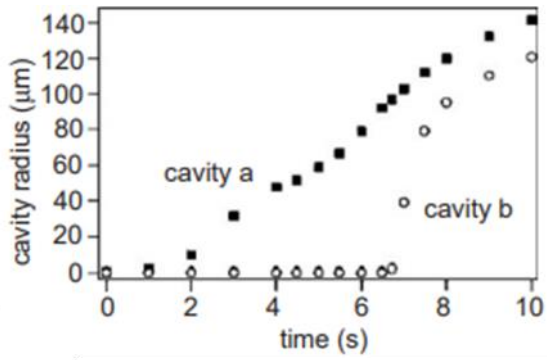

Figure1.12 Evolution of cavity radius with time obtained from a series of images taken with the video probe tack set-up of the PSA/glass interface during the loading process (Muralidharan et al. 2006).

On the other hand, the level of critical pressure obtained experimentally was larger than that predicted by the model in the same study. A possible explanation of this difference comes from the identification of the material parameters, as well as from the initial size of the cavity. This difference is also explained by the fact that the numerical model does not take into account the interactions between cavities. Subsequently this study was carried out compressible material (Murphy and Biwa 1997; Xin-Chun and Chang-Jun 2001), as well as viscous material (Lee and Mear 1994). Lopez-Pamies has developed an analytical criterion of cavity nucleation under tri-axial loading for example comparative to that of Ball (Lopez-pamies 2009). The comparison showed that the criterion of Ball was valid for some classes of materials (compressible, isotropic, hyper-elastic).On the other hand, this criterion can not be generalized as it is based on taking only one cavity into account. This brings the question of the representativeness of the cavity unique for cavitation models.

In this same context, Lopez-Pamies et al also studied the influence of tri-axial loading on the shape of the generated cavities (Nakamura and Lopez-Pamies 2012). The non-spherical shape

of the obtained cavities Figure 1.13, confirms that the appearance of cavities in nonlinear elastic materials depends on applied tri-axial loading and not just the hydrostatic component.

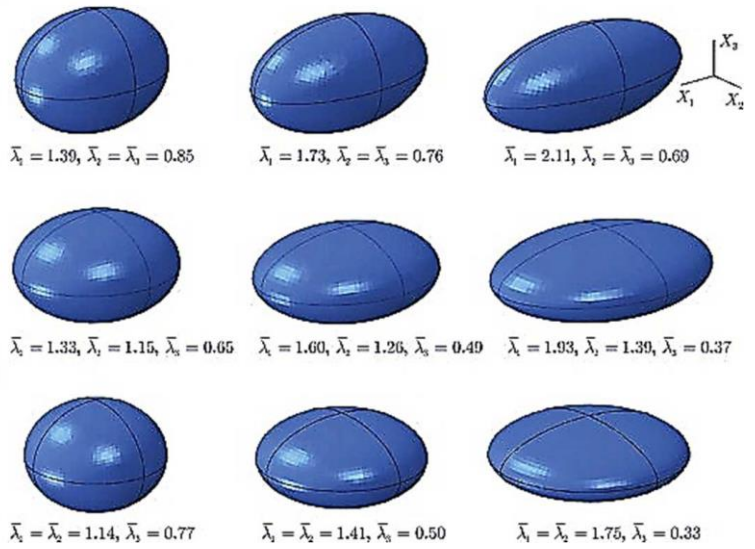

Figure1.13 Cavity shapes obtained for different types of tri-axial loading satisfying cavitation conditions (Nakamura and Lopez-Pamies 2012).

1.4.2 Cavity field models

Cavity field models involve generation of several same size cavities randomly distributed in a cubic form REV, whose size depends on the number of cavities. One of the modelling strategies used in the literature is the equivalent inclusion method (EIM): empty cavities are replaced by equivalent inclusions. The method is described in detail in the literature (Moschovidis and Mura 1975; Mura 2013).The main challenge for this method is to find the optimum properties to be assigned to the inclusion and to quantify the interactions with close cavities. In fact, replacing the empty cavities by inclusions with realistic properties makes it possible to overcome the problems of computational convergence related the interfaces between cavities and the matrix. The EIM provides the stress distribution around the cavities and gives an estimate of the interactions between cavities.

All these models are based on a pre-existing cavity/cavities justified by the hypothesis that defects are induced in the materials during the manufacturing process. Other models exist in literature where the second approach of a nucleation of cavity from a healthy polymer is taken. These models take into consideration the conditions of appearance and growth of the cavity. Ball considered this problem as a hollow sphere problem by taking an infinitely small cavity

size that tends to zero. This yielded the same criteria of cavitation as proposed by Gent. A slight difference in the criterion was observed by Dollhofer et al who considered the same calculation by integrating the strain energy from 0 to R_{ext} in the eqn 1.6 and explained this difference by the effect of surface tension which tends to close the small cavity (Dollhofer et al. 2004). In other models, the appearance of the cavity is taken to occur as a result of instability in a healthy material deduced from the balance of energy and for which analytical solutions have been developed, for example by using the principle of virtual works (Hang-Sheng and Abeyaratne 1992). This method makes it possible to consider complex loads without taking into account the position of instability. However, it is limited to cases of simple behavior laws for the resolution to be analytical.

For modelling a cavity field that appears in a healthy polymer, a solution is to use molecular dynamics. Sixou used this approach to study cavitation in a healthy amorphous polymer subjected to hydrostatic loading and showed the change in the volume (ΔV) to be linear upto a critical value of hydrostatic pressure after which the increase in volume was accompanied by the decrease in stress (Sixou 2007). Highly localised and spherical cavities were observed for the case of strong intermolecular interactions, whereas in case of weaker intermolecular interactions or higher rigidity, the regions of cavities were more diffused. The authors assumed the high mobility regions occurring before the peak stress to act as nucleation sites for the cavitation process. The same technique was used by Morozinis et al to model a perfect polyethylene network subjected to a tensile loading leading to the appearance of cavities in the initially healthy material. They found the critical stress of cavitation to correlate with the Young's modulus of the material; this observation was in qualitative agreement with macroscopic continuum mechanics analysis of Gent (Morozinis et al. 2013).

The models described above were mostly aimed at predicting the critical pressure required for the appearance of cavitation in materials. However, these works did not take into account the effects of loading rate on this criterion of cavitation. Again the coupled diffuso-mechanical loading simulating the real loading conditions as the material is subjected to gas exposure has not been reported. Jaravel developed a numerical 1D model to address the effect of both gas diffusion and mechanics on volume change of a pre-existing cavity by considering a spherical cavity at the centre of the sample as a hollow sphere problem with boundary conditions

calculated from the macroscopic conditions of the sample (Jaravel et al. 2013). In comparison to the case of pure mechanical loading, where cavity growth is a consequence of instability, in the case of coupled diffuso-mechanical loading, the cavity growth occurs as due to gas diffusion between the cavity and the rubber matrix. A significant result of the study was a temporal prediction of cavitation in real conditions that were seen experimentally including the case of no cavitation for low values of decompression rates and saturation pressures. Nevertheless, a robust 3D model for cavitation in elastomers taking into consideration the coupled diffuso-mechanical loading has not so far been defined in literature.

1.5 Mechanisms of Diffusion in Polymers

In principle, the mechanism of diffusion in case of elastomers is the movement of diffusing molecules into the vacant spaces inside the matrix created by the movement of the elastomer molecules and the speed of these diffusing molecules depends on the testing temperature and T_g of the elastomer. Silicone rubbers have a lower T_g and this show high diffusivity for most gases (Southern, 1985). Moreover, the diffusion of smaller molecules is easier than a larger molecule since smaller spaces in the matrix occur more frequently than larger ones. The vacancy in the elastomer matrix is related to the free volume of the rubber which can be related to the compressibility of the rubber (Van Amerongen 1964). In soft and rubbery polymers, the diffusion is generally Fickian. Deviations from Fickian behavior are in response to the sorption or desorption of penetrant molecules causing time-dependent structure relaxations (Chen 2005). The diffusion process is thus time as well as concentration dependent. Mathematically diffusion is characterized by the diffusion coefficient and permeability. The diffusivity or diffusion coefficient is defined by Fick's first law which states that the flux of the diffusing gas is proportional to the concentration gradient measured normal to the section.

$$\vec{J} = -D\frac{dc}{dx} \qquad eqn\ 1.7$$

Where *J* is the diffusion flux, measuring the amount of substance diffusing through a unit area during a unit time interval, *D* is the diffusion coefficient or diffusivity, dc/dx is the concentration gradient along x. This formula was proposed by Fick analogous to the equations of heat transfer developed thirty years earlier (Fourier 1822). In the transitional regime, the

second law of Fick allows to calculate the change in the concentration of the diffusing species with respect to time.

$$\frac{\partial C(x,t)}{\partial t} = -\frac{\partial j}{\partial x} = \frac{\partial D}{\partial x}\frac{\partial C}{\partial x} + D\,\frac{\partial^2 j}{\partial x^2}C \qquad eqn\ 1.8$$

The solution of this equation gives the concentration profile in the elastomeric membrane. The gas content in the material after equilibrium is reached is defined as the solubility S which is expressed in mol/Pa/m^3. The solubility coefficient, defined by Henry's law relates the equilibrium gas concentration,C_e and the solubility, S, in the elastomer to the pressure, P, of the gas:

$$P = \frac{C_e}{S} \qquad eqn\ 1.9$$

Most gases follow Henry's law at low and moderate pressures, but significant deviations may be encountered with easily condensable gases, especially at high pressures. Since H_2 is well known to be a non-condensable gas (Ramsey 1996), and the pressures under which the present work is carried out is not very high, the diffusion is considered to obey Henry's law. For specific shapes of rubber specimens, the rate of the diffusing species as well as the amount can be calculated as a function of specimen dimensions, the time t, the equilibrium concentration and the diffusion coefficient D (Crank 1975). More often, the mathematical expression for calculating the total amount of diffusing species is practically more useful than the calculation of concentration gradients along the sample dimensions.

1.6 Cavitation induced by gas decompression

In additional to purely mechanical loading, cavitation of elastomers is also induced due to decompression after gas saturation. This is due to the faster expansion of the dissolved gas in the material than its desorption which generates nuclei of cavities. For conditions of extreme loading, the damage is analogous to foaming. To describe the transient phase of gas diffusion in the material as well as the final state characterized by the penetrated amount of gas, the two main parameters are required: the diffusion coefficient D and the solubility S of the specific gas into the specific material. This indicates that the cavitation damage in elastomers due to

gas decompression depends on the nature of the gas as well as that of the elastomer (Van Amerongen 1964).

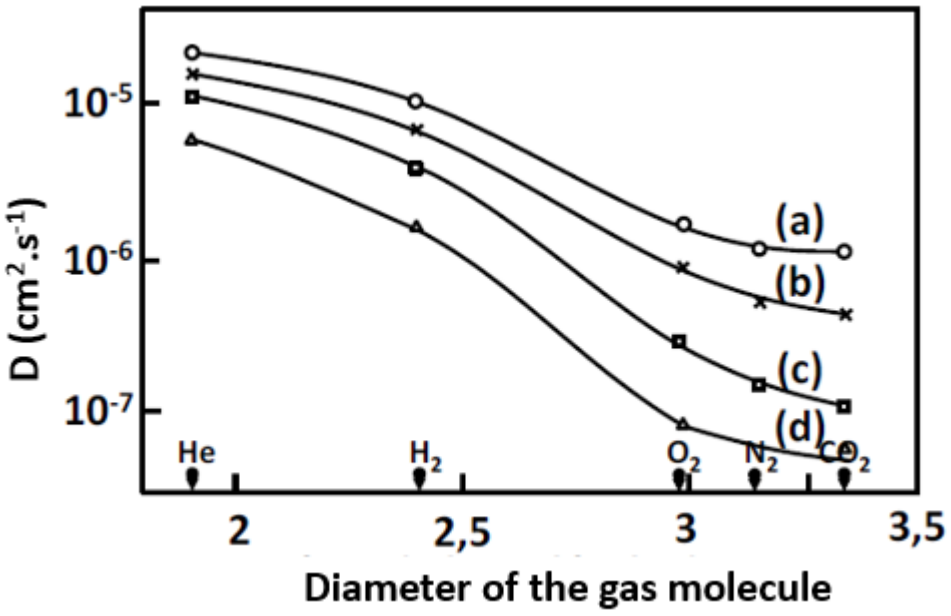

Figure1.14 Diffusion coefficient of different gases in different elastomers: (a) natural rubber, (b) NBR-20 and (c) NBR-32, and (d) nitrile [Van Amerongen 1964].

Figure 1.14 illustrates the relationship between the rate of diffusion of the gas and its size; the larger the size of the diffusing species the slower is the rate of diffusion resulting in a smaller value of diffusion coefficient, D. In addition, this figure highlights the need to know D for the material and gas studied, its value may vary by several decades when changing gas or elastomer. Moreover, the decompression conditions are also dominant factors for the level and nature of damage. This makes the studies for each gas pertinent in its own application field.

In addition to depending on the nature of the gas, the damage is also dependent on the nature of the elastomer; the resistance to cavitation increases with the increase in stiffness of the material (Peters 1990).

1.6.1 Effect of the nature of the gas

Damage induced during rapid gas decompression in elastomers has been studied experimentally in different gases such as carbon dioxide (Briscoe and Liatsis 1992a; Briscoe, Savvas, and Kelly 1994; Embury 2004; Zakaria 1990; Schrittesser et al. 2016), argon (Gent and Tompkins 1969; Stewart 1971), methane (Stevenson and Morgan 1995), and more recently

hydrogen (Jaravel et al. 2011; Kane-Diallo et al. 2016; Ono et al. 2018; Ono, Fujiwara, and Nishimura 2018a). Since, different gases have different coefficients of solubility and diffusivity in the same sample, the induced damage is of different proportions and nature for each gas (Koga et al. 2012). Furthermore, the diffusion of gas into a medium leads to expansion of the material which is also dependent on the diffusing species as seen in figure 1.15. The volumetric expansion of the material due to the concentration C of the diffusing gas is given by the following equation

$$V = V_0(1 + \propto_c C) \qquad eqn\ 1.10$$

where V_0 and V are the sample volumes before and after saturation respectively, and $\propto_c$ is the coefficient of expansion of the sample due to a concentration C.

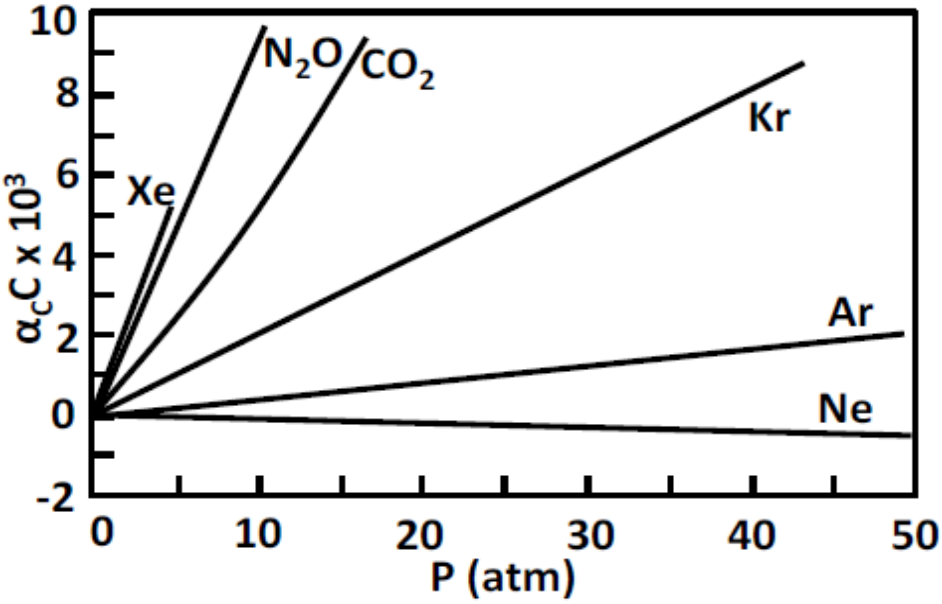

Figure1.15 Volumetric expansion coefficient for different gases in polybutadiene

CO_2 particularly has been extensively studied for an interest in the temporary plasticizer behaviour of supercritical CO_2. For CO_2 exposed rubbers, most of the studies have been focused on PDMS (Flichy et al. 2002; Royer, DeSimone, and Khan 1999; Thurecht, Hill, and Whittaker 2005) and fewer on poly-isoprene (Y. Zhang, Gangwani, and Lemert 1997) or nitrile rubber (Briscoe and Zakaria 1991). PDMS and hexane system has also been studied by Ogieglo (Ogieglo et al. 2013) while Kamiya has investigated poly-butadiene in several gases (Kamiya et al. 1998). Studies of elastomers in hydrogen are recent and few.

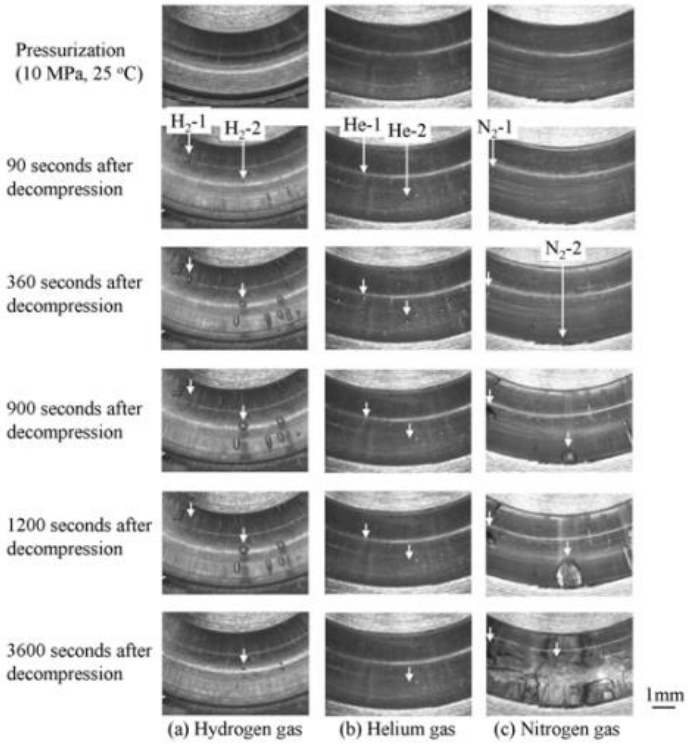

Figure1.16 Effect of the nature of the gas on the development of the damage in EPDM O-rings saturated at a pressure of 10 MPa at 25 ° C and decompressed at 33 MPa/min (Koga et al. 2012)

Figure 1.16 shows the top views of EPDM O-rings exposed to different gases at a pressure of 10 MPa: an example of the effect of the nature of the gas on the damage for elastomers. Since EPDM is transparent, it allows a visual observation of the damage. As can be seen from the figure, cavities appear earlier and are more numerous in case of helium. The size of the cavities is also smaller and short lived, about 800 seconds. Nitrogen causes more detrimental damage as compared to Helium and hydrogen. Cavities appear later but are larger in size and cracks perpendicular to the joint axis are also visible. Moreover, the damage is visible even 1 hour after the beginning of decompression. Koga has explained this difference in damage morphology to the size of the different gas molecules.

Analogous to this, Colton in his study has observed difference in number of cells generated in foams while using two different foaming agents; CO_2 generates about 1000 times more cells than nitrogen, an effect he attributes to the high solubility of CO_2 as compared to nitrogen.(Colton and Suh 1987)

1.6.2 Effect of saturation pressure

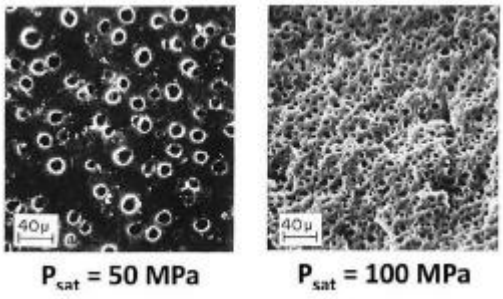

Figure1.17 Effect of saturation pressure on an SBR at 25 ° C and decompressed at 100 MPa / sec after exposure to Argon (Stewart 1971)

The saturation pressure of the gas is an important parameter for characterization of the induced damage. Studies show that at a fixed decompression rate, density of cavities decreases with the decrease in saturation pressure (Figure 1.17) and at a sufficiently low pressure cavitation could be prevented (Jaravel et al 2011, Stewart 1971). In addition, the study of the influence of the saturation pressure made it possible to check the validity of the cavitation criterion under gas decompression (Gent, 1969). For incompressible materials with simple geometries, the saturation pressure level is equivalent and opposite of the hydrostatic stress in the sample, which makes it possible to obtain the variation of hydrostatic stress in this sample subject to gas decompression. Tests at different saturation pressure levels on the same materials have, therefore, allowed to demonstrate that Gent's criterion for mechanical cavitation was only valid for weak saturation pressures (Jaravel et al, 2011). Indeed, cavitation under decompression of gas is a coupled phenomenon of gas diffusion and mechanics, which was not taken into account by Gent while defining the criterion for cavitation.

Park in his study with structural foam observed that the density of the cavities did not depend on the pressure when using iso-pentane as the blowing agent (Park and Cheung 1997). In an earlier study, Colton (1987) showed that in polystyrene foams with CO_2 as the blowing agent, the dependence of saturation pressure on the density of cavities was only seen in case of homogenous nucleation and not heterogeneous nucleation rate and more number of microcellular bubbles were produced by homogeneous nucleation.

Further study on cavitation in elastomers was done by Kane Diallo (2016) by optically tracking and statistically analyzing the cavities in EPDM after exposure to hydrogen. The analysis was enriched by the covariogram method and focused on the average size, size distribution as well as spatial distribution of cavities. This informed the size and isotropy of a representative element volume. His study could confirm the dependence of saturation pressure on the phenomenon of cavitation; increase in saturation pressure led to an increase in the number and average size of cavities and this dependence was nonlinear.

1.6.3 Effect of rate of decompression

Numerous studies in literature has examined the effect of saturation pressure on cavitation but few exist analyzing the effect of decompression speed since the experiments require a remotely controlled adjustable decompression valve. This makes it difficult to conduct the experiments or check the repeatability of the tests conducted. It has been shown that an increase in the decompression rate increases the number of cavities although the relationship is not linear (Stewart, 1971; Stevenson and Morgan 1995). The authors explained this effect to be a possible result of increase in amount of gas and the dimension of the sample which allowed for faster desorption of the gas out of the samples. Later, Jaravel's study shed more light on this relationship. He showed that with low decompression rates of less than 0.3 MPa/min for saturation at 9 MPa it was possible to avoid cavitation in 2 mm thick samples of silicone rubber.

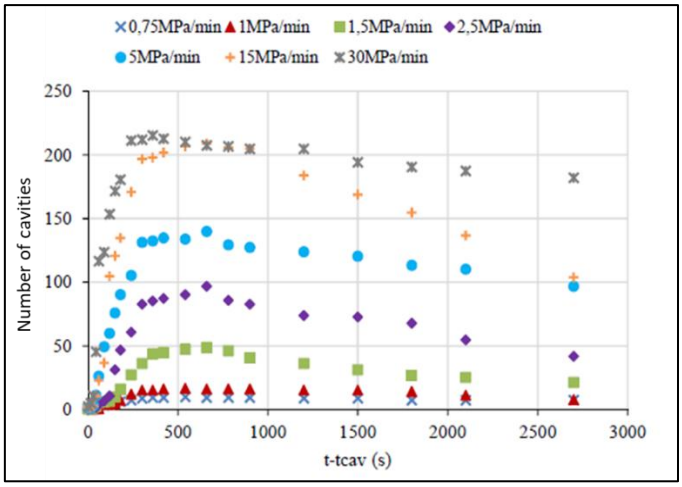

(a)

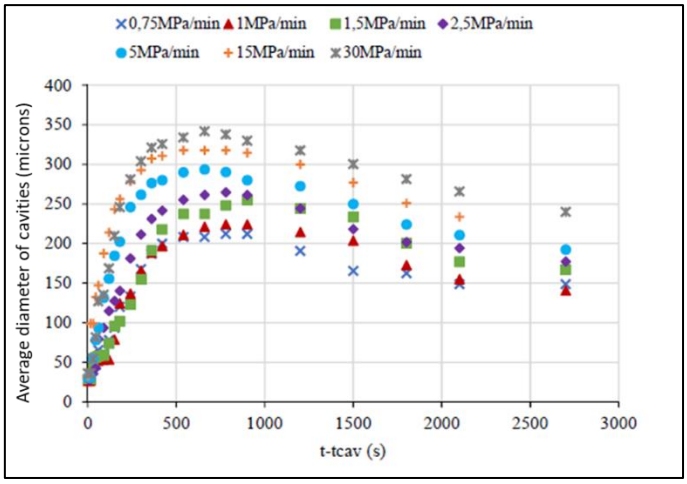

(b)

Figure1.18 Influence of the decompression rate on the (a) number and (b) average diameter of cavities in EPDM saturated at a pressure of 9 MPa (Kane-Diallo et al. 2016).

In Kane Diallo's studies on EPDM after hydrogen exposure, he confirmed an increase in the number and size of cavities with an increase in both saturation pressure and decompression rate as shown in Figure 1.18.

1.7 Morphology of the damage

In the earliest study of cavitation, Gent et al observed two populations of cavities. Satellite cavities were observed around the primary ones which were assumed to appear due to a local stress concentration. This systematic appearance of cavities was not clarified experimentally as is still an open question. This morphology of damage was later confirmed by Jaravel (2011) in his study on silicone rubbers exposed to hydrogen during decompression. The cavities observed were spherical and appear for upto 30 minutes after decompression see Figure 1.19.

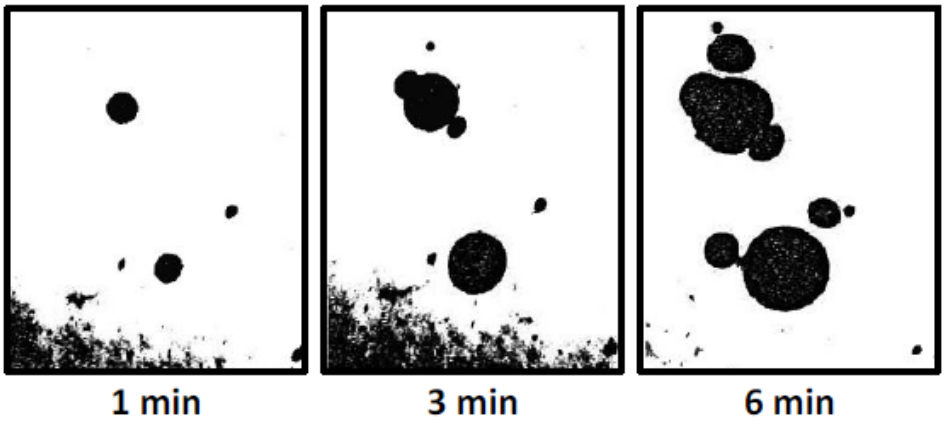

Figure1.19 Appearance of cavities in an argon saturated elastomer at 2.4 MPa. Pictures taken 1 min, 3 min, and 6 min after decompression (Denecour and Gent 1968).

Size of the cavities depends on the decompression conditions as discussed earlier. The density of cavities also depends on the decompression conditions as well as the nature of the gas i.e. the diffusion coefficient and solubility of the gas in the elastomer. The initial size of the cavities that was observed was of the order of a micrometre (Jaravel, 2011; Stewart, 1971). The damage is macroscopically reflected by the bulk swelling of the samples going up to 300% for an elastomer saturated with CO_2 in 30 seconds (Major et al. 2006). For saturation of NBR in hydrogen, the value of bulk swelling in considerably lower; volume change of 3.5% was seen at equilibrium due to hydrogen sorption whereas the higher volume change of about 20% was reached during decompression and was associated with the appearance of cavities and cracks (Ono, Fujiwara, and Nishimura 2018a).

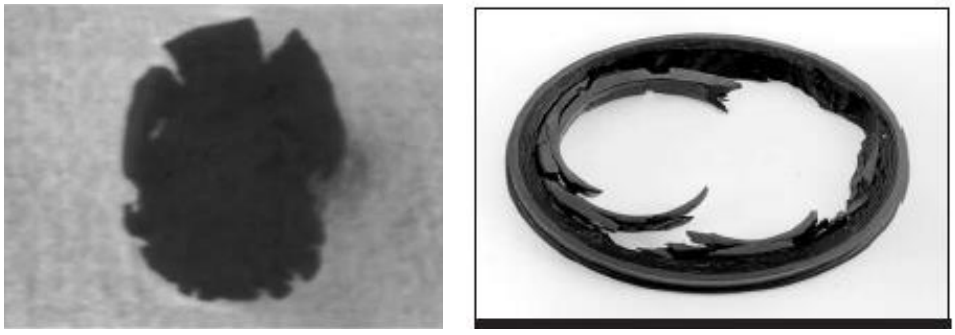

Figure1.20 Surface cracks on (a) a cylindrical polyurethane sample after rapid (Briscoe and Liatsis 1992b), and (b) on a commercial seal (Embury 2004).

In extreme cases of damage, cracks appeared and propagated to the edges of the sample as seen in Figure 1.20, which shows the cross-sectional view of a cracked polyurethane sample after

rapid CO_2 decompression and a commercial seal damaged due to explosive decompression failure: a term used in the reference.

These cracks have been seen to be preferentially oriented (Diani, Brieu, and Gilormini 2006; Mullins 1948); in the case of cylindrical sample, these cracks propagated perpendicularly to the cylindrical axis. The surface damage is due to the propagation of cracks initiated in the centre of the sample (Stevenson and Morgan 1995). However appearance of cavities close to the edge of the sample have been seen in very thin samples (Campion 1990; Pugh and Goodson 1992). Except for these extreme damage scenarios where the cracking occurs, there remains an undamaged layer at the edges of the sample: for silicone rubber exposed to hydrogen, this thickness is of the order of 500 microns. This undamaged layer is attributed to the easier desorption of gas around the edges and is dependent on the decompression conditions. In the case of structural foam, the size of the cells or bubbles range between 0.1 and 10 μm with a density varying between 109 and 1015 cells/cm^3 (Colton and Suh 1987). Their size is controlled by the concentration of the foaming agent in the polymer and the duration of the foaming process (Figure 1.21).

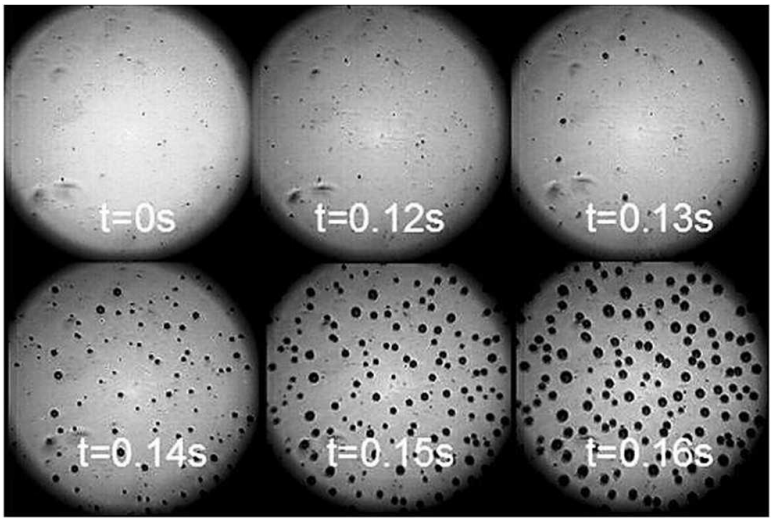

Figure1.21 Representative images of bath foaming process on thermoplastic olefin containing 100 wt % linear polypropylene saturated at 138 MPa nitrogen and decompressed at 33 MPa/sec (McCallum et al. 2008).

The damage morphology presented above, namely the number of cavities, their sizes and undamaged thickness, depends on the nature of the gas and the elastomer but also pressure conditions which have been discussed in the earlier section.

Kane Diallo (2016) addressed the cavity fields to highlight the spatial distribution of the two populations of cavities. He concluded that the distribution of cavity diameter evolved with the increase in saturation pressure or decompression rate and increased the tendency of delayed nucleation resulting in two populations. Under severe decompression conditions, the interactions were promoted between close cavities shown by the evolution of covariogram shape and associated correlation lengths. For such damage, the REV size increased significantly until it reached the size of the sample. Ono et al studied the evolution of cavitation due gas decompression with cyclic exposure showing that damage evolution was not a cumulative process of the systematic reappearance of cavities leading to coalescence. At local scale, more complex coupled diffuso-mechanical processes govern damage evolution. This study was carried out on EPDM rubber exposed to hydrogen at 9 and 15 MPa (Ono et al. 2018).

A more rigorous analysis of the cavitation at a local scale is required for a better understanding of the morphology of damage and its temporal evolution based on the local boundary conditions. The interactions between the close cavities and the possible topological constraints arising from the primary population of cavities which could contribute towards the morphology of the secondary population of cavities need to be addressed with a relevant framework of damage in rubbers.

1.8 Origin of cavities- a molecular approach

A possibility of explaining gas cavitation in elastomers is by taking a molecular approach, that is, taking the molecular structure of rubber into consideration. As mentioned in the earlier section, rubber has vacant spaces or free volume which can be considered to be nano-voids or cavities (Campion 1975). Due to variation in network density due to fluctuations of cross-linking density as well as random distribution of cross-link points, the size of free volumes ranges from 2 to 200 nm (Haward 1970). Stevenson et al., who observe cracks of several millimeters in length for above 100 °C with NBR samples saturated at 17.2 MPa, assume that there is a swelling of pre-existing cavities and cracking from areas of low density. To go in the direction of an appearance of macroscopic cavities from already pre-cavities present whose

surface cracks under certain conditions, some photos of damage in transparent samples show cavities that are not perfectly spherical with the presence of surface cracks as seen in Figure 1.22.

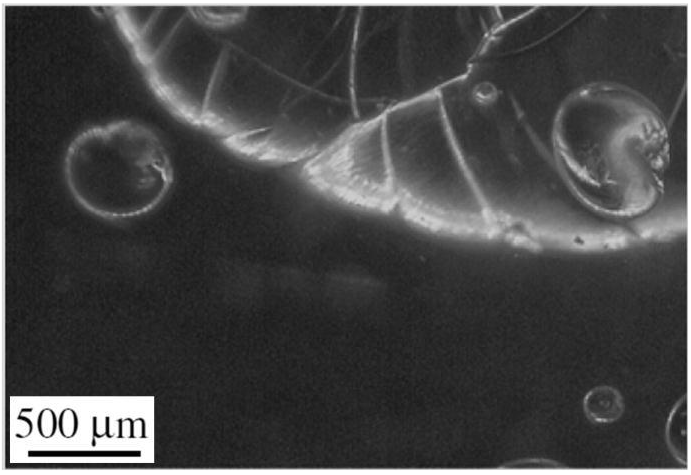

Figure1.22 Cavities obtained in EPDM after saturation with H_2 at 3 MPa and 30 ° C for 65 hours (Yamabe and Nishimura 2009).

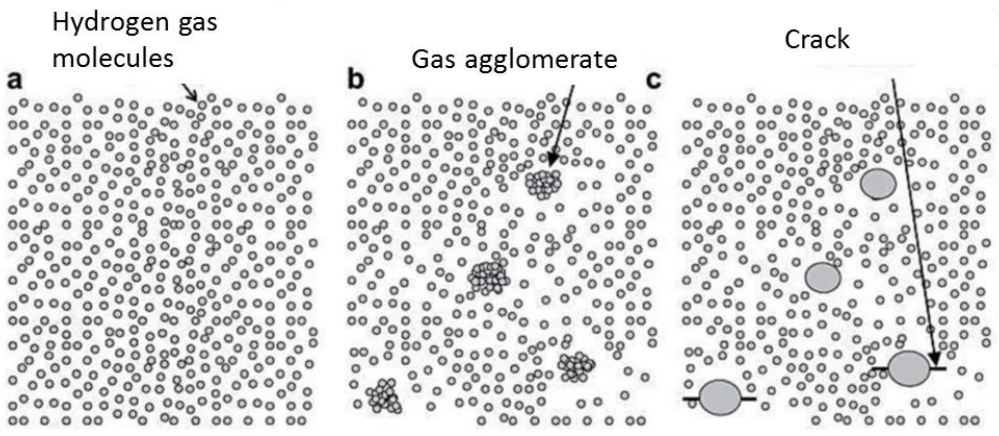

Figure1.23 (a) dissolved hydrogen at the end of saturation, (b) formation of gas bubbles by agglomerations of hydrogen molecules, (c) cavitation induced by stress concentrations induced by the bubbles (Yamabe and Nishimura 2009)

Other sites of cavity nucleation include the defects and impurities occurring due to manufacturing process of the material that cause local stress concentrations (Gent and Tompkins 1969). Another possible cause of cavitation mentioned in the literature is agglomeration of gas molecules during decompression leading to appearance of visible cavities (Yamabe and Nishimura 2009) assuming that the gas agglomerates occur in the vacancies of

the network or areas of low network density (Figure 1.23). This is similar to the earlier hypothesis in suggesting that the formation of cavities was due to free volume since that indicates that the cavities form in the areas of lower network density.

The origin of the damage is correlated with the acceleration of the desorbing gas from the sample inducing swelling of the sample (Lorge, Briscoe, and Dang 1999). Jarin noted competing phenomenon during decompression of LDPE from saturation in CH_4 in his study using LVDT: an expansion of the sample due to decrease in hydrostatic pressure and contraction due to desorption of the gas. This leads to a very quick desorption near the edge prompting an undamaged thickness and surface contraction while retaining a high gas concentration at the core of the samples (Jarrin, Dewimille, and Devaux 1994).

A recent study by Ono et al confirmed that the hydrogen content in unfilled NBR after high pressure hydrogen exposure was proportional to its fractional free volume which is in correlation with the effective cross-linking density taking the physical entanglements as well as the chemical crosslinks into account (Ono, Fujiwara, and Nishimura 2018b).

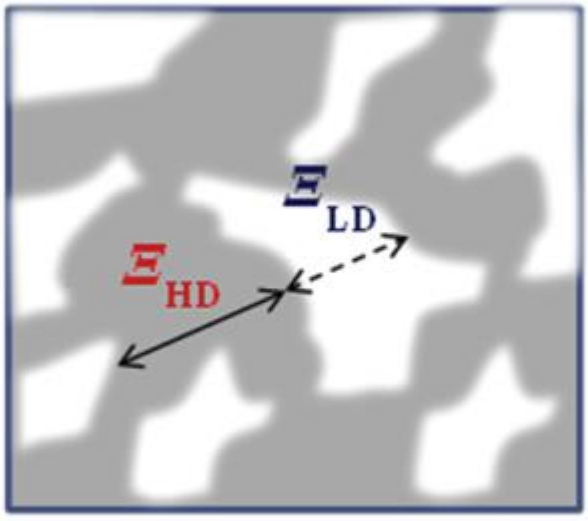

Figure1.24 Schematic image of a two-phase system. The gray and white color areas denote high-density and low-density phases, respectively.

Recently Ohyama (2017) studied the early stage of decompression failure of NBR after high-pressure hydrogen exposure using small-angle X-ray scattering (Ohyama, Fujiwara, and Nishimura 2017). Considering the voided matrix as a two phase system, the results were analyzed by the Debye-Bueche equation. The main assumptions were to treat the low density areas of the elastomer network as pre-existing nano-voids which acted as precursors for visible

cavities to appear. The low density areas were as a result of local inhomogeneity due to cross-link density which created a high density and a low density domain in the matrix denoted by Ξ_{HD} and Ξ_{LD} respectively, see Figure 1.24. The estimation of size of the precursors was averaged spatially as well as temporally, which could be a good estimation of the general size of heterogeneities. However, the estimation of local parameters with the global calculation techniques are much estimated. She also correlated the global gas content with the evolution of domain sizes, see Figure 1.25.

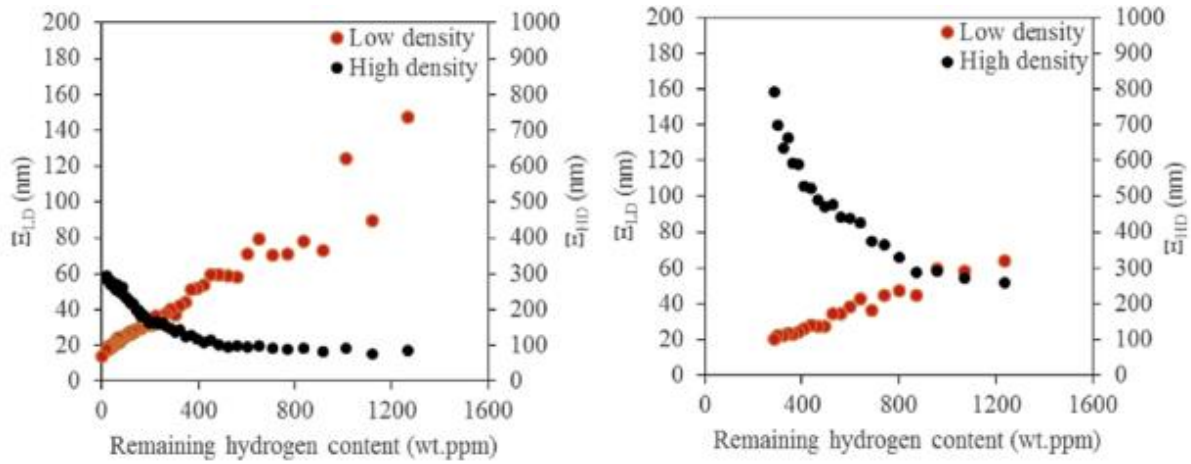

Figure1.25 Relationship between the remaining hydrogen content and the domain size of each phase (Ξ_{HD} and Ξ_{LD})in NBR : (a) DCP ratio 0.15, (b) DCP ratio 0.5

These studies address these questions of origin of cavities in a polymer due to local heterogeneities inherent in an amorphous structure due to entanglements and cross-links as well as defects arising from manufacturing process, treating them as precursors for cavitation. However, no experimental clarification is provided for these assumptions; in-situ studies at sub-micron scale could be an important step towards clarifying this assumption of structural heterogeneity of rubber matrix and localised appearance of cavitation being systematic.

1.9 Experimental tracking of cavitation

The earliest studies of cavitation in rubber were not supported with any visual tracking of the damage that could prove the appearance of cavitation was systematic with the change of slope in the tensile curves. Only later, in the work of Lindsey (1967) and Cristiano (2010, 2011),

with the visualization of damage in polyurethane samples, could these questions be cleared up (Lindsey and Lindsey 2013; Cristiano et al. 2010, 2011). Some of the techniques used in tracking damage are listed below rather briefly. The objective is to familiarize the reader with the commonly used techniques and experimental devices and their background for justification of the experimental technique chosen for the present study.

1.9.1 Volume strain measurements

In their review paper, Naqui and Robinson discussed the theory of tensile dilatometry which has been used to enable the prediction of volumetric strain of a material associated with the onset of cavitation (Naqui and Robinson 1993). However, this technique allows for the quantification of volume fraction of cavities but provide no information on the spatial distribution or morphology for damage. More recently, Castagnet et al used this technique to characterise the volume inflation of NBR due to sorption of hydrogen as well as during decompression stage, during which the volume change occurred due to hydrogen content as well as due to damage processes activated during this phase (Castagnet, Ono, and Benoit 2017)

1.9.2 Acoustic emission

This is a non-destructive testing technique involving the detection of elastic waves in solids that are a consequence of irreversible structural changes like plastic deformation or crack formation (Takaoka et al. 2008). It allows for the analysis of a large sample in a time efficient way which is of great important from an industrial point of view. For experimental purposes, this technique is used to detect the onset of cavitation by comparison of the signal generated by the damaged sample with that of an undamaged one (Yamabe and Nishimura 2011). In addition, it allows a general idea about the location of damage in a larger sample due to which it finds application in industries as a non-destructive technique (NDT) for providing valuable information about discontinuities in the sample. Even if, it is useful for obtaining an estimation of the beginning of cavitation, the size of the detectable cavities in the bulk of the sample is much higher than those reported in literature which is a major limitation. Moreover, similar to the technique of volume strain measurement, the technique provides no information about the distribution or morphology of the detected cavities.

1.9.3 Optical tracking

Optical tracking concerns essentially with acquisition of images during the testing as well as post mortem. The parameters of the acquisition depend on features that need to be temporally tracked; the technique is adaptable to the material analyzed as well as the scale at which the analysis has to be done. Moreover, in comparison to the two techniques mentioned above, this technique allows for the morphological characterization as well as the quantitative measurements of the cavitation phenomenon. The most commonly used tools in this case are the optical microscope and the scanning electron microscope (for higher resolution). Another technique is to use a CCD camera adapted to track the damage in situ with subsequent processing of the acquired images to extract quantitative and qualitative data (Kane-Diallo et al. 2016; Cristiano et al. 2010; Jaravel et al. 2011). The surface data so acquired can be extrapolated to volumetric representations with an error bar corresponding to the thickness of the sample (Russ and Dehoff 2012) limiting the technique to a samples of small dimensions.

Figure1.26 Optical tracking experimental set up (Kane Diallo 2016)

Furthermore, the 2D rendering of a 3D damage filed can introduce over or underestimation of the parameters tracked due to assumptions about out of plane size and shape of cavity size. Castagnet et al exemplified this in 2018 and were able to clarify this bias in calculation of REV done previously with optical tracking technique (Kane-Diallo et al. 2016) through 3D in-situ tomography see Figure 1.27. Another drawback is the limitation of this technique to transparent samples.

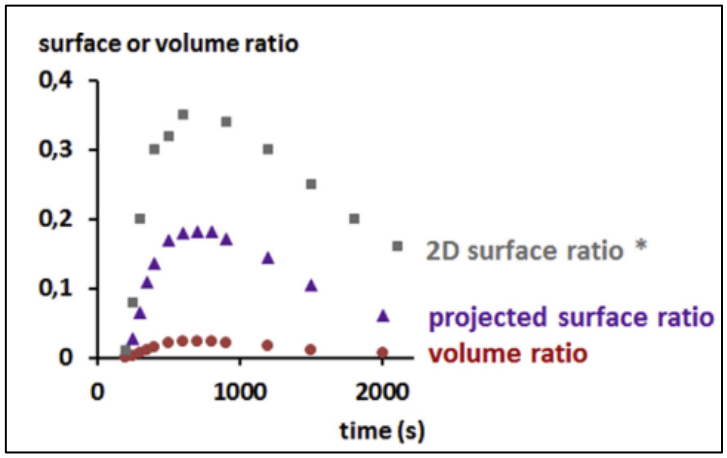

Figure1.27 Time evolution of the voided volume ratio obtained by in-situ X-ray tomography and projection through the thickness, for comparison purpose with the voided surface ratio obtained from 2D optical methods. (Castagnet et al. 2018)

1.9.4 X-Ray computed tomography

The X-ray computed tomography can be seen as a successor of classical X-ray tomography which is essentially a form of radiography: one of the oldest and widely used non-destructive technique. Computerized tomography is an improvement upon the 2D radiography as it renders a 3D reconstruction of the sample from acquired 2D images or radiographs. Over the last decade this technique has become very prominent in tracking defects and providing information on the microstructure of materials. In case of cavitation this is especially useful as in addition to the quantitative data measurements, it allows visualization of the damage, providing much needed data about the spatial distribution of the cavities in the material.

For polymeric materials, there are many studies in literature about deformation and damage mechanisms in polymer foams both ex situ (Daphalapurkar et al. 2008; Di Prima et al. 2010; Patterson, Henderson, and Smith 2013; Youssef, Maire, and Gaertner 2005) and recently in-situ (Lachambre et al. 2013; Patterson et al. 2016). In-situ studies in literature have also addressed cavitation under monotonic loading in PVF2 (Rosenberg, Brusselle-dupend, and Epsztein 2011), micronic cavities in stretched polypropylene (Farge et al. 2013) and microstructural evolution of polyamide under tension (Poulet et al. 2016). More recent developments with synchrotron X-ray beam sources have lessened the acquisition time enabling time-resolved X-ray tomography experiments giving access to data which was hitherto inaccessible. An example is the in situ tracking of bubble nucleation and growth in polyurethane foams using real time synchrotron X-ray tomography by S. Pérez-Tamarit et al

(Pérez-tamarit et al. 2019). Synchrotron sources also have improved the resolution allowing for the detection or quantification of very small cavities or defects, especially in semi-crystalline polymers (Morgeneyer et al. 2014; Laiarinandrasana et al. 2010). Further developments in equipment adapted to the synchrotron facilities enable high quality mechanical tests to track damage in structural materials. For example recently Pelerine et al 2019 developed a versatile stage to perform in situ 3D imaging using synchrotron X-ray tomography which made possible to test multiple sample geometries and load ranges upto 5KN (Pelerin et al. 2019).

The main advantage of the 3D technique is that it provides additional data that can not be accessed by 2D methods as in the study carried out by Castagnet et al (2018) who could clarify the 3D shape of the cavities in EPDM exposed to hydrogen by providing information in out of plane direction, thus providing reliable quantification of damage. This updated experimental technique provides a new and improved way to track and quantify the damage and is well suited to address the objectives of the current study.

1.10 Synthesis of study

The studies on cavitation in elastomers due to gas exposure carried so far have been focused on qualitative analysis after the decompression has already taken place. This is due to the complex experimental techniques that are required to access the phenomenon in-situ. Improved experimental techniques have provided some insights into this phenomenon: for example optical in-situ tracking and associated modelling. It also needs to be noted that damage occurs as a result of coupling between the mechanical loading and the gas loading. As such the classic criterion of cavitation due to critical hydrostatic pressure can no longer be considered solely without taking into account the phenomenon of gas diffusion in the material. Even with the improved experimental techniques, the direct access to the local gradients leading to nucleation of cavities is not possible. Moreover the models describing it are limited to the growth of a single cavity in a bulk with globally described boundary conditions. The data to access the earliest stages of cavitation correlated with the molecular structure of unfilled rubber could helpful as a means to predict the cavitation or in best cases, to avoid it altogether.

The second important factor to be analyzed is the interaction effects between cavities that could exacerbate the damage and lead to cracking in the material. With respect to studies in hydrogen, they remain few and limited to analysis at global damage field scale.

To sum up, the main focus of this thesis is the analysis of cavitation at a local scale and its correlation with the network of rubber to understand how far they are systematic. This has been done by a multi-scale experiment technique, the first step of which is to access the data of rubber matrix at sub-micron scales through SAXS. This was done for virgin materials (before hydrogen exposure) as well as after for exposed samples after decompression. Additional in-situ tests were carried out using an experimental set up that was developed specifically for the present work and is reported here for the first time. This experimental technique although in nascent stage, is the first step of developing a robust tool for such complex in situ tests. At higher scales, the damage was tracked in situ using 3D X-ray tomography which allowed for the first time a proper 3D rendering of this damage and is a marked improvement on the 2d tracking techniques used previously. Getting the data at both scales was important for the simulations done in FOXTROT, a numerical tool developed at Institut P prime for coupled problems which provided a realistic way of modelling the phenomenon of cavitation as a result of coupling between hydrostatic pressure and gas diffusion.

Chapter 2 Material Characterisation

This chapter discusses briefly the characteristics of EPDM rubber which is the material of focus of the present study. The practical usage of EPDM as seals in several industrial applications, particularly in fuel cell vehicles make it a good candidate for the study. Additionally the transparency of the unfilled EPDM selected here, and the morphology of damage when exposed to hydrogen allows for the visual observation as well as quantification of cavitation in terms of size and volume.

The chemical composition of EPDM is discussed briefly before detailing its diffusion parameters in hydrogen. This study was focused on the damage of EPDM during the decompression from an equilibrium state. Hence the hydrogen profile during desorption of the tested samples was of particular interest and is discussed with respect to different pressures and degrees of cross-linking.

The samples were provided by the HYDROGENIUS lab in Kyushu University, Japan. They were manufactured in the form of sheets of 2 mm thickness by the process of compression moulding. Sheets of 4 mm thickness were manufactured by heat compressing two sheets of 2 mm thickness. Cylindrical samples of diameter 29 mm and thickness 13 mm were also provided. Moreover all the tests mentioned herein have been performed at the HYDROGENIUS laboratory.

2.1. Chemical composition of EPDM

Ethylene propylene diene monomer rubber (EPDM rubber), is an M class synthetic rubber which mostly finds applications in areas involving solvents, acids, and other aggressive chemicals due to its properties of excellent chemical and thermal resistance. The M-class refers to the classification in ASTM standard and comprises of elastomers with a polyethylene type saturated chain. As the name suggests, EPDM comprises of ethylene, propylene and a diene monomer (See Figure 2.1). The diene monomer is added to enable sulphur vulcanisation although peroxide vulcanisation is used for better heat resistance. The percentage of the comprising components affects the properties of the resulting compound; as ethylene content approaches 50 weight percent and less, the resulting rubber is essentially amorphous. At higher

percentage of ethylene, EPDM is semi-crystalline. It should be noted that the present work is focused on amorphous EPDM.

Consequently, the application dictates the formulation of the rubber compound. For example in the recent application of EPDM relevant to present work, as O-rings in Fuel Cell Vehicles (FCVs), the JIS B2401 and allied specifications lay down standards for the properties of the O-ring materials. However, these specifications are for the final compound and do not lay any constraint for the compounding or the additives. As a result, manufacturing companies use their own specific compounding techniques and percentages of constituents, mostly undisclosed, to obtain the specified standard for properties.

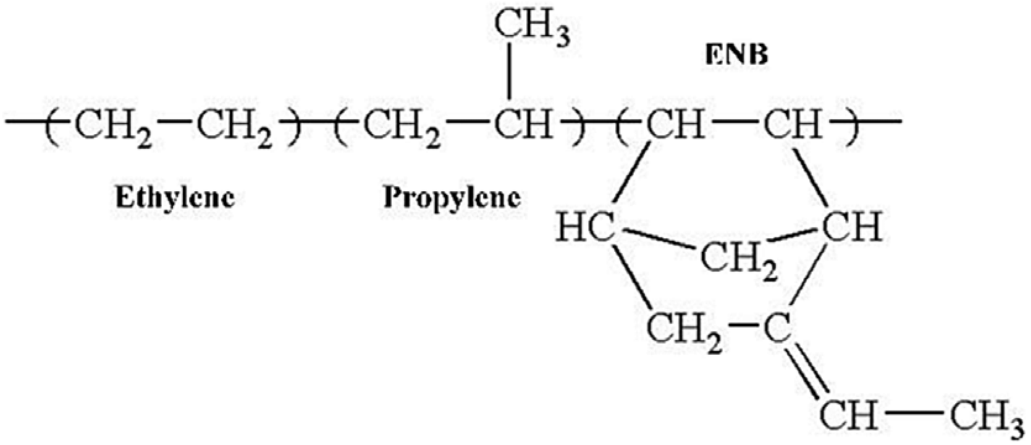

Figure 2.1 Ethylene-propylene-diene-monomer. The diene monomer in this case is ethylidene norbornene (ENB) (Wang et al. 2018)

2.1.1 Cross-link density

For practical applications, as is the case with most rubbers, EPDM is cross-linked via vulcanization and. compounded with fillers and plasticizers to attain suitable mechanical properties. Crosslinking involves linking the polymers chains to each other and essentially prevents the indefinite deformation of the material under the application of load. Increasing the degree of cross-linking or cross-link density decreases the distance between cross-links restricting the segmental motion and leading to a less flexible network (Brydson 1999).

As the rubber molecules consist of folded and convoluted chains in the relaxed state, this distance between crosslinks is expressed as the molecular weight between the cross-links rather than an actual distance. As a consequence, the molecular segments between the cross-links remain flexible. As such, the crosslink density affects the maximum extensibility of rubber.

The relationship between the cross-link density and average molecular weight between cross-links is expressed as

$$\upsilon_c = \frac{\rho}{M_c} \qquad eqn\ 2.1$$

Where υ_c is the cross-link density, M_c is the average molecular weight between cross-links and ρ is the bulk density of the dry EPDM. For the purposes of this study, the material of focus was unfilled EPDM, with peroxide crosslinking (using dicumyl peroxide) which resulted in transparent specimens allowing for the visual tracking of the damage in the samples. Specimens of different cross-linking density were chosen while the rest of the composition remained constant. The chemical composition of the samples including the concentration of crosslinking agent with the corresponding cross-link density as well as M_c for EPDM samples tested in the present study is given in Table 2.1.

For calculation of M_c (number average molecular weight between crosslinks) swelling tests were carried out using toluene as the solvent. The values of Mc were estimated suing the following Flory-Rehner equation (Flory Paul J, Rehner JR, John 1943). The value of cross-link density was calculated using equation 2.2.

$$M_c = \frac{\rho V_1 \left(v_2^{\frac{1}{3}} - (v_2/2) \right)}{\ln(1 - v_2) + v_2 + \chi v_2} \qquad eqn\ 2.2$$

Where v_2 is the volume fraction of EPDM in the EPDM-toulene mixture, ρ is the density of dry EPDM, V_1 is the molar volume of toluene and χ is the Flory solvent-polymer interaction term (Ono, Fujiwara, and Nishimura 2018a).

As seen in the table, the calculated value of M_c for EPDM with DCP 0.1 is 641766 g/mol which exceeds average molecular weight of EPDM polymer: 324546 g/mol. This value was calculated by size exclusion chromatography using a refractive index detector (RID). As such the swelling method is not suitable to estimate the value of M_c for rubbers of very low cross-link density. There are several other methods of measuring cross-link density, the most popular one being Nuclear Magnetic Resonance (NMR) method due to its speed and cost effectiveness. However, in terms of precision, the two techniques are comparable as shown in the study by Dibbanti et

al who studied the network differences in sulphur-cured rubber compounds by combining NMR and swelling methods (Dibbanti et al. 2015). Since, cross-link density was used only as a qualitative indicator of the network density, these values were considered precise enough for the present study.

SAMPLE NAMES:	EPDM 0.1	EPDM 0.5	EPDM 1.0	EPDM 1.6
EPDM (ESPRENE 505) (crude rubber) (pphr)	100	100	100	100
Stearic acid (Crosslinking accelerator) (pphr)	0.5	0.5	0.5	0.5
Dicumyl Peroxide (Cross-linking agent) (pphr)	0.1	0.5	1.0	1.6
M_c (g mol^{-1})	641766	20679	3 935	3 101
Density (g cm^{-3})	0.8679	0.870	0.873	0.874
Cross-link density (mol cm^{-3})	1.35E-06	4.21E-05	2.21E-04	2.81E-04

Table 2.1 Chemical composition of EPDM

2.2 Hydrogen release profile and diffusivity

The hydrogen content diffused into the samples due to hydrogen exposure was measured by Thermal Desorption analysis using a JSH-201 thermal desorption analyzer (J-Science Lab Co., Ltd.). Samples were cut in the form of 13 mm diameter and 2 mm thickness discs. The discs were then kept in a pressure vessel filled with hydrogen at a prescribed pressure and temperature till saturation after which the vessel was decompressed and the specimens were removed from the vessel. Following decompression, the discs were kept in the tubular oven with an Argon current, of the thermal desorption analyser that was kept at 30°C. The hydrogen concentration in Argon was measured using gas chromatography and the residual hydrogen content of the specimen was calculated. The calculation was done every 5 minutes to finally obtain the hydrogen desorption profiles for specimens of varying cross-linking densities. Thereafter, equation 2.3 was fitted to the remaining hydrogen content using least squares method to estimate the equilibrium hydrogen content and diffusion coefficient (see Table 2.2); the size of the specimen was assumed to be constant.

$$C_{H,R}(t) = \frac{32}{\pi^2} \times C_{H,E} \times \left\{ \sum_{n=0}^{\infty} \frac{\exp[-(2n-1)^2\pi^2 Dt/l^2]}{(2n-1)^2} \right\} \times \left\{ \sum_{n=0}^{\infty} \frac{\exp[-D\beta_n^2 t/r^2]}{\beta_n^2} \right\} \quad eqn\ 2.3$$

where $C_{H,R}(t)$ wt.ppm is the remaining hydrogen content in the specimen at the time t (s) after decompression, $C_{H,E}$ (wt.ppm) is the equilibrium hydrogen content of the specimen, D (m^2/s) is the diffusion coefficient, β_n is the root of the zeroth-order Bessel function, and l (m) and r (m) are the thickness and radius of the specimen, respectively. The hydrogen content of the samples at equilibrium can be calculated by extrapolation of the above equation, if required.

SAMPLE NAMES:	EPDM 0.1	EPDM 0.5	EPDM 1.6
Diffusion coefficient (D) mm^2/sec	1.66E-04	1.49E-04	1.89E-04

Table 2.2 Diffusion coefficients of EPDM with varying cross-link density calculated at a P_{sat} of 30 MPa

2.3 Hydrogen content and pressure

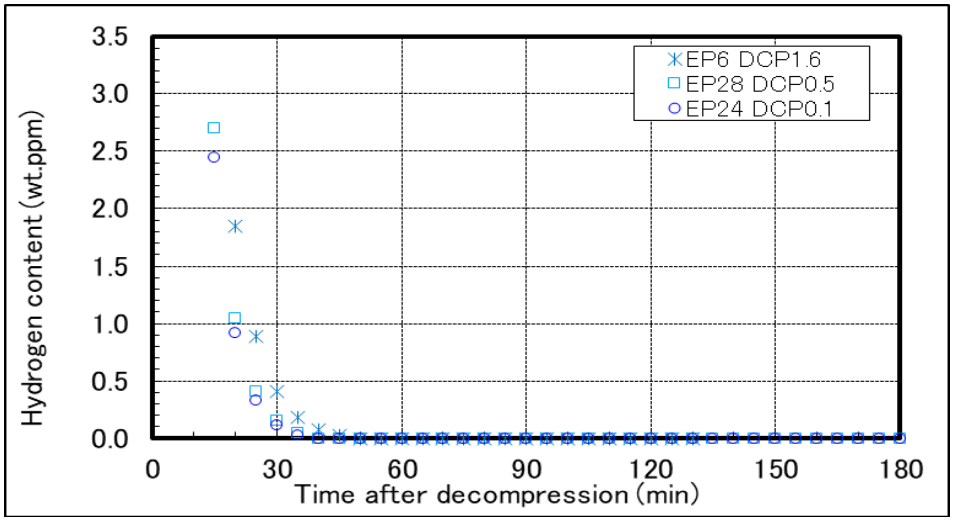

(a)

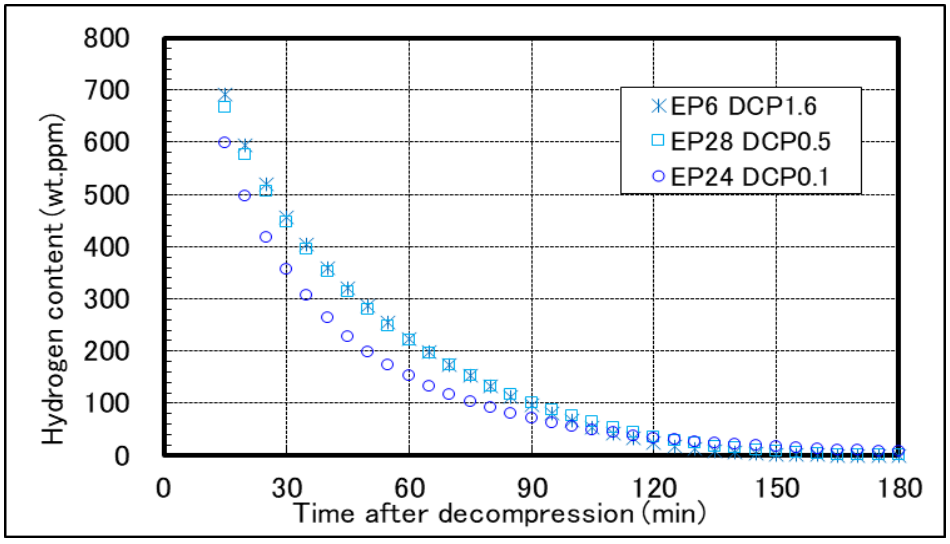

(b)

Figure 2.2 Hydrogen release profiles for EPDM of varying cross-link density at saturation pressure of a) 0.6 MPa and b) 30MPa

Figures 2.2 (a) and (b) show the hydrogen desorption profiles for EPDM for various cross-link densities at the saturation pressures of 0.6 and 30 MPa respectively. The relationship between equilibrium hydrogen content and the saturation pressure has been studies by Yamabe et al. for filled and unfilled rubbers including EPDM (Yamabe and Nishimura 2009). They could clarify that the penetrated hydrogen content was proportional to the hydrogen pressure indicating that

the diffusion of hydrogen into rubber obeyed Henry's law. Their study was done for saturation pressures up to 10 MPa.

As seen from the figures the results seem to be consistent for higher pressure of 30 MPa as well. It is also evident that the testing time for the SAXS experiments carried out here were well estimated to take into account the hydrogen desorption from the sample. For the saturation pressures of less than 1 MPa, the complete desorption has occurred by 1 hour after decompression whereas for the higher saturation pressure of 30 MPa the complete desorption occurs by 3 hours after decompression. These results are true for the samples of all crosslink densities tested here.

2.4 Volume change coefficient due to hydrogen sorption

The volume change due to the sorption of hydrogen in EPDM 1.6 was estimated in the Hycomat facility from a cubic sample (8 x 8 x 8 mm^3) with four markers at each corner of the front face. The sample was exposed at 20 MPa until saturation and pictures were taken with a CCD camera through the chamber window all along the exposure. Correlation of these pictures provided a linear swelling coefficients of 0.005 at equilibrium. Since the coefficient was found isotropic along the horizontal and vertical direction, it could be converted into a volumetric swelling coefficient of 0.015.

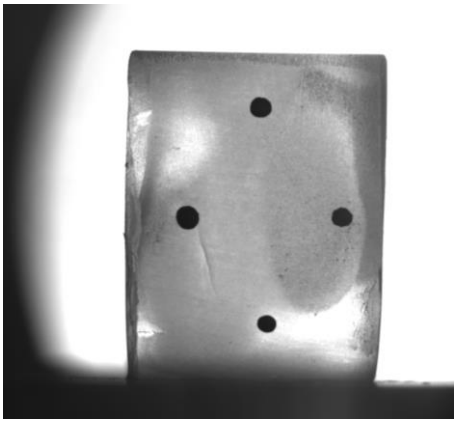

Figure 2.3 Picture of the 8x8x8 mm^3 sample used for estimation of the volume change coefficient due to hydrogen content in EPDM 1.6 with markers for image correlation.

Measurements were done for one exposure pressure only. For further Finite Element Method, it will be linearly extrapolated over the pressure range: $\Delta V/V \times 1/P$ = 0.00075 MPa^{-1}.

2.5 Mechanical properties:

In addition to the tests mentioned above, dynamic mechanical analysis (DMA) was conducted on EPDM to characterise its mechanical properties. This method analyses simultaneously both the elastic and viscous response of the material. The test is conducted by applying sinusoidal strain or stress to the material (in tension, bending, or shear) using a motor and measuring the resulting stress or strain with a force transducer or a position sensor respectively. The measured stress is separated into an in-phase component called the elastic or storage modulus E' and an out-of-phase component called the loss modulus E''.

The storage modulus represents the elastic portion and defines the material's ability to store energy elastically whereas the loss modulus represents the viscous portion and is a measure of the material's ability to dissipate energy in form of heat. The complex modulus E^c of the material if given by equation 2.4

$$E^c = E' + iE'' \qquad eqn\ 2.4$$

In the present case, the tests were carried out by applying an oscillatory displacement on a parallelepiped shaped sample placed in a thermally regulated chamber. The tests were carried out in the temperature range of -120 °C to 200 °C with the rate of temperature change of 10 °C/min. the measurements were done for three different values of frequency: 2.5, 10 and 40 Hz to ensure the reproducibility of the resulting curves. The values of elastic modulus at room temperature for samples of varying degrees of crosslinking were calculated from the curves and are listed in Table 2.3. As can be seen form the table the values of storage modulus increase with an increase in cross-linking density for EPDM 0.5 and EPDM 1.6. However, the value of modulus for EPDM 0.1 is inconsistent. This is attributed to very high extensibility of the material due to which the bending occurs during the test rendering the values less reliable for this kind of material of low crosslink density. In addition, the difference is within the difference range of the modulus tested of same material tested under different frequencies (see Figure 2.4) which is consistent with the rheological properties of viscoelastic materials.

SAMPLE NAMES:	EPDM 0.1	EPDM 0.5	EPDM 1.6
Storage modulus (E')	3 MPa	2.3 MPa	2.75 MPa

Table 2.3 Storage modulus for EDPM taken for the temperature of 30°C by taking the average of the values at the frequencies of 2.5, 10 and 40 Hz

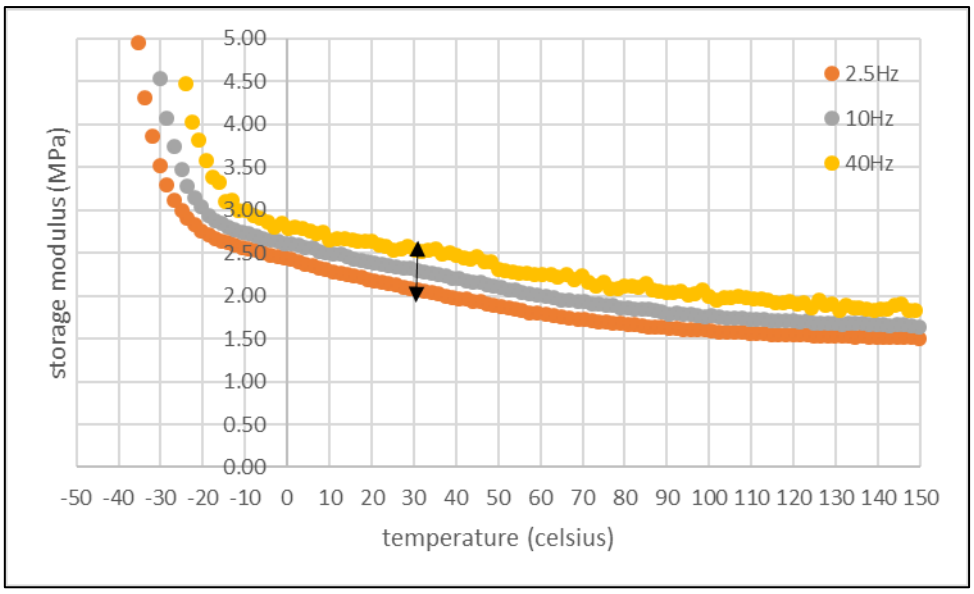

Figure 2.4 Storage modulus for EPDM 0.5 tested under different frequencies of applied deformation. The arrow shows the variation of the modulus along different frequencies which is of the order of 0.5-0.8 MPa

This characterization was done mainly to provide a background on the properties of the material of study and to furnish important data for correlation of the damage parameters to the material and diffusion characteristics of the material itself. EPDM 1.6 data also provided the set of parameters used for Finite Element Method in a first attempt for a more realistic simulation before calibrating a set of parameters for better convergence.

Chapter 3 Characterisation of EPDM at sub-micron scale using SAXS

Study of cavitation in polymers using SAXS is well established in literature for semi-crystalline microstructures (Humbert et al. 2010; B Xiong et al. 2013; Bijin Xiong et al. 2014; Pawlak, Galeski, and Rozanski 2014). However, most of analysis of this type of damage is under purely mechanical conditions (Liu et al. 2003; H. Zhang et al. 2013). In comparison, fewer publications exist for studies on polymer interactions with diffusing fluids. In-situ SAXS experiments have been widely used to study the scattering properties of polymer gels and several quantitative measurements of correlation length associated with both the thermal fluctuations as well as frozen in topological constraints exist (Geissler et al. 1997; Suzuki et al. 2010). These studies are mostly limited to swelling of polymers in liquid. Polymer substances are poly-disperse from a practical point of view, consisting of loose conformations in amorphous state and random aggregates of lamellar layers for semi crystalline microstructures. Therefore, SAXS studies for the characterisation of local heterogeneities for amorphous rubber matrix are more challenging than studies of monodisperse systems and depend on appropriate models for interpretation of the scattering patterns. In terms of in-situ SAXS experiments to analyse cavitation, these are often focused on pure mechanical problems and often in semi crystalline polymers(B Xiong et al. 2013; Defebvin et al. 2016). As has been already established, the cavitation due to gases includes a non-negligible influence of diffusion; the problem is as a result of the coupled influence of mechanical pressure and gas diffusion in the rubber matrix and needs to be treated as such (Jaravel et al. 2011).

3.1 Motivation

In order to understand the changes in the rubber matrix due to saturation with hydrogen, as well as during decompression phase which marks the beginning of cavitation, in-situ tests are essential. This could be helpful towards building a multiscale approach towards understanding of cavitation at the very beginning. The data from the sub-micron scale could be used to highlight the transition from a heterogeneous hydrogen-rubber system at equilibrium towards a voided state at the micro-scale with a spatial distribution that can be quantified from tomography views. In this way, in-situ SAXS experiments could correlate the behaviour of cavities at larger scales and also provide important information for the simulations to be carried out later.

The main aim of the SAXS experiments in the present study was to characterise the heterogeneities of the rubber matrix at submicron scale due to chemical cross-linking as well as physical crosslinking that arise due to molecular entanglements. The characterisation could give information about the nucleation of the cavities to track how far the heterogeneities of the rubber matrix could be the precursors to cavities. The question of matrix heterogeneities and the nucleation being systematic is a valid one due to the heterogeneous distribution of gas in the matrix as well as local modulus of the rubber matrix. It should be addressed locally with temporal evolution as a salient factor, keeping in mind that one intrinsic limitation of scattering techniques remains that they provide average parameters of the distribution.

However, the in-situ tests are difficult to design owing to the practical difficulties of handling hydrogen in lab conditions. The SAXS experimental set-up for the in-situ tests in hydrogen was developed by HYDROGENIUS Laboratory at Kyushu University (Japan). Following the Japanese regulations for gas use in laboratory settings and the constraints of associated safety conditions, it was ensured that the tests were done at very low pressures of less than 1 MPa. Another difficulty arising from using a laboratory X-Ray source is that the acquisition time is usually long. It significantly reduces the number of valid data points, which is particularly critical in the time just after decompression. For this reason, in the present study, both in-situ and ex-situ SAXS tests were carried out at various facilities to get as much information possible in different conditions of beam size and at various times of damage. SAXS tests were also carried out at the Kyushu Synchrotron Light Research Centre in Japan.

3.2 Experimental set-up

Unfilled EPDM samples of varying cross-linking density were provided by the HYDROGENIUS lab in Kyushu university Japan in the form of sheets of 2mm thickness manufactured by the process of compression moulding. More details have been given in the previous chapter.

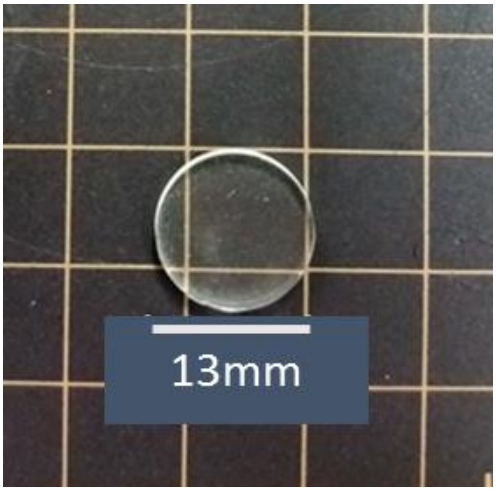

Figure 3.1.EPDM sample used for SAXS experiments done in Japan

Figure 3.2: NanoStar SAXS device

All the specimens for measurement were cut from these sheets in the form of discs of 13 mm diameter: see Figure 3.1. Similar to this, the disc specimens of 4 mm thickness were cut from a 4 mm thick sheet of EPDM rubber manufactured by hot compression of two 2mm sheets. The SAXS experiments with the lab source at the KYUSHU University were performed at room temperature on the NanoSTAR device (see Figure 3.2) equipped with a Copper anode and a 2D position sensitive proportional counter with the following conditions:

Size of the beam: 1.1 mm

Wavelength of the Cu anode: 1.54 angstrom

The details of the synchrotron source experiments and the additional tests done at the PIMM laboratory are given later in the chapter.

3.2.1 Ex-situ test

In this test series, samples were exposed to hydrogen till saturation and decompressed before the SAXS scan. The disc specimens were exposed to 99.99% hydrogen gas at 30 MPa in a high-pressure vessel for 24 hours ensuring that the sample was completely saturated after which the vessel was rapidly decompressed at a rate of more than 90 MPa /min. it should be noted that the decompression rate cannot be altered. The samples were then taken out and taped to the sample holder; see Figure 3.3, such that the beam would be incident on the central part of the specimen. The lag between the start of decompression and the first SAXS measurement was 10 minutes.

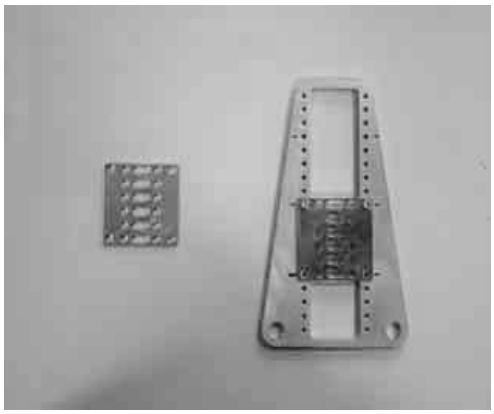

Figure 3.3. Sample holder for NanoStar device

The sample chamber of the SAXS bench was kept at atmospheric pressure to avoid the decompression of the exposed samples. The beam path between the X ray source and the detector were kept at vacuum except for the sample chamber which is separated from the beam path by a polyethylene terephthalate film. The acquisition time for the ex-situ experiments was kept at 180 seconds so as to not be affected by the bulk volume change during desorption of hydrogen. The change in bulk volume of the EPDM samples due to hydrogen desorption is already shown in the previous chapter and is quite rapid immediately after the decompression. The thickness of the samples was measured prior to hydrogen exposure. The SAXS

measurements were done after each 10 minute interval to see the evolution of the scattering spectra after the decompression from saturation in hydrogen at 30 MPa.

3.2.2 In-situ test

For performing the in-situ experiments, a device was built at the Hydrogenius laboratory with an internal chamber of 5 mm width and a diamond window on each side to allow the transmission of the X-rays. The chamber was connected to an external hydrogen cylinder through a thin metal hose equipped with a pressure gauge and valve that could be opened and closed manually. Keeping the gas safety laws of Japan, the in-situ tests could only be carried out at less than 1 MPa. The beam path between the X ray source and the detector was kept at vacuum. The in-situ device itself was kept inside the sample chamber of the SAXS equipment which was also kept in vacuum to avoid interference due to air. A schematic diagram of the set up can be seen in Figure 3.4. The acquisition time in this case was 600 seconds as a compromise between data quality and number of data points that could be attained during and immediately after decompression. The increase in the acquisition time could reduce the noise in the gas-saturated samples.

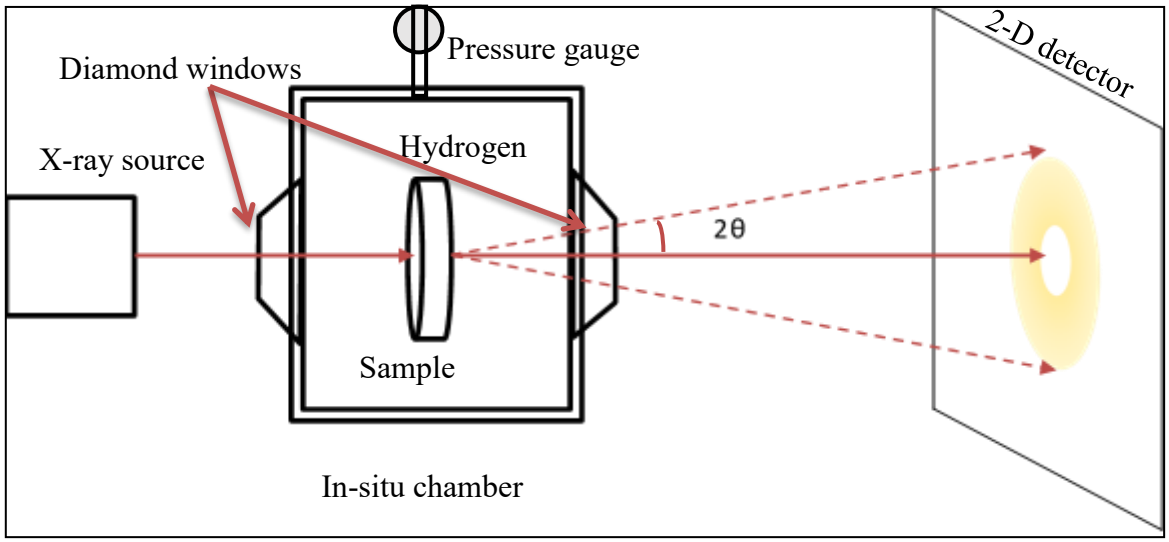

(a)

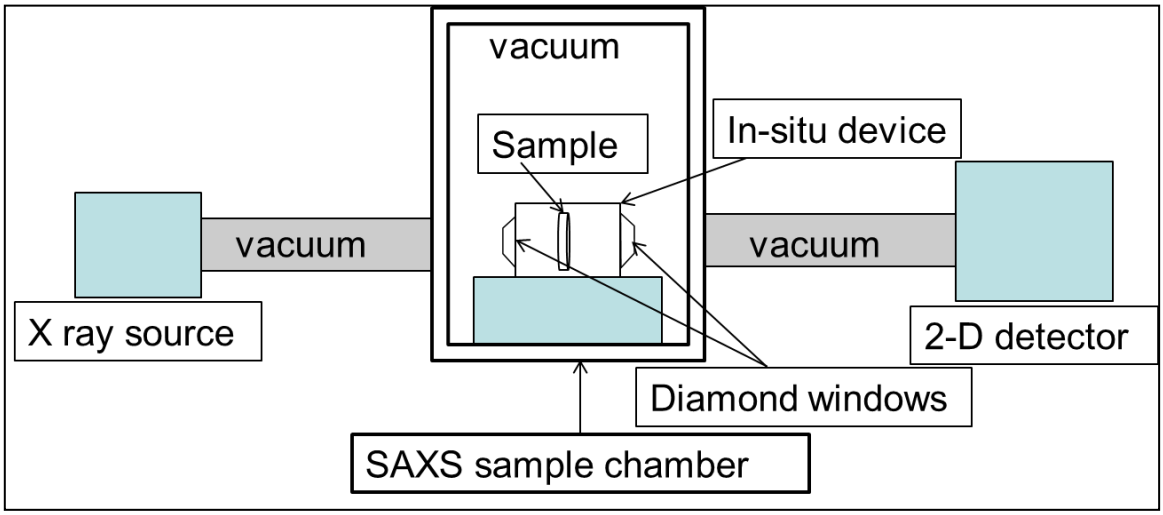

(b)

Figure 3.4(a). Schematic of the in-situ chamber (b) Schematic of the set-up for in-situ tests

For both in-situ and ex situ experiments, the interest was to get data during saturation and decompression or immediately after, hence only the central area of the sample was observed to maximise the data points in time. SAXS acquisition was done for the samples prior to exposure as well as for the vessel without samples to get the background data for correction later hereby referred to as the "blank measurement".

The in-situ tests were also carried at the KYUSHU S*ynchrotron Light Research Centre at SAGA beamline* for two samples of EPDM 0.1 of 2mm and 4 mm thickness respectively. The in-situ chamber was connected to a manual valve which was connected to a remote decompression valve. There was a lag between opening the manual valve and the remote valve causing some initial drop of pressure (approximately 0.1-0.3MPa) from the saturation pressure (P_{sat}) which was less than 1 MPa. The in-situ chamber was mounted between the ionizing chambers of the SAXS bench, see Figure 3.5.

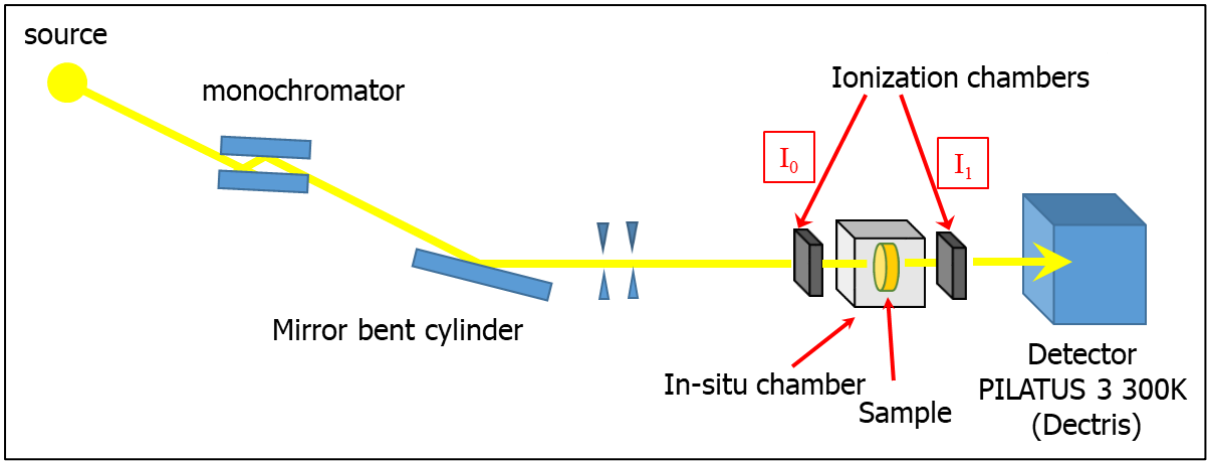

(a)

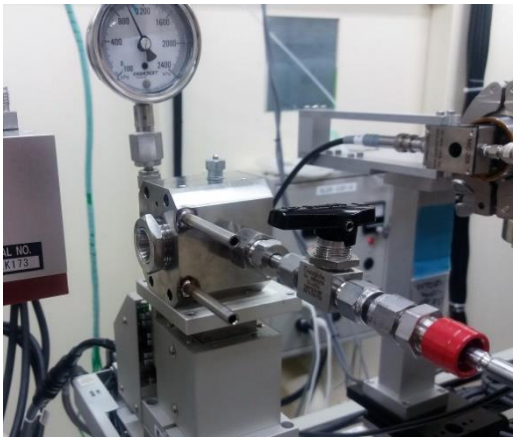

(b)

Figure 3.5 (a) Schematic of SAGA Synchrotron bench set up (b) In-situ chamber

The specifications of the experimental set-up listed below:

Camera length：2234.2 mm

Wavelength：0.15418 nm

Counting time for 2mm samples：30 sec

Counting time for 4mm samples：60 sec

The acquisition was done at equilibrium and for an hour since the beginning of decompression for both samples. As has been seen in the previous chapter, this acquisition time correspond to complete desorption for this saturation pressure of les than 1 MPa. A blank measurement was

also done for subtraction of background later. It should be noted that these experiments were also done at the saturation pressure of less than 1 MPa as the laboratory source experiments. The interest of the Synchrotron experiments was to get more data points since the acquisition time is lesser due to the high brilliance of the Synchrotron source.

3.3 Primary data processing

The primary data processing includes calibration of scattering vector, corrections for incident X ray intensity and background subtraction. The background noise refers to the scattering caused by the windows separating the sample chamber from the beam as well as due to air. For precise data analysis, this background noise must be subtracted from the signal. Mostly, the measurement of the signal with the same set up without the sample or "blank measurement" is carried out to be subtracted from the scattering data later as was done in the present study as has been mentioned in the earlier section.

For quantitative measurements, the intensity needs to be converted to absolute units with respect to the scattering intensity of a standard for which the absolute intensity is already known (pure water in the present analysis). In the present study, the images obtained from the 2D detector were radially averaged into a 1-D scattering curve of $I(q)$ since the scattering was isotropic with respect to the azimuthal angle (see Figure 3.6).

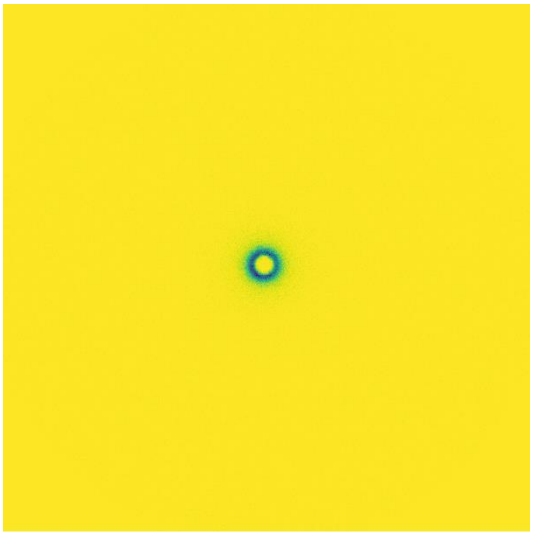

Figure 3.6 The isotropic scattering profile of EPDM 1.6 after decompression from 30 MPa.

The observed scattering profiles ($I_s(q)$) by SAXS measurements were corrected for air scattering, absorption, sample thickness, and incident intensity of X-ray, and then converted to absolute intensity using the following equation:

$$I_{\text{abs}}(q) = I_{\text{s}}(q) \cdot \frac{1}{I_0 \cdot \varepsilon \cdot T_{\text{tr}} \cdot V_{\text{ir}}} \qquad eqn\ 3.1$$

Where $I_s(q)$ is the raw scattering intensity of sample, I_0 is the incident X-ray beam intensity, ε is the detector efficiency, T_{tr} is the transmittance of X-ray through the sample and V_{ir} is the irradiated volume. Subsequently background was subtracted for carrying out further data analysis.

3.4 Scattering due to non-particulate systems

Small angle X-ray scattering can be used to study non-particulate systems like liquids, glasses and amorphous polymers where the heterogeneities arise from the difference of electron densities of different phases in case of a multiphase system or from statistical fluctuations in the single phase system. In general, heterogeneities of any kind in the colloidal range can be studied using this technique.

3.4.1 Two-Phase and Multiphase systems

A multiphase system consists of two or more phases with different scattering densities separated by an interface and in which case, the small-angle scattering is caused by the presence of regions of colloidal size, occupied by different phases.

Ideally in a two-phase or a binary system, represented in Figure 3.7, the two phases have constant electron densities and the contrast is represented by a mean square fluctuation in comparison to a particulate disperse system where the contrast is represented by the difference of mean particle and solvent densities. In addition, the contrast does not depend on the shape of the heterogeneities but the volume fraction of each phase.

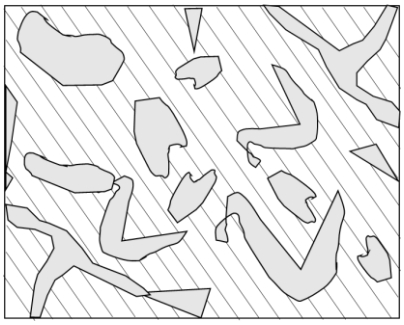

Figure 3.7. Schematic of an ideal binary system

In general, the basic expressions derived for the particle solutions still hold for a non-particulate binary system but meaning of the structural parameters is less discerning. Hence, for a two-phase system the generalized correlation function $\gamma_{0(r)}$, although containing an estimate of the average dimensions and heterogeneities, has a probabilistic meaning. Simply put, it describes the averaged surrounding as seen from a single reference point, marking the area with an excess probability of having the same matter as the said reference point.

Additionally, in contrast to the case of scattering by a homogenous particle, the volume calculated from the value of the invariant can only be regarded as an approximate estimate of an average volume of the heterogeneities in non-particulate system. It should also be noted that since no largest dimension (D_{max}), calculated from the distance distribution function, can be defined in a non-particulate system, the correlation function decreases asymptotically in the higher q values rather than having a sharp drop to zero as is the case with a particulate system.

The loss of intuitiveness for the calculations is not too major in case of the correlation length (Ξ), which might be considered a reasonably good measurement of the size of heterogeneities in the multiphase non particulate system. Interestingly, the concept of shape could be a valuable distinguishing parameter as in case of lamellar and globular systems and holds well as the derivation does not take into account the particle system.

It is well known that only the scattering by an ideal two-phase system with constant but different electron density in each phase separated by a sharp boundary obeys the Porod's law according to which the intensity decreases asymptotically in the high q region with a -4 slope: $I(q) \propto Sq^{-4}$.

The formula is valid for a non-particulate system since only the surface structure is of importance in this context, independent of large scale features. If the intensity is expressed in absolute units

and the electronic contrast is known, the formula can be used to calculate the specific surface S (total surface per unit volume) of the particles via eqn. 3.2.

$$I(q) = (\Delta\rho)^2 . \frac{2\pi}{q^4} . S \qquad eqn\ 3.2$$

The above mentioned cases have been defined for an ideal binary system which consists of two phases with constant electron density and separated by a clear interphase. The parameters, however, deviate from ideality in case of a quasi-binary system with either no clear interface between phases or fluctuations of electron density within one phase, which makes the quantitative analysis of a heterogeneous system much more difficult. A suitable approach to evaluate the diffraction pattern would be to calculate the correlation function and to interpret it with a proper formalism. It has to be noted that, in this case, the correlation function would be different than of the particle system due to the lack of a clear boundary. Consequently, the characteristic -4 slope would not be observed in the high q regions.

The Debye-Bueche function has been used to characterise the inhomogeneity in swollen polymer gels and more recently in hydrogen exposed NBR. In a similar way, Porod's law is important for characterising porous materials. These two methods of analysis pertain to the results in the current study and are discussed in detail below:

3.4.2 Debye analysis

Geissler et al while investigating PDMS gels using SAXS and SANS spectra showed that the scattering was dominated by the excess scattering of the frozen in elastic constraints in the small q regions (Geissler et al. 1997). They showed that a 2 term expression (eqn 3.3) could be used to describe the gel structure in the larger q range explored, where the first term is mathematically of lorentzian form (eqn 3.4), and the second is a squared lorentzian term (eqn 3.5). Shibayama et al used a similar scattering function for inhomogeneous swollen gels to analyse the SANS results for a series of cross-linked isoprene rubber having various network chain densities (Shibayama 1998).

$$I(q) = I_{soln}(q) + I_{ex}(q) + I_{inc} \qquad eqn\ 3.3$$

$$I_{\text{soln}}(q) = \frac{I_{\text{soln}}(0)}{\left(1 + q^2\xi^2\right)} \qquad eqn\ 3.4$$

$$I_{\text{ex}}(q) = \frac{I_{\text{ex}}(0)}{\left(1 + q^2\Xi^2\right)^2} \qquad eqn\ 3.5$$

Where I_{soln} is the scattered intensity from the corresponding polymer solution corresponding to the scattering at high q regions and the density correlation ξ corresponds to the mesh size of the network. However, the squared-Lorentz function, called the Debye-Bueche function, was considered to be most suitable to represent the excess scattering term, $I_{ex}(q)$ since this Debye-Bueche term has been often used to represent the structural inhomogeneity in polymer gels and describes the static fluctuations governed by the frozen-in elastic constraints, which act between topologically connected cross-links. The same analysis can be extended to the present study to characterize the polymer structure saturated in hydrogen by analyzing the scattering in the low q region.

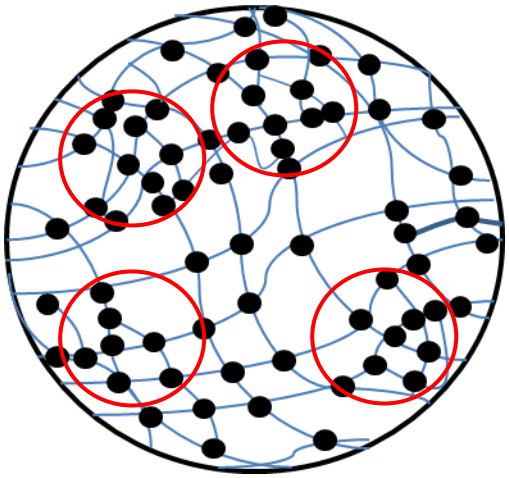

Figure 3.8 representation of the polymer matrix highlighting the local heterogeneity as represented by correlation length Ξ (Ikeda et al. 2009)

In the present case, the Debye Bueche term corresponding to the scattering due to static inhomogeneity in gels has been used to characterize the inhomogeneity in the rubber matrix treated as an inhomogeneous non particulate system, see Figure 3.8. This function has previously been used by Ohyama et al for characterization of inhomogeneity in NBR after hydrogen exposure. This has already been mentioned in the bibliography chapter of this thesis.

This Debye Bueche intensity function has been reported for an inhomogeneous system with 2 phases as the integral of the correlation function $\gamma_{0(r)}$ as follows

$$I(q) = \frac{B}{(1 + q^2\Xi^2)^2} \qquad eqn\ 3.6$$

Which can be also written as $I(q)^{-\frac{1}{2}} = B^{-\frac{1}{2}} + \left(B^{-\frac{1}{2}}\right) \times q^2 \times \Xi^2$,

where B is a constant and takes into account the irradiated volume as well as the averaged square fluctuation of electron density.

In an ideal case, according to this equation, the plot of $I(q)^{-1/2}$ vs. q^2 appears linear within the entire range of scattering vector q and for which the slope intercept ratio would give us the value of the correlation length, see Figure 3.9 (a)

However, for a quasi-two-phase system with a diffused phase boundary instead of a sharp one, there is a deviation from ideality, leading to a departure from linearity in the curve. This indicates a presence of a transition zone between two phases (Li 2013).

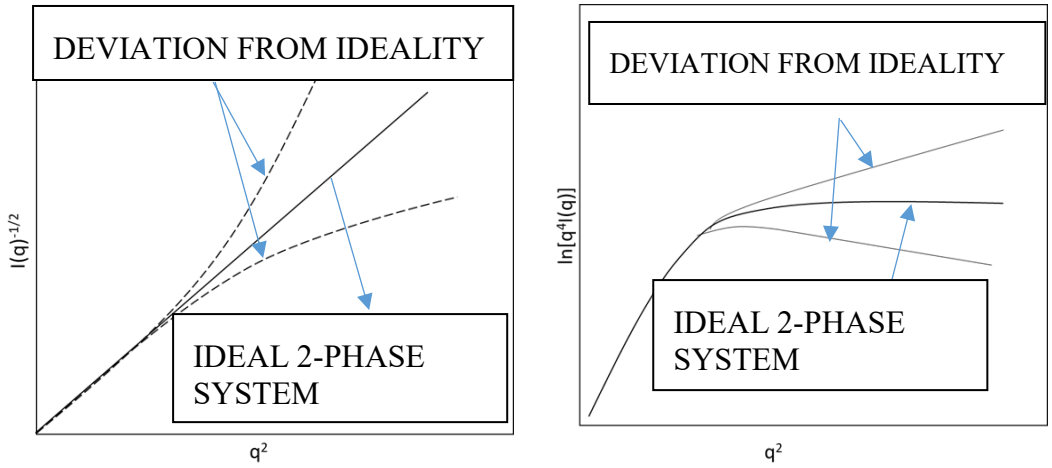

(a) (b)

Figure 3.9 Representation of (a)Debye analysis (b) Porod's plot for ideal 2 phase system and quasi-two phase system indicated by deviations from ideality (Li 2013)

As already mentioned the scattering is dominated by the excess scattering of the frozen in elastic constraints in the small q regions. Hence, the present study is aimed at calculation of the

correlation length in lower values of q; the above equation is held valid and the fitting of the curve in only the linear part of the curve is carried out.

3.4.3 Porod analysis

Theoretically, for an ideal two-phase system, the Porod's plot or the plot of $\ln[q^4.I(q)]$ vs q^2 shows a plateau as shown in Figure 3.9(b). It has already been cleared that although this law holds for the non-particulate system, a well-defined interface should be present to separate the individual phases. However, for a quasi-two phase system without a sharply defined boundary separating the two phases, the curve deviates from ideality similar to the Debye analysis. As such specific volume cannot be quantified for such a system. However, the analysis is carried out to ascertain the presence of a clear interface in the present study to understand whether the phase separation is well defined in the rubber matrix and how it is affected by the exposure to hydrogen. More precisely, Porod's plot would indicate if cavitation occurs after decompression from gas exposure at very low pressure.

3.5 X-Ray scattering for samples before exposure and at equilibrium

Figure 3.10 (a) and (b) show the absolute scattering intensities $I\ (q)$ for EPDM 0.1 and 0.5 respectively in unexposed state as well as at equilibrium (P_{sat} < 1 MPa). In both cases, the upturn can be clearly seen in the low q regions (q < 0.2) which indicates the existence of inhomogeneity in the matrix structure. In polymer gels, this upturn is an indicator of existence of localized clusters in solution (Suzuki et al. 2010). This cluster-like structure has also been observed for such systems as graft copolymers and polyelectrolyte solution (Hourdet et al. 1998; Borsali, Nguyen, and Pecora 1998). As for the polyisoprene/toluene system, Geissler et al. and Horkay et al. observed a similar upturn and clarified that this upturn originates from the dense cluster of undissolved amorphous polymers (Horkay et al. 2000; Geissler et al. 1997).

In the similar vein, the small upturn in the low q regions seen in the graphs can be interpreted as characteristic of network inhomogeneity in the form of dense clusters of rubber molecules interspersed in the area of lower density. The spectra of the rubber-hydrogen system at P_{sat}

show very little change in comparison with the unexposed one and this can be seen in the curves for both EDPM 0.1 and EPDM 0.5.

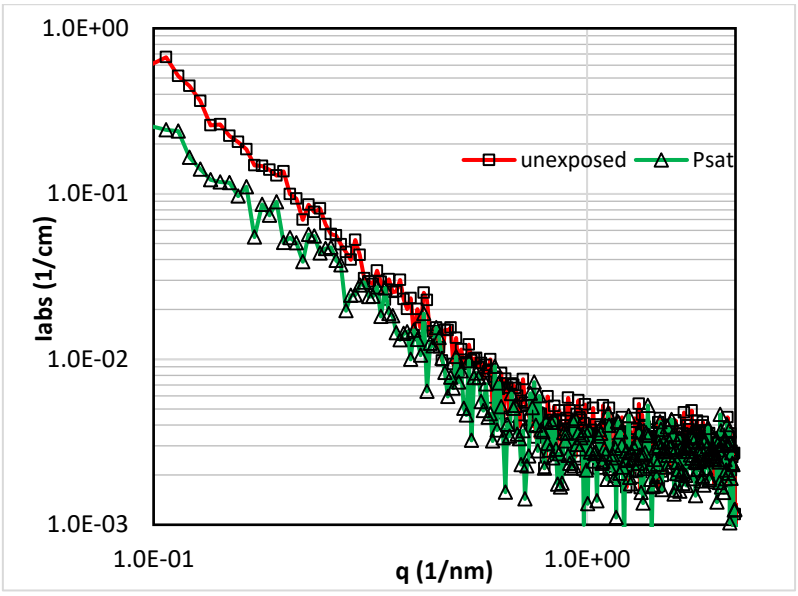

(a)

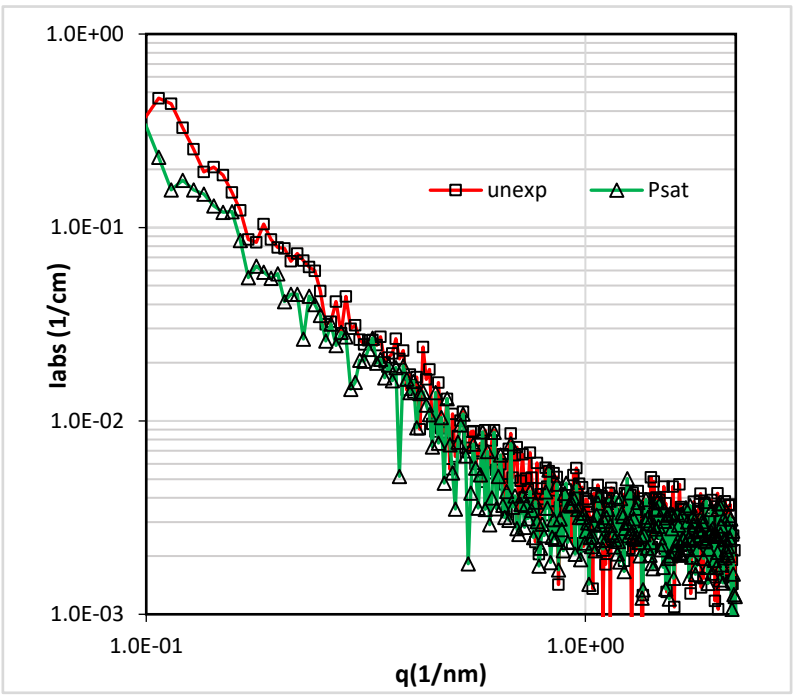

(b)

Figure 3.10. Scattering curves for the samples at unexposed state and at equilibrium for (a) EPDM 0.1 and (b) EPDM 0.5

The difference in the curves can be, in part, attributed to the scatter in the data. This is evidenced in the graph showing the curves for unexposed EPDM 0.1 sample with different acquisition times both in in-situ and ex-situ conditions, see Figure 3.11. The in-situ and ex situ conditions for the unexposed samples refer to the tests done within the in-situ pressure chamber and in the classic normal sample holder described previously respectively. As the scattering intensity is corrected for background in both cases, the only contributing factor for the difference in the curves is the acquisition time and the variation due to an instrumental error caused by the variation in the incident X-Ray beam.

The reason that only a small difference in seen in the scattering spectra could be due to the very low saturation pressure leading to a small penetrated gas content. This could be seen in the previous chapter with the penetrated gas amount being least at 0.6 MPa as compared to higher pressures. This combined with the fact that hydrogen is a very light gas leads to a very small change in the scattering spectra of samples at equilibrium as compared to unexposed ones.

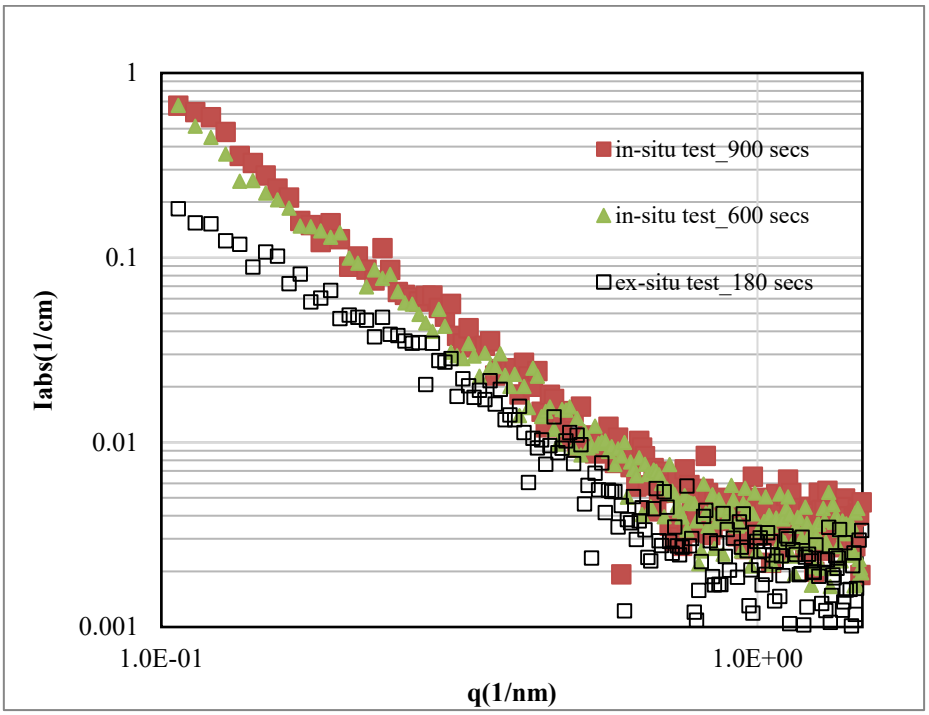

Figure 3.11 Scattering curves for EPDM 0.1 in unexposed state with different acquisition times both in in-situ and ex-situ conditions.

Looking at the same graphs in the high q region, it can be seen that the slopes of intensity curves are higher than -4 which indicates lack of a clear interface which is valid for the non-particulate quasi binary system. This can be supported by the Porod's plot shown in Figure

3.12 which clearly indicates the lack of a plateau in the high q region for both EPDM 0.1 and 0.5. The lack of a clear interface is indicative of lack of cavitation which is consistent with literature as already discussed in earlier chapters; no cavities are seen during the compression phase. Clearly, since the Porod's law does not apply in the present case, the size of the heterogeneities is not calculable for virgin samples or samples at equilibrium.

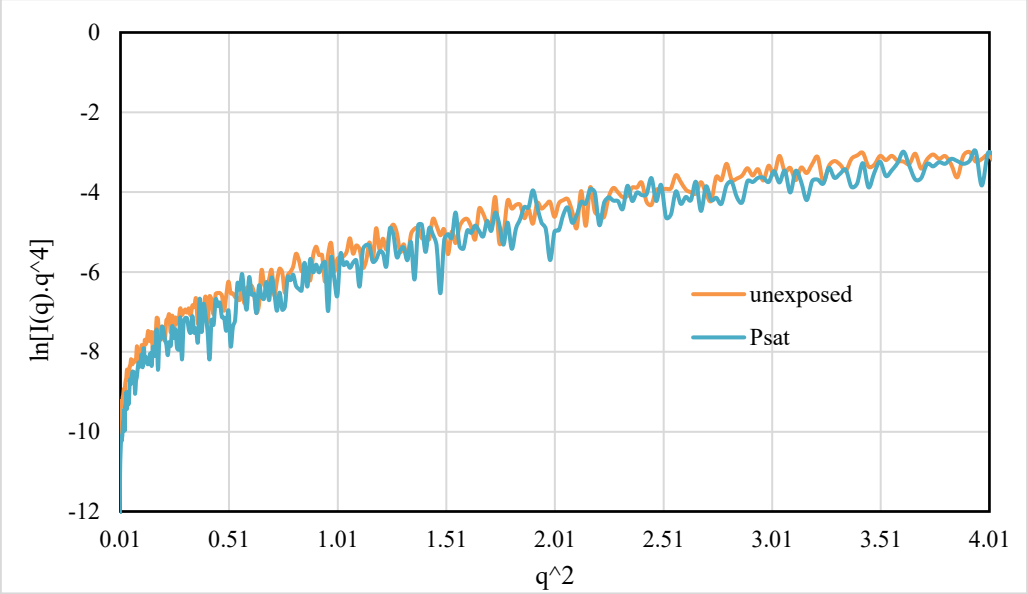

(a)

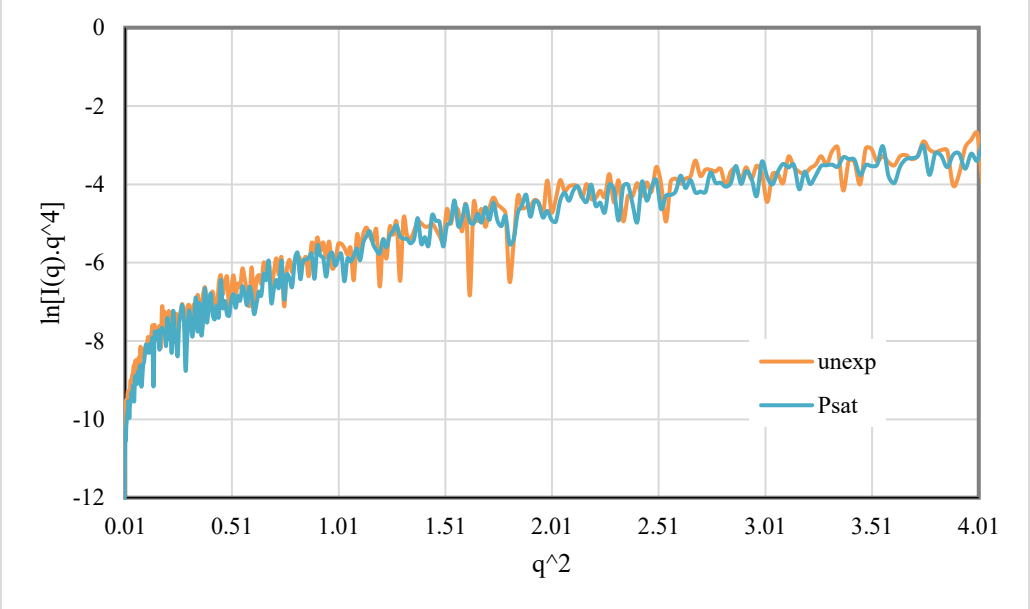

(b)

Figure 3.12 Porod's plot for (a) EPDM 0.1 and (b) EPDM 0.5 at at unexposed state and at equilibrium.

3.5.1 Effect of cross-link density on scattering intensity

It can be seen in Figure 3.13 that the spectra of EPDM 0.1 and 0.5 in the unexposed state are almost superimposing on each other. These spectra were taken for samples inside the pressure chamber with acquisition time of 600 seconds. Similar result is seen in the spectra for unexposed samples taken without the pressure chamber as seen in Figure 3.14

Figure 3.13 shows the absolute scattering intensities $I\ (q)$ for EPDM 0.1 to 0.5 in unexposed state. The graph shows the same trend as could be observed for the samples in the in-situ experiment: upturn in the low q regions (q < 0.2) indicating the existence of inhomogeneity in the matrix structure. Furthermore, it is evident that an increase in the DCP ratio from 0.1 to 0.5 does not affect the scattering intensity values to a discernable degree.

Suzuki et al (2010) in her study on natural rubber noted that the difference in the $I(q)$ at the very beginning was decreasing with increasing DCP content from 0 to 2 phr and noted that the contribution from the DCP to the scattering was negligible and the change could be due to the consequence of peroxide linking. In any case, the DCP ratio change from EPDM 0.1 to EPDM 0.5 is very small in comparison to Suzuki et al's study and therefore, difference in the spectra shown above results is not significant enough. This can be verified for EPDM samples of higher cross-link densities in future experiments.

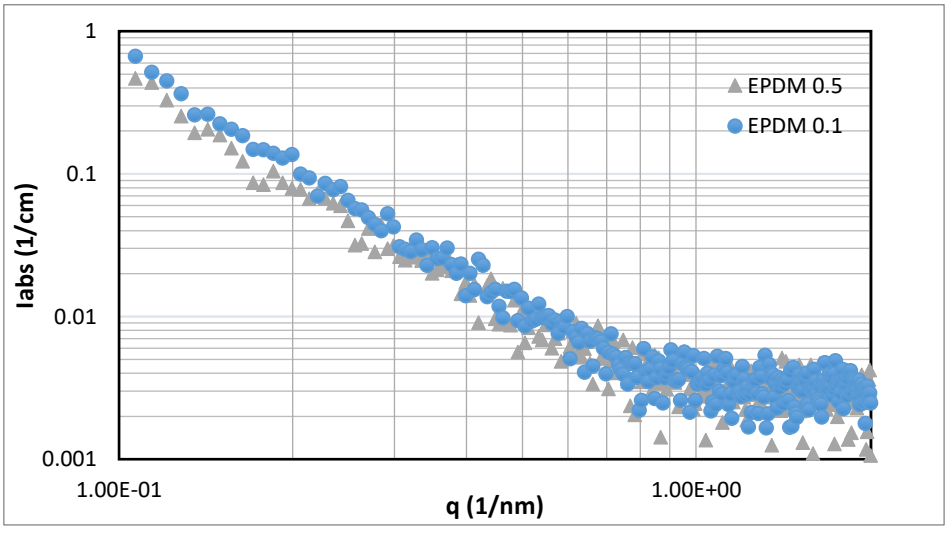

Figure 3.13 Absolute scattering intensities $I\ (q)$ for EPDM 0.1 to 0.5 in unexposed state.

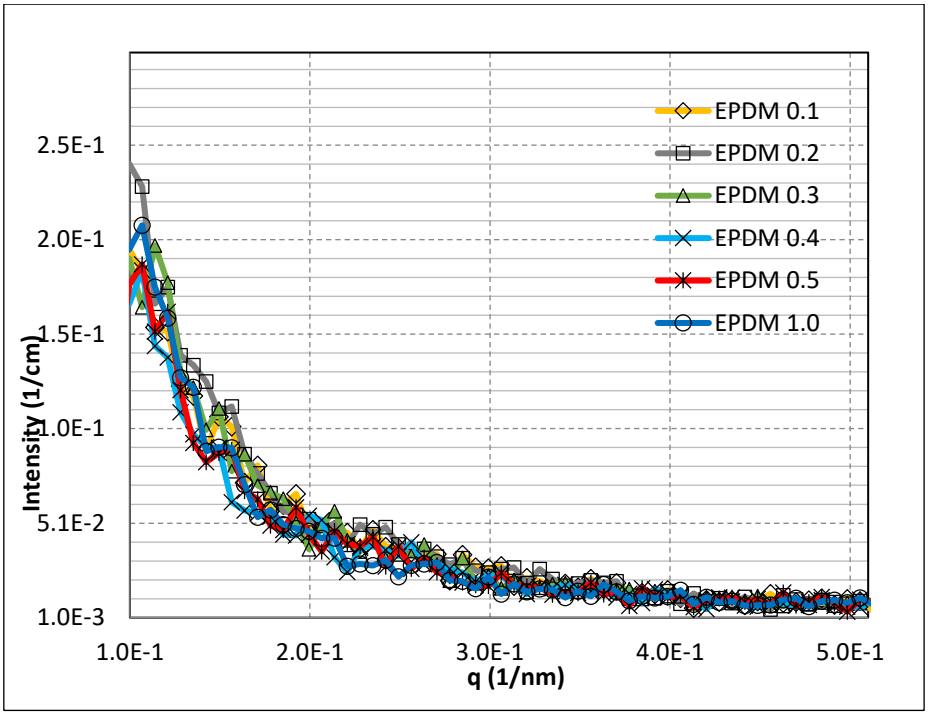

(a)

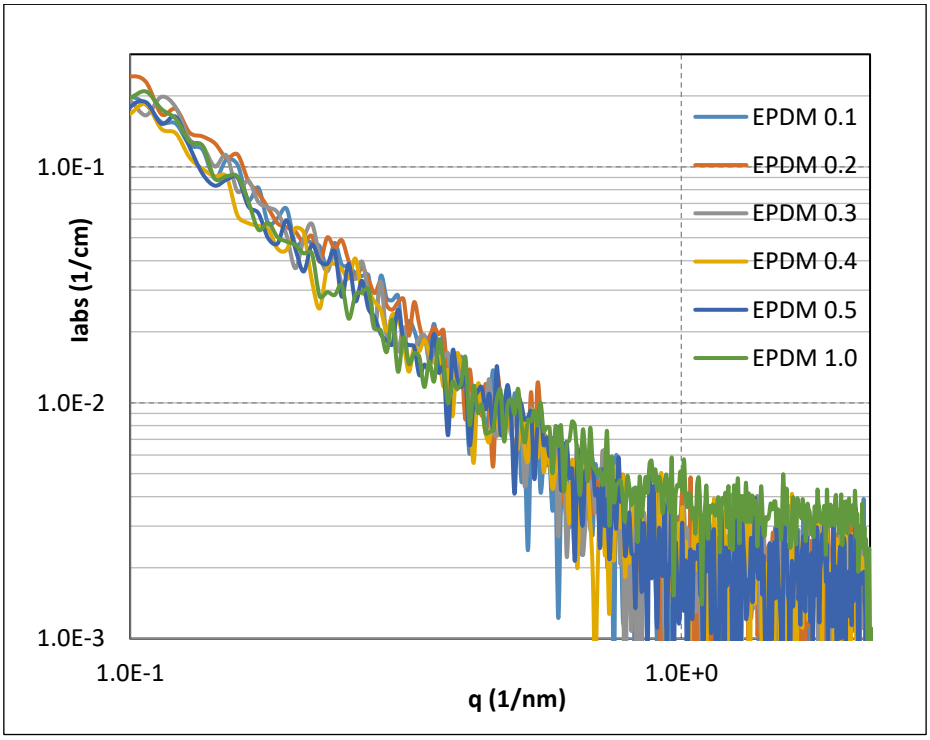

(b)

Figure 3.14. Spectra of unexposed samples of EPDM 0.1, 0.2, 0.3, 0.4, 0.5 and 1.0 in (a) normal scale (b) log scale

3.6 Scattering intensities for exposed samples

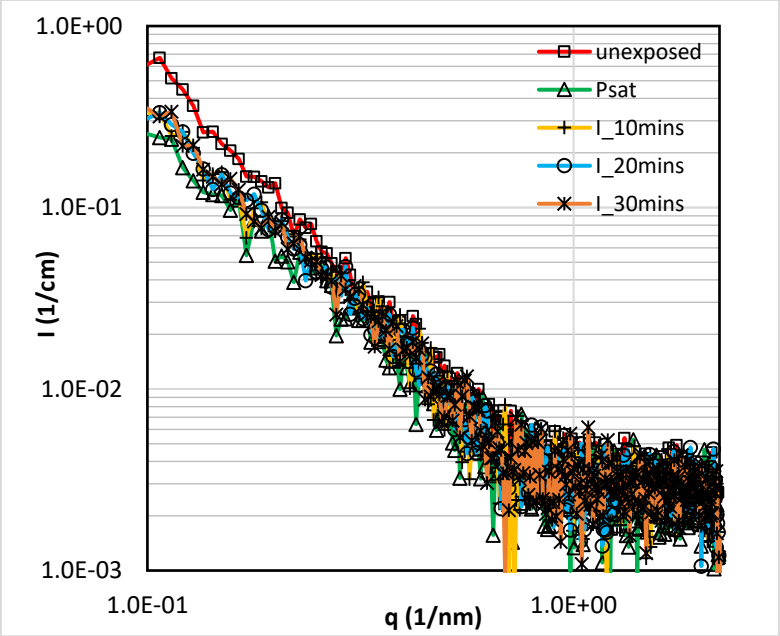

(a)

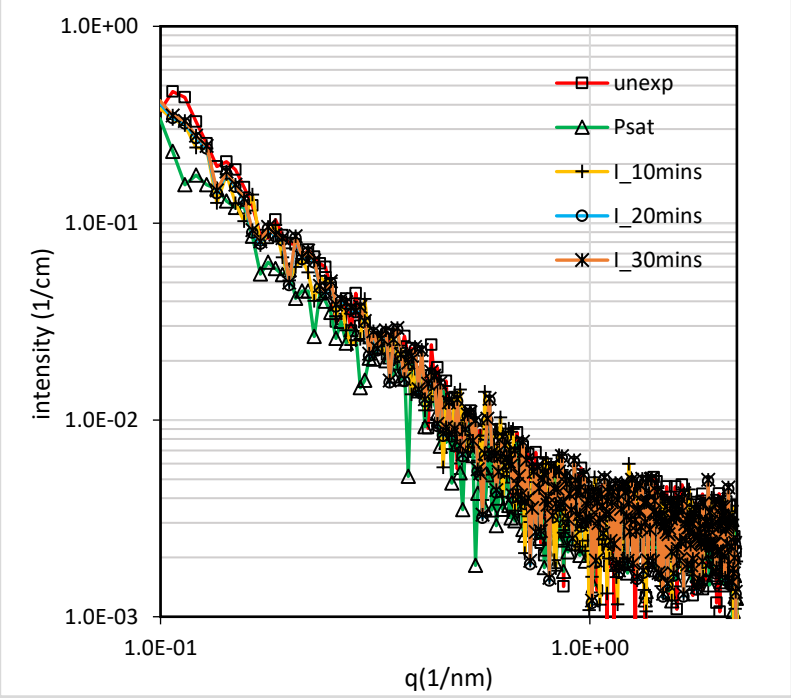

(b)

Figure 3.15. Spectra of (a) EPDM 0.1 and (b) EPDM 0.5 showing absolute intensity vs scattering vector q. I_10, I_20, I_30 refer to intensities at 10, 20 and 30 min after the start of decompression

Figures 3.15 show the scattering curves for EPDM 0.1 and EPDM 0.5 samples for the in-situ test. As can be seen form the curves, any qualitative assessment is not possible as the curves

show very little change from unexposed to decompressed stages. This was the observed earlier for unexposed and saturated samples for in-situ tests.

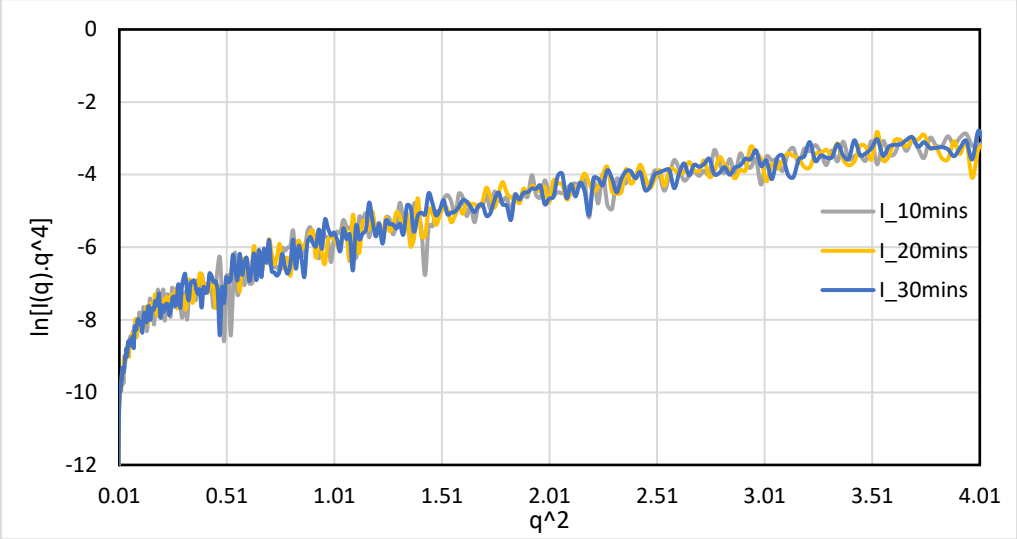

(a)

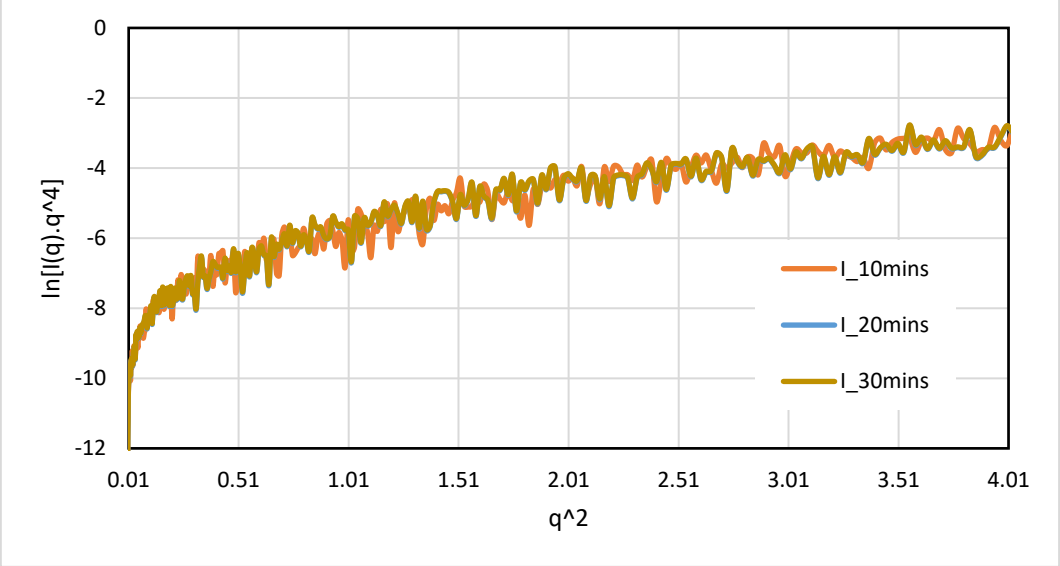

(b)

Figure 3.16 Porod's plot for (a) EPDM 0.1 and (b) EPDM 0.5 at 10, 20 and 30 minutes after the beginning of decompression.

Again, it is clear that the Porod's law is not followed by the current rubber gas system even during decompression, this can be evidenced from Figure 3.16 which clearly shows lack of a plateau in the higher q region. Therefore, the quantification of any possible change in the inhomogeneity of the rubber matrix is done by Debye analysis in order to calculate the

correlation length at unexposed state as well as after exposure to hydrogen for both EPDM 0.1 and 0.5 by fitting the linear part of the curve of $I(q)^{-\frac{1}{2}}$ vs q^2; see Figure 3.17.

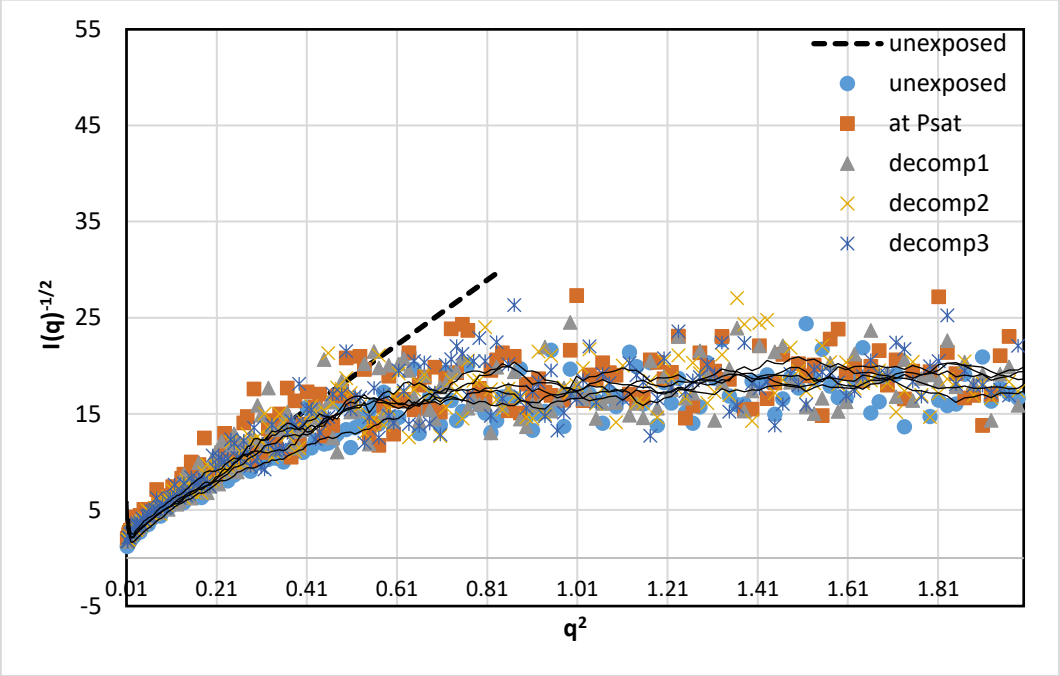

Figure3.17. The Debye analysis for EPDM 0.1. The dotted line is the linear least squares fitting of the linear part of the graph for the unexposed spectra. A similar fit was done for the rest of the curves.

It can be seen that after the initial linear part, the curve deviates from ideality of a binary two-phase system, as explained earlier. However since, the interest was to calculate the correlation length Ξ in the low q regions, it could be done by fitting the linear part of the curve with a straight line using classic least squares method and calculating the value of by dividing the slope and the intercept as has already been explained in the earlier section. The results of the calculation are given in the Table 3.1.

Ξ (nm)	UNEXPOSED	AT Psat	I_10	I_20	I_30
EPDM 0.5	4.5	3.9	4.2	4.1	4.1
EPDM 0.1	4.2	3.9	4.1	3.9	3.98

Table 3.1. Correlation length for unexposed as well as exposed samples. Psat, I_10, I_20, I_30 refer to the values for samples at equilibrium and after 10, 20 and 30 min after decompression

As is evident from the values of correlation length (Ξ), there is no significant difference in the size of the inhomogeneity, either in comparison from unexposed to exposed rubber or from samples of different DCP ratios. This is because the calculation is based on fitting the raw data and the differences in the values lie within the error bar for the calculations which can easily be a few nanometers (Geissler et al. 1997).

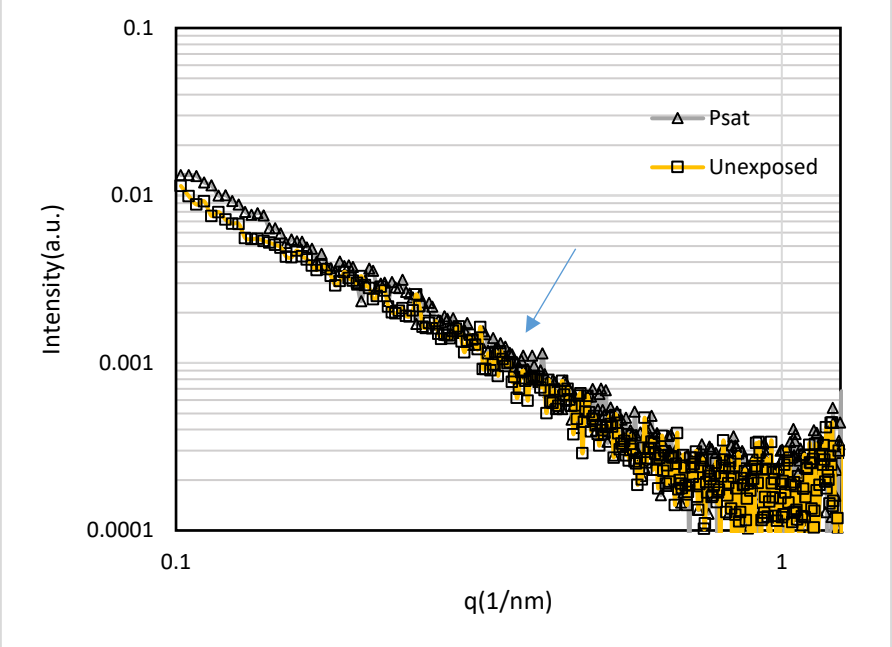

Figure 3.18. Spectra for EPDM 0.1 (4mm thickness). The arrow shows the slight plateau that appears in both curves for unexposed sample and the sample at equilibrium.

Figure 3.18 shows the spectra for the EPDM sample of 4 mm thickness taken at the synchrotron facility, for unexposed and exposed sample ($P_{sat} < 1MPa$). It was possible to do the acquisition for every minute since the start of decompression up to an hour. The results is consistent with the results from the lab source as can be seen from the graph. The curves of the intensities for the unexposed sample are almost superimposing on curves for the sample at equilibrium. Again, this is due to the very low saturation pressure. For synchrotron experiments, the value of intensity has been corrected for volume transmittance and detector efficiency before subtracting the background. However, the intensity was not converted into absolute units since the interest here was to see the change in the spectra in comparison to the laboratory results rather than any quantitative measurements, which in any way would not be possible for the rubber-hydrogen matrix after exposure to very low saturation pressure as has

been seen in the earlier results. However, the data is much less noisy in comparison to the lab source data.

An interesting observation in the curve is an appearance of a plateau as shown by the arrow. Since the graphs had a lot of scatter, and this phenomenon was not seen in any of the earlier curves, additional tests were done with a smaller beam size to explore a larger q range with less noisy data. These results are discussed in the section below and include scattering curves for unexposed and exposed samples after decompression (ex-situ). This could help to evaluate the possible permanent change in the rubber matrix due to high pressure hydrogen exposure after the expulsion of hydrogen.

3.6.1 Scattering for longer q-range

These tests were carried out by S. Tencé-Girault at laboratory PIMM, Arts et Métiers ParisTech.

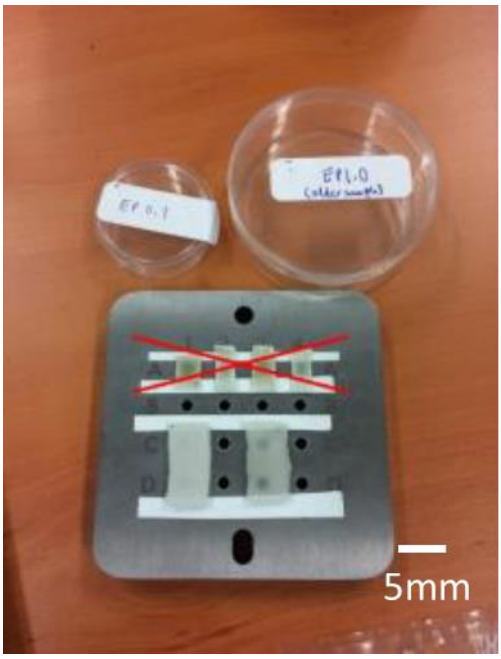

Figure 3.19. Sample holder with the rectangular samples such that two areas of the samples could be irradiated

Samples of 5×10 ×2mm were cut from the same 2 mm sheets as used for previous tests. The samples were exposed to Hydrogen in HYCOMAT facility in a chamber for 24 hours after which it was decompressed at 30 MPa per minute. The samples were then sent to the PIMM laboratory where they were mounted on the sample holder as seen in Figure 3.19 and SAXS

experiments were carried out on them. The time of hydrogen exposure and the time of SAXS experiment was set apart by a week to ensure the complete desorption of hydrogen from the sample. For investigation of the broader q range the minimum wave vector was taken to be at q = 0.005 $Å^{-1}$ or 0.05 nm^{-1}. In addition to samples of DCP ratio 0.1, 0.5, 1.0 samples of DCP ratio 1.6 were also investigated.

Two areas of each sample were observed, with the following experimental conditions:

- The beam size is 200 µm

- Copper wavelength 1.54189 Å

- Counting time 600 seconds

Samples studied:

- EP 0.1 unexposed and EP 0.1 expo H

- EP 0.5 unexposed and EP 0.5 expo H

- EP 1.0 unexposed and EP 1.0 expo H

- EP 1.6 unexposed and EP 1.6 expo H

The spectra of the unexposed samples are reported in Figure 3.20. Regardless of the sample, the two zones analyzed were identical, hence only one curve is shown in the graphs.

A small plateau can be seen in the graphs which becomes more prominent in the Lorentz corrected intensity plot of $q^2 xI\ (q)$ vs q as shown in Figure 3.21. The change of scale from nm to Å should be noted along the x-axis. The position of these maxima, which defines a characteristic dimension over which the scattering occurs, is shown in Figure 3.21.

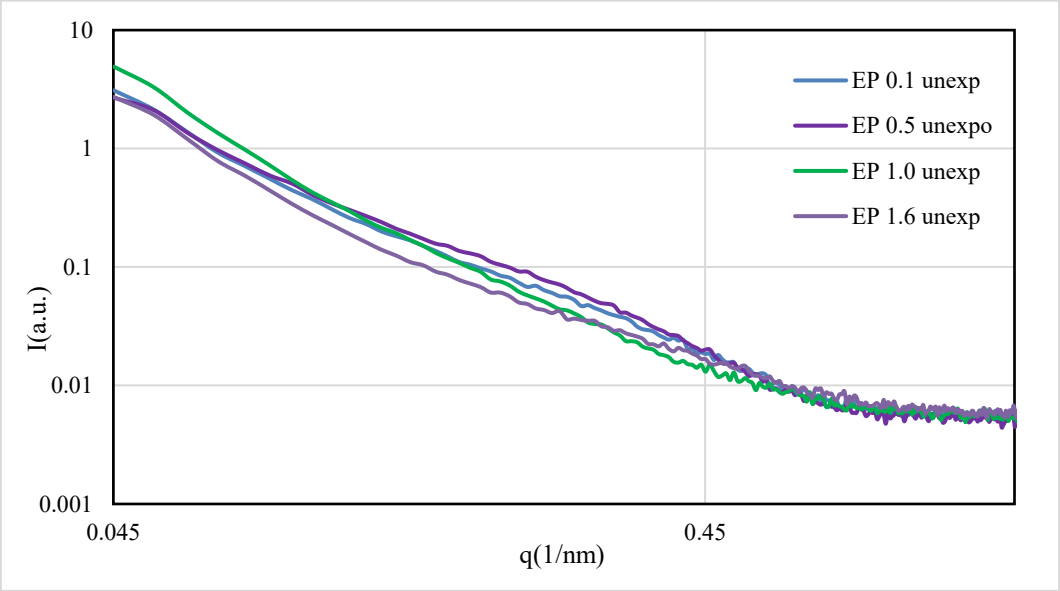

Figure 3.20. Spectra for unexposed samples done at PIMM. A small plateau cam be observed at approximately between 0.2 to 0.3 nm

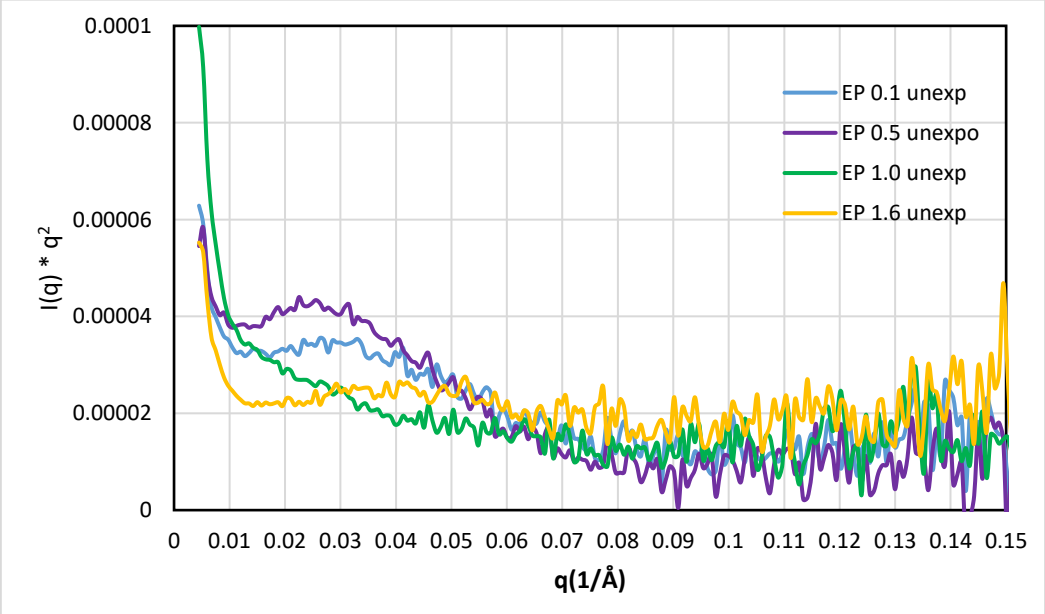

Figure 3.21 Lorentz corrected plot for unexposed samples done at PIMM

Although this maxima is not seen in the previous lab source results, it could be due to the limited q-range explored as well as the large noise in the data. Although the polymers lack long range order, the appearance of this maxima suggests a somewhat ordered distribution of the high density and low density phases of the rubber matrix which is not directly proportional to the cross-link density as is seen from the Table 3.2.

SAMPLE	q_{max} ($Å^{-1}$)	$2\pi/q_{max}$ (Å)	$2\pi/q_{max}$ (nm)
EP 0.1 unexposed	0.030	210	21
EP 0.5 unexposed	0.025	250	25
EP 1.0 unexposed	<0.015	>420	>42
EP 1.6 unexposed	0.038	165	16.50

Table 3.2: characteristic size of long-range order for EPDM samples of varying cross-linking.

After hydrogen exposure, the spectra of the samples are altered as in evident from Figure 3.22, which shows the scattering spectra of unexposed as well as exposed samples. Figure 3.23 shows the Lorentz corrected plot for exposed samples.

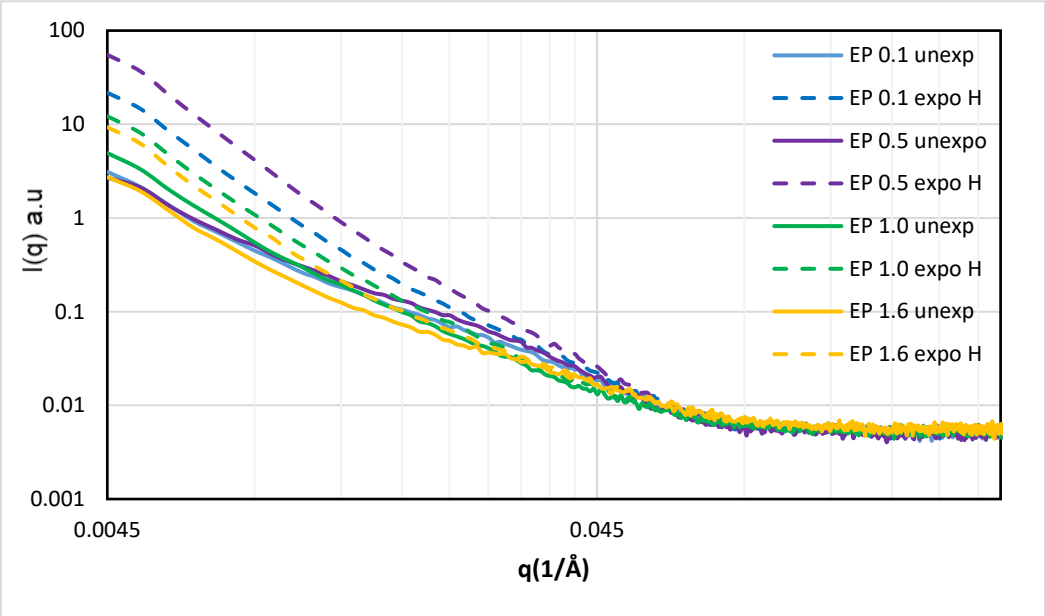

Figure 3.22. Spectra for unexposed and exposed samples done at PIMM. There is no plateau observed for these curves

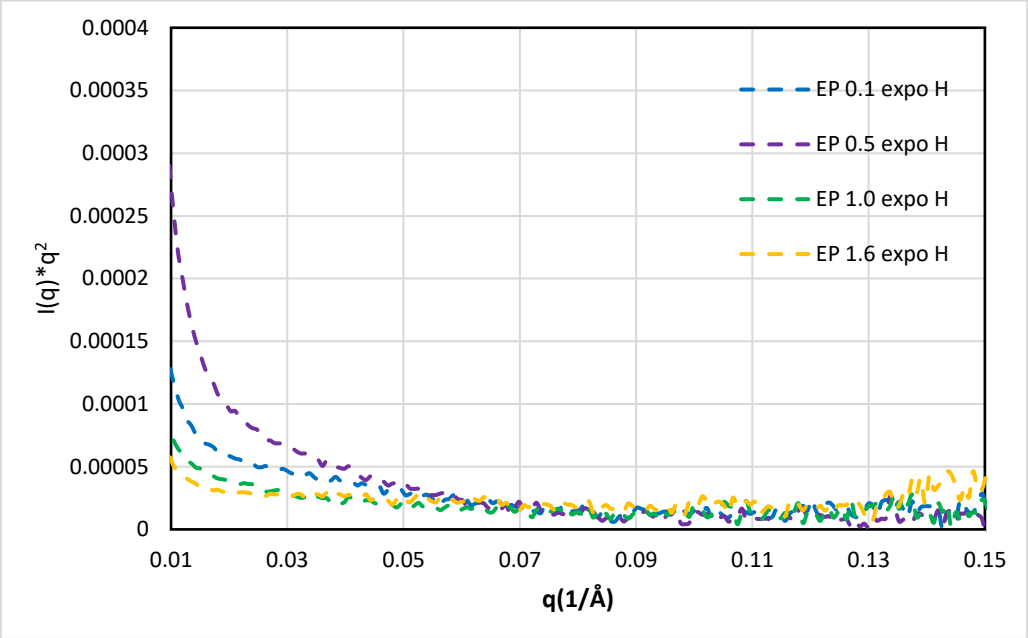

Figure 3.23 Lorentz corrected plot for exposed samples done at PIMM. A central diffusion scattering is observed.

In the logarithmic representation $Log\ [I(q)]$ vs $Log\ [q]$, shown in Figure 3.24 for each sample it is seen that this central diffusion appears linear between q = 5×10^{-3} $Å^{-1}$ and q = 1.6×10^{-2} $Å^{-1}$, the exponent has changed from the unexposed state to the exposed one. The slopes are fitted in the low q region as well as high q region for the exposed samples as the cavities that appear after exposure are of very large sizes visible in the low q-range. In the high q-range the slopes of the curves alter but do not change significantly. On the other hand, in the low q-regions the slope approaches that of -4 indicative of a clear interface between two phases. This corresponds to the cavities that remain in the sample even after complete desorption. This is also visible in the change of colour of the sample which was more pronounced for lower cross-link densities indicating a permanent damage due to high pressure decompression.

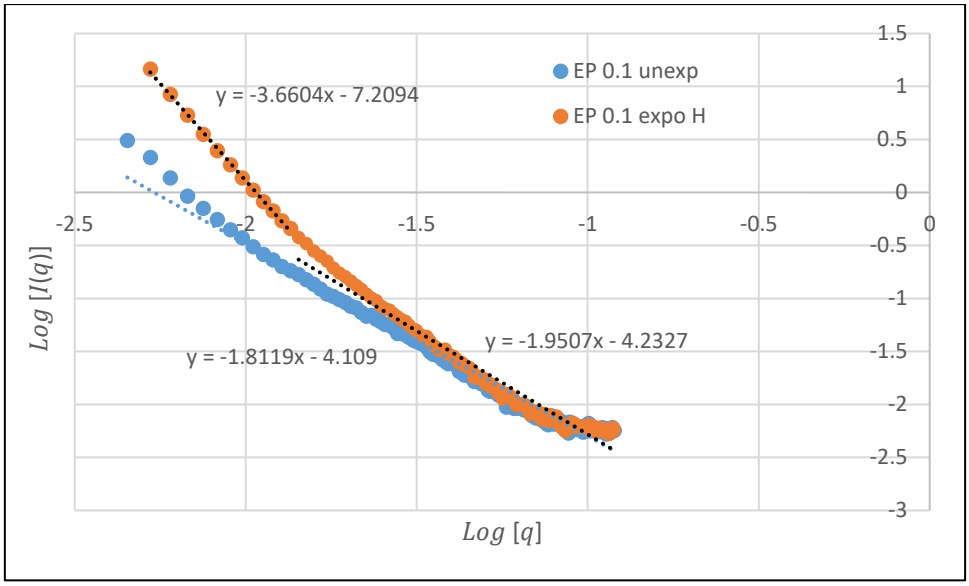
EP 0.1 unexp
EP 0.1 expo H
y = -3.6604x - 7.2094
y = -1.8119x - 4.109
y = -1.9507x - 4.2327
Log [I(q)]
Log [q]
1.5
1
0.5
0
-0.5
-1
-1.5
-2
-2.5
-3
-2.5
-2
-1.5
-1
-0.5
0

(a)

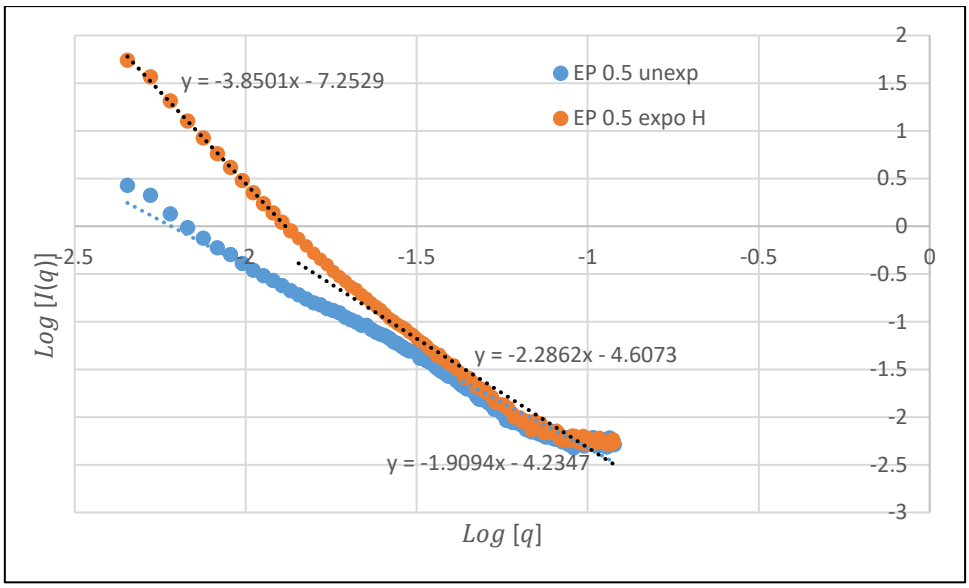
EP 0.5 unexp
EP 0.5 expo H
y = -3.8501x - 7.2529
y = -2.2862x - 4.6073
y = -1.9094x - 4.2347
Log [I(q)]
Log [q]
2
1.5
1
0.5
0
-0.5
-1
-1.5
-2
-2.5
-3
-2.5
-2
-1.5
-1
-0.5
0

(b)

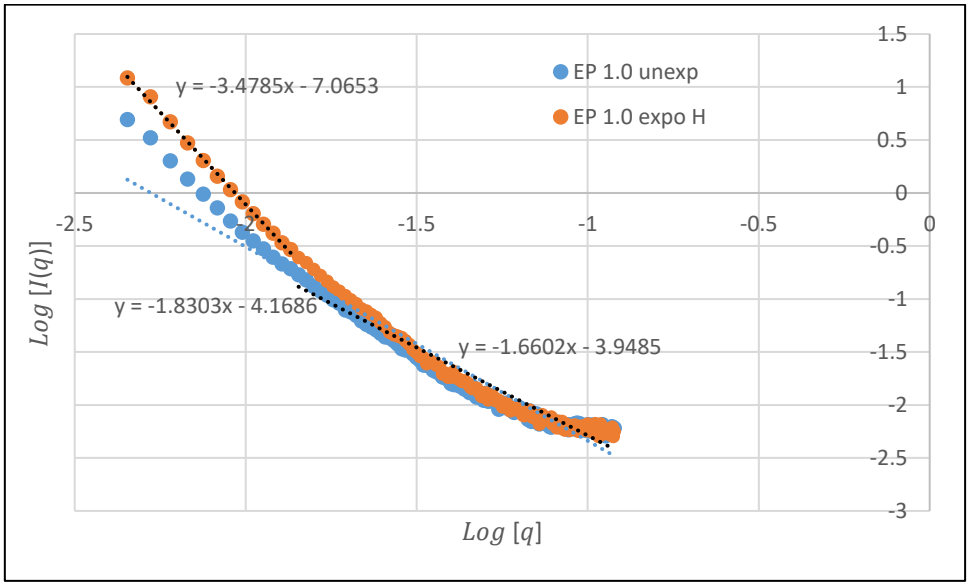

(c)

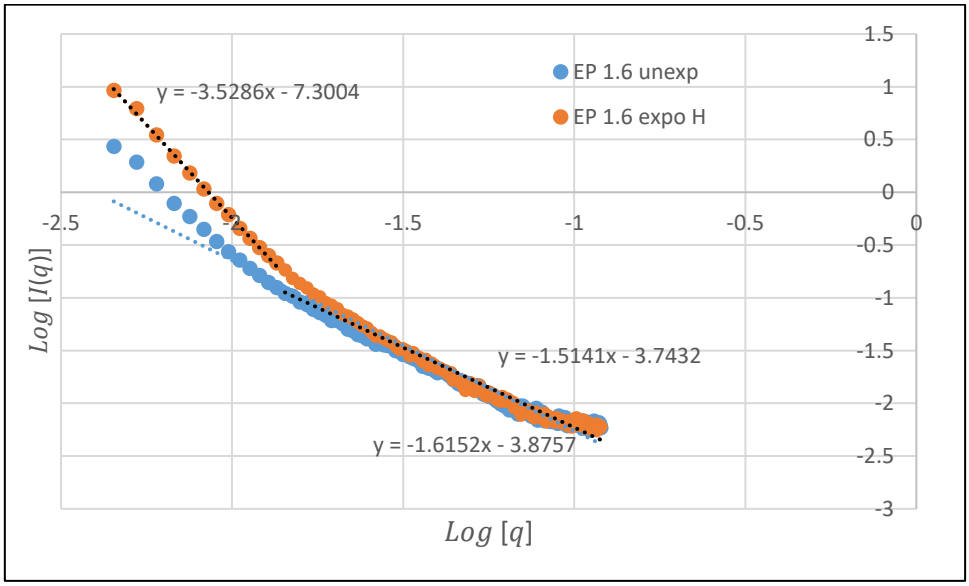

(d)

Figure 3.24 Log scale curves for scattering intensities of (a) EPDM 0.1(b) EPDM 0.5 (c) EPDM 1.0 and (d) EPDM 1.6 in unexposed state and after exposure to hydrogen. EP refers to EPDM and unexposed state refers to the state of sample after desorption. The linear fit is done intensity values at high q. the slopes are given by the equation displayed on the curve.

The altered spectra are also evident from the Lorentz corrected plot for exposed samples which show no maxima, see Figure 3.2. However, it can be seen that the intensity spectra are different even after the time lag between the hydrogen decompression and the SAXS experiment which

indicates that there is some reorganization of the static inhomogeneity in the rubber matrix which is irrespective of the cross-linking degree.

3.6.2 High-pressure exposure: scattering intensity during hydrogen desorption

These high-pressure ex situ experiments were carried out for samples of EPDM with DCP ratio of 1.0 in addition to the EPDM 0.1 and 0.5 samples immediately after hydrogen exposure at a pressure of 30 MPa. As already explained the lag between the beginning of decompression and the first acquisition is 10 minutes.

Looking at the scattering intensities of EPDM 0.1 and 0.5 for unexposed state and after exposure show a visible change in the intensity values at I_{min} (Figure 3.25). This points to a large central diffusion scattering that could be due to a heterogeneous dispersion of hydrogen molecules within the polymer matrix or the presence of cavitation that could be visibly seen in the samples after decompression.

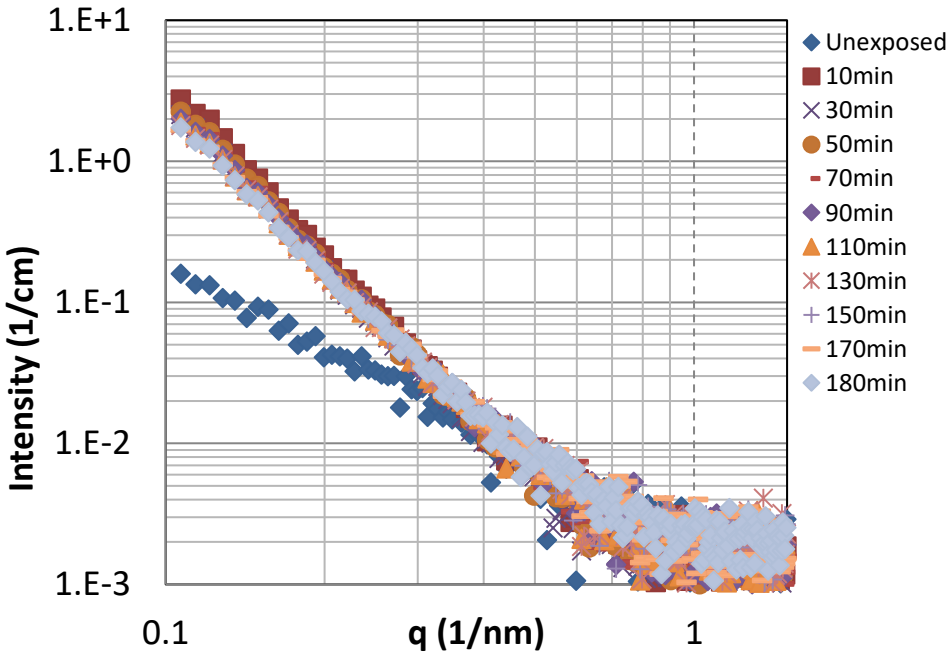

(a)

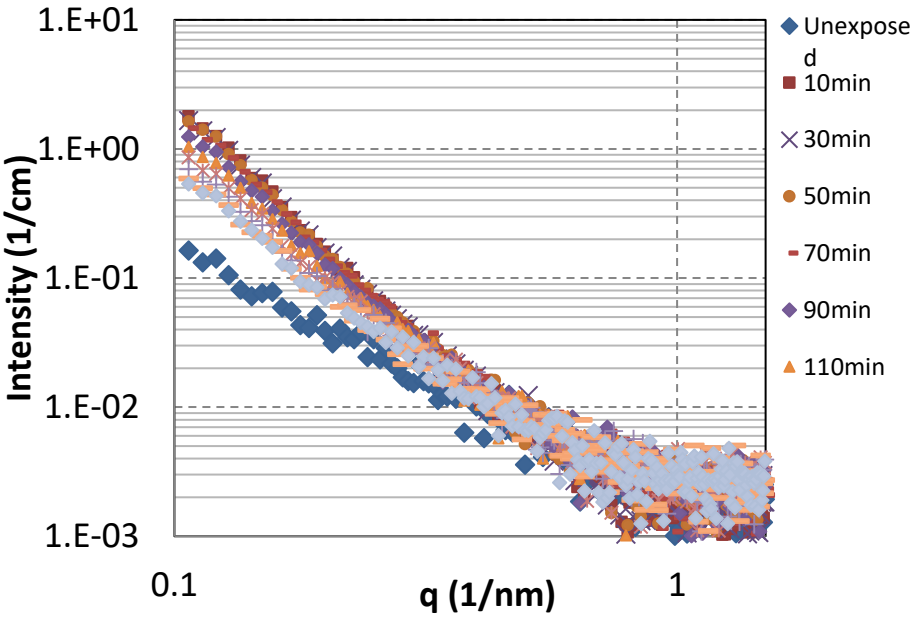

(b)

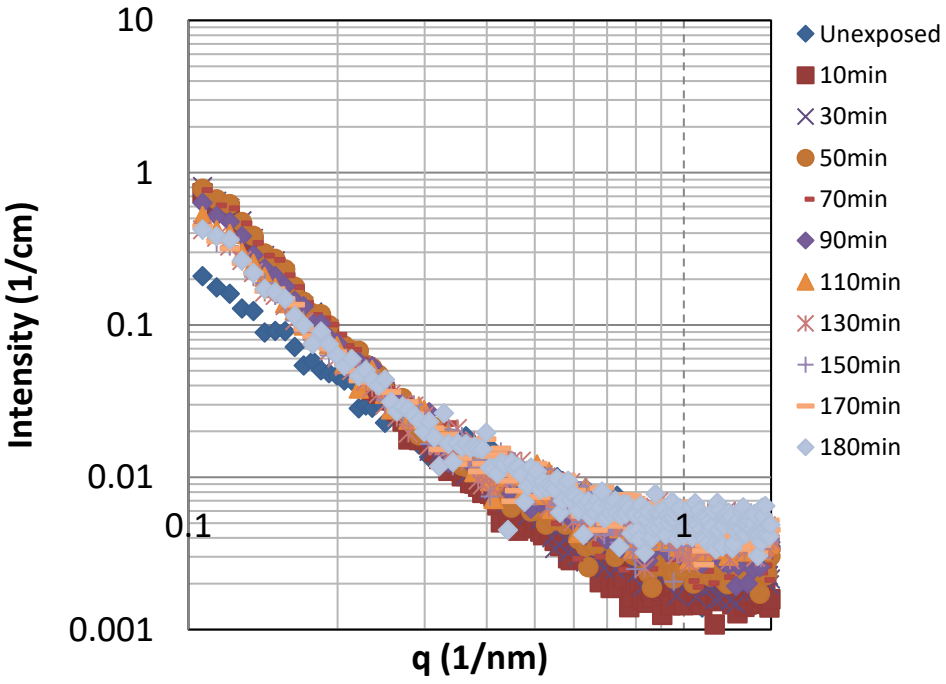

(c)

Figure 3.25 Spectra of (a) EPDM 0.1(b) EPDM 0.5 and (c) EPDM 1.0 for unexposed sample and for times after decompression. Only some of the spectra are shown here since curves for adjacent times overlap each other.

It can also be seen that the value of intensity increases after hydrogen exposure; see Figure 3.25, which indicates an increase in contrast. Again, this could be attributed to the increased contrast between the voids and matrix, which is further supported by the increase in the slope of the intensity at low q regions. The characteristic slope of q^{-4} is seen for EPDM 0.1 but does not appear for samples other cross-link densities even after cavitation. The slope approaches that of -4 in case of EPDM 0.5. Moreover, the characteristic slope is observed for the curves immediately after decompression and decreases as desorption continues. The lack of the -4 slope for other samples could be due to the very close packing of the cavities along with the diffusion on hydrogen in the rubber matrix, which makes it difficult to identify a clear interface. Another contributing factor is the transient state of the voids which are evolving during the 180 seconds of acquisition time that could lead to a difficulty in detecting a sharp interface. Moreover, the slope of the curves decreases in the subsequent data points which is consistent with the deflation of cavities as desorption occurs, thereby decreasing the possibility of observing an interface of the cavities in the rubber matrix. As such, the intensity values can only be interpreted to signify either an increase the number of scattering objects or an increase in the size of existing scattering objects.

As we can see, the curve at 180 minutes approaches the curve for the unexposed sample but does not overlap on it. It can be concluded that the gas-matrix tends to come back to the state of the unexposed rubber matrix but does not completely attain it. This is consistent with the results discussed earlier for the samples tested after complete desorption of hydrogen.

To quantify the change in inhomogeneity, the Debye analysis was done in similar way to in-situ experiments to calculate the correlation length. The change in correlation length with time after decompression can be seen in Figure 3.26. The first plotted point in red at the axis corresponds to the value of correlation length for the virgin material. It can be seen that after decompression the value of correlation length increases since the heterogeneity is now a function of cavities as well as the static fluctuations of the rubber matrix. Thereafter, the graph shows a decreasing trend which could be correlated with the global desorption leading to a gradual deflation of the cavities. However, the value does not reach the value of the unexposed rubber matrix.

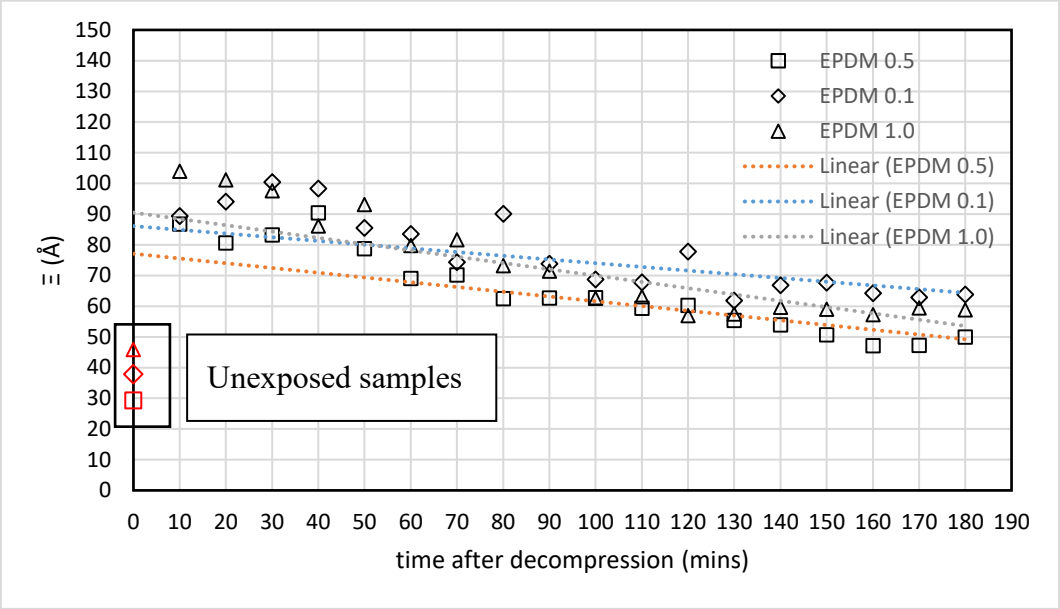

Figure 3.26 Temporal evolution of correlation length of EPDM 0.1, 0.5 and 1.0. The trend line is plotted for each sample.

3.7 Conclusions

The main aim of this experimental campaign was to characterise EPDM at various stages of gas exposure to understand if the microstructural heterogeneity of rubber induces cavitation and if crosslink density could be used as an indicator of this heterogeneity. The in-situ tests conducted on EPDM 0.1 and 0.5 do not show any change in the correlation length, which would indicate a change in the size of heterogeneities in the rubber matrix due to the hydrogen exposure. This is however due to the low saturation pressure and is supported by the results from the ex situ experiments which clearly show an increase in the correlation length after decompression from high-pressure exposure. However, the results from the synchrotron source experiments showed a slight and diffused plateau that could be a possible indicator of a correlated structure. To clarify this, additional scattering experiments were carried out exploring a longer q-range which could enable the acquisition at a lower value of q that is $0.05nm^{-1}$. This plateau was observed again in case of unexposed samples which became clearer in the Lorentz corrected plots. However, the position of these maxima were not directly correlated with the cross-link density of the samples. After exposure, no maxima were detected in the curves. This was as a result of large central scattering that was superimposed on the initial spectra due to scattering by the cavities that appeared in the sample after decompression

from high pressure. It is important to note that these experiments were carried out after the complete desorption of hydrogen form the sample. Results from the scattering experiments done immediately after decompression during the desorption of hydrogen indicate that the spectra of the exposed samples taken immediately after decompression show a marked difference from the spectra of the unexposed sample and these spectra tend to approach those of the unexposed samples as the desorption progresses. However, the spectra of the exposed samples do not superimpose those of the unexposed samples even after complete desorption of the gas, indicating a permanent structural change in the rubber matrix after single hydrogen exposure. As a general conclusion, it can be underlined that the hydrogen exposure leads to microstructural change in the rubber matrix which is retained even when the gas is fully desorbed. It was also seen that the heterogeneity of the rubber matrix at the sub-micron scale is not directly correlated with the cross-link density. Additionally, the low pressure experiments are not enough to calibrate the degree of heterogeneity in rubber matrix; the in-situ experiments carried out in the present study showed that no change in the correlation length, corresponding to the matrix heterogeneity, was observed after hydrogen exposure.

A better characterisation of these samples could be possible with high pressure in-situ tests in future. Nevertheless, the tests performed in the present study offer a starting point for designing such complex experiments for future studies. In the present case, the tests give an insight about the size of heterogeneity in amorphous rubber matrix and highlight the effect of hydrogen on the rubber matrix at very low scales.

Chapter 4 In-situ tracking of cavities at micron scale using 3D X-Ray Tomography

Introduction

The difficulties in observation and quantification of the phenomenon of cavitation in elastomers due to gas decompression are limiting factors for the study of their cavity nucleation and interactions. Typically, the techniques applied for detection of cavities due to gas decompression are the same as those used for mechanically induced cavitation and their applicability is restricted by the properties of the elastomer. Additionally, the properties of hydrogen and the safety measures associated with it lead to strong limitations in conducting experiments at the high pressure and require well developed and sophisticated experimental set ups. This makes it more significant for the studies of cavitation to be specific to hydrogen taking into consideration the practical applications and safety constraints. Recently, a 3D analysis technique of micro-tomography, has been used to study cavitation providing an efficient way to visualize the morphology of the damage in the sample by exploiting the change in optical properties of the material due to the presence of voids (Masquelier and Marco 2013). This provides an access to the quantitative data such as cavity size, number of cavities per unit volume as well as their location in the sample volume. Recently, Castagnet et al (2018) used this technique to evaluate the bias in calculation of Morphological RVE done previously using 2D techniques.

Considering the discussion above, the present study aims clarify the question of kinetics of inflation of cavities at the scale of a single cavity or a group of very close ones. So far, the cavitation in rubber due to high pressure hydrogen has been done only at global damage field scale. Here, we have used the 3D in-situ tomography technique to track the cavitation in EPDM rubber to better understand the local phenomenon of cavitation like growth kinetics with emphasis on boundary conditions and interaction effects using the image analysis tool.

4.1 Experimental set up

4.1.1 Samples

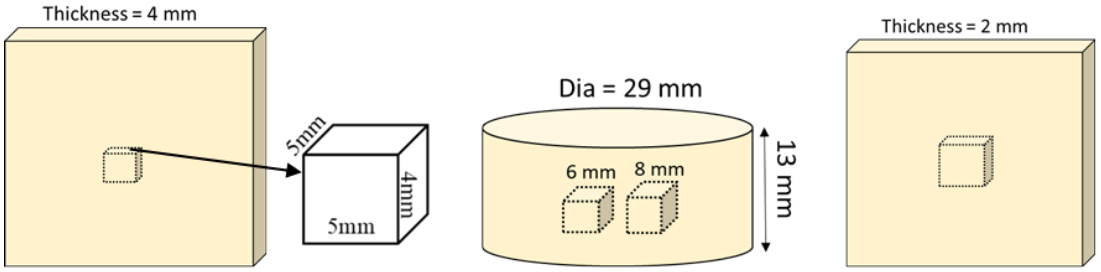

(a) (b) (c)

Figure 4.1 Schematic of (a) flat sheets of 4 mm thickness from which 5× 5× 4 samples were cut. (b) Cylinders from which cubic samples of 8 mm and 6 mm edge were cut (c) flat sheets of 2 mm thickness from which rectangular samples of 20× 20 ×2 mm were cut.

Different geometries of the samples were chosen to ensure a practically suitable saturation time and to capture the damage in as much a representative way as possible at the global scale. Samples of unfilled, peroxide linked EPDM were cut from 15×15 cm plates of 4 mm and 2mm thickness. All samples were taken from the centre of the samples to eliminate any inhomogeneity at the edge due to manufacturing processes. Rectangular samples of EPDM 1.6 and EPDM 0.5 with dimensions of 5 ×5 ×4 mm were cut from the 4mm thick sheets, see Figure 4.1(a) henceforth referred to as Type-1 samples.

Additionally, samples of EPDM 1.6 with dimensions 20×20×2mm were cut from 2 mm sheets, see Figure 4.1(b), henceforth referred to as Type-2 samples. These samples were selected to compare with the thicker samples to evaluate the effect of geometry on the morphology and kinetics of damage.

Square samples of EPDM 1.6 and EPDM 0.5 of 8 mm and 6 mm edge were cut from cylindrical samples of 29 mm diameter and 13 mm thickness, see Figure 4.1(c), henceforth referred to as Type-3 samples. These samples were chosen to evaluate the possible anisotropy introduced in the damage morphology by the geometry of the sample.

4.1.2 Decompression conditions

Tests were carried out at two different decompression conditions:

i. At a saturation pressure of 8 MPa with a pressure release rate of 1.6 MPa/min: samples of **different dcp ratios** were tested in these conditions to evaluate the effect of crosslinking on the size of cavities at a local scale.
   These conditions were calibrated in the Hycomat facility after testing several decompression conditions in order to have detectable cavities with reasonable rate of inflation that could be tracked via the X-ray tomography.
ii. At saturation pressure of 12 MPa with a pressure release rate of 2.5 MPa/min: samples of **different geometries** were tested in these conditions to evaluate the geometrical contribution to the kinetics and/or the morphology of cavities. These conditions were an extension of the tests carried out in previous studies on EPDM (Kane-Diallo et al, 2016).

These conditions also allowed for the comparison of the decompression conditions for samples of same dcp ratio.

4.1.3 Hydrogen decompression tests

For the present study, the experiments were carried out at room temperature. The samples were placed in the chamber which was filled with hydrogen till the required saturation pressure and kept as such till the sample was saturated. The saturation time was calculated for the both EPDM 0.5 and EPDM 1.6 for different geometries, using the equation 3.1. proposed by Crank based on Fick's theory for 1D diffusion through an infinite plate of thickness e exposed to a constant gas content CH_2 on each of the faces.

$$C_t = C_{\infty H_2}(1 - 8\pi^2 \sum_{n=1}^{\infty} \frac{1}{(2n-1)^2} \exp[-(2n-1)^2 \pi^2 \frac{Dt}{e^2}]) \qquad \textit{eqn } 3.1$$

$$C_{\infty H_2} = P_{ext} S_g \qquad \textit{eqn } 3.2$$

where C(t) is the gas content at the centre of the plate at time t after the beginning of exposure, assumed to be zero at t = 0, $C_{\infty H_2}$ is calculated by Henrys law as given in equation 3.2., D is the

diffusion coefficient of hydrogen in EPDM, e is the thickness of the sample. P_{ext} is the external pressure of the gas and Sg is the solubility of the gas in EPDM. The summation was done for 250 terms. Coefficients Sg and D were deduced prior to the tomography test from permeation tests and have been noted in Chapter 2.

In the last part of the experiment, a stage was 3D printed and used to place more than one specimen in the XPRESS chamber. Consequently, the images so obtained for multiple samples had more noise to data ratio as compared to the images obtained in case of a single specimen.

4.1.4 In situ tomography set up

The in situ X-ray micro-tomography was done using an Ultratom tomograph developed by RX Solutions® (Figure 4.2(a)). The device essentially consists of three X-ray source tubes with micro-focus, nano-focus and high voltage specifications, a sample mount on top of a rotation stage, and two types of X-ray detectors: Varian detector for classical and CCD camera for high-resolution acquisitions respectively.

For the present experiments, the tomograph was fitted with the cylindrical pressure chamber (XPRESS chamber) as seen in Figure 4.2 (b), which allows the tests to be carried out in different gaseous environments. Other details of the device are given in below

- Gases in which in-situ tests can be performed: N_2, CO_2 and $\mathbf{H_2}$
- Maximum operating pressure: 200 bars
- Maximum operating temperature : 150°C
- Remotely controlled
- Compression and decompression rate : regulated

The sample was centred on the rotation axis inside the chamber at a distance of 36-mm from the X-ray source (voltage 80 kV, current 375 µA). The Varian X-ray detector was used which consisted of an X-ray CsI scintillator screen settled on an amorphous silicon layer with 1920x1536 sensitive elements.

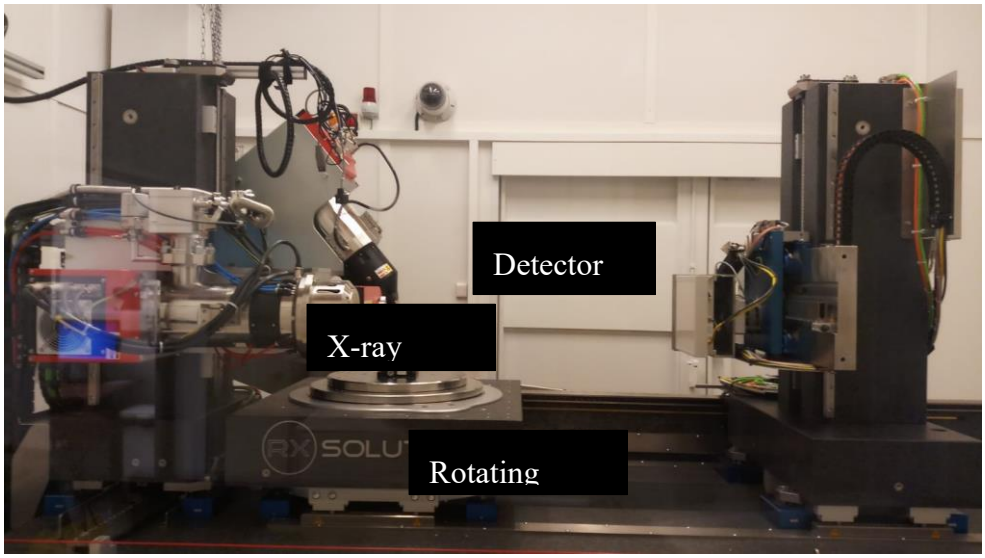

(a)

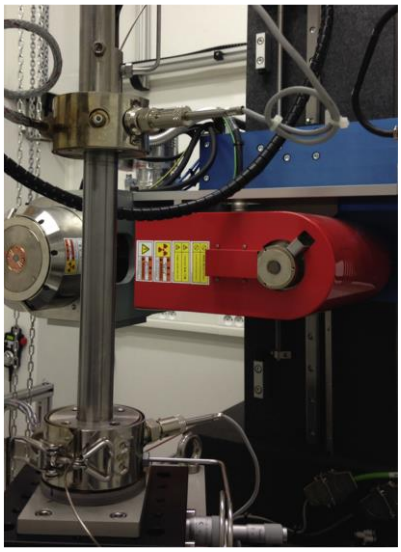

(b)

Figure 4.2 (a) Ultra Tomograph (b) XPRESS chamber for in-situ tracking of cavities in H_2

4.2 Data treatment

4.2.1 Image reconstruction

During the tomography experiment, the model rotates in small steps about an axis of rotation while taking a sequence of 2D radiographs which are later numerically reconstructed into a 3D

image displaying the internal structure of the sample which in the present case refers to the cavity damage field.

For our study, the image slices obtained from the test as explained above were then reconstructed by a conventional filtered back projection algorithm using the commercial software supplied by RX solutions. Various parameters like spot correction, ring artefact correction, contrast equalisation and offsetting of the image to account for the source displacement were carefully selected manually, adaptable to the raw images collected, to optimise the reconstruction for further post processing. In the present study, the main challenge was to get a good quality image without introducing many artefacts due to the kinetics of the transient phenomenon. Since, each radiograph corresponds to an average of multiple images, the number of which determines the acquisition time for each rotation, better resolution images are extracted with a higher acquisition time. However, a higher acquisition time introduced artefacts due to very rapid dilation of cavities which resulted in a poor 3D reconstruction.

These artefacts due to the distorted images of tracked cavities are not a trivial problem as they affect the quantitative measurements accessible from the image processing later. Hence, it was necessary to optimise the acquisition parameters to ensure that growth of cavities within one rotation required for a complete reconstruction was minimum and image quality was good enough.

For the present study, the device was configured for the following acquisition parameters: 200 projections taken over 100 seconds corresponding to a complete 360° rotation. A schematic of the procedure can be seen in Figure 4.3 (a). The acquisition was done for 3600 seconds starting at the beginning of decompression, see Figure 4.3 (b).

The error estimation associated with the evolution of the cavity size during the acquisition of the stack was done previously in a study by Castagnet et al on EPDM samples saturated in Hydrogen at a pressure of 12 MPa and decompressed at 2.5 MPa/min. The error percentage was calculated using MATLAB code and was estimated to be 3.2% between the ideal acquisition parameters and much degraded ones (Castagnet et al. 2018).

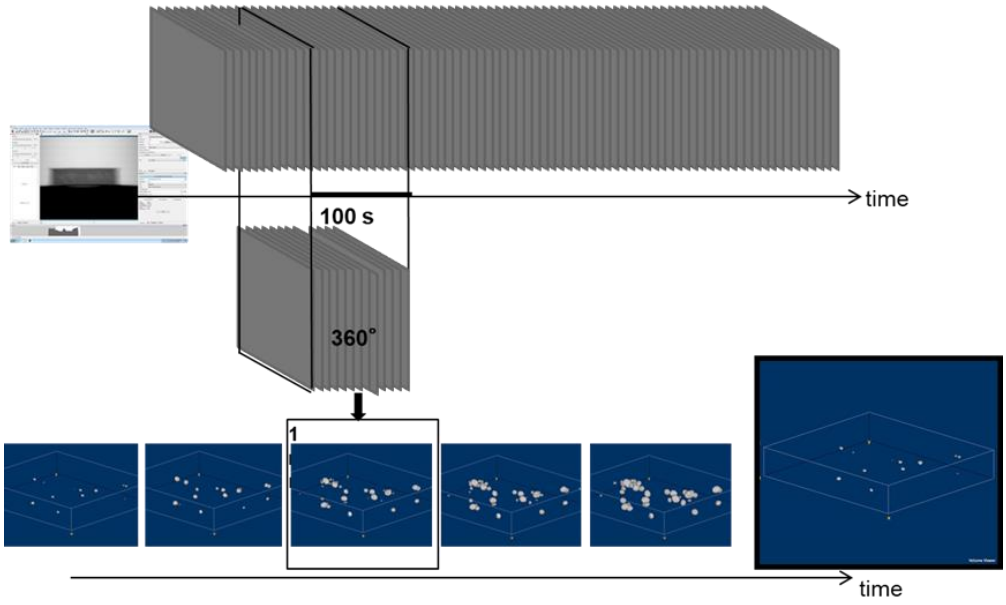

(a)

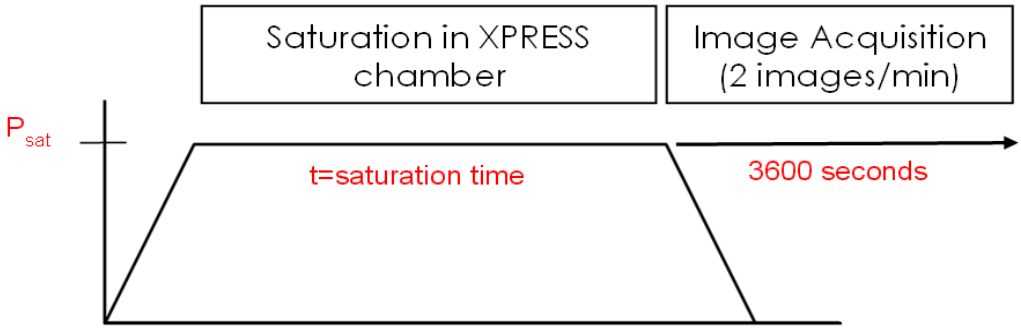

(b)

Figure 4.3 (a) schematic of the acquisition parameters for the present tomography experiments (b) schematic of the experimental procedure for tomography

4.2.2 Image-processing and post-treatment

The image processing was done using the Fiji plug-in of ImageJ software. A dedicated macro for segmentation was defined for each sample after carefully calibrating the steps for optimum results. Prior to segmentation the images were cropped to eliminate the noise and unusable data generated from an uneven surface as seen in Figure 4.4.

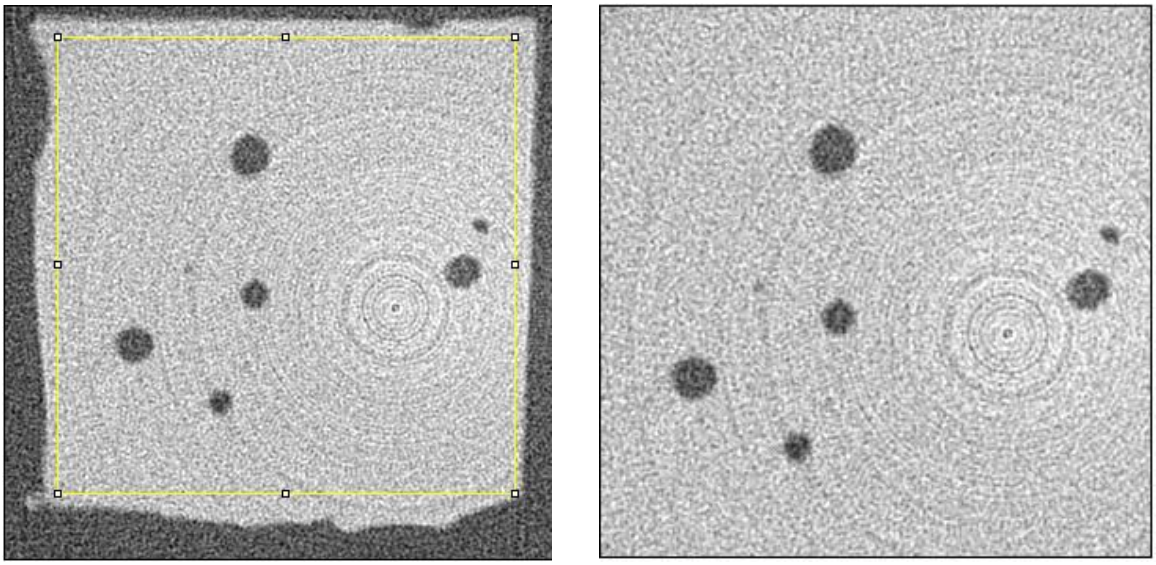

Figure 4.4 Type-1 sample of EPDM 1.6 exposed to hydrogen at 12 MPa and decompressed at 2.5 MPa/min at the time step of 700-800 secs after decompression.

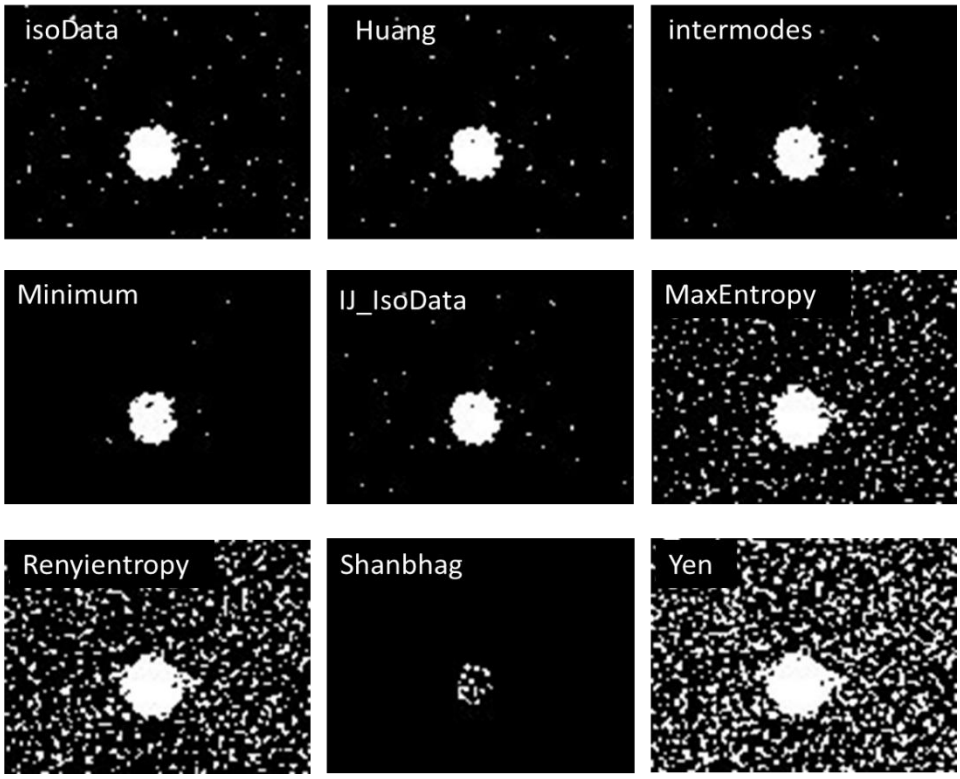

Figure 4.5 Various in-built thersholding filters applied on the same isolated cavity from Type-1 sample of EPDM 0.5 at the time step of 350-450 seconds.

The segmentation was done in four major steps, the first being the application of various mathematical operations in the form of filters to smooth the data: noise minimization and contrast enhancement. In the second step, the thresholding was done to convert the greyscale images into binary ones using an inbuilt binarisation algorithm to ensure consistency in data

treatment. The choice of binarisation filter affects the quantitative analysis of cavities. Figure 4.5 illustrates various filters applied to the same cavity at the same time step without any application of primary enhancement of contrast and smoothening or secondary step of noise removal. It is evident from this figure that the choice of filter also dictates the noise level in the image which necessitates several steps of noise removal after binarisation. As such, the binarisation technique has to be chosen to optimise the capture of volume of cavities without losing too many pixels at the edge and without generating too much noise that would require too many steps of noise removal and compromise the data in later steps.

In the present study, the auto-thresholding filters of Huang, Intermodes or Isodata were used depending on the raw image. The threshold values of these filters are 37745, 38245 and 38496 respectively.

After image processing, a MATLAB code was used to generate 'vtk' format files for every sample that allowed the visualisation of temporal evolution of cavities with an open source software: Paraview (Figure 4.6).

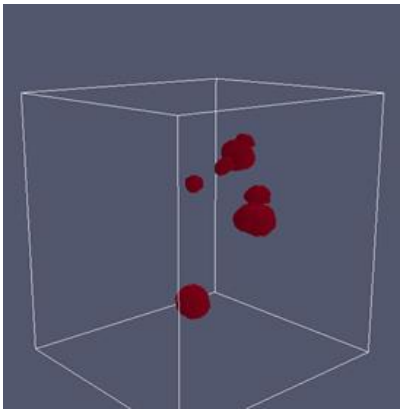

Figure 4.6 3D visualisation of .vtk files generated by MATLAB using Paraview

This was helpful in choosing the cavities for local quantitative analysis from the global damage field. In the last part of the experimental campaign in the Tomograph, cavitation was simultaneously tracked in three samples leading to a lower quality of images. These images were binarised with manual thresholding to get the optimum segmentation. MATLAB code was written for labelling the cavities similar to the Fiji software plugin. The labelling ensured that the cavities could be tracked over time using the PARAVIEW software where any errors in the labelling process due to noise and other artefacts were eliminated. As the deflation of the

cavities is very slow as compared to the inflation, only some reconstructed images were segmented for the deflation stage of the cavities.

4.3 Classification of damage based on morphology

For local analysis, cavities were locally selected from a global damage field and classified into separate groups based on spatial position in the sample. This classification was done by fitting a box around the cavity with side equal to the maximum diameter attained by the cavity as shown in Figure 4.7. The size of the box was taken such that it would contain the single cavity throughout its evolution. In the cases that the cavities could be contained in the box without any intrusion by other cavities all through their evolution, were termed as “isolated cavities”. The cavities that couldn’t be contained in a single box without intrusion from other cavities during the whole evolution were termed as close cavities.

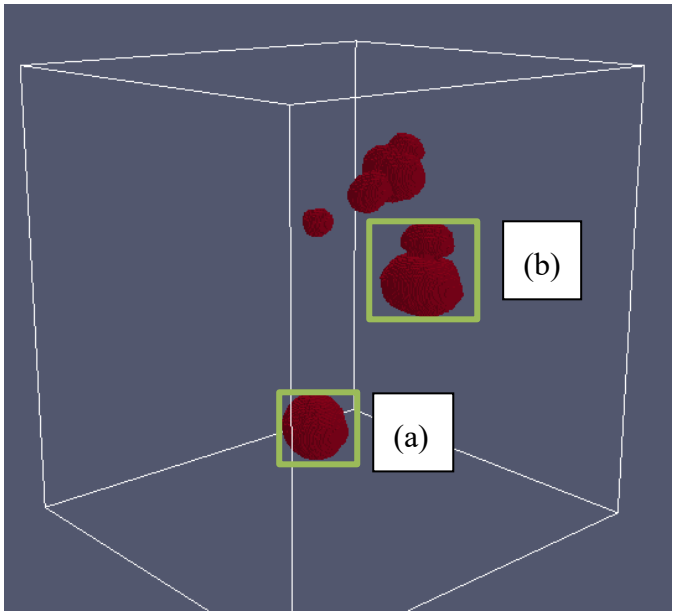

Figure 4.7 (a) Isolated cavity (b) Close cavities

In most cases, however, the close cavities formed a cluster, consisting of a network of very close cavities that were not visually distinguishable and could not be quantitatively analysed by the image processing software. This was due to the low resolution of the Tomograph, which allows the cavities to be distinctly identified with a minimum distance of 32 microns between the cavity borders. As such, groups of 2 to 6 very close cavities that could be distinguished into separate cavities were chosen from the global damage field for quantitative assessment of their

kinetics to clarify any interaction between these cavities. Large clusters of cavities that were not accessible for quantitative analysis were nevertheless qualitatively analysed for providing some insights into the evolution of the global damage field.

More than 50 cavities were manually selected from global damage fields of Type-1 samples of EPDM 1.6, out of which 45 cavities were considered for this study as they did not transition to cracking. In a similar way, 20 isolated cavities were picked from the Type-1 samples of EPDM 0.5. Additionally, 9 cavities were taken from Type-3 samples of EPDM 1.6. for analysing the interaction between cavities, 9 groups of close cavities with the number ranging from 2-6 cavities were chosen from Type-1 and Type-3 samples of EPDM 1.6 for analysis. Clustering was analysed using Type-2 samples of both EPDM 0.5 and EPDM 1.6.

4.4 Inflation characteristics of isolated cavities

As the first step in quantitative analysis, several parameters of the chosen cavities were calculated using 3D manager plugin of Fiji software: size, anisotropy, location and distance between cavities.

The volume of cavities was calculated at each time step by the method of counting voxels to minimise the over or underestimation introduced due to fitting with an ellipse. However, this method introduces certain artefacts when the size of the cavity is very small due to pixelisation. The location refers to the centre of mass of the cavities.

The anisotropy was calculated by taking the ratio of diameters along x and y axes and defined as sphericity in this document henceforth. For a perfectly spherical cavity the value of sphericity is 1 indicating a completely isotropic cavity.

Distance to the free surface was calculated taking the cropped voxels into account for each cavity manually, see Figure 4.8. It should be noted that due to the manual calculation, the error bar in this case is in the range of 50-150 microns. Hence, the distance from the free surface mentioned henceforth in the present document is the actual distance from the free surface of the sample and not of the cropped image. Thereafter, these parameters were used to calculate the inflation characteristics of these cavities which are detailed below. As the effect of these

parameters is convoluted, discussing them in rigorous steps is not possible. The sections below tackle more than one parameter simultaneously at times, since the effect of parameters cannot be detailed separately from one another.

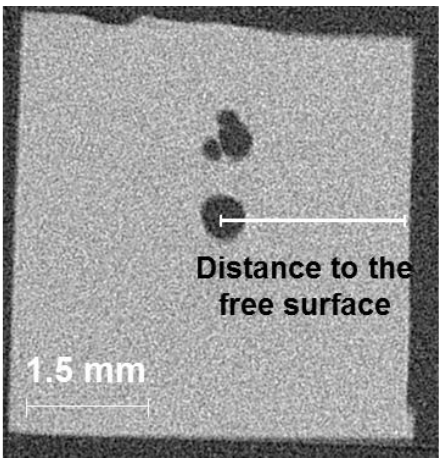

Figure 4.8 distance to the free surface of the sample is calculated from the centre of mass of the cavity.

4.4.1 Rate of inflation

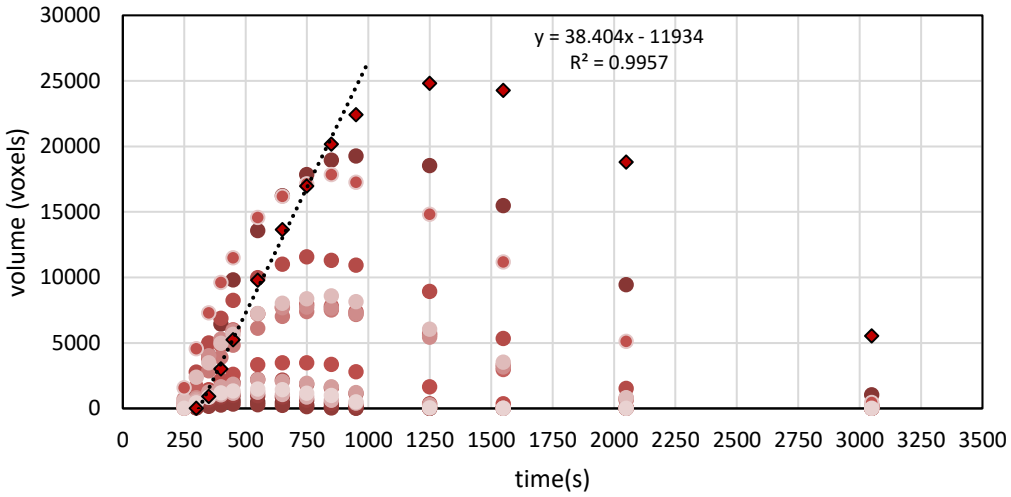

Figure 4.9 Volume evolution of cavities in type-1 samples of EPDM 0.5. P_{sat} 8 MPa, decompression rate of 1.6 MPa/min

For calculating the rate of inflation as a first step, volume evolution of each cavity was plotted against time as seen in Figure 4.9 which shows the evolution of cavities of Type-1 sample of EPDM 0.5. exposed to hydrogen at 8 MPa and decompressed at a decompression rate of 1.6 MPa/min. Since the time step of 100 seconds corresponds to one data point for volume, the mid-point of the time step has been considered for the corresponding value of volume in the time axis of all the graphs henceforth, for example for the time step of 200-300 seconds, the

value of volume is plotted at time point of 250 seconds. As seen in the Figure 4.9 the volume evolution curve of the cavities is generally parabolic.

The rate of inflation of the cavities was done by linearly fitting the first part of the curve corresponding to the growth of the cavity. Usually, the first detected volume of the cavity is prone to high error due to rapid inflation and biases introduced during image processing; this effect is typical of first appearing cavities nucleated during the earliest stage of decompression (within 200 seconds of decompression). Hence, the first data point was generally omitted during the linear fitting of the curve to calculate the rate of inflation. However, for the cavities nucleated later and detected at sufficiently high value so as not be severely affected by image processing biases, the linear fitting included the first data point of calculated volume (Figure 4.9); smallest cavities with very few data points (less or equal to 3) in the range of inflation were not fitted to analyse the rate.

4.4.2 Evolution of anisotropy

Figure 4.10 shows the evolution of anisotropy, characterised by sphericity, of the cavities in Type-1 samples of EPDM 1.6 tested under the decompression conditions of P_{sat} = 8MPa and decompression rate of 1.6 MPa per min. It can be seen from the Figure 4.10 (a) that the anisotropy is high at the beginning of the inflation and with time the cavities become more spherical. This can be attributed to the artefacts due to the rapid volume increase at the very beginning of decompression; deviation from perfect isotropy is expected due to the pixelisation as a result of image processing and as a good estimate, 0.8 can be said to represent an almost spherical cavity.

Figure 4.10 (b) shows the evolution of anisotropy of cavities with delayed nucleation. These cavities nucleate at 350 to 500 seconds after decompression and are described in the later section. As can be seen from the graph, they tend to have almost constant anisotropy ratio throughout their evolution. This is due to their low rate of inflation at the time of nucleation and as such the artefacts introduced due to rapid kinetics are lesser.

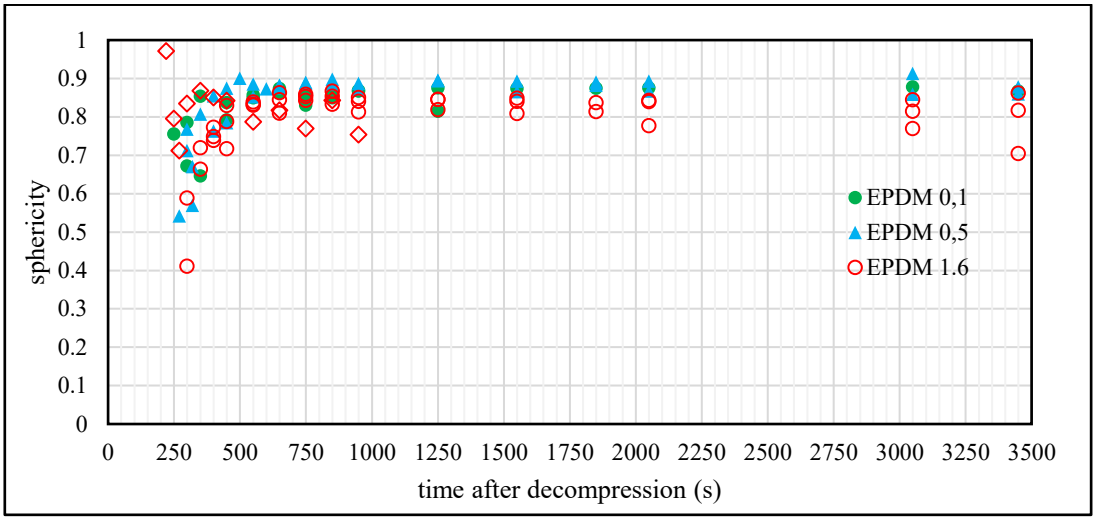

(a)

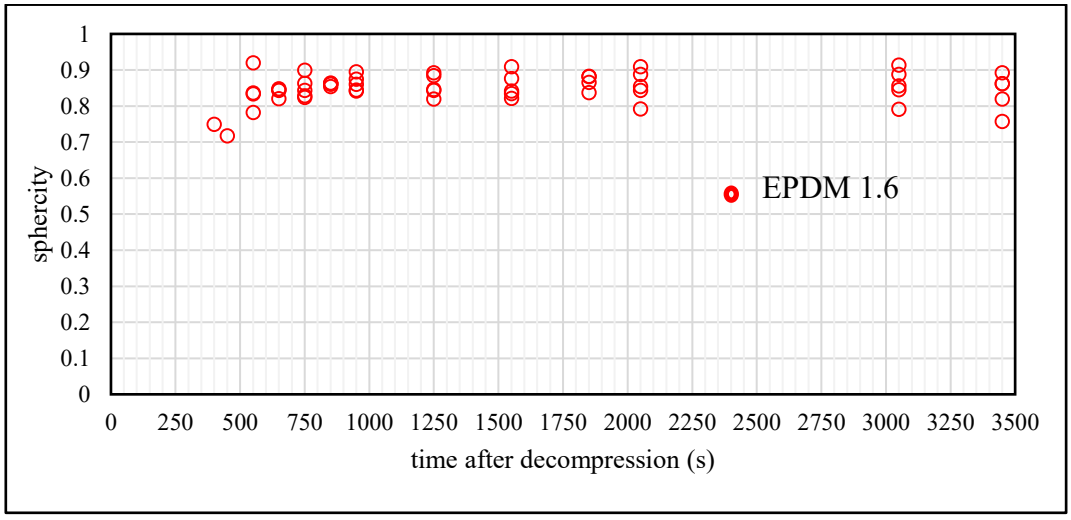

(b)

Figure 4.10: plots of temporal evolution of anisotropy during volume evolution of a) isolated primary cavities b) isolated cavities with delayed nucleation in EPDM 1.6 samples of Type-1. P_{sat} 8 MPa, $\dot{P}$ 1.6 MPa/min

Generally, anisotropy of isolated cavities can be attributed to the following factors: The first factor is the **geometry of the sample**. This has already been addressed in the literature by Castagnet et al who considered the EPDM sample of dimensions 10×10 with a thickness 2 mm, saturated with hydrogen at 12 MPa and decompressed at 2.5 MPa/min. resulting in anisotropic boundary conditions (Castagnet et al. 2018). However, the work was focused on the full cavity field and only average anisotropy ratio was discussed. Having said that, it was seen in their study that the average anisotropy ratio was maximum at the beginning of nucleation and at the deflation stage. However, during the growth of the cavities, the cavities remained largely

spherical. The anisotropy was assumed to be influenced by the shape of the sample that contributed an anisotropic boundary conditions leading to flattening of cavities in the plane of thickness of the sample. As the damage was reversible and no cracking was observed with their samples, this assumption of anisotropy introduced by the geometry of the sample seems reasonable.

The second factor contributing to the anisotropy is the transition of cavities to cracking: some cavities become flattened during evolution showing a tendency to transition into a crack. This is accompanied by a rapid shift (jump) in the normally parabolic volume evolution curve as a result of a sudden increase in volume. An explanation of this could be the cracking of the cavity walls that becomes more apparent during deflation. This is illustrated in Figure 4.11, which shows the evolution of some of the isolated cavities of Type-1 sample of EPDM 1.6 at adjacent time steps

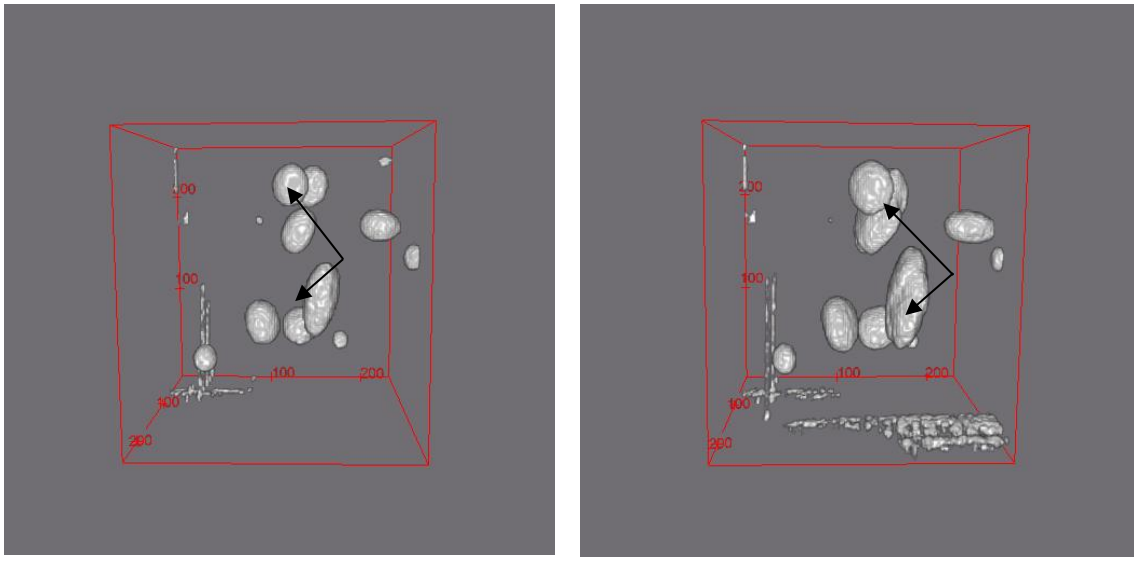

Figure 4.11 Snapshots of cavities in the Type-1 sample of EPDM 1.6

Figure 4.12 shows the evolution of anisotropy of selected isolated cavities in EPDM 1.6 Type-1 samples. The decrease in the sphericity seen in the graph corresponds to the flattening of the cavity which becomes increasingly apparent during deflation. An illustration of this phenomenon can be seen in Figure 4.11 where the evolution of cavities is clearly seen to be anisotropic even during inflation. It can be observed that this “beginning” of cracking is not due to coalescence but as a result of growth of a single cavity.

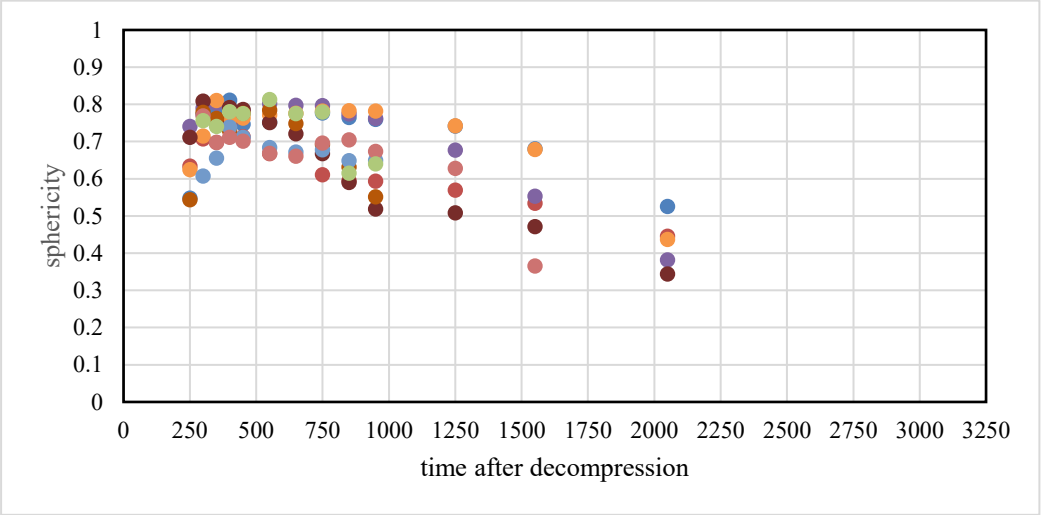

Figure 4.12 Evolution of anisotropy of selected isolated cavities from Type1 samples of EPDM 1.6 that flatten during deflation. P_{sat} 8 MPa, $\dot{P}$ 1.6 MPa/min

However, it must be considered that this assumption is strongly dependent on the resolution of the technique. In the present study, this phenomenon was only observed in Type-1 samples of EPDM 1.6. The generality of this phenomenon as well as possible geometrical influence of the sample shape remains to be experimentally verified. Additionally, the possible coalescence of cavities that might be observable at better resolutions as well as the non-reversibility of this damage needs to be examined in further future studies.

In the present study, the focus is to access the kinetics of the cavities prior to cracking; hence, the cavities which are considered to transition into cracking as discussed above have been excluded from the analysis.

4.5 Factors influencing the growth kinetics of isolated cavities

This section discusses the various factors influencing the growth kinetics of isolated cavities taken from Type 1 samples of EPDM 1.6. The same analysis is done for the samples of EPDM 0.5 and is discussed in the later section.

Figure 4.13 shows the maximum volume (V_{max}) attained by the isolated cavities versus the distance from the free surface for the Type-1 EPDM 1.6 samples with the pressure conditions of P_{sat} 8 MPa and $\dot{P}$ 1.6 MPa/min.

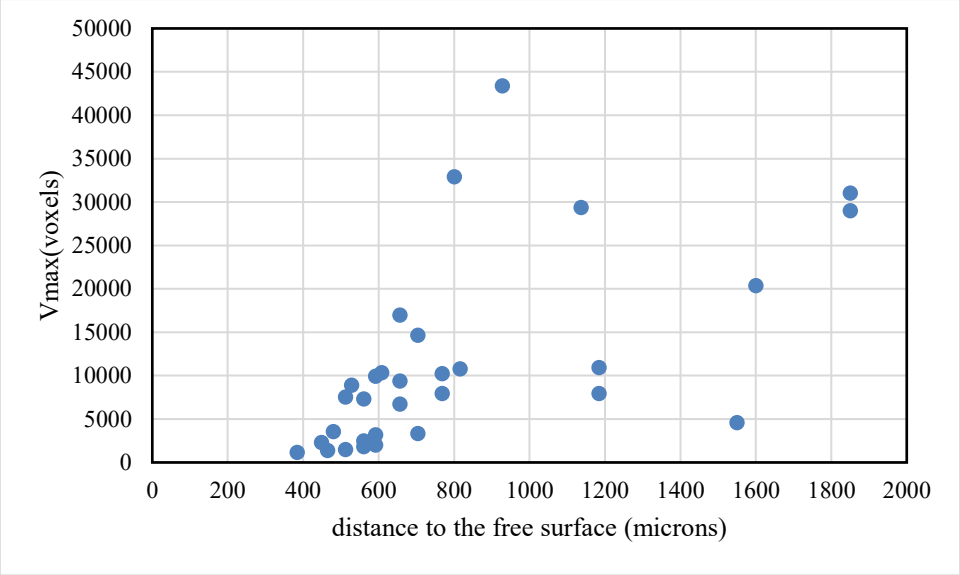

Figure 4.13 Effect of distance to the free surface on the V_{max} of cavities in Type-1 samples of EPDM 1.6

An increasing trend with a large scatter is observed in the first part of the graph indicating that the maximum volume attained by the cavities is affected by the closeness to the free surface of the sample. In the above graph the limiting value is observed in the range of 800-900 microns after which the values corresponding to the maximum volume are random. This value is a broadly estimated one and with more statistical analysis could be found to be a rather arbitrary one. Nevertheless, it could be said that the proximity to the edge drives the maximum volume of the cavities and is a first order factor for the inflation kinetics of cavities upto a limiting distance. This might be attributed to the rapid desorption of the gas from the surface leading to rapid deflation of the cavities. This assumption is an early one and will be tackled in the later sections as well.

For cavities that occur in the bulk of the sample, i.e. cavities occurring at a distance of more than 800-900 microns in the above graph can be taken to have isotropic boundary conditions in terms of global boundary conditions. In such cases, the edge factor is no longer a dominant one for the cavity evolution. For such cavities, the local boundary conditions such as proximity to other cavities or nucleation of new cavities close to the existing one need to be analysed as the major contributing factors in the temporal evolution of the cavity. These cavities were tentatively termed as **bulk cavities** while the cavities with centroids at a distance of less than

800-900 microns from the surface were termed as **edge cavities**. The edge effect on the rate of inflation is discussed in the next section.

4.5.1 Effect of distance from the free surface on rate of inflation

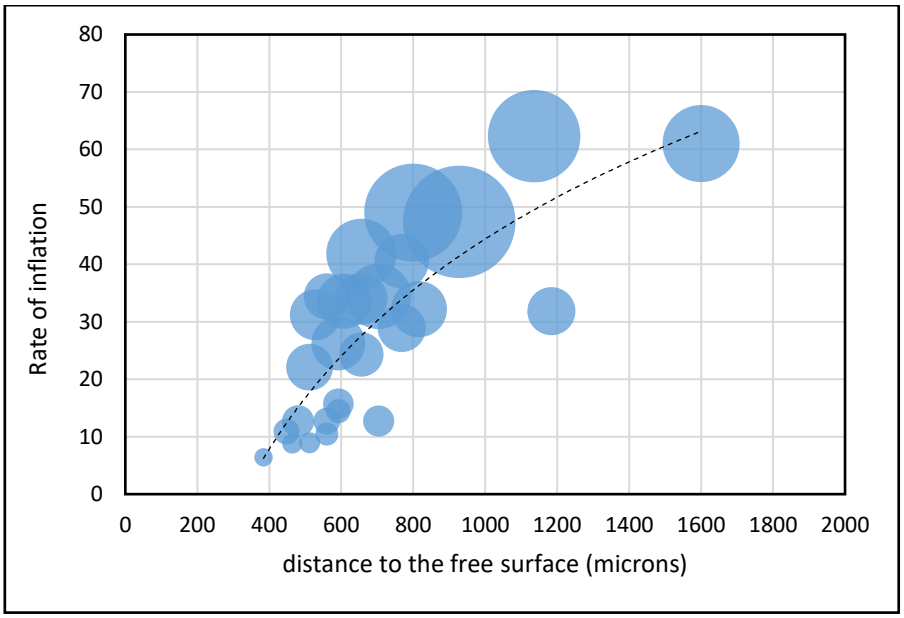

Figure 4.14 Effect of distance to the free surface on the rate of inflation and V_{max} of cavities from Type-1 sample of EPDM 1.6.

Figure 4.14 shows the rate of inflation of the same cavities discussed above and shown in Figure 4.13 as function of distance from the free surface: the size of the bubble corresponds to the V_{max} the cavities. The scale of the bubble was chosen to make sure that the smaller cavities remained visible while larger cavities were distinct. It can be observed that the rate of inflation sharply increases with the distance to the free surface for the so called edge cavities. Thereafter, the rate of inflation shows a similar trend as the V_{max}: more scattered, indicating that the distance to the free surface and rate of evolution of the cavities is not systematic for the bulk cavities. This also suggests that the life of the cavities is driven by global desorption in the edge cavities.

4.5.2 Effect of time of nucleation

Figure 4.15 displays the same cavities as seen in Figure 4.14 with additional points corresponding to the cavities that have a delayed nucleation shown as the filled spheres with thick boundaries. These cavities have been termed as secondary cavities in literature and refer

to a cluster of satellite cavities surrounding the primary ones (Gent 2011). However, it is seen that although these secondary cavities do not necessarily nucleate closer to primary or initial cavities, they nucleate a bit later than the initial ones. These cavities as seen in the graph show slower kinetics than the primary cavities appearing in the same sample (Type-1) and exposed to the same decompression conditions. The nucleation of these cavities was mostly seen at 350 to 500 seconds after decompression such that the mechanical pressure on the sample exerted by the gas in the chamber is completely released.

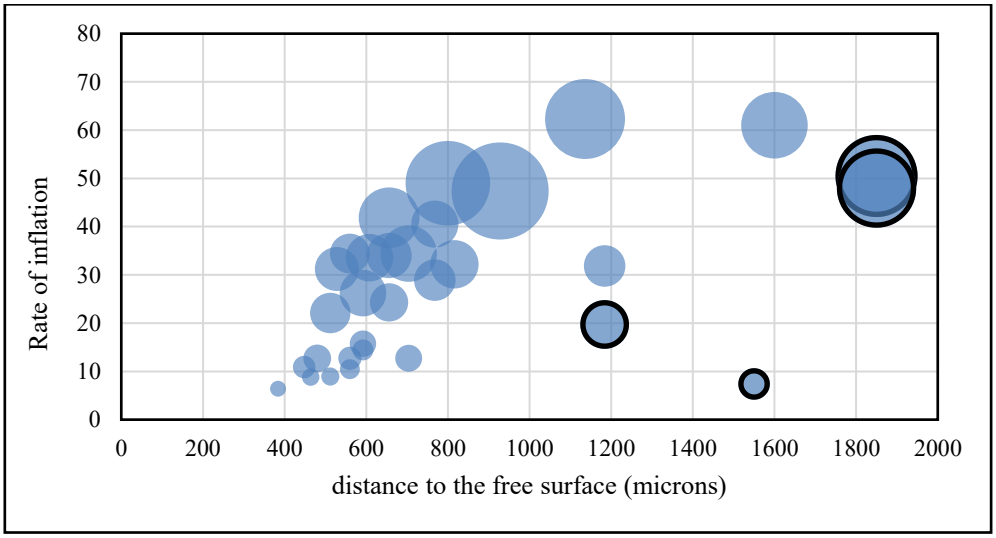

Figure 4.15 Effect of delayed nucleation of rate of inflation and V_{max} of cavities taken from Type-1 sample of EPDM 1.6. P_{sat} 8 MPa, Ṗ 1.6 MPa/min

The lack of mechanical pressure could be assumed to be a contributing factor in the slow kinetics of these cavities. However, the earlier nucleating cavities are detected at 200 to 350 seconds after decompression where the gas pressure is either very low or completely zero making this assumption rather broad. Another factor that could contribute to the slower kinetics is the different iso-conditions due to global desorption leading to different local diffusion fields. This question has been addressed in the later part of the chapter with simulations.

4.5.3 Effect of pressure conditions

Figure 4.16 shows the rate of inflation of isolated cavities in samples at two different pressure conditions. The yellow spheres correspond to the sample with more drastic decompression conditions: P_{sat} 12 MPa and Ṗ 2.5 MPa/min as compared to the decompression conditions

analysed so far as represented by blue spheres: P_{sat} 8 MPa and $\dot{P}$ 1.6 MPa/min. It should be noted that the cavities with delayed nucleation have not been plotted in curve such that only the effect of geometry can be clarified here.

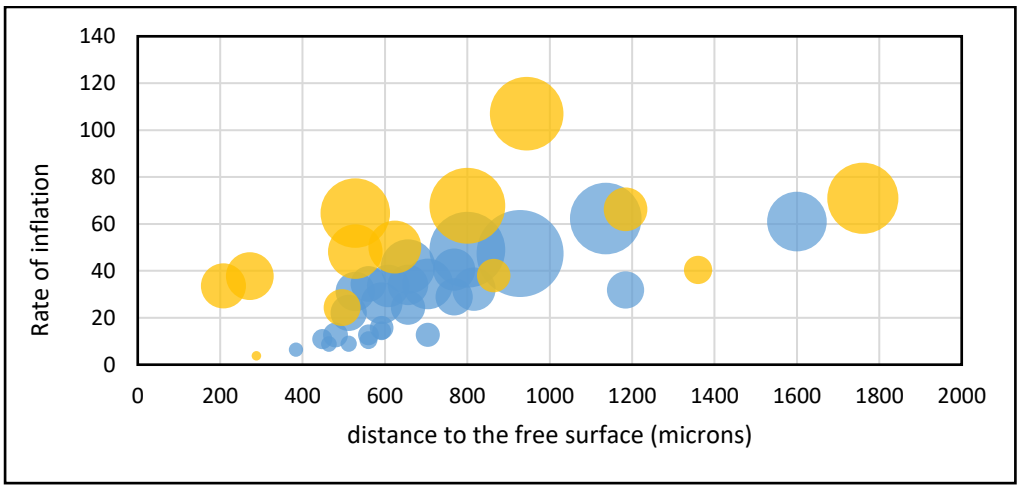

Figure 4.16 Effect of decompression conditions of rate of inflation and V_{max} of cavities. The yellow spheres correspond to cavities in samples under more drastic decompression conditions

It can be seen that the cavities under more drastic decompression conditions have a faster growth rate than the cavities under less intense decompression conditions even as they occur at the same distance from the free surface. A shifting in the vertical direction can be seen in the scatter graph of the yellow spheres indicative of general increase in the value of the rate of inflation of the cavities as the pressure conditions are made more severe. It should be noted that the cavities corresponding to the more drastic decompression conditions (shown here in yellow) were picked up from samples with different dimensions which is compared in the next section. The cavities corresponding to the blue spheres however have all been taken from the Type-1 sample.

4.5.4 Effect of sample geometry

Figure 4.17 shows plots of the rates of inflation for cavities taken from two different geometries for the same pressure conditions: P_{sat} 12 MPa and $\dot{P}$ 2.5 MPa/min; the spheres with thick boundaries correspond to cavities in Type-1 samples whereas the yellow filled spheres correspond to cavities taken from Type-3 samples. It is evident that the rate of inflation or maximum volume show no trend with respect to geometry indicating that the shape of the sample does not affect the kinetics of the cavities at a local scale. Looking at the graph globally,

the initial section shows an increasing trend irrespective of the geometry of the sample whereas the later part of the graph shows more random data points. This trend seen here with respect to the distance from the free surface is consistent with the previous results. Tentatively this reinstates the fact that the distance to the free surface remains the dominant limiting factor for the growth of cavities irrespective of the geometry of the sample. Needless to say, the data points for cavities taken from Type-1 sample are few and this assumption remains to be verified in a more statistical manner.

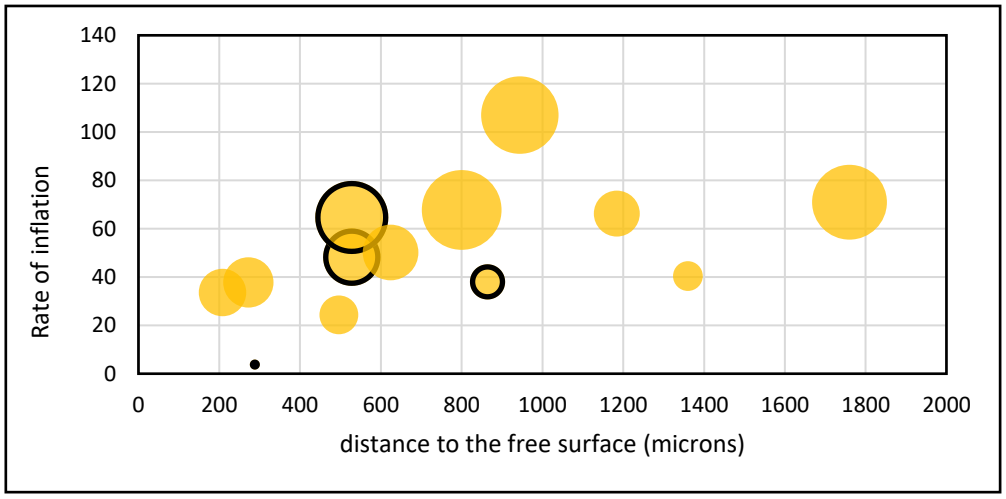

Figure 4.17 Effect of geometry on rate of inflation and V_{max} of cavities.

4.5.5 Comparison with samples of different cross-link densities

As a comparison to EPDM 1.6 the samples of EPDM 0.5 were tested in the same decompression conditions: P_{sat} = 8 MPa and $\dot{P}$ = 1.6 MPa/min with sample dimensions of 5×5×4 mm (Type-1). Similar to samples of EPDM 1.6, the volume evolution of cavities were plotted against time and the maximum volume was calculated. Figure 4.18 shows the maximum volume (V_{max}) attained by the cavity as a function of distance from the free surface for EPDM 0.5. It can be seen that the maximum volume of the cavity shows a liner trend with the distance from the free surface, and doesn't show any normalisation at the distance of 800 microns. However, since the number of data points are few, the same conclusion cannot be excluded for EPDM 0.5.

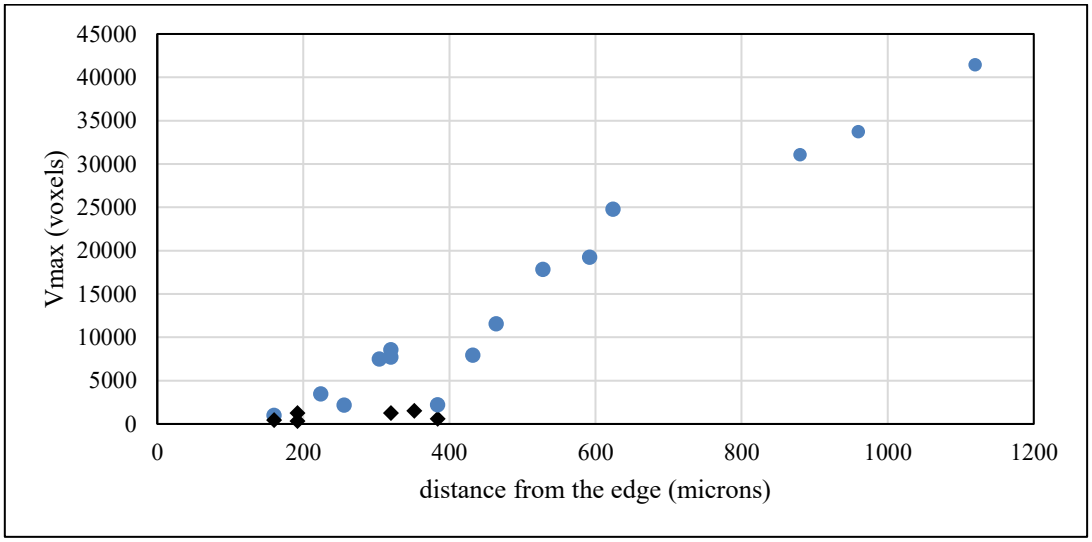

Figure 4.18 Effect of distance to the free surface on V_{max} of cavities taken from Type-1 sample of EPDM 0.5

Additionally, the cavities that are closer to two edges, shown in black diamonds in the graph, have the least V_{max} value which is consistent with the conclusion that distance to the free surface is the dominant factor for kinetics of the cavities regardless of the cross-link density. The effect of cross-link density on the limiting distance at which the edge and bulk cavities can be differentiated could be clarified with more experiments in future.

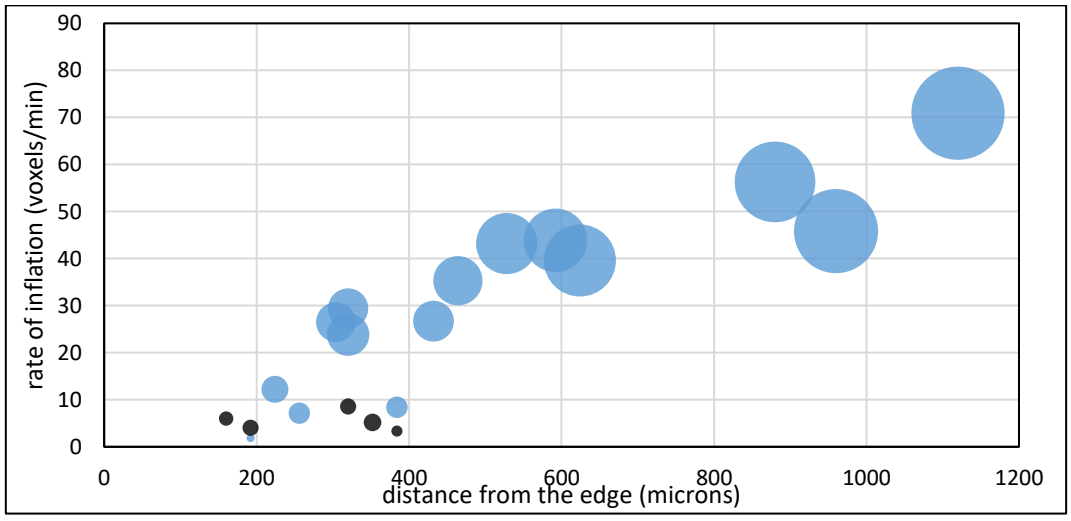

Figure 4.19 Effect of distance to the free surface on the rate of inflation and V_{max} of cavities taken from Type-1 sample of EPDM 0.5

Figure 4.19 shows the rate of inflation and V_{max} of cavities in EPDM 0.5 as a function of distance from the free surface. The size of the bubbles corresponds to the V_{max} of the respective cavity. The black spheres correspond to the cavities close to two free surfaces. As seen in Figure

4.19, the rate of inflation shows a similar trend as the V_{max}. The cavities closer to the free surface have a lower inflation rate as well as smallest V_{max} and show an increasing trend as seen in the first part of the curve. However, unlike the graph for the V_{max} vs distance from the edge, we can tentatively observe the stabilisation of the curve in the later part of the curve after the distance of 800 microns from the edge indicating that the edge effect is no longer the first order parameter driving the growth kinetics of cavities. It is important to note that the edge effect may be related to the global diffusion kinetics of the sample which is essentially characterised by the diffusivity of the gas in each sample and could be varied with variation in cross-link density of the sample. For the sample presented here i.e. EPDM 1.6 and EPDM 0.5, the variation in cross-link density or even the diffusivity is not significantly different as discussed in chapter 2 of this document. For this reason, an effect of cross-link density on the growth kinetics as analysed for isolated cavities is not seen in terms of either rate of inflation or $V_{\max}$ of the cavities. Nevertheless, the estimation of edge effect and its quantifications as related to the global desorption, have been analysed by complimentary simulations, the results of which are discussed in the next section.

4.6 Relationship of growth kinetics of cavities with macroscopic desorption

To correlate the kinetics of cavitation ($V_{\max}$, rate of inflation and spatial distribution) with diffusion characteristic of the sample, simulations of the decompression cycle were carried out in ABAQUS.

The model consisted of the sample with the same dimensions as the samples tested in the tomography experiment: Type-1 sample, in a pure diffusion condition was simulated as a heat transfer problem which is analogous to mass transfer if the value of density and specific heat is set as unity. The simulation was done for EPDM 1.6 which has a diffusion coefficient of 1.89E-4 mm^2/sec.

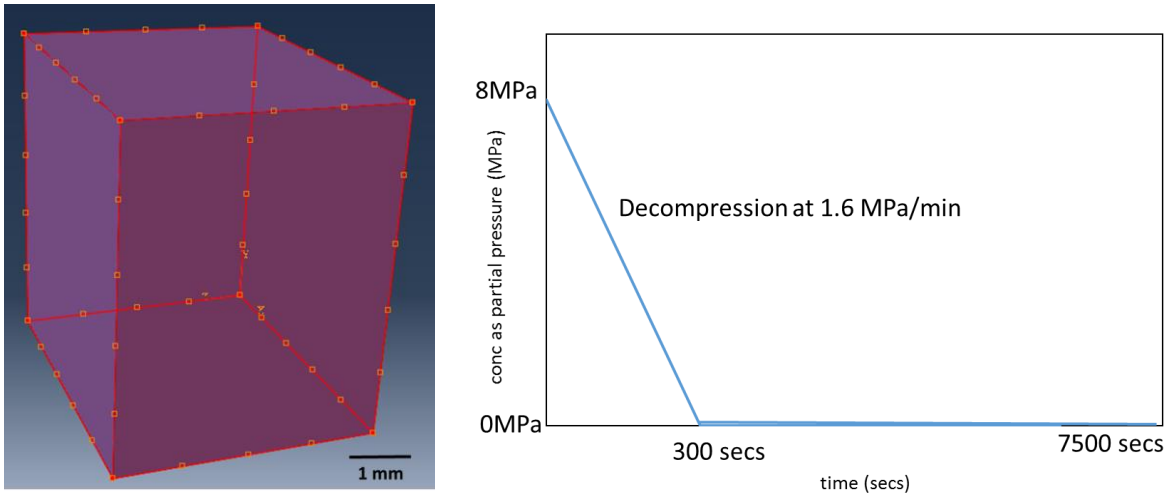

(a) (b)

Figure 4.20 (a) Predefined field: constant concentration throughout the sample of magnitude 8 reflecting the sample saturated at 8MPa (b) amplitude of boundary condition applied, reflecting the decompression stage

The model simulated the decompression stage of the hydrogen exposure, taking the initial state of the sample at equilibrium which was defined by taking a predefined field of constant concentration of 8 MPa through the sample defining the initial condition as that of a saturated sample as seen in Figure 4.20 (a). The application of boundary conditions involved putting the concentration of the sample edges at zero mimicking the decompression phase of the hydrogen exposure for the conditions of Psat 8 MPa and Ṗ 1.6 MPa/min as seen in Figure 4.20 (b).

The sample was meshed with a standard linear heat transfer element of DC3D8 type. Prior to actual simulations, the test for mesh sensitivity was carried out for a regular mesh with different mesh sizes of 0.2, 0.1 and 0.05mm. The same simulation of a pure diffusion problem was carried with different mesh sizes and the concentration gradients along the path from the centre of the sample to the edge were plotted along different axes. Since the results were isotropic, only the curves corresponding to concentration gradients of hydrogen in terms of partial pressure along z-axis are shown in Figure 4.21. The sensitivity to mesh size is more pronounced at the coarse mesh level of size 0.2 and decreases as the mesh size is reduced. However, the curves for mesh size 0.1 and 0.05 are seen to almost superimpose. Consequently, the mesh size of 0.1 was taken to be most suitable for regular meshing, illustrated in Figure 4.22.

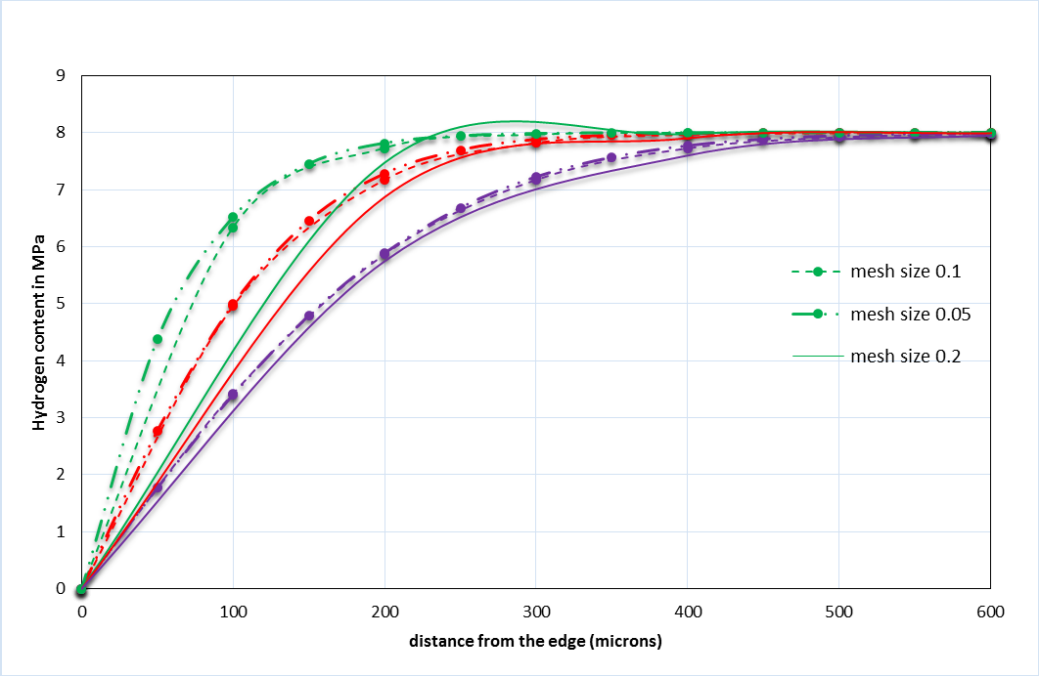

Figure 4.21 Curves for comparison of different mesh sizes. The green, red and purple lines correspond to the curves for 300, 500 and 1000 seconds after decompression respectively

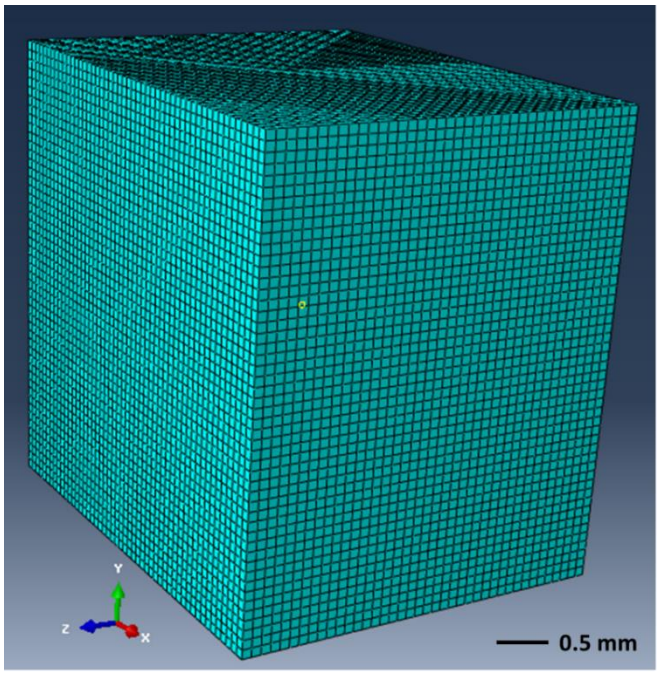

Figure 4.22 Illustration of the mesh size 0.1 for Type-1 sample

Figure 4.23 displays the concentration gradient of hydrogen in the sample 1000 seconds after decompression. Since the concentration gradient is isotropic, the values taken along the path as seen in the figure are taken to be representative of the sample.

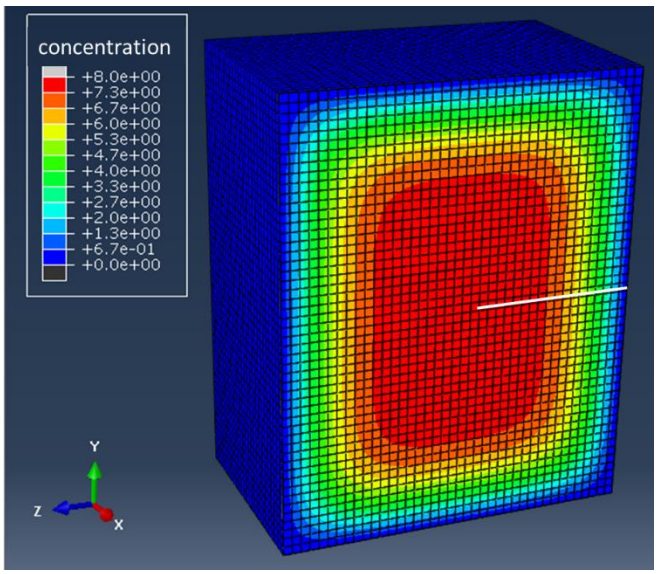

Figure 4.23 Hydrogen concentration at 1000 secs after decompression. The white line shows the path along z axis from the centre of the sample to the edge.

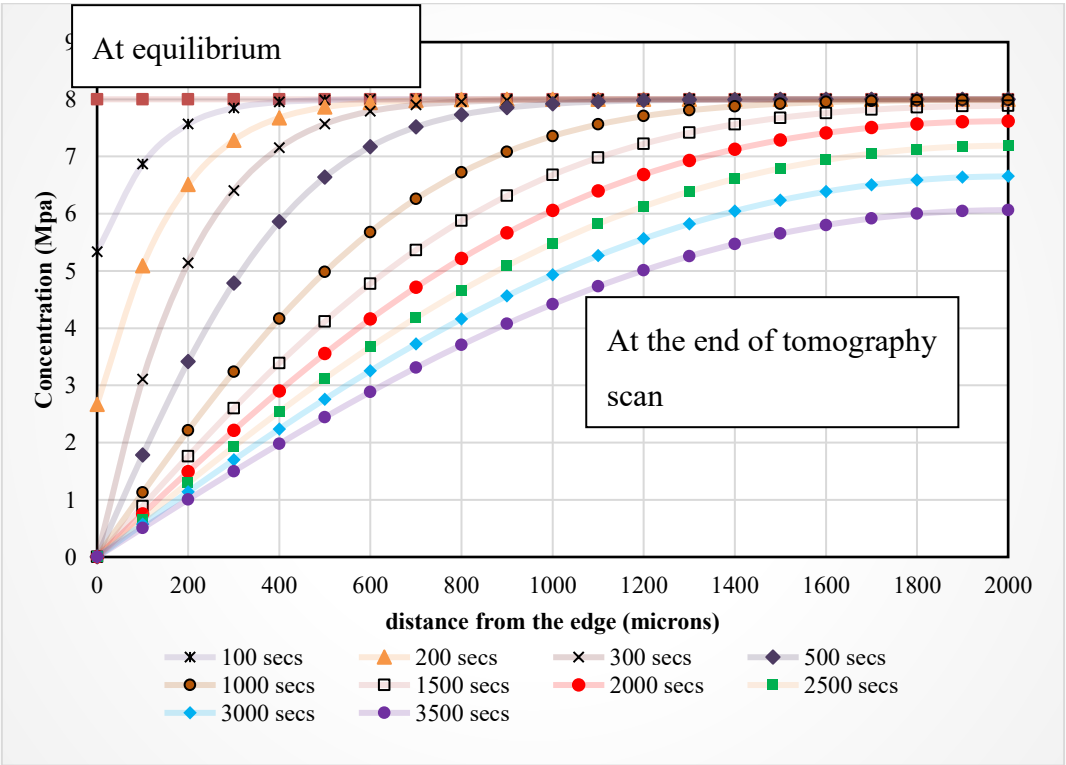

Figure 4.24 Curves for the evolution of concentration gradient of hydrogen in EPDM 1.6 after the beginning of decompression

Figure 4.24 shows the curves showing the variation of hydrogen gas concentration expressed as partial pressure (MPa) along the path from the edge of the sample to the centre of the sample. The red curve seen in the graph corresponds to equilibrium concentration. Thereafter the values of time indicate the time after decompression at which the concentration is calculated. The last curve seen here in purple shows the curve at 3500 seconds, which marks the end of the tomography acquisition. It can be seen that a gradient appears on the external surface or the edge of the sample at the beginning of the decompression which travels through the bulk of the sample rapidly at first and then gradually as the desorption of gas takes place.

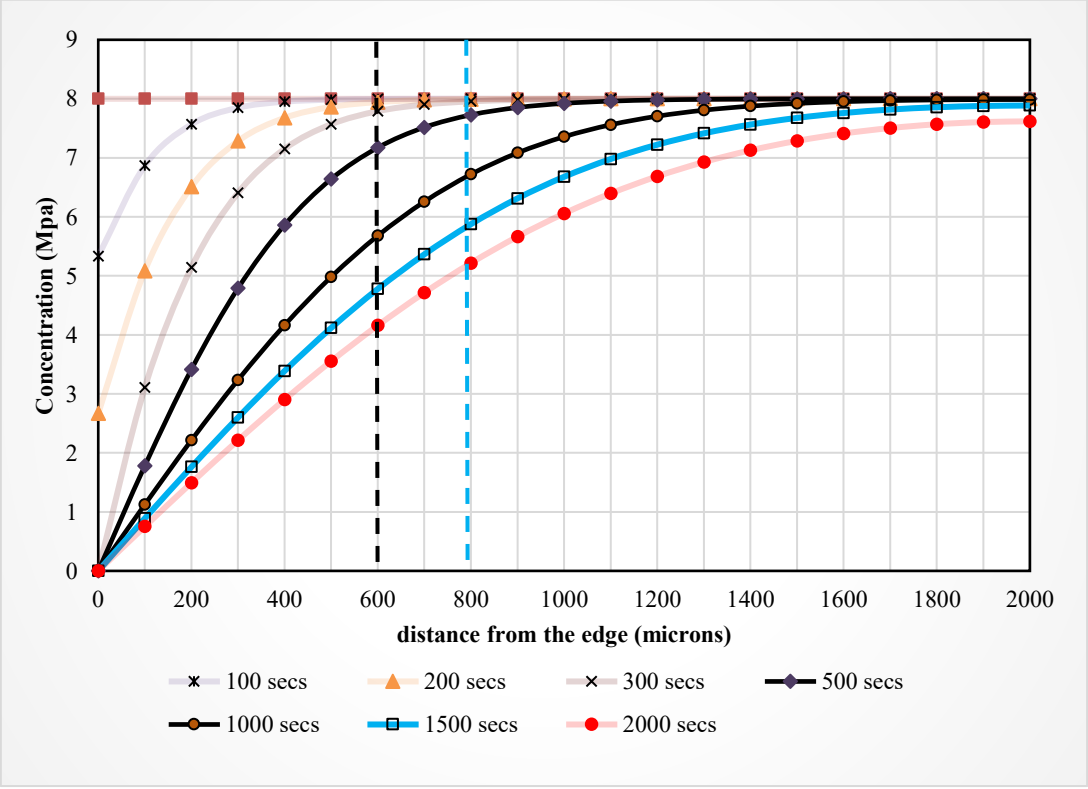

Figure 4.25 Selected curves taken from Figure 4.24

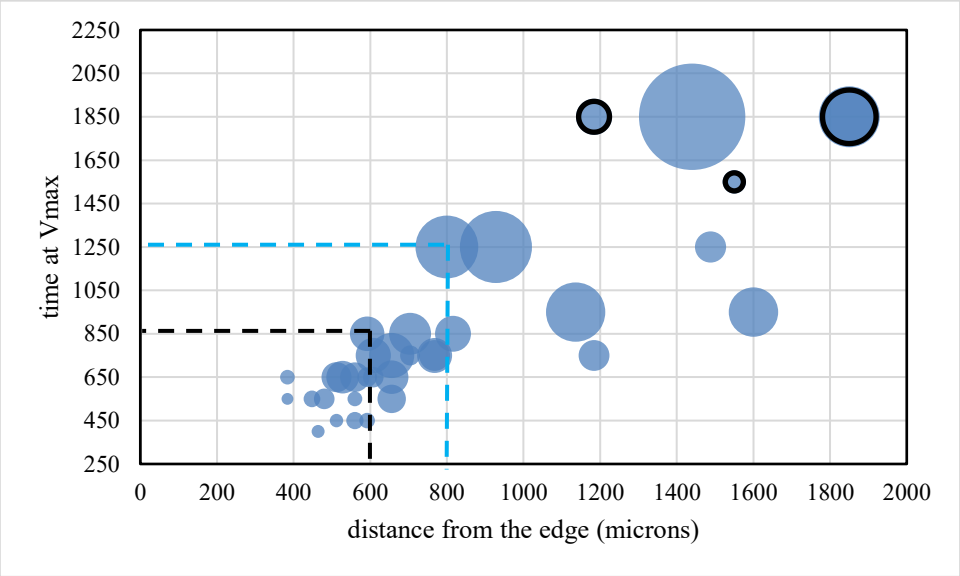

Figure 4.26 Plots of time at Vmax of isolated cavities taken from Type-1 sample of EPDM 1.6. The size of the bubbles correspond to the Vmax of the cavities

The edge effect described in the earlier sections can be analysed by looking at the selected curves of global desorption shown in Figure 4.25 and comparing them with the graph shown in Figure 4.26 which plots the time at which the cavities have attained the maximum volume with the distance from the free surface. The size of the bubbles represent the size of the cavities. Looking at the first section of both graphs demarcated by black dotted lines, it is seen that the maximum volume of the cavities is reached by 850 seconds after decompression and not further than that. There is a linear trend observed with respect to the distance from the free surface; the more we move from the edge, the more time the cavity takes to attain its maximum volume. Looking at the curves for the global desorption, this timeline is shown as the space between two bold black lines corresponding to the concentration gradient of the gas at 500 and 1000 seconds after decompression. The black dotted line corresponds to the same distance of 600 microns from the free surface. The intersection of these lines show the curves for the concentration gradients during the evolution of these cavities that have previously been termed as edge cavities. The edge effect is corroborated here as the concentration varies rapidly during this time at this distance from the free surface.

Looking at the second section marked by blue dotted lines in Figure 4.26 and corresponding to the distance of 800 microns from the edge, the same effect is observed i.e. an increasing trend towards the time taken to attain the maximum volume while moving away from the free surface. Again, the global desorption gradients lie between the black and bold blue line in

Figure 4.25, which again show rapid decrease in the gas concentration. Beyond the distance of 800 microns, the time to attain maximum volume no longer shows an increasing trend with respect to the distance from the free surface; the time of V_{max} ranges between 750 to 1850 seconds. Looking at the curves for global desorption between 750 to 1850 seconds, this area lies between the curve for the concentration at 500 seconds and the concentration at 2000 seconds. These curves clearly show the beginning of curvature for as we move from edge to centre of the sample indicating that the global desorption does indeed drive the life of the cavity. This is further corroborated by the curves seen in Figure 4.27 which correspond to the beginning of deflation for all cavities.

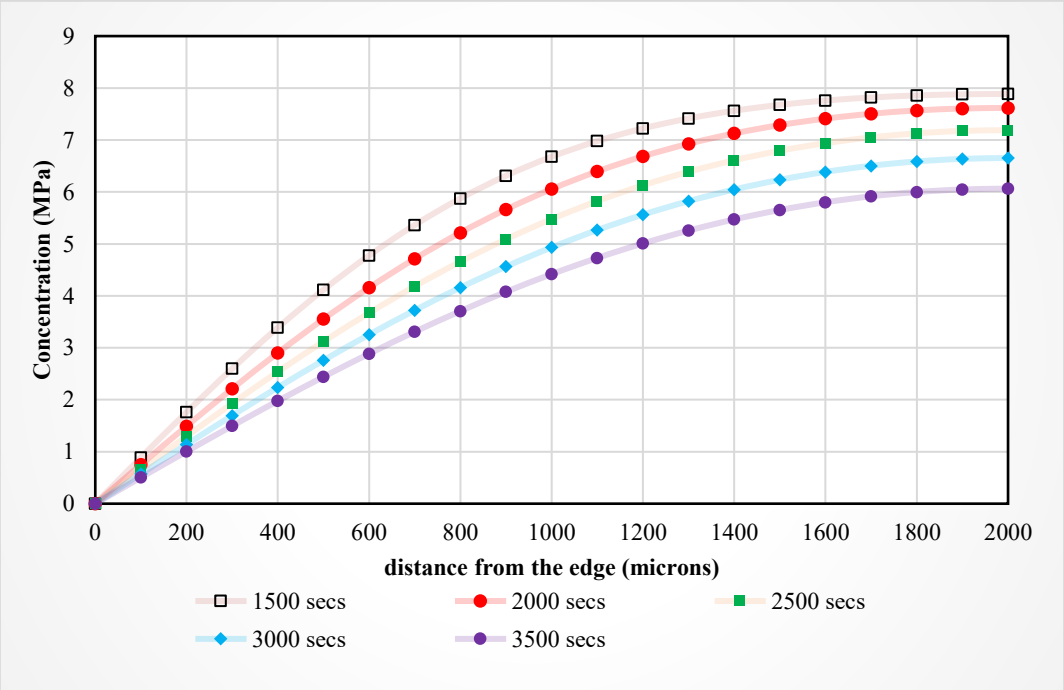

Figure 4.27 Curves indicating concentration gradient of hydrogen in EPDM 1.6 at the time step at which all cavities were seen to be in deflation stage. These curves have been selected from Figure 4.24

It is clear that the earliest times seen here as 500 seconds shows a sharp decrease in the concentration towards the edge of the sample whereas for the cavities in the core, the curves for the later times steps, correspond to their deflation. It should be noted that many of the isolated bulk cavities do not deflate completely at the end of the tomography scan. This might be due to the gas content still present in the sample core that can be clearly seen in the last

curve corresponding to the concentration gradient in the sample at the end of the tomography scan.

Interestingly, the idea of delayed nucleation being driven by different iso- conditions does not seem to be correct as these cavities occur in the bulk, shown in Figure 4.26 as the spheres with black borders, and nucleate at 350-500 seconds after decompression. At the distance of 1200 microns from the edge, the curves corresponding to the nucleation of these cavities takes place at almost constant concentration of 8 MPa. This could raise the question of the delayed nucleation being as a result of local stress concentration or interaction effects leading to the nucleation of these cavities. While the question of nucleation cannot be accessed with the present observation, the interaction effects between close cavities have been addressed in the next section.

As mentioned earlier, this simulation is purely driven by diffusivity of the gas in the specific material and the magnitude of the concentration at equilibrium. Since the diffusion coefficient to EPDM does not vary significantly with respect to cross-link densities from 0.5 and 1.6, the results from the above simulation can be interpreted for both these samples.

4.7 Inflation characteristics of close cavities

The sections details the characteristics of the close cavities and analyses them in comparison with the isolated cavities. Groups of close cavities were taken from the global damage field of Type-1 and Type-3 samples of EPDM 1.6 as described in the earlier section of the chapter. Similar to isolated cavities, the volume evolution of these cavities was plotted against time and the results were analysed taking isolated cavities as a reference for kinetics.

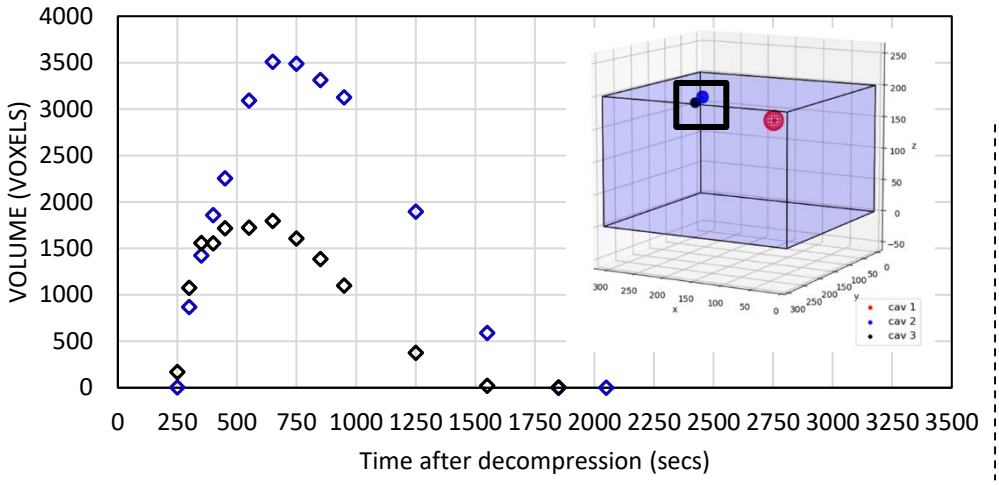

Figure 4.28: Volume evolution of close cavities at the edge of the sample as shown in the schematic to the right from Type-1 EPDM 1.6 sample

Figure 4.28 shows the volume evolution of the first chosen pair of close cavities, illustrated by the schematic, in EPDM 1.6 exposed at the pressure conditions of P_{sat} 8 MPa and decompression rate of 1.6 MPa/min. It should be noted that the schematic represents only selected cavities and is not representative of the actual damage field of the sample.

It can be seen that the cavities show very low V_{max} in comparison to the isolated cavities that have been tackled in the previous section. However, since both these cavities are closer to the edge, it is not clear whether this is due to the proximity to the edge or another cavity. The comparison of these boundary conditions: proximity to the free surface and proximity to another cavity needs to be addressed with another example of the close cavities in the bulk in comparison to the cavities close to the free surface where the effect could be convoluted.

This is clarified in case close cavities in the bulk as shown in Figure 4.29 which shows the evolution of three cavities in bulk for the same sample under the same decompression conditions (P_{sat} = 8 MPa, $\dot{P}$ = 1.6 MPa/min). The graph is important in illustrating the interaction between cavities.

The larger cavity is termed as the primary cavity as it nucleates first. The second cavity in blue nucleates closer to the primary cavity while the cavity in red nucleates farther but at the same time. Comparing the two secondary cavities we can see that the kinetics are almost the same. Both cavities have almost the same V_{max} and rate of inflation. The lower volume and rate of inflation is attributed to the delayed nucleation rather than different local boundary conditions.

Additionally, the evolution of the larger cavity remains unaffected by the nucleation of another cavity close to it. In fact, the primary cavity shows similar kinetics to the isolated cavities.

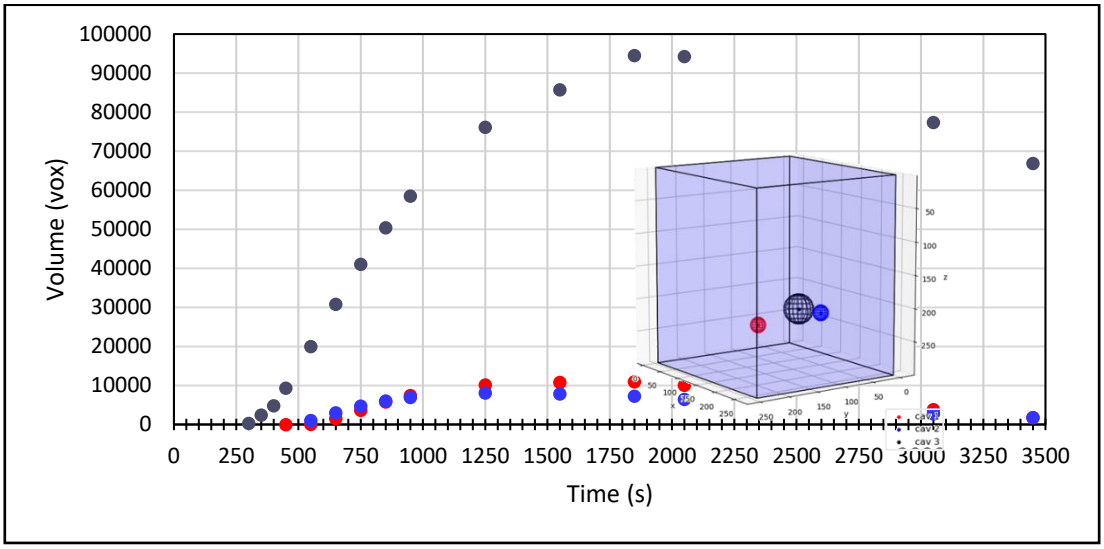

Figure 4.29 Volume evolution of 3 selected cavities from the global damage field of Type-1 EPDM 1.6 sample.

This can also corroborated by the curves taken for same material albeit at more drastic decompression conditions. Figure 4.30 shows the plots of two close cavities taken from Type-3 samples of EPDM 1.6.

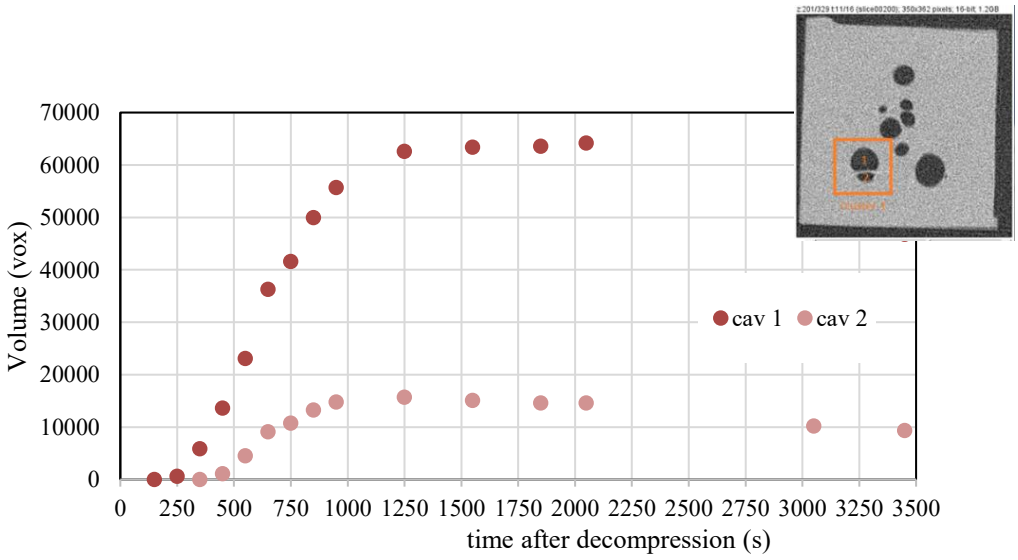

Figure 4.30 Volume evolution of 2 cavities of the selected group as shown by the raw image on the right. Cavity 1 is nucleated first while cavity 2 is nucleated later close to it.

The plots show the same trend i.e the primary cavity remains unaffected by the proximity of a second cavity. The slower kinetics of the secondary cavity are as a result of the delayed nucleation which are consistent with results already discussed for isolated cavities. It should also be noted that the flat shape of the curve at the top is an image-processing artefact.

The similarity to the isolated cavities of these close cavities is clarified by looking at the curves for the isolated cavities taken from Type-1 sample of EPDM 1.6 shown in Figure 4.31. The red markers correspond to the cavities with delayed nucleation.

As can be seen with the close cavities discussed above which showed slower kinetics due to delayed nucleation, similar kinetics are observed in the isolated cavities with delayed nucleation. Again, the primary cavities in the groups of cavities discussed above show the kinetics similar to the isolated cavities nucleated earlier shown by black markers in Figure 4.31.

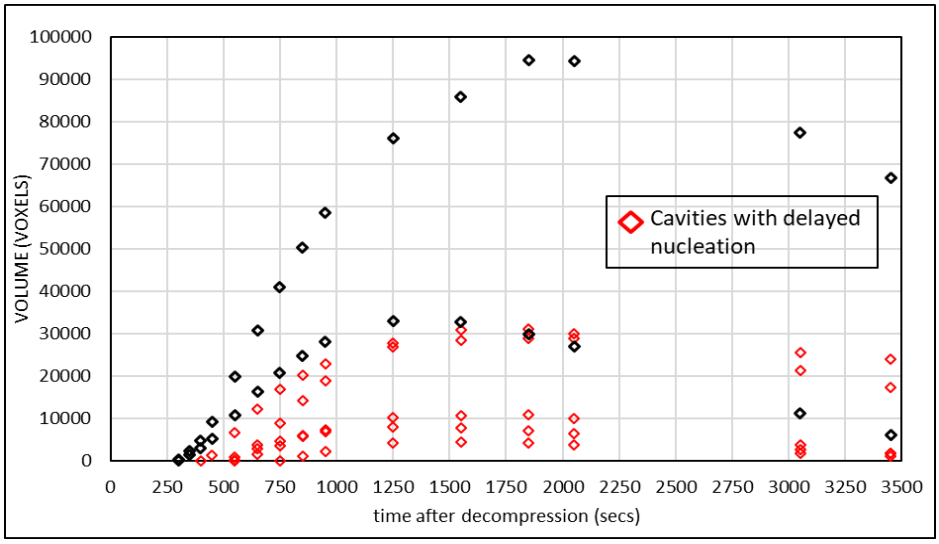

Figure 4.31 Volume evolution of isolated cavities taken from Type-1 sample of EPSM 1.6. P_{sat} = 8 MPa, $\dot{P}$ = 1.6 MPa/min

Figure 4.32 shows the snapshot of the groups of cavities taken from the global damage field of the flat sample (Type-3) of EPDM 1.6 under the decompression conditions of P_{sat} = 8 MPa and $\dot{P}$ = 1.6 MPa/min. The volume evolution of the cavities are shown in Figure 4.33 (a) to (d).The cavity are labelled numerically in the order of their appearance. The cavity to be nucleated earliest has been termed the primary cavity.

From the plots shown in Figure 4.33, it is clear that in all cases the primary cavity is the largest cavity. In some cases, two close cavities in a group were detected at the same time step but do not inflate to the same size; it should be noted that detection of the cavities in the same time step does not preclude the fact of their simultaneous nucleation. In fact, due to the resolution of the tomography, the time of nucleation is broadly used and signifies the time the cavity is detected at the earliest possible step which in most cases is significantly later than the nucleation time. Since the inflation is very quick in the earliest time steps, the first captured volume of the cavity has a large error bar both in terms of quantitative value and the time step where it is detected. It is highly probable that even when the cavities are detected at the same time step, one of the cavities which grows to be the larger one should have nucleated earlier than the cavity that inflates to a lower volume.

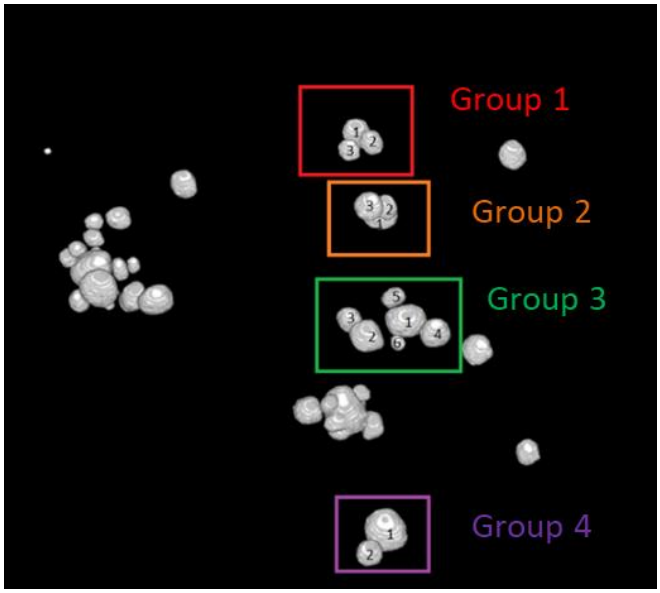

Figure 4.32 Snapshot of the global damage field of flat sample of 2 mm thickness of EPDM 1.6. 4 groups were selected to be quantitatively analysed. The red orange, purple and green boxes enclose groups 1, 2, 3 and 4 respectively. Group 4 contains 6 cavities

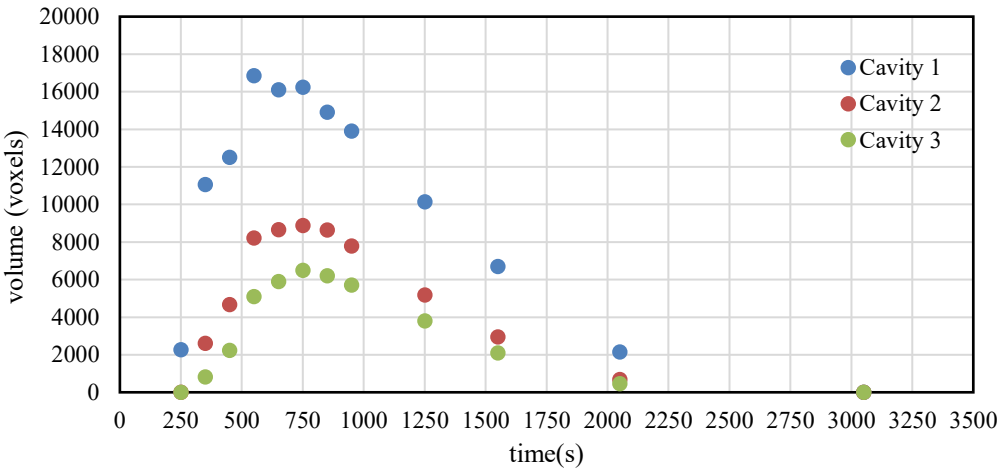
volume (voxels)
time(s)
Cavity 1
Cavity 2
Cavity 3

(a)

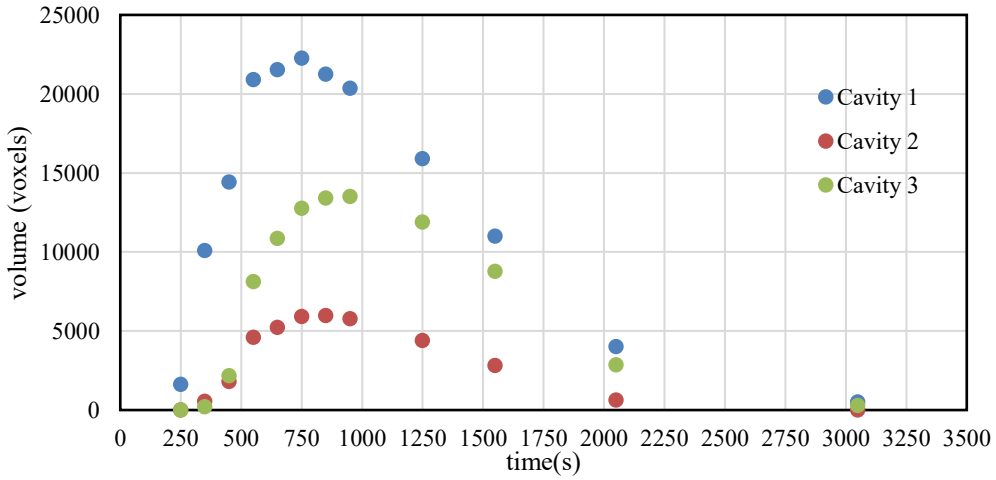
volume (voxels)
time(s)
Cavity 1
Cavity 2
Cavity 3

(b)

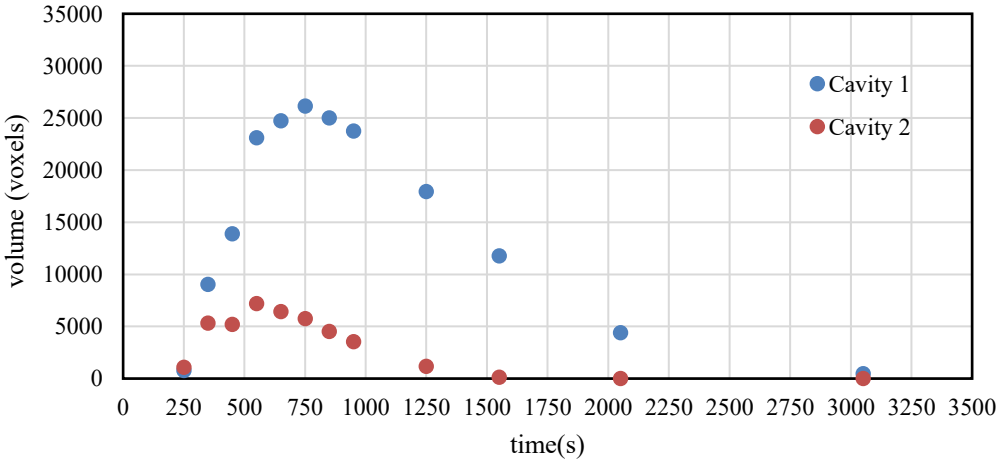
volume (voxels)
time(s)
Cavity 1
Cavity 2

(c)

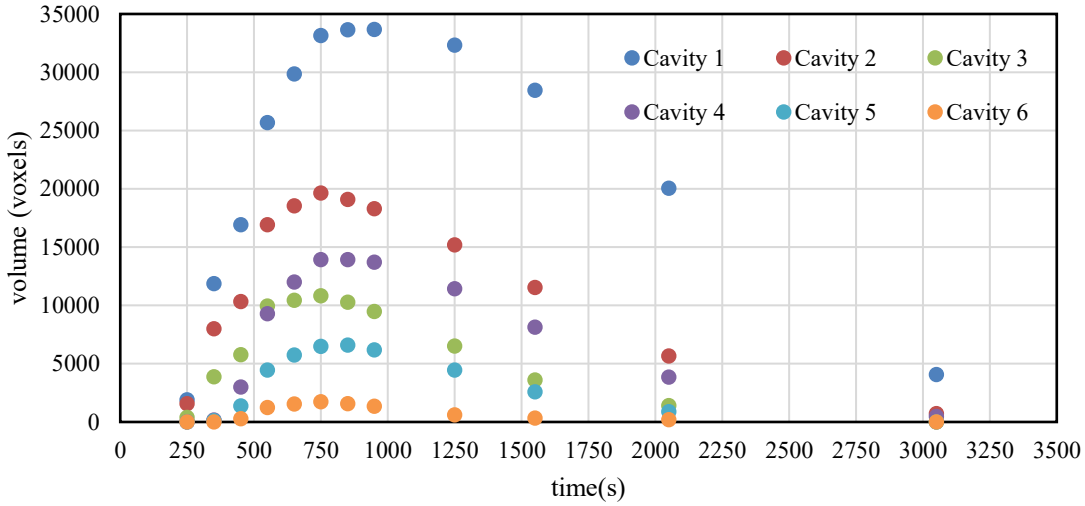

(d)

Figure 4.33 Volume evolutions of (a) group 1 (b) group 2 (c) group 3 and (d) group 4 shown in Figure 4.32. The cavities are named in order of their appearance.

Figure 4.34 shows plots for groups of close cavities consisting of 3 cavities and 2 cavities respectively, taken from another flat sample of EPDM 1.6 (Type-3) under the same decompression conditions. The group with 3 cavities (Figure 4.34 (a)) consists entirely of cavities with delayed nucleation. The graph is characteristic of secondary cavities with a less steep slope for inflation as well as deflation.

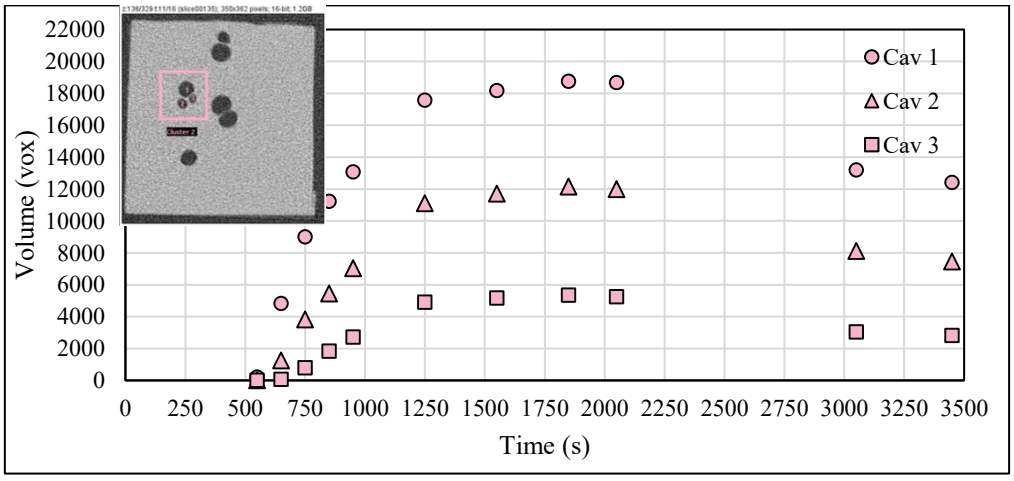

(a)

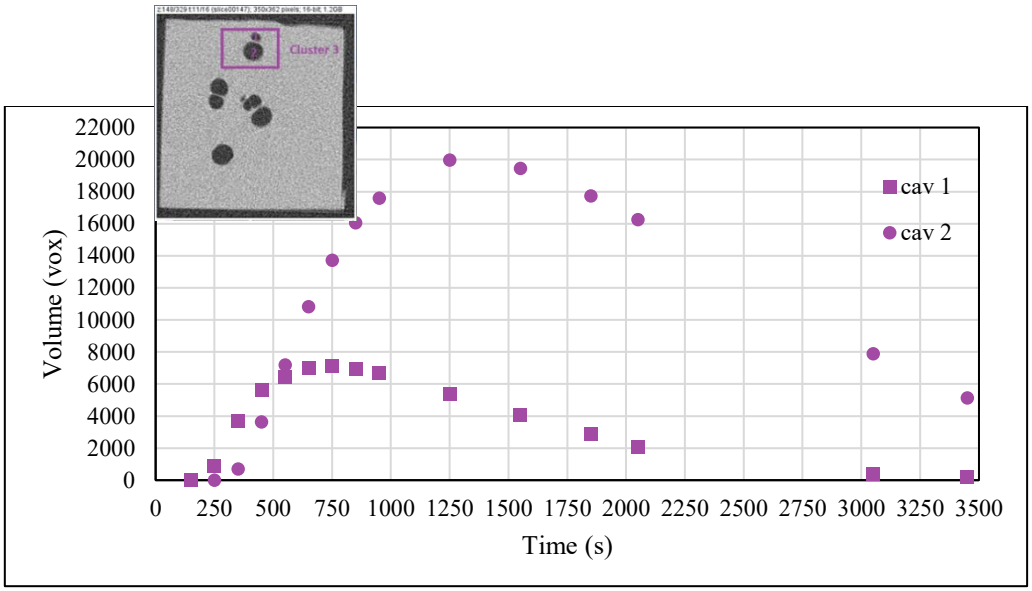

(b)

Figure 4.34 volume evolution of groups consisting of (a) 3 cavities and (b) 2 cavities.

In Figure 4.34 (b) it can be seen that the primary cavity does not inflate to be the largest cavity. This is explained by the edge effect that has been explained in the earlier section. The distance to the edge of the primary cavity is 516 μm; the cavities at this distance from the free surface have been described as edge cavities in the previous sections already. Hence, this primary cavity behaves as an edge cavity resulting in lower volume attributed to faster deflation due to global desorption.

Figure 4.35 shows the plots of distances between the three cavities of group 1 as shown in Figure 4.32 for Type-3 sample of EPDM 1.6. The blue and red markers correspond to the distance of primary cavity to cavity 2 and cavity 3 respectively. In the groups of close cavities examined, the distance between the centroids of the cavities which has been termed as core to core distance (c-c), that is the between the centres of the primary and the secondary cavity is never below 290 to 320 microns. Since we were able to pick only some of the groups owing to the limitation of the image processing software in discretizing the very close cavities, it could be possible that some cavities nucleate closer to each other than the above value. However, this value of 290 to 320 microns could be taken as the upper limit for the distance between cavities to form a group and thus be distinguished from the so called isolated cavities. For the distance between the borders of the cavity (b-b), we were limited by the resolution to a minimum of 2

voxels corresponding to 32 microns below which the cavities were indistinguishable. The watershed filter could be applied to separate (or segment) such merged cavities prior to quantitative analysis. However, the minimum distance after the filter was also seen to be 32 microns. It is very probable that the minimum distance between the cavity walls of two very close cavities could be found much less than this value with higher resolution experiments carried out in synchrotron facilities.

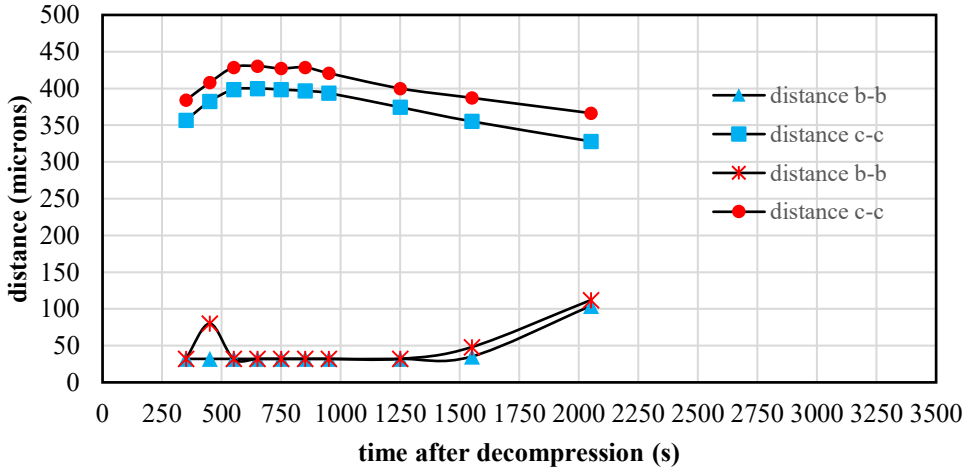

Figure 4.35 Distances between the three cavities of group 1 as shown in Figure 4.32

As seen in Figure 4.35, the core to core distance of the cavities increases and then decreases. This initial increase could be as a result of increase in the bulk volume of the sample after the pressure release. Additionally, the error bar in calculation of the distances in the first time steps after decompression is 1 to 2 pixels which corresponds to the increase we see in the initial part of the graph. In the later part, the decrease in the core to core distance is consistent with the global decrease in volume of the sample due to desorption. The border to border distance remains constant in the initial part of the graph which is due to the resolution of the tool as explained earlier. It is very probable that the decrease of the distance between the cavity borders during inflation is not quantifiable with the current resolution. However, the increase in the border to border distance is visible during the deflation stage as seen in the graph.

4.7.1 Anisotropy

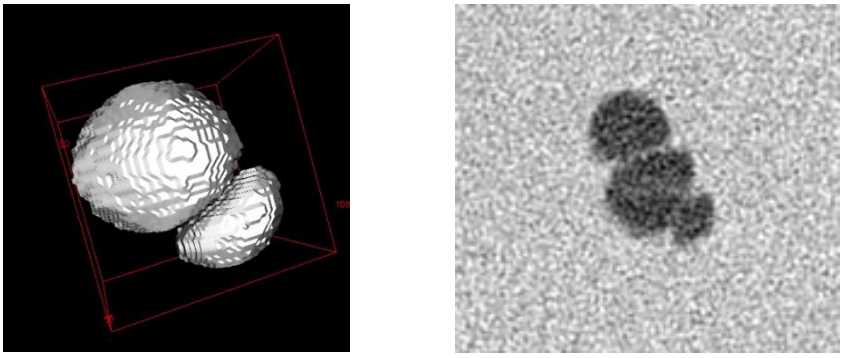

(a) (b)

Figure 4.36 (a) 3D picture of a group of 2 cavities b) raw image of a group of 3 cavities taken from Type-1 sample of EPDM 1.6

The main contributing factor to the anisotropy of close cavities is the topological effect created by the proximity of cavities that could crowd the shape of the cavity, this is illustrated in Figure 4.36 (a) which shows a group of cavities taken from Type-1 sample of EPDM 1.6. This topological effect is more pronounced when the cavity is sandwiched between two cavities as is seen in Figure 4.36 (b) which shows another group of cavities taken from the same sample.

This is further collaborated by the plots of anisotropy for 3 groups of cavities taken from the Type-3 EPDM 1.6 in Figure 4.37. The three groups of cavities refer to group 1, 2 and 4 as shown in Figure 4,32. It can be seen that the anisotropy increases with time characterized by the dip in the curve of sphericity as the cavities inflate. This is due to crowding of the cavities leading to a topological anisotropy.

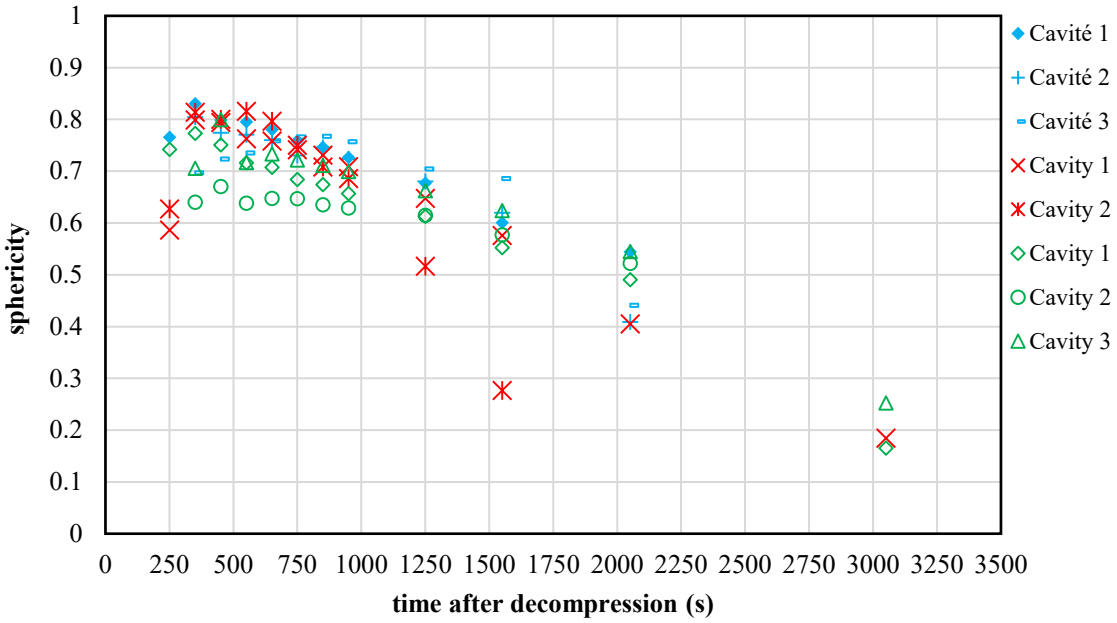

Figure 4.37: Plots for evolution of anisotropy for cavities in 3 clusters selected from the global damage filed of 2 mm flat samples of EPDM 1.6. Each color represents cavities in that cluster. The cavities appear spherical only for a short time during inflation.

From these observations, it can be concluded that the interaction effects between close cavities with borders at a minimum distance of 32 microns is rather trivial. The kinetics of close cavities mimic those of isolated ones, with other factors like distance to the free surface and time of nucleation being the first order parameters that drive the kinetics of inflation. The proximity to other cavities remains a second order parameter mainly affecting the topological isotropy of the cavities rather than growth kinetics. These conclusions are, however, valid for the minimum distance measurable due to the Tomograph resolution. Furthers studies in using Synchrotron sources with better resolution could help bring more clarity to these interaction effects at lesser distances between borders of close cavities.

4.7.2 Qualitative observations of clustering

Clustering, as explained in earlier sections of the chapter refers to a group of cavities that become indistinguishable visually and as such the quantitative assessment of these cavities is not possible. However, these clusters have been observed qualitatively in this section.

Qualitatively, the flat samples of Type-3 show less clustering effect than the cubic ones. In the cubic samples analysed (Type-1 and Type-2), it was observed that the growth of the clusters

was along a path continuing from the primary cavities and could be assumed to be related to the gas diffusion path. This leads to a clustering effect in the bulk of the sample where the gas desorption is slow. Since the cavities in the flat samples are closer to the free surface in the direction of thickness, desorption of gas is more rapid leading to a less clustered damage morphology. This path of clustering can also be called a path of nucleation and can be visualised from temporal evolution of the global damage field of 6 mm and 8 mm cubic samples (Type-2), see Figure 4.38.

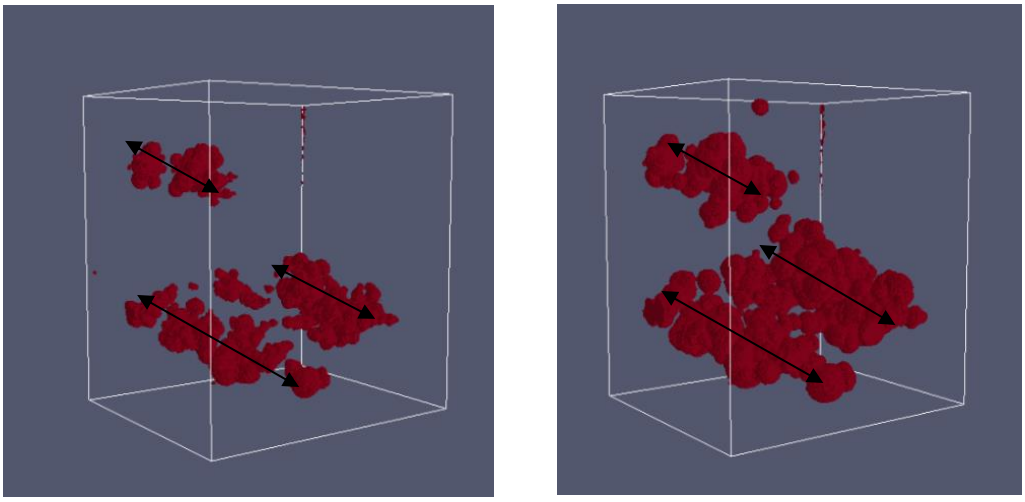

Figure 4.38 Snapshots of the sample at 2 time steps showing the path of nucleation illustrated here with arrows.

It is probable that the nucleation of new cavities is systematic to the presence of initial cavities even though the kinetics of the cavities are not really affected by the proximity of close cavities as seen by tomography results.

Figure 4.39 show the snapshots of Type 3 sample of EPDM 1.6 exposed to pressure conditions of P_{sat} = 12 MPa and $\dot{P}$ = 2.5 MPa/min. Figure 4.39 (a) shows the initial stage where nucleation of cavities is seen to occur randomly throughout the sample. Figure 4.39 (b) shows the maximum volume stage of the cavity field and Figure 4.39 (c) shows the deflation stage where it can be seen that the contraction occurs as more of a global phenomenon giving the impression of a convex hull collapsing on itself. This observation supports the fact that while nucleation is a local phenomenon, the deflation of cavities is driven by global gas desorption.

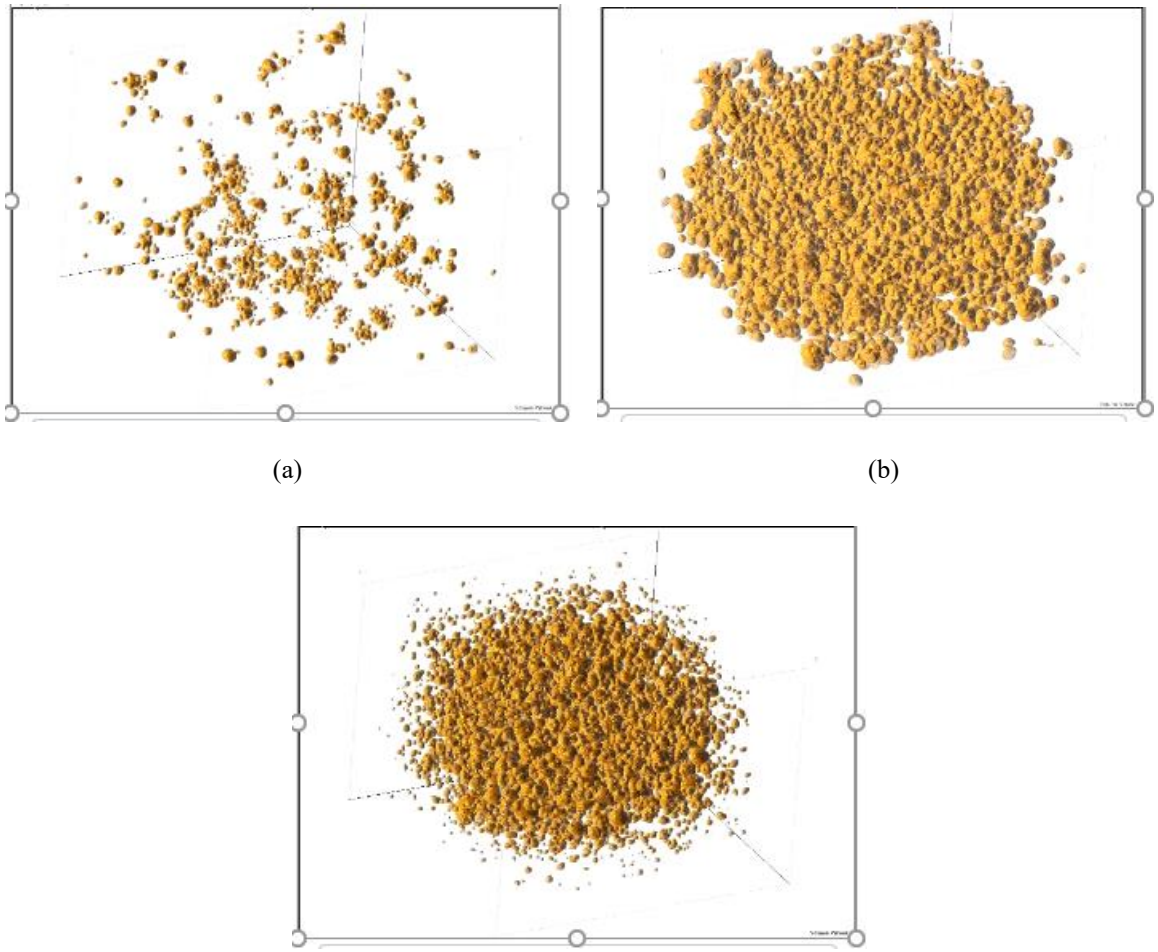

(a) (b)

(c)

Figure 4.39 Global damage field of Tupe-2 sample of EPDM 1.6 exposed to pressure conditions of Psat = 12 MPa and $\dot{P}$ = 2.5 MPa/min

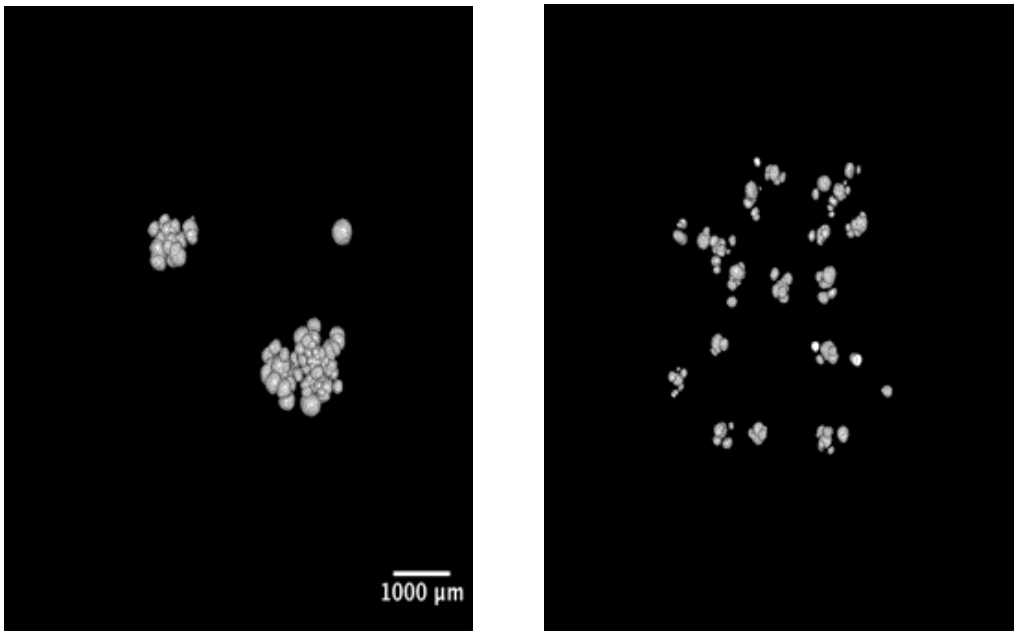

(a) (b)

Figure 4.40 Global damage fields of Type-3 samples of (a) EPDM 0.15 and (b) EPDM 1.6 exposed at the presure coditons of Psat = 12 MPa and $\dot{P}$ = 2.5 MPa/min

Figure 4.40 shows the global damage fields of Type-3 samples of EPDM 0.15 and EPDM 1.6 exposed at the presure coditons of P_{sat} = 12 MPa and $\dot{P}$ = 2.5 MPa/min. Looking at these figures, it can be observed that the averge size of the cavities comprising the clusters decreases with the increase in crosslink denisty. This is a qualitative observation at the global damage scale. Locally, however, as discussed before, the size and kinetics of the cavities analysed in the present study did not show any effect of the cross link density. Again, it must be noted that the difference in crosslink densities of the samples shown in the above figures is markely higher than the samples analysed in the present study.

4.8 Conclusions

The objective of the present study was to discriminate various factors affecting growth kinetics of cavitation at a local scale and to clarify interaction between cavities through comparative characterisation of isolated and close cavities. We also attempted to clarify the minimum distance of this interaction and provide a qualitative insight into the inflation and deflation

characteristics of cavities. Since we were limited by the resolution of the tools, the very earliest stages of nucleation were not accessible for robust quantitative analysis. Indeed the nucleation time of the cavities described here refers to the first time step at which the cavity becomes detectable. The volumes of the first detected cavities vary from very small (≈18 voxels) to very large (≈1000 voxels). This variability occurs due to the conflict between the acquisition time of the Tomograph and the very high rate of inflation at the beginning of cavity appearance. The earliest cavities normally first appear at 150 to 300 seconds after decompression at which is either towards the end of the decompression phase or completely after it. These cavities were termed as primary cavities in the document. During the quantitative analysis the cavities nucleating during the decompression phase and immediately after it show no difference in kinetics. However, the kinetics are highly influenced by the proximity to the free surface. In fact, by analysing the graphs for rate of inflation and the maximum volume attained by the cavities, two sets of cavities could be distinguished based on their growth kinetics. These cavities were termed as edge cavities and bulk cavities, a terminology that was based on the first order parameters governing their growth. The growth of edge cavities was strongly limited owing to the proximity to the free surface whereas the growth kinetics of bulk cavities were more determined by other factors such as time of nucleation or other local boundary conditions.

The secondary cavities which refer to the isolated cavities that nucleate after the primary cavities showed slower kinetics possibly due to the global desorption and changing iso conditions. It should also be noted that the edge cavities do not appear as secondary cavities supporting the argument that fast desorption at the free surface limits the maximum volume of the edge cavities thereby, making the “cavity life” short.

The classification of edge and bulk cavities was supported by the simulations carried out to see the temporal evolution of gradients of concentration along the sample geometry. There was good agreement between the experimental results and the diffusion simulation which pointed to this edge effect being directly related to the diffusion characteristics of the sample.

Isolated cavities were observed to be temporally isotropic during inflation and the flattening of cavities was visible during deflation which suggests the transitioning of the cavity into a crack. It should be noted that the formation of crack does not necessarily include coalescence. Isolated cavities were seen to become cracks which is seen in the increase of anisotropy accompanied by abrupt increase in volume deviating from the regular parabolic graph. As the study of

cracking was not the aim of the present study, these cavities were excluded from analysis. However, the flattening of isolated cavities shown in the graphs above showed the beginning of transition from cavity to crack. The reason for factors leading to the beginning of this phenomenon are not clarified yet.

Groups of close cavities consisting of 2-6 cavities were also analysed with respect to the distance between cavities and their respective evolution in comparison with the kinetics of isolated cavities to see whether the interaction between cavities is a salient factor in their growth kinetics. An attempt was made to clarify the distance between cavities at which the interaction is perceptible. These groups of cavities were chosen from a global damage field. Again, the limitation of the tool allowed for the quantification of characteristics of cavities with a minimum distance of 2 voxels (32 microns). From our tests, the interaction between cavities did not appear to be of a major consequence in terms of kinetics of the cavities. Other factors like proximity to the edge and delayed nucleation were driving factors for kinetics in these cavities also, much like isolated cavities. Since we were limited by the resolution, the minimum distances between the cavities could not be accessed. However, the maximum distance between the centres of the nucleating cavities to form a group was shown to be 290-320 microns.

Clustering of cavities i.e., number of cavities nucleating very close to each other, appeared in all samples. However, thicker samples and cubic samples showed much more clustering than the flat samples which is explained by the slow desorption of gas from the bulk of the samples with more thickness. Consequently, the clustering was seen to occur along a path which could also be seen as a path of nucleation for the secondary cavities and could be related to the gas diffusion path or could be due to the local stress and diffusion conditions arising from the very initial cavities. The nucleation of primary cavities was always random in all samples leading to the important conclusion that nucleation is a localized phenomenon while the deflation of the cavities seemed to be more driven by the global desorption. The fact that edge cavities have a shorter life span supports this idea. Additionally, a qualitative observation of clusters in samples of different cross-link densities showed that the average size of the cavities consisting a cluster are larger for weakly cross linked samples. However, the parameters of cavity size seem to be comparable for the samples of different cross-link densities analysed at the scale of isolated cavities as well as groups of close cavities

Nevertheless, the data for local kinetics seen here is an important step for the simulations carried out later to provide an experimental reference point for isolated or single cavity and groups of close cavities.

Chapter 5 Investigation of interaction effects between close cavities using Finite Element Simulations

One aim of the previous chapter of this document was to investigate the possible interaction of close cavities from in-situ tomography views. Some characteristics of these cavities (growth kinetics, shape, delayed nucleation time) was evaluated and compared to those of isolated cavities. The analysis was based only on morphological considerations. Due to the full coupling between diffusion and mechanics and the lack of direct tracking of the gas content field, the discussion on mechanisms of cavity growth depending on their surrounding medium is not trivial. Only fully-coupled microstructure simulations of the phenomenon can provide complementary data about the diffusion problem and bring the additional material needed to address this question. As explained in the following section, such fully coupled simulations raise substantial numerical problems that the development of this new internal Finite Element Code FOXTROT aims to overcome. This code has been developed at Institut Pprime by Mikaël Gueguen and Jean-Claude Grandidier.

This chapter depicts the step forward that was attempted in a final perspective part of this study, based on this tool.

5.1 Difficulties in simulation of cavity growth due to gas decompression

As mentioned in Chapter 1, numerical studies for the modelling of cavity growth under purely mechanical loading exist in literature (Lopez-pamies 2009; Ravi-chandar and Lopez-pamies 2014). However, only a few studies have been conducted at the cavity scale for decompression failure in gas-exposed polymers at high pressure. The major difficulty of this simulation lies in the calculation of the equilibrium volume of the cavity V_{cav} at each time step of the computation, since it depends on the mechanical balance between applied external pressure, surface tension and internal pressure inside the cavity (P_{int}). This internal pressure itself depends on the number of gas molecules contained inside the cavity (updated from the gas flux at the cavity wall) and the volume V_{cav} via the perfect gas law

$$PV = nRT$$

where P is the pressure, V is the volume, n is the number of moles of the gas, R is the universal gas constant and T is the temperature. Therefore, the solution to this fully-coupled problem at the cavity wall must be calculated by iterating the two physical phenomenon simultaneously. The problem is even more emphasized in rubbers, due to the application of high-pressure loading to quasi-incompressible materials.

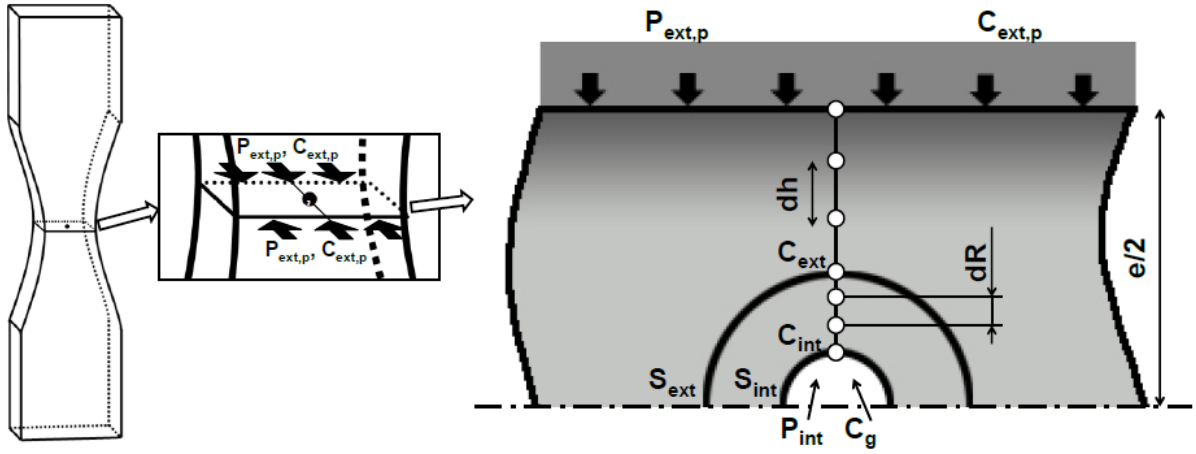

Figure 5.1 Hollow-sphere model developed by Jaravel et al. (2012) for the modelling of cavity growth under decompression.

As a first step, Jaravel et al (Jaravel et al. 2013) had previously developed a hollow-sphere model depicted in Figure 5.1. The cavity (smallest half-circle; several radii ranging from 50 up to 500 nm) was located in the core of a rubber shell (second half-circle indexed $_{ext}$). The boundary conditions of pressure P_{ext} and gas content c_{ext} applied to the spherical hollow-sphere were deduced from a bulk diffusion problem through the thickness of the macroscopic sample (with boundary conditions $P_{ext,p}$ and gas content $c_{ext,p}$) but the problem was solved using Matlab® along the radius of the hollow sphere, as plotted with white dots in Figure 5.1. The evolution of the internal pressure and gas concentration inside the cavity (P_{int} and c_{int} respectively) could be computed in this way.

An interesting point was that both the surface tension at the cavity wall and finite strain elasticity of the rubber matrix (quasi-incompressible neo-hookean constitutive law) were taken into account. A strong limitation of this study was the 1D solving framework that prevented simulation of close cavities. In addition, the diffusion and mechanical problems were sequentially solved within the time step.

In order to extend the possibility of this simulation to non-1D situations (e.g. several cavities or non-hydrostatic mechanical loadings superimposed to the pressure release), the study of Kane Diallo et al (2016) was carried out using Finite Element Method. This study was done by modelling the cavity as a solid medium, in order to stabilize cavity wall problems from the pressure continuity ensured by the mesh.

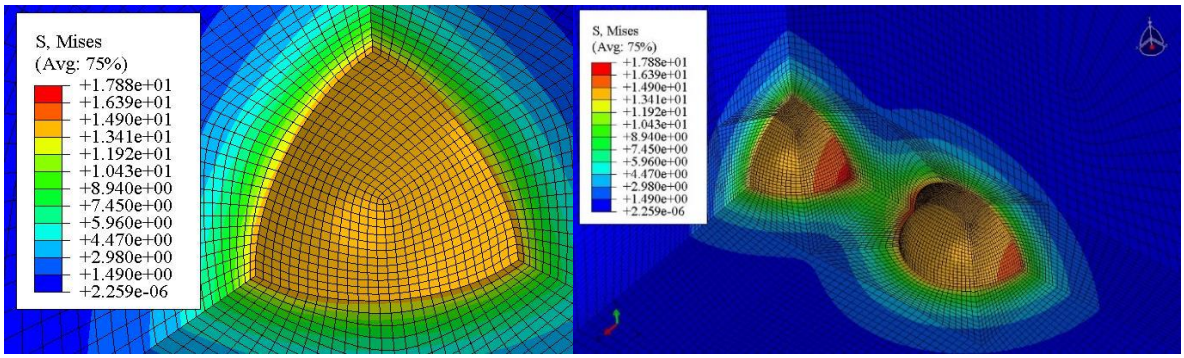

Figure 5.2 Finite Element simulation of the growth of one or two pre-existing cavities (radius 5 µm) in a bulk elastic medium exposed to hydrogen diffusion and decompressed (Kane Diallo et al 2015). The cavity is modelled as an "equivalent solid medium" not represented here.

The pressure dependence of the Young modulus of this "equivalent solid medium" (not represented in Figure 5.2) was tabulated from an analogy between bulk modulus and perfect gas law. The diffusion coefficient, solubility and volume change parameter were those of hydrogen in air. The structure was meshed with C3D8HT elements and the problem was solved using the heat transfer framework available in Abaqus®. The main interest of this proposal was to make the simulation of 3D situations possible. However, the analogy with solid medium was questionable and the simulation framework had to be restricted: the rubber matrix behavior was linear elastic, surface tension was not taken into account finally, and convergence was obtained by careful selection of material and loading parameters.

5.2 Development of an alternate solution with the internal Finite Element Code FOXTROT

In order to solve these problems, an internal code has been in development for several years at Institut Pprime, developed by Mikaël Gueguen and Jean-Claude Grandidier. The strategy is to keep the Finite Element framework but to improve the solving of the diffuso-mechanical problem and to take into account the surface tension.

As illustrated in Figure 5.3, the cavity is modelled as a void with continuity of the gas concentration at the cavity wall. The cavity is viewed as a free surface with boundary conditions that create a gas flux at the cavity wall. The problem is solved as a pressure one. The coupled diffuso-mechanical aspect is imposed through the same pressure loading which has two physical connotations: the mechanical hydrostatic pressure and a partial pressure corresponding to the gas content at any point, by a factor equal to the solubility given by Henry's law.

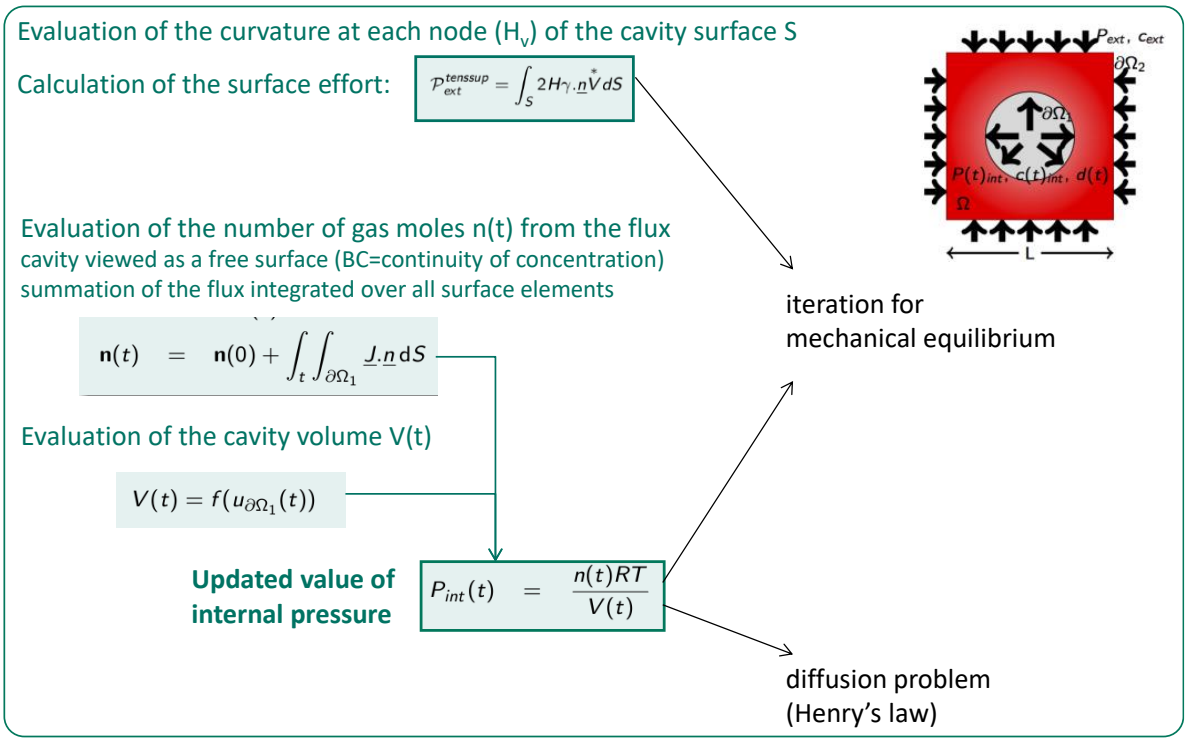

Figure 5.3 Strategy of the internal Foxtrot software for diffuso-mechanical and cavity interaction modelling in cavity growth context.

A first major improvement of this model is the calculation of the curvature of the cavity surface at each node for each iteration of equilibrium search. No solid element was available in

Abaqus® to directly obtain the curvature of the cavity. Therefore, the load corresponding to surface tension can be applied to each surface element and integrated into the search for mechanical equilibrium.

Another major improvement is the ability to update the internal pressure from the perfect gas law involving the current value of the cavity volume and the number of gas moles contained inside the cavity, updated from the gas flux at the cavity wall integrated from the cavity surface and the history of diffusion effect with an explicit scheme.

So far, a linear elastic constitutive law has been prescribed for the surrounding media. Extension to finite strain elasticity is considered for future work but was beyond the scope of this work.

5.3 Use of FOXTROT software in the context of present work

5.3.1 Main considerations

The simulations in the present work were conducted with the main following considerations:

- A pre-existing cavity, with a size of the order of those observed in the experiment by in-situ tomography, was immersed into a cubic matrix of much larger size. The aim was to simulate a bulk cavity, i.e. to apply similar boundary conditions at the surface of the cubic model than those of the sample and to have vanishing gradient effects due to the cavity when getting close to the free surface. The estimated size of morphological Representative Volume Element of cavity fields evaluated from covariogram analysis in Kane Diallo's work (Kane-Diallo et al. 2016) was used as a guideline.
- The model was meshed with linear tetrahedron elements C3D4 in the bulk, and a diffuso-mechanical coupling from finite element method was solved in the bulk. The coupling solver use the equivalence between mass diffusion and heat transfer equilibrium; therefore we have considered concentration as the degree of freedom of the diffusion problem related to the heat transfer equilibrium. The gas diffusivity is

related to the thermal conductivity and an additional constant term is added to the speed term of the mass balance of gas (the ρC_p constant).

- Diffuso-mechanical coupling and cavity interaction was treated at the interface using the strategy depicted in Figure 5.3, and explained in the previous paragraph.
- The pressure loading was the same as applied in Tomography experimental campaigns, with a saturation pressure of 8MPa and a decompression rate of 1.6 MPa/min. The initial value was 0, indicating that the cavity is empty. As explained above, pressure corresponds to both mechanical and diffusion loadings.
- Surface tension was not taken into account here, for several reasons. The first one was to minimize the complexity level of the calculation. The second one was related to the initial size of the cavity (200 µm), which exceeded the range of radii for which the surface tension causes a considerable increase in the critical hydrostatic stress for unstable cavity expansion (Fond 2001).

5.3.2 Limitations arising from the choice of realistic material parameters of EPDM 1.6

As a first step, a series of calculations were conducted with parameters as close as possible to ones used during the experiments carried out on EPDM 1.6. A cavity with an initial diameter (8 µm) close to the tomography resolution was placed at the centre of a cube with edge of 20 microns which was then placed in the centre of another cube of edge 40 microns. This assembly was finally placed in a cubic box of size comparable to the actual sample size (4x4x4 mm^3) to realistically simulate the conditions under which an isolated cavity exists in bulk of the sample (illustrated in Figure 5.4). This strategy allowed for adaptable mesh size along the different geometries. For the wall of the cavity very fine mesh was used which became coarser as we moved away from the cavity Figure 5.4.

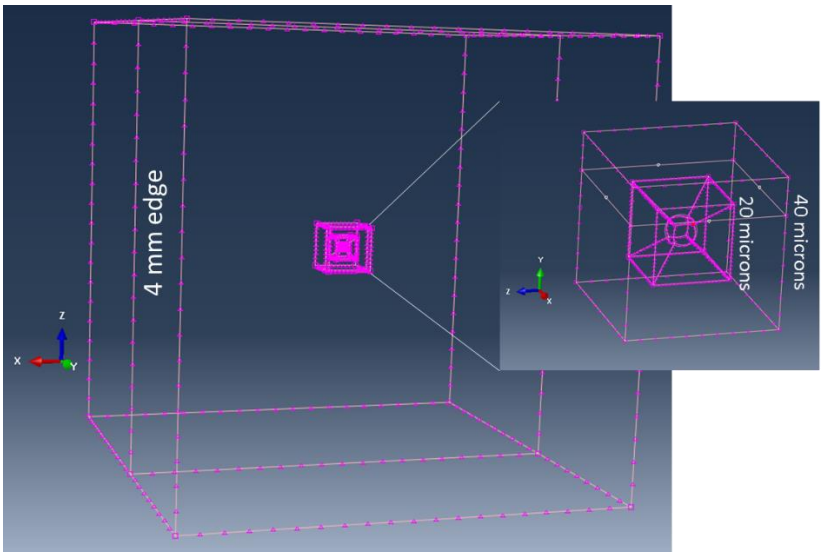

(a)

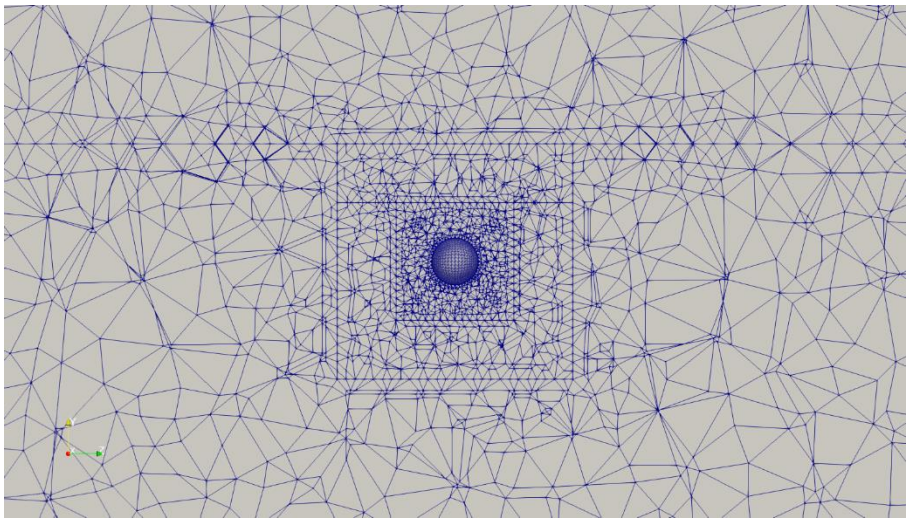

(b)

Figure 5.4: Illustration of (a) 8µm-diameter cavity immersed in a boxes of different sizes (b) variable mesh size around and far from the cavity.

The material parameters, listed in Table 5.1 were selected as close as possible to those of EPDM 1.6. The corresponding value of diffusivity D was 1.89e-04 mm²/s.

Material parameters inspired from EPDM 1.6	
E = 2.75 MPa	diffusivity D = 1.89e-04 mm^2/s
ν = 0.49	Solubility S = 1
density ρ = 1	Volume change = 2.5e-04 / MPa
	"Specific heat" = 1

Table 5.1 Material parameters used as a first step to mimic EPDM 1.6

The reliability of these calculations is questionable, at least on two main points, illustrated in Figure 5.5 which displays the time evolution of the applied pressure (green curve, left axis), internal pressure of the cavity (red curve; left axis) and volume of the cavity (blue curve; right axis).

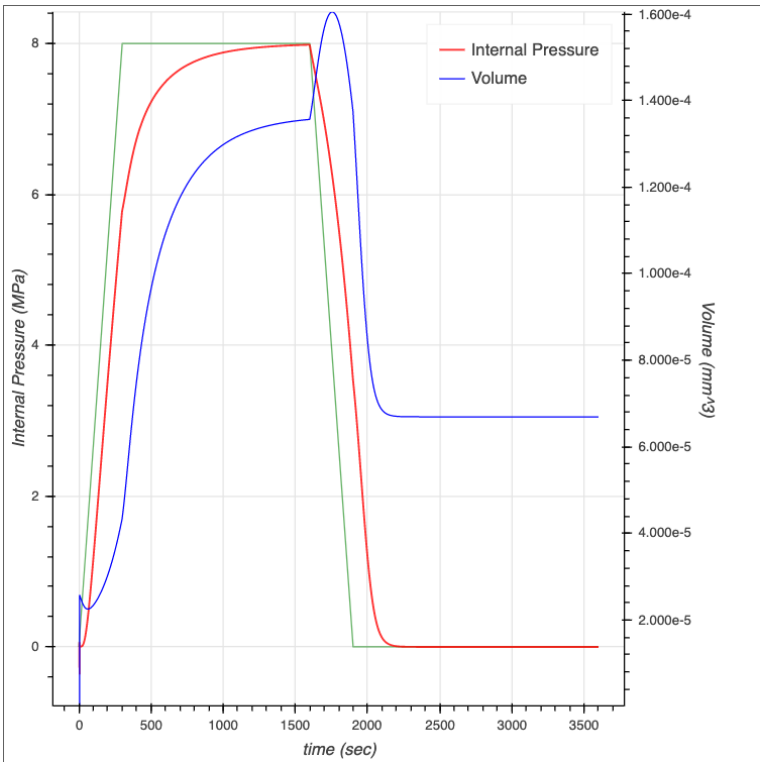

Figure 5.5: Evolution of the internal pressure and volume of the cavity simulated in the model depicted in Figure 5.4, with material parameters inspired from EPDM 1.6

The first problem is the sensitivity to the time step detectable from instabilities in the transient stages like at the beginning of pressurization. The low elastic modulus, combined with quasi-incompressibility and application of rather high pressure, may promote such instabilities. The second problem is the meaningless residual volume observed at the end of the pressure cycle, considering the fact that the matrix behavior is elastic and that the sample is fully desorbed.

It is important to underline that the same model under pure mechanical conditions (i.e. the pressure loading only has the meaning of hydrostatic pressure) or weakly coupled diffuso-mechanical loading (through volume change coefficient without any gas exchange at the cavity wall) leads to stable and physically consistent solutions, returning to the initial configuration at the end of the pressure cycle. The above depicted problems clearly originate from the full coupling between diffusion and mechanics at the cavity wall.

5.4 Simulation of the cavity growth using modified parameters

The questions of the high dependency of these calculations on the mesh size, time step and material parameters must be addressed for robust modelling with further studies but are beyond the aim of the present work.

In the present study, the focus was shifted to reliable simulation of cavity growth, by using a modified set of material parameters, mesh size and time step which had previously yielded reliable results in a study conducted at Institut Pprime on simulation of the single cavity growth. The focus was to compare these results to those obtained with simulation of growth of a pair of close cavities, with all other parameters kept identical.

5.4.1 Model geometry and mesh

The model geometry and mesh used in this second simulation series for one cavity is presented in Figure 5.6. The initial diameter of cavities was 0.2 mm and the size of the box in which the cavity was placed was 20x20x20 mm^3.

Two more models with the same part dimensions of 20x20x20 mm^3 were computed containing two cavities with the same initial diameter of 0.2 mm. However, the distance between the cavities, d, was varied, with the first model containing cavities separated by a distance of 0.8 mm and the second model containing cavities separated by a distance of 0.4 mm, between cavity centers. It should be noted that the mesh size was coarser than the one used in previous case.

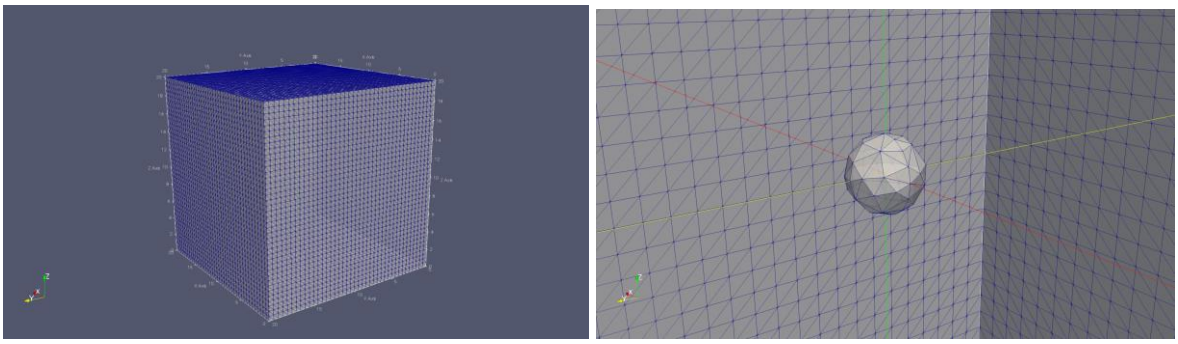

Figure 5.6: Example of the one-cavity model used with modified parameters

5.4.2 Material and loading parameters

Table 5.2 displays the modified material parameters. It can be noted that the modulus was significantly raised such that the volume change due to hydrogen sorption was decreased and that the value of diffusivity $D = \lambda / \rho C_p$ was increased (1E02 mm^2/s).

Modified material parameters	
E = 1000 MPa	conductivity D = 1e-02 mm^2/s
ν = 0.49	Solubility S = 1
density ρ = 1e-04	Volume change = 1e-05 / MPa
	"Specific heat" C_p = 1

Table 5.2 Modified material parameters used to for comparison between one and two close cavities

Saturation pressure was kept equal to 8 MPa, with a pressurization ramp of 1 s, a saturation time of 15 s and a decompression ramp of 1s. The total computed time was 30s. It should be

noted that the use of specific heat in this case has no physical meaning and is used as a numerical damping factor to drive the calculation towards a reliable result.

5.4.3 Single-cavity model

Figure 5.7 displays the temporal evolution of the applied pressure (boundary condition) (green curve; left axis), internal pressure in the cavity (red curve; left axis) and the volume of the cavity (blue curve; right axis) during the pressure cycle.

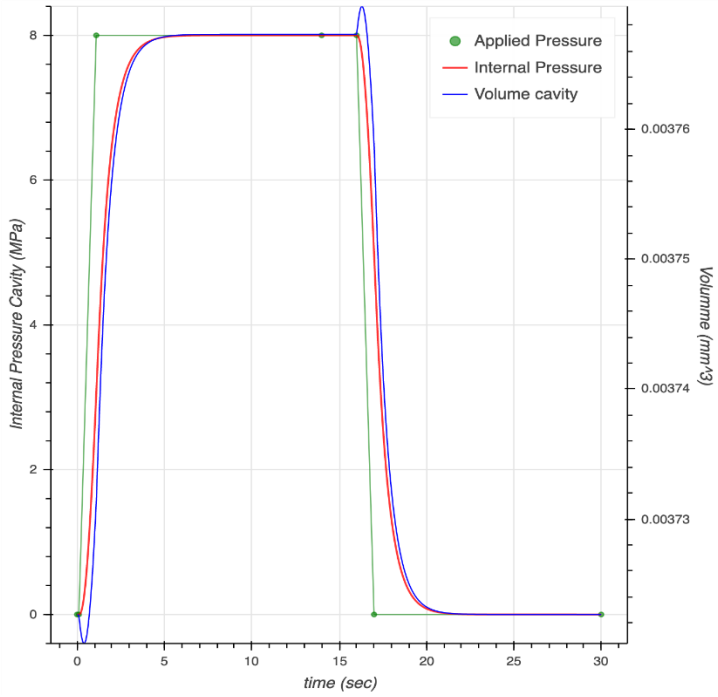

Figure 5.7: Pressure and volume evolution of one central cavity (initial diameter 0.2mm) saturated at 8 MPa

During the saturation stage, the internal pressure increases and stabilizes rather fast, due to the high diffusivity value. The cavity volume first decreases due to the mechanical pressure and then increases as the gas penetrates into the cavity. Subsequently, the cavity volume stabilizes to a value depending on both the equilibrium content of gas inside the cavity and the surrounding swelling of the bulk matrix due to equilibrium hydrogen content.

As a comparison, Figure 5.8 shows the volume change of the cavity obtained from simulations with (blue curve) and without (orange curve) gas exchange at the cavity. The latter case can be

compared to an adiabatic situation in the context of a heat transfer problem. Hence, the cavity remains compacted all along the pressurization and saturation stages. In these simulations, the expansion coefficient was ten times larger than in Figure 5.7. It can be noted that the stabilized volume at saturation was only slightly smaller, suggesting that within this range of expansion coefficient, the indirect effect of bulk swelling had minor effect. The internal pressure is seen to decrease during decompression in a consistent way while the cavity volume is first seen to increase as a result of the mechanical pressure release, and then decrease back to the initial value.

All this phenomenology is consistent with the previous results obtained by Jaravel et al. and Kane Diallo et al. in the different frameworks reported in section 5.1.

It can be noticed that the volume inflation of the cavity is very small. This is due to the stiffness of the matrix and its linear elastic behavior which leads to an overestimated stress increase during inflation and limits the growth in comparison with the one expected in real rubber.

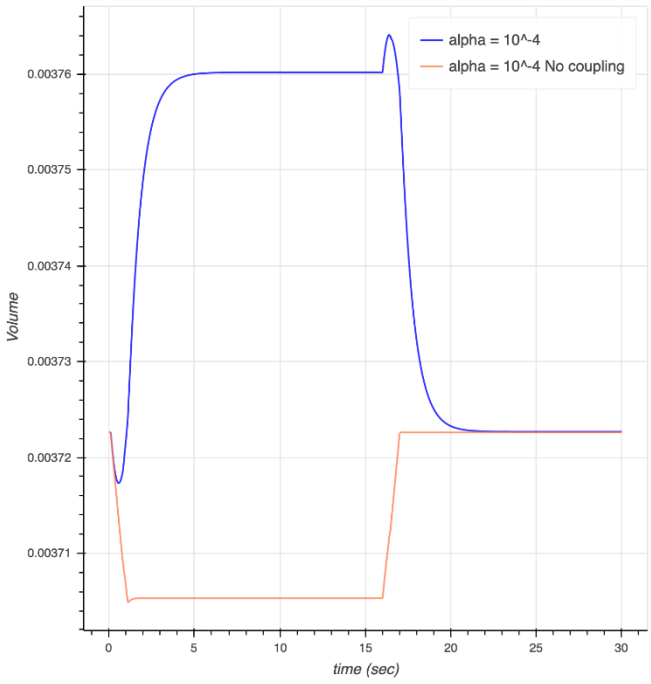

Figure 5.8: Time evolution of the computed volume of the cavity with (blue curve) and without (orange) gas exchange at the cavity wall (volume change parameter due to hydrogen sorption = 1e-04 MPa^{-1})

Figure 5.9 illustrates a primary analysis of the response of the bulk in close proximity to the cavity. These graphs show the evolution of the displacement magnitude and the gas content at three different points around the cavity, i.e. at 0.1 mm from the cavity surface along the three directions x, y and z. The gas content profile was identical whatever the direction. Small differences were observed on the displacement magnitude, probably due to the discretization error.

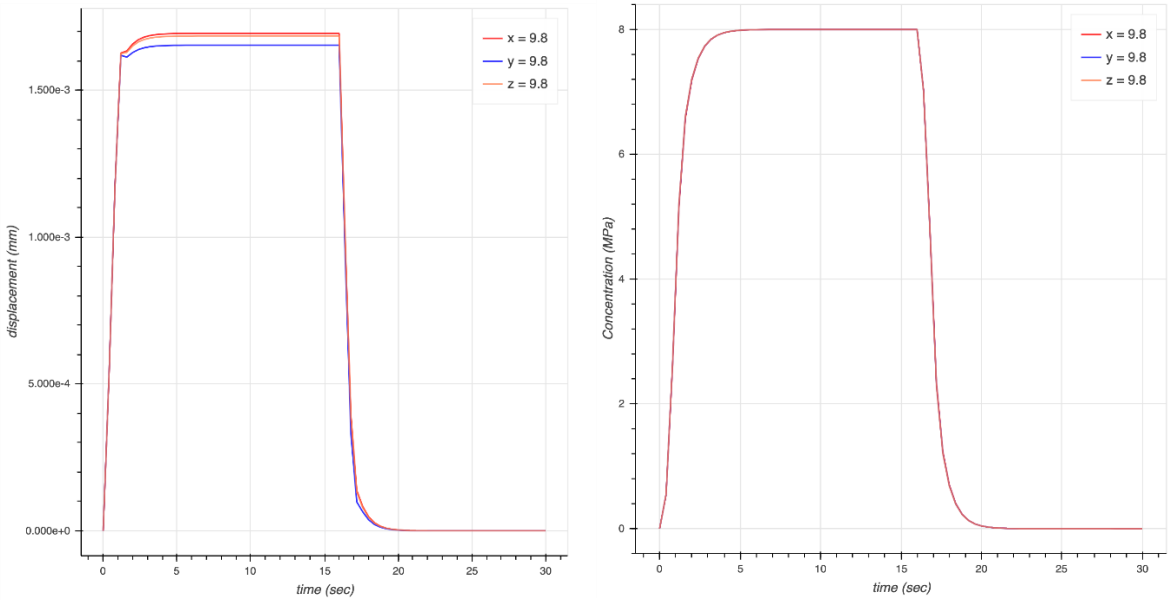

(a) (b)

Figure 5.9: Evolution of (a) displacements magnitude and (b) gas content at three different points close to the cavity. Coordinates of the cavity centre were (10; 10; 10). Coordinates of probes labelled "x = 9.8", "y = 9.8" and "z = 9.8" were respectively (9.8; 10; 10), (10; 9.8; 10) and (10; 10; 9.8).

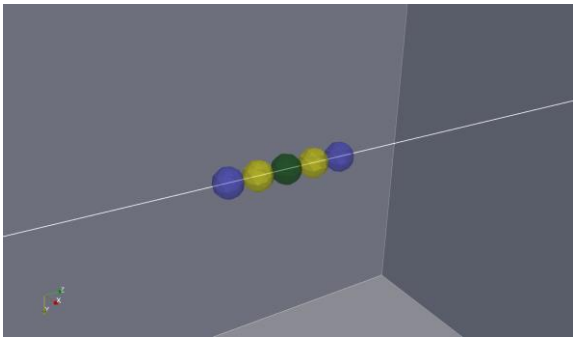

Figure 5.10: View of the location of cavities (diameter 0.2mm) in the one-cavity model (green), two-cavity model with a core-to-core distance d of 0.8mm (blue) or 0.4mm (yellow); white line shows the path for gas concentration profile plot in Figure 5.11 (line between (10,10,0) and (10,10,20) points).

Figure 5.11 plots the gas concentration profile through the sample, along the path plotted in white line in Figure 5.10, for different times of the pressure history.

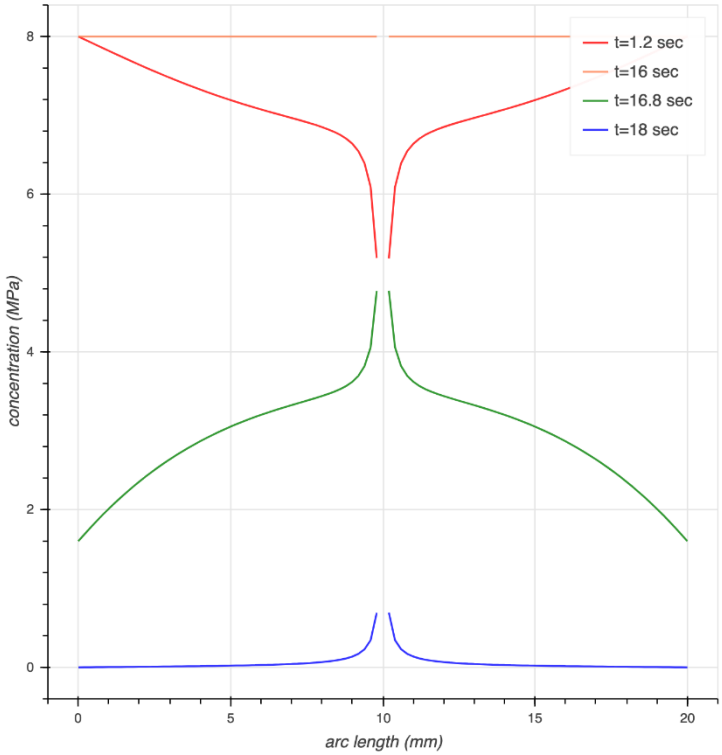

Figure 5.11: Gas concentration profile through the sample along the direction plotted in white line in Figure 5.10.

The red curve in Figure 5.11 (1.2s) was obtained just after the end of pressurization. Concentration equals the applied partial pressure at the sample surface. A symmetrical gradient is visible through the thickness. The cavity corresponds to the curve interruption since no output from the Finite Element calculation is available in areas without material. It is clear that the presence of the cavity creates a kind of “concentration well” with a spatial width around 0.2mm on each side when extrapolating the linear regimes observed from the cavity edges.

The flat orange curve (16s) was obtained at the end of saturation. The gas content is homogeneous at any point of the matrix.

The green curve (16.8s) corresponds to the concentration profile during decompression. Value at the free surface corresponds to the current value of the loading pressure ramp. A significantly higher concentration is obtained close to the cavity which “traps” gas molecule for a while. Figure 5.12 shows the gas pressure field (corresponding to the gas content one). Again, the sharp gradient is observed over a shell about one diameter thick around the cavity.

The blue curve (18s) is obtained 1s after the end of decompression. It is almost flat to zero, except around the cavity where an excess of gas can be observed. It can be assumed that the full desorption of this residual gas could take a time significantly longer than the time scale of bulk desorption.

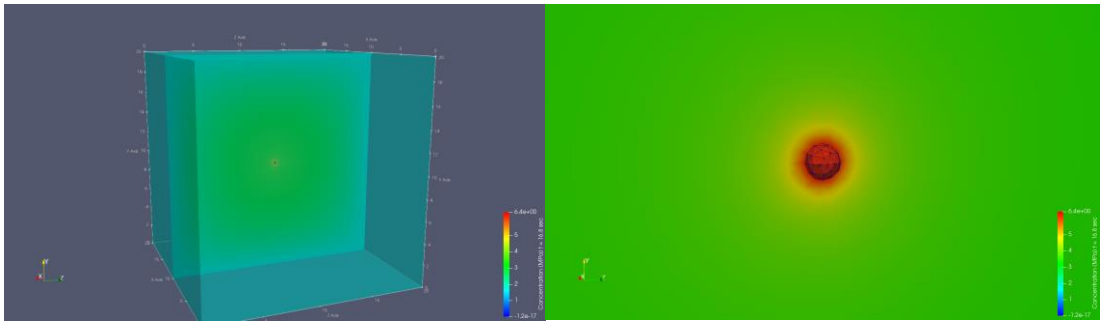

Figure 5.12: Pressure fields (corresponding to the gas concentration one) in the full model and around the cavity after 16.8s i.e. during decompression (80% of pressure release)

5.4.4 Two-cavity models

In order to discuss the possible interaction between close cavities, two two-cavity models were simulated, with the same initial diameter of 0.2mm for all of them and a core-to-core distance d of 0.8mm (blue cavities in Figure 5.10) and 0.4 (yellow cavities in Figure 5.10). In the initial configuration, the edge-to-edge distance corresponded respectively to three and one diameter.

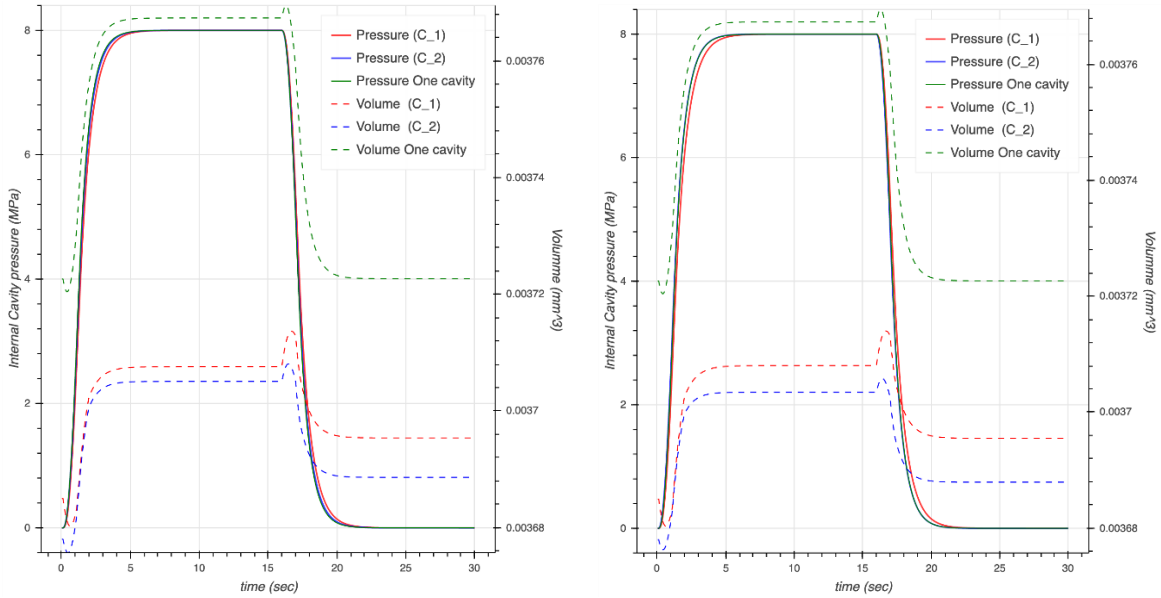

(a) (b)

Figure 5.13: Pressure and volume evolution of the two cavities (C_1 and C_2) compared to those of the single one for a core-to-core distance d of (a) 0.8mm and (b) 0.4mm.

Figure 5.13 compares the time evolution of internal pressure and the volume change of the two cavities (called C_1 and C_2 in the graphs) to those of the single one for the two core-to-core distances d.

During saturation, the phenomenology was similar to that commented before for one single cavity. The main difference was that the stabilized volume of the two cavities was significantly smaller than that of the single cavity, like if the sorbed gas was distributed into the two cavities.

The pressure kinetics was almost the same. A small difference between C_1 and C_2 curves was observed before saturation for d=0.8mm and a little bit more distinguishable for d=0.4mm.

Again, the volume evolution was very small. Its evolution was a little bit different between C_1 and C_2. There was no physical reason for this since the model was symmetrical to the plotted axis and since the initial size of the two cavities was the same. The scatter was even more important for d=0.4mm. Moreover, a residual value was observed at the end of the pressure cycle. More simulations should be conducted to evaluate how far the spatial discretization and subsequent cumulative effects could be responsible for these differences.

The possible interaction effect can be mainly discussed from the gas concentration profiles plotted in Figure 5.14 at the same intermediate times as in Figure 5.11 for the single cavity. Regarding the gradient in the bulk matrix around the cavity or the pair of cavities, the global phenomenology is similar between the two two-cavity models and the one-cavity one. As a complement, Figure 5.15 displays the concentration profiles during (16.8s) and after decompression (18s) for the two models. The sharpness of concentration gradients seems unchanged. Curves appear shifted by the difference of core-to-core distance.

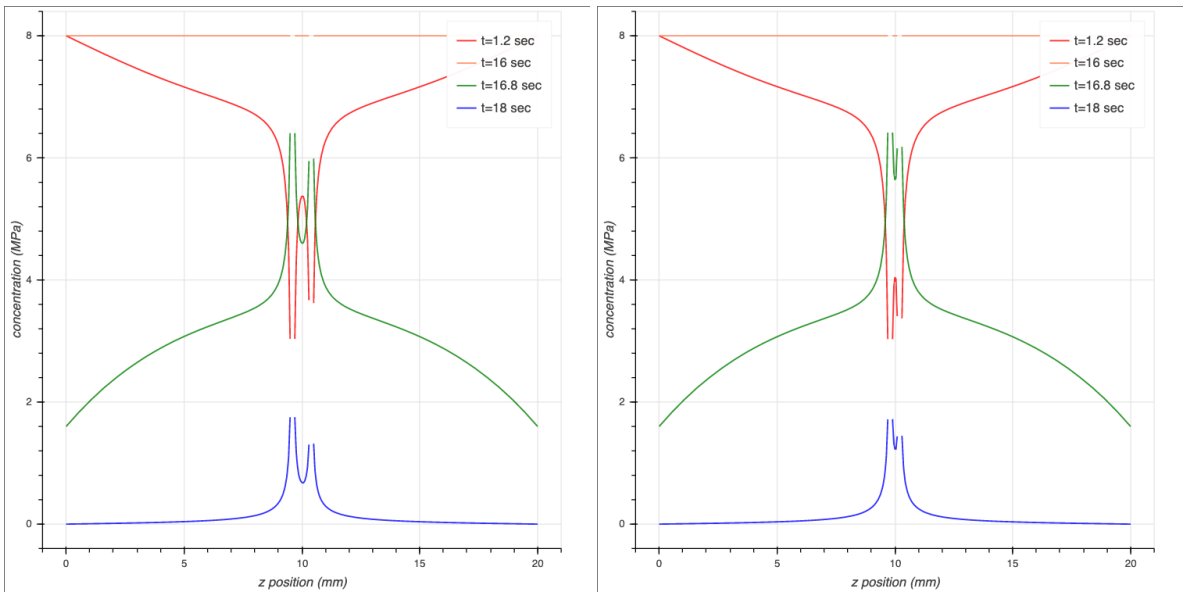

(a) (b)

Figure 5.14: Gas concentration profiles at different times of the pressure cycle for the two-cavity models with core-to-core distance d of (a) 0.8mm and (b) 0.4mm

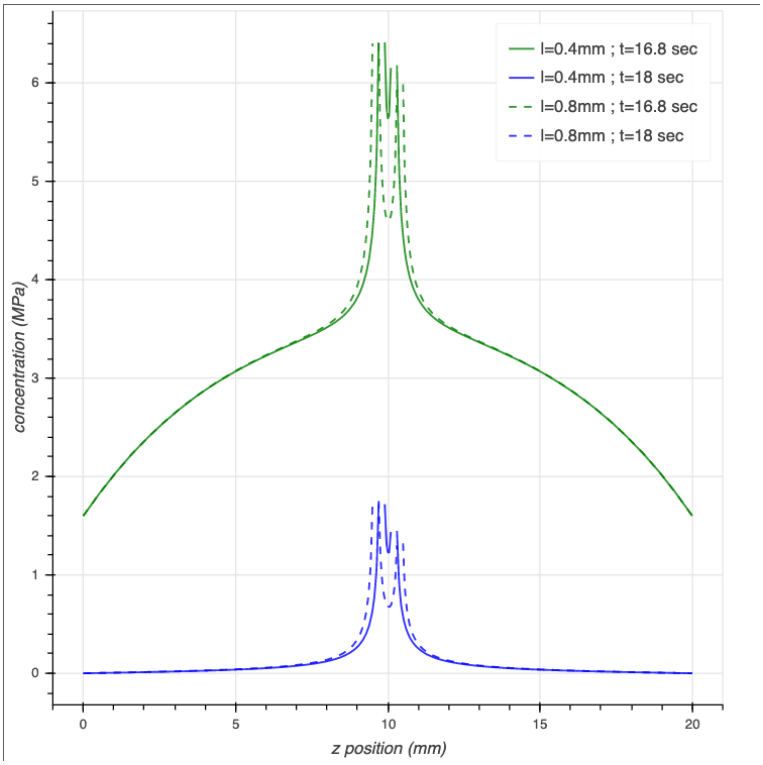

Figure 5.15: Gas concentration profiles in the two two-cavity models during (16.8s) and after (18s) decompression.

An interesting difference, confirmed by the concentration fields viewed in Figure 5.16, deals with the significant residual gas concentration observed between the two cavities, especially when they are close to each other by one diameter only. This residual value remains high even when the bulk matrix around the pair of cavities is almost fully desorbed.

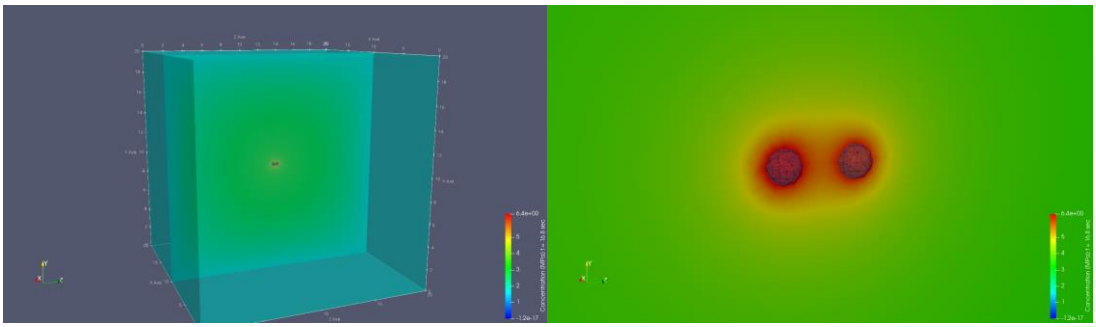

Figure 5.16: Pressure fields (corresponding to the gas concentration one) in the full model and around the cavity after 16.8s i.e. during decompression (80% of pressure release) in the two-cavity model with core-to-core distance d=0.4mm

5.5 Conclusions

The simulation of cavity growth resulting from gas decompression using Finite Element Method in a quasi-incompressible medium under high-pressure while considering the problem as a fully coupled diffuso-mechanical one is a quite a huge challenge. Therefore, the development of the internal code Foxtrot is an unprecedented attempt in literature. The aim of developing this code was to use it in the present work to highlight the two physical fields interacting during the inflation / deflation of close cavities.

Beyond the questionable fact that the above simulations are based on a pre-existing large cavity, there are other numerical limitations such as sensitivity to the mesh size and time step, as well as the limitation of the tool to linear elastic behaviour law characterizing the matrix. Hence, only a few simulations could be possible which nevertheless provided a qualitative comparison. Pairs of 0.2 mm-diameter cavities, separated by a distance of 0.6 mm (3 times the diameter) and 0.2 mm (equal to the diameter) between their borders, were simulated and compared to a single cavity under the same pressure cycle (saturation pressure 8 MPa).

In the latter case, a significant gas content gradient was observed around the cavity over a distance of about one diameter. The growth was logically isotropic. In the former case, the accuracy and spatial extension of gradients around cavities was almost similar to the ones in the bulk direction. On the other hand, a residual gas content was observed in the ligament between cavities. This “trapped” gas concentration was very close to the value at the cavity surface when the ligament thickness equaled the diameter of the cavity.

These preliminary simulations indicate a rather local growth process and weak interaction between cavities as soon as the thickness of the ligament separating them exceeds the value equivalent to three times the cavity diameter, but at this stage any transition of these results to interpret the “real rubber” investigated in Chapter 4 must be very careful, even based on dimensionless considerations. Among other limitations, the sharpness of gradients and volume change of cavities directly derives from the material parameters which were far from the ones of real rubber.

General Conclusions and Perspectives

The work presented in this manuscript focused on the cavitation in unfilled EPDM rubber induced after saturation in hydrogen during decompression. This experimental campaign was possible thanks to collaboration between Hydrogenius laboratory at Kyushu University (Japan) and Institut Pprime (France) funded by the French program “Investissements d’Avenir” Labex Interactifs (reference ANR-11-LABX-0017-01).The main aim was to shed light on how far the heterogeneity of the rubber matrix and cavitation were systematic. For this purpose, experiments were carried out at two scales,

At sub-micron scale SAXS experiments were carried out for samples in equilibrium state as well as immediately after decompression. For the in-situ tests, a novel pressure chamber was designed with diamond windows which allowed the SAXS experiments to be carried out for samples in saturated state to characterize the structural changes in EPDM rubber matrix if any due to hydrogen exposure using the parameter of correlation length. These experiments were also repeated using Synchrotron X-ray source (SAGA-LS) in Japan. Complementary ex-situ tests were performed after exposure by S. Tencé-Girault (Arkema & PIMM laboratory at ENSAM ParisTech).

The results from the in-situ test at low pressure do not indicate a change in the size of heterogeneities in the rubber matrix due to the hydrogen exposure. This is contrary to the calculations from the ex-situ test which clearly show increase in the correlation length after decompression from high-pressure exposure (30 MPa). This could be pointed out that at low saturation pressure, the penetrated hydrogen content is very small which is not enough to affect any changes in the rubber matrix. However, the results from the synchrotron source experiments showed a slight and diffused plateau that could be a possible indicator of a correlated structure. To clarify this, additional scattering experiments were carried out exploring a longer q-range which could enable the acquisition at a lower value of q that is $0.05nm^{-1}$. This plateau was observed again in case of unexposed samples which became clearer in the Lorentz corrected plots. However, the position of these maxima were not directly correlated with the cross-link density of the samples. After exposure, the maxima were no longer detected. This was as a result of large central scattering that was superimposed on the

initial spectra due to scattering by the cavities that appeared in the sample after decompression from high pressure. It is important to note that these experiments were carried out after the complete desorption of hydrogen form the sample. Results from the scattering experiments done immediately after decompression during the desorption of hydrogen indicate that the spectra of the exposed samples taken immediately after decompression show a marked difference from the spectra of the unexposed sample and these spectra tend to approach those of the unexposed samples as the desorption progresses. However, the spectra of the exposed samples do not superimpose those of the unexposed samples even after complete desorption of the gas, indicating a permanent structural change in the rubber matrix after single hydrogen exposure. As a general conclusion, it can be underlined that the hydrogen exposure leads to microstructural change in the rubber matrix which is retained even when the gas is fully desorbed. It was also seen that the heterogeneity of the rubber matrix at the sub-micron scale is not directly correlated with the cross-link density. Additionally, the low pressure experiments are not enough to calibrate the degree of heterogeneity in rubber matrix; the in-situ experiments carried out in the present study showed that no change in the correlation length, corresponding to the matrix heterogeneity, was observed after hydrogen exposure.

At higher scales, tracking of cavitation in EPDM was carried out using time resolved 3D in-situ tomography, the main aim of which was to clarify the interaction between cavities at a local scale through comparative characterization of isolated and close cavities. An attempt was also made to clarify the minimum distance of this interaction and provide a qualitative insight into the inflation and deflation characteristics of cavities at the scale accessible due to the resolution of the tool (30 microns). For this purpose two different cross-link densities of EPDM were tested with different decompression conditions and sample geometries.

The earliest cavities were observed at 150 to 300 seconds after decompression at which is either towards the end of the decompression phase or completely after it. These cavities were termed as primary cavities in the document. During the quantitative analysis the cavities nucleating during the decompression phase and immediately after it show no difference in kinetics. However, the kinetics are highly influenced by the proximity to the free surface. In fact for cavities with a distance of about 800-900 microns in case of EPDM 1.6 and 700-800 microns for EPDM 0.5, this driving force superseded any other local boundary condition. These cavities

were termed as edge cavities distinguished from the bulk cavities which nucleated in the core of the sample and whose kinetics were dependent on the local boundary conditions and time of nucleation. The edge cavities were seen to have a short life driven by the global desorption. The classification of edge and bulk cavities was supported by the simulations carried out to see the temporal evolution of gradients of concentration along the sample geometry. There was good agreement between the experimental results and the diffusion simulation which pointed to this edge effect being directly related to the desorption field of the sample.

The secondary cavities which refer to the cavities that nucleate after the primary cavities showed slower kinetics possibly due to the global desorption and changing iso-conditions. It should also be noted that the edge cavities do not appear as secondary cavities supporting the argument that fast desorption at the free surface limits the maximum volume of the edge cavities thereby, making the “cavity life” short.

Isolated cavities were observed to be temporally isotropic during inflation and the flattening of cavities was visible during deflation which suggests the transitioning of the cavity into a crack. It should be noted that the formation of crack does not necessarily include coalescence. Isolated cavities were seen to become cracks which is seen in the increase of anisotropy accompanied by abrupt increase in volume deviating from the regular parabolic graph. As the study of cracking was not the aim of the present study, these cavities were excluded from analysis. However, the flattening of isolated cavities shown in the graphs above showed the beginning of transition from cavity to crack.

Clustering of cavities i.e., number of cavities nucleating very close to each other, appeared in all samples. However, thicker samples and cubic samples showed much more clustering than the flat samples which is explained by the slow desorption of gas from the bulk of the samples with more thickness. Additionally, the clustering was seen to occur along a path which could also be seen as a path of nucleation for the secondary cavities and could be related to the gas diffusion path or could be due to the local stress and diffusion conditions arising from the very initial cavities. The nucleation of primary cavities was always random in all samples leading to the important conclusion that nucleation is a localized phenomenon. The fact that edge cavities have a shorter life span supports this idea.

Clustering was analysed quantitatively with respect to distance between cavities and their respective evolution to compare with the kinetics of isolated cavities and to clarify the distance

between cavities at which the interaction is perceptible. From our tests, the interaction between cavities did not appear to be of a major consequence in terms of kinetics of the cavities. Other factors like proximity to the edge and delayed nucleation were driving factors for kinetics in these cavities also, much like isolated cavities. Since we were limited by the resolution, the minimum distances between the cavities could not be accessed. However, the maximum distance between the centres of the nucleating cavities to form a cluster was shown to be 290-320 microns. A more qualitative analysis of clustering leads to a more global conclusion that while nucleation seems to be a very localized process whereas deflation of cavities seems to be driven by the macroscopic desorption field of the sample.

The results of 3D in-situ tomography campaign, while providing novel observations of the phenomenon, do not make it possible to understand the nature of the diffuso-mechanical characteristics which govern the growth, and possibly the interaction of cavities under gas decompression. For this purpose, in the later part of the study, simulations of the growth of cavities in strongly coupled diffuse-mechanical conditions were attempted using an internal Finite Elements code (Foxtrot) developed by M. Gueguen and J.C. Grandidier. These simulations are inherently very complex from a numerical point of view and the framework in which these calculation can be successful in the present state is significantly different from the real case of the elastomer (EPDM) studied here. The main assumptions that were made for these simulations include the pre-existence of a cavity in the elastomer matrix in the initial state are, the linear elastic behavior law governing the matrix and no introduction of a criterion of rupture of the cavity wall accompanying its growth. Nevertheless, the novelty of the present work in comparison to the studies in literature is the calculation of gas exchange at the cavity wall at every step, such that the internal pressure and volume of the cavity take into account the mechanical loading during the pressure cycle as well as the diffusion aspect.

The series of simulations carried out in the present work showed that the gas concentration fields around the cavity have strong gradients over a range roughly equivalent to its diameter. When the distance between two cavities is of this order, a significant gas concentration remains in the ligament separating the cavities during desorption. The validity of this result in the more realistic framework of the hyperelastic elastomer remains to be confirmed. However, this result

could explain the possibly influence of cavitation to the subsequent evolution of the damage in general, and contribution to the nucleation of other peripheral cavities in particular.

Perspectives: Future work, as a continuation of the present project at a larger scale could be proposed as follows.

As a first direct perspective of this study, it could be interesting to conduct more in-situ SAXS experiments with a higher pressure which could provide much needed data about the rubber-hydrogen matrix at equilibrium and at the very beginning of decompression. The tests performed in the present study offer a starting point for designing such complex experiments for future studies. It is also important to explore a broader q range by Ultra Small Angle X-Ray Scattering (uSAXS) which could make the variation of the scattering accessible at very low values of q.

Nevertheless, scattering methods provide average estimation of the diffusing entities and for actual observable cavities, direct visual and optical tracking provides useful complementary data. Still based on tomography experiments, the use of a synchrotron radiation source would significantly improve the space and time resolution and make it possible to better detect earlier stages of cavitation. The question of minimum distance for interaction of cavities could be better addressed. Such experiments could also provide information about coalescence by quantitatively analysing clusters which were not accessible with the present resolution.

However, the experimental tracking of this kind of damage has limitations even with very advanced tools. The very beginning of cavity nucleation and the transition from a heterogeneous gas-polymer equilibrium state to a damaged medium, cannot be observed from the currently available experimental tools even by decreasing the space resolution down to the micron. In addition, the diffusion field of the sample cannot be directly measured. For this reason, the improvement of the Finite Element tool Foxtrot is of vital importance. The immediate improvements include implementation of finite strain elasticity and clarifications as well as corrections of numerical convergence / stability limitations.

In the more general context of this study, many open questions still exist. One of the current issues being investigated is the evolution of damage upon pressure cycling which directly raises questions on the interaction effect between close cavities. Factors that could influence the global gas content and gas content heterogeneity in the rubber matrix before decompression is

also worth being investigated. These include the saturation pressure (which changes the solubility) and several microstructural parameters such as cross-link density and effect of fillers. Finally, the present work was focused on rubbers exposed to hydrostatic pressure which is far from the realistic conditions that rubber seals are subjected to in the hydrogen transport and delivery system. Therefore, further work on these material should emphasize on including the effect of mechanical loading in addition to the pressure induced due to gas exposure; many practical limitations could be expected for carrying out these experiments.

Résumé étendu en français

IN-SITU INVESTIGATION OF CAVITY NUCLEATION AND GROWTH IN HYDROGEN-EXPOSED EPDM DURING DECOMPRESSION

La thèse traite de l'endommagement par cavitation des élastomères exposés à de fortes pressions de gaz diffusant. Ce phénomène résulte de l'expansion locale du gaz préalablement absorbé, lorsque la désorption hors du polymère est trop lente par rapport au chargement imposé. Elle vise à mieux comprendre le mécanisme élémentaire de formation, puis de croissance et de coalescence des cavités, isolées ou en proche voisinage. Dans ce dernier cas, une éventuelle interaction doit effectivement être caractérisée pour éclairer la coalescence et la transition vers des fissures macroscopiques.

Le travail a été mené sur série d'Ethylène Propylène Diène Monomer (EPDM) non-renforcés, avec une densité de points de réticulation variable, exposés à des pressions allant jusqu'à 30 MPa. Le volet expérimental s'appuie sur deux des techniques expérimentales in situ les plus récentes : la diffusion des rayons X aux petits angles (SAXS) qui vise à caractériser les hétérogénéités du système réseau élastomère – hydrogène à l'échelle submicronique (chapitre 3), et la tomographie X in-situ (sous des pressions allant jusqu'à 12 MPa) qui fournit des vues 3D résolues en temps des cavités, pendant et après décompression, et permet de préciser les mécanismes (chapitre 4). Un second volet tente brièvement de discuter les effets d'interaction entre cavités voisines à partir de simulations Eléments Finis en conditions diffuso-mécaniques fortement couplées (chapitre 5).

Chapitre 1 - Bibliographie

Dans les élastomères, la cavitation d'origine purement mécanique fait référence à l'apparition et à la croissance de défauts présents intrinsèquement dans la matrice de caoutchouc. Il s'agit soit de vides sous-micrométriques préexistants dans la matrice de caoutchouc en raison de l'inhomogénéité du réseau ou d'impuretés qui peuvent provoquer des concentrations de contraintes locales conduisant à la nucléation de cavités. Sous l'application de contraintes

externes suffisamment importantes, ces défauts se développent élastiquement jusqu'à l'extensibilité maximale des chaînes macromoléculaires environnantes et à la rupture du réseau. Peu d'études existent sur la cavitation sous décompression de gaz. Jusqu'à présent, la littérature sur le sujet s'est concentrée sur une analyse qualitative après que la décompression a déjà eu lieu et n'ont été étayées que par de rares suivis visuels du dommage au cours de la décompression. Cela est dû à la complexité des techniques expérimentales nécessaires pour accéder au phénomène in situ. Des techniques expérimentales in-situ, notamment tomographiques, ainsi que des modélisations diffuso-mécaniques fortement couplées, ont récemment permis de mieux comprendre ce phénomène et d'accéder à une quantification fiable de la morphologie et de la cinétique des champs de cavités. Leur sensibilité à plusieurs types de facteurs extérieurs, dont les conditions d'exposition et de décompression, a également pu être caractérisée.

Peu d'études abordent la question de l'origine des cavités, en raison des hétérogénéités locales inhérentes à une structure amorphe (e.g. les enchevêtrements, les noeuds de réticulations ainsi que des défauts résultant du processus de fabrication) qui agissent comme précurseurs de la cavitation. Aucune clarification expérimentale n'est fournie pour ces hypothèses. Des études in situ à une échelle submicronique pourraient être une étape importante vers la clarification de cette hypothèse.

Le deuxième facteur important à analyser est l'effet d'interaction entre les cavités qui pourrait aggraver les dommages et conduire à des fissures dans le matériau. Dans la première étude de cavitation, Gent et al ont observé deux populations de cavités, à savoir des cavités satellites supposées apparaître autour de cavités primaires en raison d'une concentration de contraintes locales. Le caractère systématique ou non de cette initiation différée n'a pas été clarifié expérimentalement et reste encore une question ouverte. Cette morphologie des dommages a été confirmée par Jaravel (2011) dans son étude sur les caoutchoucs de silicone exposés à l'hydrogène lors de la décompression. Kane Diallo (2016) a abordé les champs de cavités pour mettre en évidence la distribution spatiale des deux populations de cavités. Il a conclu que la distribution du diamètre de la cavité évoluait avec l'augmentation de la pression de saturation ou du taux de décompression et augmentait la tendance à la nucléation différée et à la formation de deux populations. Ono et al ont étudié l'évolution de la décompression due à la cavitation due aux gaz avec une exposition cyclique montrant que l'évolution des dommages n'était pas

un processus cumulatif classique avec réapparition systématique des cavités conduisant à la coalescence. À l'échelle locale, des processus diffuso-mécaniques couplés plus complexes régissent l'évolution des dommages.

Dans ce contexte, l'objectif principal de cette thèse est l'analyse de la cavitation au niveau local, avec une attention particulière portée sur la notion d'hétérogénéité de la distribution et sa corrélation avec le réseau de caoutchouc pour comprendre dans quelle mesure elles sont systématiques. Cela a été fait par une technique d'expérimentation à plusieurs échelles, dont la première étape consiste à accéder aux données de la matrice de caoutchouc à des échelles sub-microniques via SAXS. Cela a été fait pour les matériaux vierges (avant exposition à l'hydrogène) ainsi qu'après décompression. Des tests in situ supplémentaires ont été effectués en utilisant un montage expérimental qui a été développé spécifiquement pour le présent travail et est rapporté ici pour la première fois. Cette technique expérimentale, bien qu'en phase naissante, est la première étape du développement d'un outil robuste pour des tests in situ aussi complexes. À des échelles plus élevées, les dommages ont été suivis in situ à l'aide d'une tomographie à rayons X 3D qui a permis pour la première fois un rendu 3D correct de ces dommages et constitue une nette amélioration par rapport aux techniques de suivi 2D utilisées précédemment. L'obtention des données aux deux échelles était importante pour les simulations effectuées dans FOXTROT, un outil numérique développé à l'Institut P prime pour les problèmes couplés qui a fourni un moyen réaliste de modéliser le phénomène de cavitation résultant du couplage entre la pression hydrostatique et la diffusion de gaz.

Chapitre 2 - Matériaux

Le matériau sur lequel porte la présente étude est le caoutchouc EPDM (Ethylene Propylene Diene Monomer). L'EPDM est un caoutchouc synthétique qui trouve principalement des applications dans les domaines impliquant des solvants, des acides et d'autres produits chimiques agressifs en raison de ses propriétés d'excellente résistance chimique et thermique. Il est notamment utilisé pour la fabrication de joints dans un certain nombre d'applications industrielles, en particulier dans les véhicules à pile à combustible et d'infrastructures associées. De plus, la morphologie et la cinétique de l'endommagement généré dans cet élastomère est accessible par les différentes techniques mises en œuvre dans le travail.

Dans le cas présent, le pourcentage d'éthylène est tel que l'élastomère ne cristallise pas. Des échantillons présentant trois densités volumiques de points de réticulation (qualifiés par la suite d'EPDM 0.1, 0.5 et 1.6) ont été fournis par le laboratoire HYDROGENIUS de l'Université de Kyushu, au Japon. Ils ont été découpés soit dans des feuilles de 2 mm d'épaisseur moulées par compression, soit dans des feuilles de 4 mm d'épaisseur fabriquées par compression thermique de deux feuilles de 2 mm d'épaisseur. Des échantillons cylindriques de diamètre 29 mm et d'épaisseur 13 mm ont également été fournis.

Plusieurs tests ont été effectués pour caractériser les matériaux, principalement pour fournir des données importantes pour la corrélation des paramètres d'endommagement avec le matériau et les caractéristiques de diffusion du matériau lui-même. En effet, l'étude est centrée sur les dommages de l'EPDM pendant la décompression à partir d'un état d'équilibre. Par conséquent, le profil d'hydrogène pendant la désorption des échantillons testés est d'un intérêt particulier et est discuté en fonction des différentes pressions et degrés de réticulation. L'évolution de la teneur en hydrogène a été suivie par TDA (Thermal Desorption Analysis) au sein de disques de 13 mm de diamètre et 2 mm d'épaisseur placés sous un balayage d'argon après saturation sous pression d'hydrogène et décompression.

La concentration d'hydrogène dans l'Argon a été mesurée par chromatographie en phase gazeuse et la teneur en hydrogène résiduel de l'échantillon a été calculée. Le coefficient de diffusion de l'hydrogène dans l'EPDM et la solubilité sont déduits de la courbe obtenue.

Chapitre 3 – Caractérisation sub-micronique par diffusion des rayons X aux petits angles

L'objectif de ce chapitre est de caractériser les hétérogénéités du mélange hydrogène – EPDM dans différentes conditions : avant exposition, à l'équilibre sous pression de gaz, et pendant la décompression puis la désorption.

L'étude de la cavitation dans les polymères utilisant la méthode des SAXS (Small-Angle X-ray Scattering) est bien établie dans la littérature pour les microstructures semi-cristallines. Cependant, la plupart des analyses de ce type de dommages se font dans des conditions purement mécaniques. En comparaison, moins de publications existent pour les études sur les

interactions des polymères entre les polymères et les fluides diffusants. Les expériences SAXS in situ ont été largement utilisées pour étudier les propriétés de diffusion des gels polymères et il existe plusieurs mesures quantitatives de la longueur de corrélation associées à la fois aux fluctuations thermiques et au gel des contraintes topologiques. Ces études se limitent principalement au gonflement des polymères dans un liquide. D'un point de vue pratique, les substances polymères sont poly-dispersées, consistant en des conformations lâches à l'état amorphe et des agrégats aléatoires de couches lamellaires pour des microstructures semi-cristallines. Par conséquent, les études SAXS pour la caractérisation des hétérogénéités locales pour la matrice de caoutchouc amorphe sont plus difficiles que les études des systèmes monodisperses et dépendent de modèles appropriés pour l'interprétation des modèles de diffusion.

Afin de comprendre les changements dans la matrice de caoutchouc dus à la saturation en hydrogène, ainsi que pendant la phase de décompression qui marque le début de la cavitation, des tests in situ sont indispensables. Cependant, les tests in situ sont difficiles à concevoir en raison des difficultés pratiques de manipulation de l'hydrogène en laboratoire. Un dispositif expérimental SAXS pour les tests in situ dans l'hydrogène a été développé par le Laboratoire HYDROGENIUS de l'Université de Kyushu (Japon). Conformément aux réglementations japonaises relatives à l'utilisation du gaz en laboratoire et aux contraintes des conditions de sécurité associées, il faut s'assurer que les tests sont effectués à des pressions très basses inférieures à 1 MPa. Une autre difficulté résultant de l'utilisation d'une source de rayons X de laboratoire est que le temps d'acquisition est généralement long. Il réduit considérablement le nombre de points de données valides, ce qui est particulièrement critique juste après la décompression. Pour cette raison, dans la présente étude, des tests SAXS in situ et ex situ ont été effectués dans diverses installations afin d'obtenir le plus d'informations possible dans différentes conditions de taille de faisceau et à différents moments de dommages. Des tests SAXS ont également été effectués au Kyushu Synchrotron Light Research Center au Japon. Ces campagnes ont été complétées par des mesures SAXS effectuées chez Arkema par S. Tencé-Girault, avec un diamètre de faisceau incident plus faible, sur la même série d'EPDM non-exposés et après décompression sous 30 MPa.

Les tests in situ effectués sur EPDM 0,1 et 0,5 ne montrent aucun changement dans la longueur de corrélation, ce qui indiquerait un changement dans la taille des hétérogénéités dans la matrice de caoutchouc en raison de l'exposition à l'hydrogène. Ceci est cependant dû à la faible

pression de saturation et est confirmé par les résultats des expériences ex situ qui montrent clairement une augmentation de la longueur de corrélation après décompression à partir d'une exposition à haute pression. Cependant, les résultats des expériences de source synchrotron ont montré un plateau léger et diffus qui pourrait être un indicateur possible d'une structure corrélée. Pour clarifier cela, des expériences de diffusion supplémentaires ont donc été menées en explorant une plage de q plus longue qui pourrait permettre l'acquisition à une valeur inférieure de q qui est de 0,05 nm-1. Ce plateau a été observé à nouveau en cas d'échantillons non exposés. Cependant, les résultats ne sont pas directement corrélés à la densité de réticulation des échantillons.

Après l'exposition, aucun maximum n'est détecté. Cela est dû à une diffusion centrale importante qui se superpose aux spectres initiaux, en raison de la diffusion par les cavités apparues dans l'échantillon après décompression à haute pression. Il est important de noter que ces expériences ont été réalisées après la désorption complète de l'hydrogène de l'échantillon. Les spectres des expériences de diffusion effectuées immédiatement après la décompression pendant la désorption d'hydrogène montrent une différence marquée par rapport aux spectres de l'échantillon non exposé. Ces spectres ont tendance à se rapprocher de ceux des échantillons non exposés au fur et à mesure de la désorption, sans toutefois se superposer même après désorption complète du gaz. Ceci indique un changement structurel résiduel dans la matrice de caoutchouc après une seule exposition à l'hydrogène.

Les tests effectués dans la présente étude offrent un point de départ pour concevoir de telles expériences complexes pour de futures études. Dans le cas présent, les tests donnent un aperçu de la taille de l'hétérogénéité dans la matrice de caoutchouc amorphe et mettent en évidence l'effet de l'hydrogène sur la matrice de caoutchouc à très faible échelle.

Chapitre 4 – Suivi des cavités à l'échelle micronique par tomographie RX in-situ

L'approche par SAXS analyse les hétérogénéités en moyenne dans le volume à des échelles fines. L'approche complémentaire qui fait l'objet de ce chapitre permet une visualisation directe de l'endommagement en 3D résolue en temps des cavités, pendant et après

décompression, mais travaille à des échelles supérieures. Cette expérience de tomographie in-situ sous décompression d'hydrogène est inédite dans la littérature. Les difficultés d'observation et de quantification du phénomène de cavitation des élastomères dues à la décompression des gaz sont des facteurs limitants pour l'étude de leur nucléation et de leurs interactions. Typiquement, les techniques appliquées pour la détection des cavités dues à la décompression des gaz sont les mêmes que celles utilisées pour la cavitation induite mécaniquement et leur applicabilité est déjà limitée par les propriétés de l'élastomère. De plus, les propriétés de l'hydrogène et les mesures de sécurité associées conduisent à de fortes limitations dans la conduite d'expériences à haute pression et nécessitent des montages expérimentaux bien développés et sophistiqués.

Ici, nous avons utilisé la technique de tomographie in situ 3D pour suivre l'endommagement à l'échelle d'une seule cavité ou d'un groupe de cavités très proches, avec un intérêt particulier porté aux effets de bord libre et aux effets d'interaction entre cavités. Différentes géométries des échantillons ont été choisies de façon à capter l'endommagement de la manière la plus représentative possible à l'échelle tout en limitant le temps de saturation. La micro-tomographie à rayons X in situ a été réalisée à l'aide d'un tomographe Ultratom développé par RX Solutions®, équipé de la chambre de pression cylindrique (chambre XPRESS) qui permet de réaliser les tests dans différents environnements gazeux. Les essais ont été réalisés sous des pressions d'hydrogène allant jusqu'à 12 MPa. Dans les conditions expérimentales optimisées, la taille du voxel est de 16µm et l'acquisition d'une visualisation s'effectue en 100s à partir de 200 images acquises. Étant donné ces résolutions limitées, les toutes premières étapes de la nucléation ne sont pas accessibles avec une précision robuste. Le temps de nucléation des cavités décrit ici se réfère au premier pas de temps auquel la cavité devient détectable. Les premières cavités apparaissent généralement entre 150 et 300 secondes après la décompression (ces cavités sont appelées cavités primaires), soit vers la fin de la phase de décompression soit complètement après. Les premiers volumes détectés pour les cavités primaires varient fortement, de la vingtaine au millier de voxels.

Une procédure d'analyse d'images est appliquée de façon spécifique à une sélection de cavités isolées ou en proche voisinage.

S'agissant des cavités isolées, deux familles (dites « de bord » ou « en volume ») sont distingués à partir de leur cinétique de croissance et de leur volume maximal. La croissance des cavités de bord est fortement limitée en raison de la proximité de la surface libre tandis que

la cinétique de croissance des cavités en volume est davantage déterminée par d'autres facteurs tels que le temps de nucléation ou d'autres conditions aux limites locales. Les cavités primaires nucléées en volume pendant la phase de décompression et immédiatement après celle-ci ne montrent aucune différence de cinétique. Les cavités secondaires (qui se réfèrent aux cavités isolées qui se sont nucléées après les cavités primaires) ont une cinétique de croissance plus lente. Une simulation de la désorption globale de l'hydrogène à l'échelle de l'échantillon montre que le comportement des cavités secondaires, ainsi que la moindre « durée de vie » des cavités de bord se corrèle à l'évolution de la concentration en gaz au point matériel. Ceci suggère que la quantité de gaz localement présente est une force motrice de la croissance des cavités.

Les cavités isolées sont isotropes pendant la croissance tandis qu'un aplatissement est visible pendant la déflation, ce qui suggère la transition de la cavité vers une fissure, avec une brusque augmentation de l'anisotropie. Ce phénomène n'a pas été approfondi dans le cadre de la thèse. En effet, la résolution de la tomographie in-situ ne permet pas de discriminer mécanisme de fissuration et clusters de cavités dans une direction donnée.

Le second volet de l'analyse porte sur des groupes de quelques cavités (2 à 6) en proche voisinage. L'objectif est de voir, par comparaison aux cavités isolées, dans quelle mesure la présence d'une autre cavité modifie la cinétique de croissance. La distance entre cavités voisines est également mesurée pour éventuellement déterminer une distance critique pour ce phénomène d'interaction. La résolution spatiale de la tomographie borne la distance entre cavités à une valeur minimale de 2 voxels (32 microns).

Dans la gamme de distance explorée (c'est-à-dire pour une distance maximale entre les centres des cavités de 290 à 320 microns), les essais montrent que l'interaction entre les cavités n'affecte pas leur cinétique de croissance. L'effet est en tous cas de second ordre comparativement à d'autres facteurs comme la proximité du bord libre ou le caractère retardé de la nucléation, tout comme pour les cavités isolées. Il n'y a pas non plus d'effet détectable d'anisotropie induite.

L'analyse quantitative par cavité n'est pas possible avec la présente résolution spatiale dans le cas de clusters très regroupés, tels que couramment observé dans les échantillons épais et/ou les pressions de saturation / vitesses de décompressions élevées. Des observations qualitatives

suggèrent néanmoins une évolution de l'endommagement le long d'un chemin qui pourrait également être considéré comme un chemin de nucléation pour les cavités secondaires. Il pourrait être lié au chemin de diffusion du gaz ou pourrait être dû à la contrainte locale et aux conditions de diffusion résultant de la toute première cavité.

Une conclusion importante du travail est que la nucléation est un phénomène localisé tandis que la déflation des cavités semble être davantage due à la désorption globale.

Dans la gamme étroite de densités de réticulation étudiée, les paramètres de taille de cavité semblent être comparables que ce soit à l'échelle de cavités isolées ou pour les cavités en proche voisinage. La taille des clusters de cavités est en revanche plus élevée pour le matériau faiblement réticulé.

Chapitre 5 – Simulation Eléments Finis de l'interaction entre cavités voisines en conditions fortement couplées

Dans un contexte diffuso-mécanique fortement couplé, l'interprétation des mécanismes observés au chapitre précédent se heurte à l'impossibilité d'accéder expérimentalement aux champs mécaniques et de concentration de gaz. Les codes éléments finis existants rencontrent des problèmes de convergence que le code interne Foxtrot développé à l'Institut Pprime tente de surmonter. Dans une dernière partie exploratoire de la thèse, il a été mis à profit pour comparer les gradients générés par une paire de cavités comparativement à une cavité isolée.

Des études numériques pour la modélisation de la croissance des cavités sous chargement purement mécanique existent dans la littérature. Cependant, seules quelques études ont été menées à l'échelle de la cavité dans le cas de la décompression dans les polymères exposés aux gaz à haute pression. Les codes éléments finis existants rencontrent des problèmes de convergence pour résoudre de problème. La difficulté majeure réside dans le calcul du volume d'équilibre de la cavité V_{cav} à chaque pas de temps du calcul, car il dépend de l'équilibre mécanique entre la pression externe appliquée, de la tension superficielle et de la pression interne à l'intérieur de la cavité (P_{int}) qui dépend elle-même du nombre de molécules de gaz contenues à l'intérieur de la cavité (mis à jour à partir du flux gazeux au niveau de la paroi de la cavité) et du volume V_{cav} via la loi des gaz parfaits dans le cas présent :

$$PV = nRT$$

où P est la pression, V est le volume, n est le nombre de moles de gaz, R est la constante de gaz universelle et T est la température. Par conséquent, la solution à ce problème entièrement couplé au niveau de la paroi de la cavité doit être calculée en itérant simultanément les deux phénomènes physiques. Le problème est même accentué dans les caoutchoucs, du fait de l'application de charges haute pression sur des matériaux quasi incompressibles.

En raison du couplage complet entre diffusion et mécanique et de l'absence de suivi direct du champ de contenu gazeux, la discussion sur les mécanismes de croissance des cavités en fonction de leur milieu environnant n'est pas anodine. Seules les simulations de microstructure entièrement couplées du phénomène peuvent fournir des données complémentaires sur le problème de diffusion et apporter le matériel supplémentaire nécessaire pour répondre à cette question. Cependant, de telles simulations entièrement couplées posent des problèmes numériques importants que le développement de ce nouveau code interne d'éléments finis FOXTROT vise à surmonter. La stratégie consiste à conserver le cadre des éléments finis mais à améliorer la résolution du problème diffuso-mécanique.

La cavité est modélisée comme un vide avec continuité de la concentration de gaz au niveau de la paroi de la cavité. La cavité est considérée comme une surface libre avec des conditions aux limites qui créent un flux de gaz au niveau de la paroi de la cavité. Le problème est résolu comme un problème de pression. L'aspect diffuso-mécanique couplé est imposé par la même charge de pression qui a deux sens physiques: la pression hydrostatique mécanique et une pression partielle correspondant à la teneur en gaz en tout point, à la solubilité près donnée par la loi de Henry.

Dans un premier temps, une série de calculs a été réalisée avec des paramètres aussi proches que possible de ceux utilisés lors des expériences menées sur EPDM 1.6. Cependant, plusieurs problèmes ont été rencontrés qui proviennent clairement du couplage fort entre la diffusion et la mécanique au niveau de la paroi de la cavité.

Dans un deuxième temps, les calculs ont été réalisés en utilisant un ensemble modifié de paramètres matériau, de taille de maillage et de pas de temps qui avait précédemment donné des résultats fiables pour la simulation de la croissance d'une seule cavité. Le module a été significativement augmenté, la variation de volume due à la sorption d'hydrogène a été diminuée et la diffusivité $D = \square / \square C_p$ rendue beaucoup plus rapide.

L'objectif était de comparer ces résultats à ceux obtenus par simulation de croissance d'une paire de cavités en proche voisinage, tous les autres paramètres restant identiques. Le diamètre initial des cavités était de 0,2 mm et la taille de la boîte dans laquelle la cavité était placée était de 20x20x20 mm3. Deux autres modèles avec les mêmes dimensions de pièce de 20x20x20 mm3 ont été calculés contenant deux cavités avec le même diamètre initial de 0,2 mm mais séparées par deux distances différentes (0.8 et 0.4 mm entre les centres des cavités). La pression de saturation était égale à 8 MPa.

Dans le cas d'une seule cavité, un gradient de teneur en gaz significatif a été observé autour de la cavité sur une distance d'environ une fois le diamètre. La croissance était logiquement isotrope. Dans le cas de deux cavités, la précision et l'extension spatiale des gradients autour des cavités étaient presque similaires à celles de la direction globale. En revanche, une teneur résiduelle en gaz a été observée dans le ligament entre les cavités. Cette concentration de gaz «piégé» était très proche de la valeur à la surface de la cavité lorsque l'épaisseur du ligament était égale au diamètre de la cavité.

Ces simulations préliminaires indiquent un processus de croissance plutôt localisé et une faible interaction entre les cavités dès que l'épaisseur du ligament les séparant dépasse la valeur équivalente à trois fois le diamètre de la cavité. Elles sont qualitativement cohérentes avec les observations expérimentales du chapitre précédent. Néanmoins, toute transition directe au caoutchouc réel doit être prudente à ce stade.

List of Figures

List of Tables

Bibliography

Amerongen, G J Van. 1964. “Diffusion in Elastomers.” *Rubber Chemistry and Technology* 37 (5): 1065–1152.

Ball, John Macleod. 1982. “Discontinuous Equilibrium Solutions and Cavitation in Nonlinear Elasticity.” *Philosophical Transactions of the Royal Society of London. Series A, Mathematical and Physical Sciences* 306 (1496): 557–611.

baron Fourier, Jean Baptiste Joseph. 1822. *Théorie Analytique de La Chaleur*. F. Didot.

Borsali, Redouane, Huy Nguyen, and R Pecora. 1998. “Small-Angle Neutron Scattering and Dynamic Light Scattering from a Polyelectrolyte Solution: DNA.” *Macromolecules* 31 (5): 1548–55.

Briscoe, B.J, and D. Liatsis. 1992a. “Internal Crack Symmetry Phenomena during Gasinduced Rupture of Elastomers.” *Rubber Chemistry and Technology* 65: 350–73.

Briscoe, B J, and D Liatsis. 1992b. “Internal Crack Symmetry Phenomena during Gas-Induced Rupture of Elastomers.” *Rubber Chemistry and Technology* 65 (2): 350–73. https://doi.org/10.5254/1.3538617.

Briscoe, B J, T Savvas, and C T Kelly. 1994. “‘Explosive Decompression Failure’ of Rubbers: A Review of the Origins of Pneumatic Stress Induced Rupture in Elastomers.” *Rubber Chemistry and Technology* 67 (3): 384–416.

Briscoe, B J, and S Zakaria. 1991. “Interaction of CO2 Gas with Silicone Elastomer at High Ambient Pressures.” *Journal of Polymer Science Part B: Polymer Physics* 29 (8): 989–99.

Brydson, John Andrew. 1999. *Plastics Materials*. Elsevier.

Busse, Warren F. 1938. “Physics of Rubber as Related to the Automobile.” *Journal of Applied Physics* 9 (7): 438–51.

Callister, William D, and David G Rethwisch. 2007. *Materials Science and Engineering: An Introduction*. Vol. 7. John wiley & sons New York.

Campion, R P. 1975. “The Influence of Structure on Autohesion (Self-Tack) and Other Forms of Diffusion into Polymers.” *The Journal of Adhesion* 7 (1): 1–23.

Castagnet, Sylvie, David Mellier, Azdine Nait-Ali, and Guillaume Benoit. 2018. “In-Situ X-Ray Computed Tomography of Decompression Failure in a Rubber Exposed to High-Pressure Gas.” *Polymer Testing* 70 (September): 255–62. https://doi.org/10.1016/J.POLYMERTESTING.2018.07.017.

Castagnet, Sylvie, Hiroaki Ono, and Guillaume Benoit. 2017. "ScienceDirect Swelling Measurement during Sorption and Decompression in a NBR Exposed to High-Pressure Hydrogen." *International Journal of Hydrogen Energy* 42 (30): 19359–66. https://doi.org/10.1016/j.ijhydene.2017.06.138.

Chazeau, Laurent, J D Brown, L C Yanyo, and S S Sternstein. 2000. "Modulus Recovery Kinetics and Other Insights into the Payne Effect for Filled Elastomers." *Polymer Composites* 21 (2): 202–22.

Chen, Pu. 2005. *Molecular Interfacial Phenomena of Polymers and Biopolymers*. Taylor & Francis US.

Colton, Jonathan S, and Nam P Suh. 1987. "Nucleation of Microcellular Foam: Theory and Practice." *Polymer Engineering & Science* 27 (7): 500–503.

Crank, John. 1975. *The Mathematics of Diffusion*. Clarendon Press.

Cristiano, Antonella, Alba Marcellan, Bert J Keestra, Paul Steeman, and Costantino Creton. 2011. "Fracture of Model Polyurethane Elastomeric Networks," 355–67. https://doi.org/10.1002/polb.22186.

Cristiano, Antonella, Alba Marcellan, Rong Long, Chung-yuen Hui, J A N Stolk, and Costantino Creton. 2010. "An Experimental Investigation of Fracture by Cavitation of Model Elastomeric Networks" 48: 1409–22. https://doi.org/10.1002/POLB.

Daphalapurkar, N P, J C Hanan, N B Phelps, H Bale, and H Lu. 2008. "Tomography and Simulation of Microstructure Evolution of a Closed-Cell Polymer Foam in Compression." *Mechanics of Advanced Materials and Structures* 15 (8): 594–611.

Defebvin, Juliette, Sophie Barrau, Grégory Stoclet, Cyrille Rochas, and Jean-Marc Lefebvre. 2016. "In Situ SAXS/WAXS Investigation of the Structural Evolution of Poly (Vinylidene Fluoride) upon Uniaxial Stretching." *Polymer* 84: 148–57.

Denecour, R L, and A N Gent. 1968. "Bubble Formation in Vulcanized Rubbers." *Journal of Polymer Science Part A-2: Polymer Physics* 6 (11): 1853–61. https://doi.org/doi:10.1002/pol.1968.160061103.

Diani, Julie, Mathias Brieu, and Pierre Gilormini. 2006. "Observation and Modeling of the Anisotropic Visco-Hyperelastic Behavior of a Rubberlike Material." *International Journal of Solids and Structures* 43 (10): 3044–56.

Diani, Julie, Bruno Fayolle, and Pierre Gilormini. 2009. "A Review on the Mullins Effect." *European Polymer Journal* 45 (3): 601–12.

Dibbanti, Murali Krishna, Michele Mauri, Lucio Mauri, Gabriele Medaglia, and Roberto Simonutti. 2015. "Probing Small Network Differences in Sulfur-cured Rubber Compounds by Combining Nuclear Magnetic Resonance and Swelling Methods." *Journal of Applied Polymer Science* 132 (43).

Dollhofer, J., A. Chiche, V. Muralidharan, C. Creton, and C. Y. Hui. 2004. "Surface Energy Effects for Cavity Growth and Nucleation in an Incompressible Neo-Hookean Material - Modeling and Experiment." *International Journal of Solids and Structures* 41 (22–23):

6111–27. https://doi.org/10.1016/j.ijsolstr.2004.04.041.

Embury, P. 2004. “High-Pressure Gas Testing of Elastomer Seals and a Practical Approach to Designing for Explosive Decompression Service.” *Sealing Technology*, no. June: 6–11.

Farge, Laurent, Stéphane Andre, Andrzej Pawlak, Christophe Baravian, Sarah C Irvine, and Adrian-Marie Philippe. 2013. “A Study of the Deformation-induced Whitening Phenomenon for Cavitating and Non-cavitating Semicrystalline Polymers.” *Journal of Polymer Science Part B: Polymer Physics* 51 (10): 826–41.

Flichy, N M B, S G Kazarian, C J Lawrence, and B J Briscoe. 2002. “An ATR− IR Study of Poly (Dimethylsiloxane) under High-Pressure Carbon Dioxide: Simultaneous Measurement of Sorption and Swelling.” *The Journal of Physical Chemistry B* 106 (4): 754–59.

Flory, Paul J. 1953. *Principles of Polymer Chemistry*. Cornell University Press.

Fond, C. 2001. “Cavitation Criterion for Rubber Materials: A Review of Void-growth Models.” *Journal of Polymer Science Part B: Polymer Physics* 39 (17): 2081–96.

Geissler, Erik, Ferenc Horkay, Anne Marie Hecht, Cyrille Rochas, Peter Lindner, Claudie Bourgaux, and Guy Couarraze. 1997. “Investigation of PDMS Gels and Solutions by Small Angle Scattering.” *Polymer* 38 (1): 15–20. https://doi.org/10.1016/S0032-3861(96)00490-9.

Gent, A. N. 2011. “Cavitation in Rubber: A Cautionary Tale.” *Rubber Chemistry and Technology*. https://doi.org/10.5254/1.3538266.

Gent, A. N., and Byoungkyeu Park. 1984. “Failure Processes in Elastomers at or near a Rigid Spherical Inclusion.” *Journal of Materials Science* 19 (6): 1947–56. https://doi.org/10.1007/BF00550265.

Gent, A. N., and D. A. Tompkins. 1969. “Nucleation and Growth of Gas Bubbles in Elastomers.” *Journal of Applied Physics* 40: 2520–25. https://doi.org/10.1063/1.1658026.

Gent, A N, and P B Lindley. 1959. “Internal Rupture of Bonded Rubber Cylinders in Tension.” *Proceedings of the Royal Society of London. Series A. Mathematical and Physical Sciences* 249 (1257): 195–205.

Griffith, Alan Arnold. 1921. “VI. The Phenomena of Rupture and Flow in Solids.” *Philosophical Transactions of the Royal Society of London. Series A, Containing Papers of a Mathematical or Physical Character* 221 (582–593): 163–98.

Grobler, J H A, and W J McGill. 1994. “Effect of Network Heterogeneity on Tensile and Tear Strengths of Radiation, Peroxide, Efficient and Conventional Cured Polyisoprene.” *Journal of Polymer Science Part B: Polymer Physics* 32 (2): 287–95.

Hang-Sheng, Hou, and Rohan Abeyaratne. 1992. “Cavitation in Elastic and Elastic-Plastic Solids.” *Journal of the Mechanics and Physics of Solids* 40 (3): 571–92.

Haward, R N. 1970. “Occupied Volume of Liquids and Polymers.” *Journal of Macromolecular Science—Reviews in Macromolecular Chemistry* 4 (2): 191–242.

Hocine, N Aït, A Hamdi, M Naït Abdelaziz, P Heuillet, and Fahmi Zaïri. 2011. “Experimental and Finite Element Investigation of Void Nucleation in Rubber-like Materials.” *International Journal of Solids and Structures* 48 (9): 1248–54.

Horkay, Ferenc, Peter J Basser, Anne-Marie Hecht, and Erik Geissler. 2000. “Osmotic and SANS Observations on Sodium Polyacrylate Hydrogels in Physiological Salt Solutions.” *Macromolecules* 33 (22): 8329–33.

Hourdet, D, F L’alloret, A Durand, F Lafuma, R Audebert, and J P Cotton. 1998. “Small-Angle Neutron Scattering Study of Microphase Separation in Thermoassociative Copolymers.” *Macromolecules* 31 (16): 5323–35.

Humbert, S, O Lame, J M Chenal, C Rochas, and G Vigier. 2010. “New Insight on Initiation of Cavitation in Semicrystalline Polymers : In-Situ SAXS Measurements,” 7212–21. https://doi.org/10.1021/ma101042d.

Ikeda, Yuko, Norihito Higashitani, Kensuke Hijikata, Yota Kokubo, Yuichi Morita, Mitsuhiro Shibayama, Noboru Osaka, Takuya Suzuki, Hitoshi Endo, and Shinzo Kohjiya. 2009. “Vulcanization: New Focus on a Traditional Technology by Small-Angle Neutron Scattering.” *Macromolecules* 42 (7): 2741–48.

Jaravel, Julien, Sylvie Castagnet, Jean-claude Grandidier, and Guillaume Benoît. 2011. “On Key Parameters in Fl Uencing Cavitation Damage upon Fast Decompression in a Hydrogen Saturated Elastomer.” *Polymer Testing* 30 (8): 811–18. https://doi.org/10.1016/j.polymertesting.2011.08.003.

Jaravel, Julien, Sylvie Castagnet, Jean-claude Grandidier, and Mikaël Gueguen. 2013. “International Journal of Solids and Structures Experimental Real-Time Tracking and Diffusion / Mechanics Numerical Simulation of Cavitation in Gas-Saturated Elastomers.” *International Journal of Solids and Structures* 50 (9): 1314–24. https://doi.org/10.1016/j.ijsolstr.2013.01.001.

Jarrin, Jacques, Bernard Dewimille, and Elizabeth Devaux. 1994. “Blistering of Thermoplastic Materials Used in the Petroleum Industry.” In *SPE Annual Technical Conference and Exhibition*. Society of Petroleum Engineers.

Jiang, H, W Su, P T Mather, and T J Bunning. 1999. “Rheology of Highly Swollen Chitosan / Polyacrylate Hydrogels” 40: 4593–4602.

Kabaria, Hardik, Adrian J Lew, and Bernardo Cockburn. 2015. “A Hybridizable Discontinuous Galerkin Formulation for Non-Linear Elasticity.” *Computer Methods in Applied Mechanics and Engineering* 283: 303–29.

Kamiya, Yoshinori, Keishin Mizoguchi, Katsuhiko Terada, Yukihiko Fujiwara, and Jin-sheng Wang. 1998. “CO 2 Sorption and Dilation of Poly (Methyl Methacrylate)” 9297 (97): 472–78.

Kane-Diallo, Ousseynou, Sylvie Castagnet, Azdine Nait-Ali, Guillaume Benoit, and Jean Claude Grandidier. 2016. “Time-Resolved Statistics of Cavity Fields Nucleated in a Gas-

Exposed Rubber under Variable Decompression Conditions - Support to a Relevant Modeling Framework." *Polymer Testing* 51: 122–30. https://doi.org/10.1016/j.polymertesting.2016.03.004.

KOGA, Atsushi, Tadahisa YAMABE, Hiroyuki SATO, Kenichi UCHIDA, Junichi NAKAYAMA, Junichiro YAMABE, and Shin NISHIMURA. 2012. "A Visualizing Study of Blister Fracture in Rubber O-Rings." *NIPPON GOMU KYOKAISHI* 85 (5): 162–67. https://doi.org/10.2324/gomu.85.162.

Lachambre, J, E Maire, J Adrien, and D Choqueuse. 2013. "In Situ Observation of Syntactic Foams under Hydrostatic Pressure Using X-Ray Tomography." *Acta Materialia* 61 (11): 4035–43.

Laiarinandrasana, Lucien, Thilo F Morgeneyer, Henry Proudhon, and Cédric Regrain. 2010. "Damage of Semicrystalline Polyamide 6 Assessed by 3D X-ray Tomography: From Microstructural Evolution to Constitutive Modeling." *Journal of Polymer Science Part B: Polymer Physics* 48 (13): 1516–25.

Lee, B J, and M E Mear. 1994. "Studies of the Growth and Collapse of Voids in Viscous Solids." *Journal of Engineering Materials and Technology* 116 (3): 348–58.

Li, Zhi Hong. 2013. "A Program for SAXS Data Processing and Analysis." *Chinese Physics C* 37 (10). https://doi.org/10.1088/1674-1137/37/10/108002.

Lindsey, Gerald H, and Gerald H Lindsey. 2013. "Triaxial Fracture Studies Modeling of Shear Ductile Fracture Considering a Changeable Cut-off Value for Stress Triaxiality Internal Fracture of Glass under Triaxial Tension Induced by Thermal Shock Triaxial Fracture Studies *" 4843 (1967). https://doi.org/10.1063/1.1709232.

Lion, A, C Kardelky, and P Haupt. 2003. "On the Frequency and Amplitude Dependence of the Payne Effect: Theory and Experiments." *Rubber Chemistry and Technology* 76 (2): 533–47.

Liu, Li-Zhi, Benjamin S Hsiao, Bruce X Fu, Shaofeng Ran, Shigeyuki Toki, Benjamin Chu, Andy H Tsou, and Pawan K Agarwal. 2003. "Structure Changes during Uniaxial Deformation of Ethylene-Based Semicrystalline Ethylene− Propylene Copolymer. 1. SAXS Study." *Macromolecules* 36 (6): 1920–29.

Lopez-pamies, Oscar. 2009. "Onset of Cavitation in Compressible , Isotropic , Hyperelastic Solids," 115–45. https://doi.org/10.1007/s10659-008-9187-8.

Lorge, O, B J Briscoe, and P Dang. 1999. "Gas Induced Damage in Poly (Vinylidene Fluoride) Exposed to Decompression." *Polymer* 40 (11): 2981–91.

Major, Z, K Lederer, M Moitzi, M Mitterhuber, T Schwarz, and R W Lang. 2006. "Test and Failure Analysis Methodology for Elastomeric Seals Exposed to Explosive Decompression [Prüfungs- Und Versagensanalyse Für Die Explosive Dekompression Elastomerer Dichtungen]." *Gummi, Fasern, Kunststoffe*.

Masquelier, I, and Y Marco. 2013. “Fatigue Damage in Carbon Black Filled Natural Rubber Investigated by X-Ray Microtomography and Scanning Electron Microscopy.” *Constitutive Models for Rubber VIII*, 393.

McCallum, Tara J, Marianna Kontopoulou, Chul B Park, Anson Wong, and Seong G Kim. 2008. “Effect of Branched PP Content on the Physical Properties and Cell Growth during Foaming of TPOs.” *Journal of Applied Polymer Science* 110 (2): 817–24.

Morgeneyer, Thilo F, Henry Proudhon, Peter Cloetens, Wolfgang Ludwig, Quentin Roirand, Lucien Laiarinandrasana, and Eric Maire. 2014. “Nanovoid Morphology and Distribution in Deformed HDPE Studied by Magnified Synchrotron Radiation Holotomography.” *Polymer* 55 (25): 6439–43.

Morozinis, Athanasios K, Christos Tzoumanekas, Stefanos D Anogiannakis, and Doros N Theodorou. 2013. “Atomistic Simulations of Cavitation in a Model Polyethylene Network.” *Polymer Science Series C* 55 (1): 212–18.

Moschovidis, Zissis Andrew, and T Mura. 1975. “Two-Ellipsoidal Inhomogeneities by the Equivalent Inclusion Method.” *Journal of Applied Mechanics* 42 (4): 847–52.

Mullins, L. 1948. “Effect of Stretching on the Properties of Rubber.” *Rubber Chemistry and Technology* 21 (2): 281–300.

Mura, Toshio. 2013. *Micromechanics of Defects in Solids*. Springer Science & Business Media.

Muralidharan, Vijayanand, C Y Hui, J Dollhofer, C Creton, and Y Y Lin. 2006. “Machine Compliance and Hardening Effects on Cavity Growth in Soft Adhesives” 26: 117–24. https://doi.org/10.1016/j.ijadhadh.2005.03.001.

Murphy, Jeremiah G, and Shiro Biwa. 1997. “Nonmonotonic Cavity Growth in Finite, Compressible Elasticity.” *International Journal of Solids and Structures* 34 (29): 3859–72.

Nakamura, Toshio, and Oscar Lopez-Pamies. 2012. “A Finite Element Approach to Study Cavitation Instabilities in Non-Linear Elastic Solids under General Loading Conditions.” *International Journal of Non-Linear Mechanics* 47 (2): 331–40.

Naqui, S I, and I M Robinson. 1993. “Tensile Dilatometric Studies of Deformation in Polymeric Materials and Their Composites.” *Journal of Materials Science* 28 (6): 1421–29.

Nishimura, S. 2014. “Fracture Behaviour of Ethylene Propylene Rubber for Hydrogen Gas Sealing under High Pressure Hydrogen,” no. 12: 360–66.

Oberth, A. E., and R. S. Bruenner. 1965. “Tear Phenomena around Solid Inclusions in Castable Elastomers.” *Transactions of the Society of Rheology* 9 (2): 165–85. https://doi.org/10.1122/1.548997.

Ogieglo, Wojciech, Hans van der Werf, Kristianne Tempelman, Herbert Wormeester, Matthias Wessling, Arian Nijmeijer, and Nieck E. Benes. 2013. “N-Hexane Induced Swelling of Thin PDMS Films under Non-Equilibrium Nanofiltration Permeation Conditions, Resolved by Spectroscopic Ellipsometry.” *Journal of Membrane Science* 437: 313–23.

https://doi.org/10.1016/j.memsci.2013.04.039.

Ohyama, Keiko, Hirotada Fujiwara, and Shin Nishimura. 2017. "ScienceDirect Inhomogeneity in Acrylonitrile Butadiene Rubber during Hydrogen Elimination Investigated by Small-Angle X-Ray Scattering." *International Journal of Hydrogen Energy* 43 (2): 1012–24. https://doi.org/10.1016/j.ijhydene.2017.10.162.

Ono, Hiroaki, Hirotada Fujiwara, and Shin Nishimura. 2018a. "Penetrated Hydrogen Content and Volume Inflation in Unfilled NBR Exposed to High-Pressure Hydrogen–What Are the Characteristics of Unfilled-NBR Dominating Them?" *International Journal of Hydrogen Energy* 43 (39): 18392–402. https://doi.org/10.1016/j.ijhydene.2018.08.031.

Ono, Hiroaki, Azdine Nait-ali Ousseynou, Kane Diallo, Guillaume Benoit, and Sylvie Castagnet. 2018. "Influence of Pressure Cycling on Damage Evolution in an Unfilled EPDM Exposed to High-Pressure Hydrogen." *International Journal of Fracture*. https://doi.org/10.1007/s10704-018-0266-y.

Park, Chul B, and Lewis K Cheung. 1997. "A Study of Cell Nucleation in the Extrusion of Polypropylene Foams." *Polymer Engineering & Science* 37 (1): 1–10.

Patterson, Brian M, Nikolaus L Cordes, Kevin Henderson, Jason J Williams, Tyler Stannard, Sudhanshu S Singh, Angel Rodriguez Ovejero, Xianghui Xiao, Mathew Robinson, and Nikhilesh Chawla. 2016. "In Situ X-Ray Synchrotron Tomographic Imaging during the Compression of Hyper-Elastic Polymeric Materials." *Journal of Materials Science* 51 (1): 171–87.

Patterson, Brian M, Kevin Henderson, and Zachary Smith. 2013. "Measure of Morphological and Performance Properties in Polymeric Silicone Foams by X-Ray Tomography." *Journal of Materials Science* 48 (5): 1986–96.

Pawlak, Andrzej, Andrzej Galeski, and Artur Rozanski. 2014. "Cavitation during Deformation of Semicrystalline Polymers." *Progress in Polymer Science* 39 (5): 921–58.

Payne, Arthur R. 1962. "The Dynamic Properties of Carbon Black-loaded Natural Rubber Vulcanizates. Part I." *Journal of Applied Polymer Science* 6 (19): 57–63.

Pelerin, Maxime, Andrew King, Lucien Laiarinandrasana, and Henry Proudhon. 2019. "Development of a Versatile Mechanical Testing Device for In Situ Synchrotron Tomography and Diffraction Experiments."

Pérez-tamarit, S, E Solórzano, R Mokso, and M A Rodríguez-pérez. 2019. "In-Situ Understanding of Pore Nucleation and Growth in Polyurethane Foams by Using Real-Time Synchrotron X-Ray Tomography." *Polymer* 166 (November 2018): 50–54. https://doi.org/10.1016/j.polymer.2019.01.049.

Peters, L. 1990. "Silica Reinforcement of Oil Field Elastomers for Improved Decompression Resistance." *Rubber World* 203 (3): 30–35.

Poulet, Pierre-Alexis, Gilles Hochstetter, Andrew King, Henry Proudhon, Sébastien Joannès,

and Lucien Laiarinandrasana. 2016. “Observations by In-Situ X-Ray Synchrotron Computed Tomography of the Microstructural Evolution of Semi-Crystalline Polyamide 11 during Deformation.” *Polymer Testing* 56: 245–60.

Prima, M A Di, K Gall, D L McDowell, R Guldberg, A Lin, T Sanderson, D Campbell, and S C Arzberger. 2010. “Cyclic Compression Behavior of Epoxy Shape Memory Polymer Foam.” *Mechanics of Materials* 42 (4): 405–16.

Pugh, T, and J Goodson. 1992. “Developing Elastomer Seals for Downhole Safety Valves[Materials Must Withstand Explosive Decompression and Methyl Alcohol Swell].” *Offshore, Incorporating the Oilman* 52: 39–40.

Ramsey, Norman F. 1996. “1 - Thermal Beam Sources.” In *Atomic, Molecular, and Optical Physics: Atoms and Molecules*, edited by F B Dunning and Randall G B T - Experimental Methods in the Physical Sciences Hulet, 29:1–20. Academic Press. https://doi.org/https://doi.org/10.1016/S0076-695X(08)60783-8.

Ravi-chandar, Victor Lefèvre K, and Oscar Lopez-pamies. 2014. “Cavitation in Rubber : An Elastic Instability or a Fracture Phenomenon ?” https://doi.org/10.1007/s10704-014-9982-0.

Rosenberg, E, N Brusselle-dupend, and T Epsztein. 2011. “A Mesoscale Quantification Method of Cavitation in Semicrystalline Polymers Using X-Ray Microtomography.” *Materials Science & Engineering A* 528 (21): 6535–44. https://doi.org/10.1016/j.msea.2011.04.091.

Royer, Joseph R, Joseph M DeSimone, and Saad A Khan. 1999. “Carbon Dioxide-Induced Swelling of Poly (Dimethylsiloxane).” *Macromolecules* 32 (26): 8965–73.

Rudin, A, and P Choi. 2013. “Chapter 4-Mechanical Properties of Polymer Solids and Liquids.” *The Elements of Polymer Science & Engineering*, 149–229.

Russ, John C, and Robert T Dehoff. 2012. *Practical Stereology*. Springer Science & Business Media.

Schrittesser, B., G. Pinter, Th. Schwarz, Z. Kadar, and T. Nagy. 2016. “Rapid Gas Decompression Performance of Elastomers – A Study of Influencing Testing Parameters.” *Procedia Structural Integrity* 2: 1746–54. https://doi.org/10.1016/j.prostr.2016.06.220.

Shibayama, Mitsuhiro. 1998. “Spatial Inhomogeneity and Dynamic Fluctuations of Polymer Gels” 30: 1–30.

Sixou, B. 2007. “Molecular Dynamics Simulation of the First Stages of the Cavitation Process in Amorphous Polymers.” *Molecular Simulation* 33 (12): 965–73. https://doi.org/10.1080/08927020701502057.

Stevenson, A, and G Morgan. 1995. “Fracture of Elastomers by Gas Decompression.” *Rubber Chemistry and Technology* 68: 197–211.

Stewart, Charles W. 1971. “Nucleation and Growth of Bubbles in Elastomers.” *Rubber Chemistry and Technology* 44 (5): 1363–79. https://doi.org/10.5254/1.3544817.

Suzuki, Takuya, Noboru Osaka, Hitoshi Endo, Mitsuhiro Shibayama, Yuko Ikeda, Hanako Asai, Norihito Higashitani, Yota Kokubo, and Shinzo Kohjiya. 2010. “Nonuniformity in Cross-Linked Natural Rubber as Revealed by Contrast-Variation Small-Angle Neutron Scattering.” *Macromolecules* 43 (3): 1556–63.

Takaoka, Masanori, Tatsuya Sakoda, Masahisa Otsubo, Shigeru Akaiwa, Masatoshi Iki, and Shigeharu Nakano. 2008. “Studies of Elastic Waves in Ethylene Propylene Rubber Using Acoustic Emission Sensor.” *IEEJ Transactions on Fundamentals and Materials* 128 (10): 641–46.

Thoguluva, Raghavan, and Dr Thoguluva Vijayaram. 2019. “A TECHNICAL REVIEW ON RUBBER,” August.

Thurecht, Kristofer J, David J T Hill, and Andrew K Whittaker. 2005. “Equilibrium Swelling Measurements of Network and Semicrystalline Polymers in Supercritical Carbon Dioxide Using High-Pressure NMR.” *Macromolecules* 38 (9): 3731–37.

Wang, Weiwang, Yasuhiro Tanaka, Tatsuo Takada, Shinya Iwata, Hiroaki Uehara, and Shengtao Li. 2018. “Influence of Oxidation on the Dynamics in Amorphous Ethylene-Propylene-Diene-Monomer Copolymer: A Molecular Dynamics Simulation.” *Polymer Degradation and Stability* 147: 187–96.

Williams, M L, and R A Schapery. 1965. “Spherical Flaw Instability in Hydrostatic Tension.” *International Journal of Fracture Mechanics* 1 (1): 64–72.

Xin-Chun, Shang, and Cheng Chang-Jun. 2001. “Exact Solution for Cavitated Bifurcation for Compressible Hyperelastic Materials.” *International Journal of Engineering Science* 39 (10): 1101–17.

Xiong, B, O Lame, J M Chenal, C Rochas, R Seguela, and G Vigier. 2013. “In-Situ SAXS Study and Modeling of the Cavitation / Crystal-Shear Competition in Semi-Crystalline Polymers : In Fl Uence of Temperature and Microstructure in Polyethylene.” *Polymer* 54 (20): 5408–18. https://doi.org/10.1016/j.polymer.2013.07.055.

Xiong, Bijin, Olivier Lame, Jean-Marc Chenal, Cyrille Rochas, Roland Seguela, and Gerard Vigier. 2014. “In-Situ SAXS Study of the Mesoscale Deformation of Polyethylene in the Pre-Yield Strain Domain: Influence of Microstructure and Temperature.” *Polymer* 55 (5): 1223–27.

Yamabe, Junichiro, and Shin Nishimura. 2009. “Influence of Fillers on Hydrogen Penetration Properties and Blister Fracture of Rubber Composites for O-Ring Exposed to High-Pressure Hydrogen Gas.” *International Journal of Hydrogen Energy* 34 (4): 1977–89. https://doi.org/10.1016/j.ijhydene.2008.11.105.

Yerzley, Felix L. 1939. “Adhesion of Neoprene to Metal.” *Industrial & Engineering Chemistry* 31 (8): 950–56.

Youssef, Souhail, Eric Maire, and Roger Gaertner. 2005. “Finite Element Modelling of the Actual Structure of Cellular Materials Determined by X-Ray Tomography.” *Acta*

Materialia 53 (3): 719–30.

Zakaria, S. 1990. “Why Rubber Explodes.” *Chemtech* 20 (8): 492–95.

Zhang, Huan, Arthur K Scholz, Yannick Merckel, Mathias Brieu, Daniel Berghezan, Edward J Kramer, and Costantino Creton. 2013. “Strain Induced Nanocavitation and Crystallization in Natural Rubber Probed by Real Time Small and Wide Angle X-Ray Scattering,” 1125–38. https://doi.org/10.1002/polb.23313.

Zhang, Yi, Kishore K Gangwani, and Richard M Lemert. 1997. “Sorption and Swelling of Block Copolymers in the Presence of Supercritical Fluid Carbon Dioxide.” *The Journal of Supercritical Fluids* 11 (1): 115–34. https://doi.org/https://doi.org/10.1016/S0896-8446(97)00031-4.

Résumé

Le domaine de recherche concerne l'endommagement par cavitation des élastomères exposés à de fortes pressions de gaz diffusant. Ce phénomène résulte de l'expansion locale du gaz préalablement absorbé, lorsque la désorption hors du polymère est trop lente par rapport au chargement imposé. Dans le cas de l'hydrogène qui nous intéresse ici, l'enjeu est le développement de matériaux polymères performants pour les structures de stockage et de distribution d'hydrogène gazeux hyperbare. En conditions d'usage, ces matériaux sont exposés à de fortes pressions d'hydrogène qui diffuse en leur sein et génèrent ensuite de forts endommagements lorsque la pression hydrostatique est relâchée. Les études de laboratoire sur ce sujet restent peu nombreuses, a fortiori sous environnement hydrogène. Sur le plan expérimental, ceci s'explique par la délicate manipulation de l'hydrogène et par le contexte des fortes pressions. Sur le plan de la simulation numérique, un verrou important est lié aux couplages forts entre diffusion et mécanique dans la résolution de l'équilibre de la cavité à chaque instant de son évolution.

Cette thèse vise à mieux comprendre le mécanisme élémentaire de formation, puis de croissance et de coalescence des cavités, isolées ou en proche voisinage. Dans ce dernier cas, une éventuelle interaction doit effectivement être caractérisée pour éclairer la coalescence et la transition vers des fissures macroscopiques.

Le travail a été mené sur série d'Ethylène Propylène Diène Monomer (EPDM) non-renforcés, avec une densité de points de réticulation variable, exposés à des pressions allant jusqu'à 30 MPa. Le volet expérimental s'appuie sur deux des techniques expérimentales in situ les plus récentes.

La diffusion des rayons X aux petits angles (SAXS) vise à caractériser les hétérogénéités du système réseau élastomère – hydrogène à l'échelle submicronique, et éventuellement à détecter les premiers stades de cavitation. Dans la gamme des faibles pressions accessible sous environnement hydrogène, les hétérogénéités ne sont pas assez marquées pour définir plus qu'une distance de corrélation, qui varie très peu comparativement au matériau non exposé. Après exposition à une pression plus élevée (30 MPa), une augmentation de la distance de corrélation est observée, révélant une modification de l'hétérogénéité de la matrice, irréversible même après désorption complète de l'échantillon. À l'échelle micronique, des expériences de tomographie X in-situ (sous des pressions allant jusqu'à 12 MPa) fournissent des vues 3D résolues en temps des cavités, pendant et après décompression. Ces expériences ont permis de mieux comprendre la cinétique de croissance des cavités dans différentes conditions aux limites locales (dans le volume de l'échantillon, à proximité d'autres cavités, près d'une surface libre) et de les interpréter en regard des propriétés de diffusion de l'échantillon lui-même. Plusieurs populations de cavités, présentant des comportements différents, ont ainsi pu être distinguées en fonction de leur distance à la surface libre de l'échantillon, en lien avec la désorption globale de l'échantillon. Comparativement à cet effet de bord libre, la présence d'une autre cavité en proche voisinage (i.e. à une distance bord à bord supérieure ou égale à 30µm) n'a qu'une influence minime. Les résultats suggèrent que la croissance de la cavité est un processus très local.

Dans un contexte diffuso-mécanique fortement couplé, l'interprétation des mécanismes se heurte à l'impossibilité d'accéder expérimentalement aux champs mécaniques et de concentration de gaz. Les codes éléments finis existants rencontrent des problèmes de convergence que le code interne Foxtrot développé à l'Institut Pprime tente de surmonter. Dans une dernière partie exploratoire de la thèse, il a été mis à profit pour comparer les gradients générés par une paire de cavités comparativement à une cavité isolée.

Mots clés : Cavitation, Élastomères, Éléments finis, Méthode des, Endommagement, mécanique de l'(milieux continus), Hydrogène, Matériaux--Effets des hautes pressions, Tomographie

ABSTRACT

The optimum design and formulation of seals used in hydrogen transport system is crucial for the purposes of safety of operation and well as economic sustainability of hydrogen as energy carrier. The exposure of the sealing materials to hydrogen and subsequent decompression causes cavitation damage. The studies so far on this subject have been few due to the strong limitations arising from the safety issues related to hydrogen testing in laboratory conditions. This study addresses the cavitation in Ethylene Propylene Diene Rubber (EPDM) due to pressure release after exposure to high-pressure hydrogen up to 30 MPa. Three different unfilled EPDM with variable cross-link density were investigated.

The study was based on some of the newest in-situ experimental techniques which allow a time-resolved tracking of the evolution of damage. On one side, in-situ SAXS (Small Angle X-ray Scattering) tests of hydrogen-exposed EPDM were aimed at the characterisation of EPDM at submicron scale as a function of network heterogeneity and for tracking the possible onset of distinguishable cavities. At the low pressure range accessible with the device, heterogeneities were not marked enough to define more than a correlation length that was significantly changed compared the unexposed material, whatever the cross-link density. After the exposure at higher pressure (30 MPa) a change in correlation length was observed corresponding to the change in heterogeneity of the matrix which was found to be non-reversible even after full desorption of the sample. At a higher scale, in-situ X-ray tomography was used to provide time-resolved 3D views of damage during and after hydrogen pressure release. These experiments provided insight into the growth kinetics of cavities in different local boundary conditions (within the bulk, close to other cavities, close to a free surface) correlated with the diffusion characteristics of the sample itself. Classification of cavities as bulk and edges cavities was possible with respect with different kinetics depending on their proximity to the free surface of the sample. This could be correlated with the diffusion characteristics of the material. The dependence of kinetics of cavities on the proximity of another cavity was found to be trivial at the scale investigated (above 30 µm between cavity borders) suggesting that growth is a very local process.

The previous studies have clarified that the cavitation in rubber is a coupled diffuso-mechanical phenomenon and so far, the numerical tools available have not addressed the problem as such. Therefore, the development of a numerical tool aimed at solving such coupled problems has also been addressed in the present work. This numerical tool called Foxtrot, developed at Institut PPRIME, is in the early stages of development but is a crucial step towards the more realistic simulation of this phenomenon of cavitation.

In this fully coupled diffuso-mechanical context, the interpretation of mechanisms is highly limited by the lack of experimental access to the mechanical and gas content fields. Commercial Finite Element codes face convergence problems that the internal code developed at the Pprime Institute (Foxtrot) is trying to overcome. In the last exploratory part of the thesis, the code was used to as a step towards a more realistic simulation of the phenomenon. In particular, gradients around a pair of cavities were compared to those obtained around an isolated cavity.

Keywords: Cavitation, Elastomers, Finite element method, Continuum damage mechanics, Hydrogen, Materials at high pressures, Tomography